THÈSE

Pour obtenir le grade de

DOCTEUR DE L'UNIVERSITÉ GRENOBLE ALPES
et de l'UNIVERSITE CENTRAL CHINA NORMAL UNIVERSITY

École doctorale : PHY - Physique
Spécialité : Physique Subatomique et Astroparticules
Unité de recherche : Laboratoire de Physique Subatomique et Cosmologie

Mesure de la section efficace des photons directs isolés dans les collisions pp à 13 TeV avec le détecteur ALICE au LHC

Isolated direct photon cross section measurement in pp collisions at 13 TeV with the ALICE detector at LHC

Présentée par :

Ran XU

Direction de thèse :

Gustavo CONESA BALBASTRE Chargé de recherche HDR, CNRS - Délégation Alpes	Directeur de thèse
Daicui ZHOU Professeur, Central China Normal University	Directeur de thèse

Rapporteurs :

François ARLEO
Chargé de recherche HDR, Université de Nantes
Shuang LI
Professeur, China Three Gorges University

Thèse soutenue publiquement le **26/05/2025**, devant le jury composé de :

Guoliang MA Professeur, Fudang Universuity	Président
François ARLEO Chargé de recherche HDR, Université de Nantes	Rapporteur
Shuang LI Professeur, China Three Gorges University	Rapporteur
Cvetan Valeriev CHESHKOV Directeur de recherche, CNRS Délégation Rhône Auvergne	Examinateur
Marie GERMAIN Chargée de recherche, CNRS Délégation Bretagne et Pays de Loire	Examinatrice
Xiaomei LI Professeure, China Institute of atomic energy	Examinatrice
Johann COLLOT Professeur, Université Grenoble Alpes	Examinateur
Yaping WANG Professeur, Central China Normal University	Examinateur

分类号_____ 密级_____

U D C _____ 编号_____

華中師範大學

博士学位论文

题目：ALICE 实验 13 TeV 质子-质子碰撞中孤立光子散射截面测量

学位申请人姓名：徐冉

申请学位学生类别：全日制博士

申请学位学科专业：粒子物理与原子核物理

指导教师姓名：周代翠 教授

毛亚昱 教授

Gustavo CONESA BALBASTRE 教授

博士学位论文

论文题目：ALICE 实验 13 TeV 质子-质子碰撞中孤立光子散射截面测量

论文作者：　徐　冉

指导教师：　周代翠 教授，

毛亚显 教授，

Gustavo CONESA BALBASTRE 教授

学科专业：粒子物理与原子核物理

研究方向：高能物理实验

华中师范大学物理科学与技术学院

&

法国格勒诺布尔阿尔卑斯大学亚原子物理和宇宙学实验室

2025 年 5 月

Dissertation

Isolated direct photon cross section measurement in pp collisions at 13 TeV with the ALICE detector at LHC

By

Ran XU

Supervisors: DaiCui Zhou, Yaxian Mao

Gustavo Conesa Balbastre

Specialty: Particle Physics and Nuclear Physics

Research Area: High Energy Physics Experiment

College of Physical Science and Technology

Central China Normal University

Grenoble subatomic physics and cosmology laboratory

University Grenoble-Alpes

May. 2025

摘　要

粒子物理学标准模型（Standard Model，SM）涵盖了参与相互作用的基本粒子（夸克、轻子）与传递相互作用的媒介粒子 — 胶子、光子、W/Z 玻色子及希格斯玻色子，统一描述了自然界四种基本相互作用中的三种（强相互作用、电磁相互作用及弱相互作用）及其基本粒子的相互作用规律。量子色动力学（QCD）作为标准模型中描述强相互作用的基础理论，其核心特性表现为色禁闭和渐近自由。色禁闭表明夸克和胶子无法单独存在，只能约束在介子、重子等色中性强子内部。渐近自由则揭示了在非常高能量或很短的距离下，夸克间的相互作用强度降低（耦合常数小），粒子行为趋近自由粒子。低能区的强耦合效应导致 QCD 的非线性方程无法通过解析方法求解。而在高能区，QCD 的渐近自由特性使得耦合常数足够小，允许理论计算使用微扰论方法展开。微扰量子色动力学（pQCD）就是基于此构建的系统化计算框架，用于对高能物理中的粒子产额、喷注形成等关键探针进行定量预测，为探索强子内部结构及验证 QCD 理论体系提供了重要研究手段。部分子分布函数 (PDFs) 是研究高能碰撞中强子行为的重要理论工具。它通过量化强子内部夸克、反夸克及胶子（统称为部分子）携带不同动量分数（x，通常称为 Bjorken-x）的概率分布，桥接了非微扰过程的 QCD 理论和微扰过程主导的实验测量。

光子呈色中性且不参与强相互作用，使得它们在产生时间内携带的信息不受最终状态效应的改变，直到它们被探测器检测到。依据产生来源，光子可分为产生于硬散射初期的瞬时光子（direct prompt photon），部分子碎裂产生的碎裂光子（fragmentation photon）以及末态强子衰变产生的衰变光子（decay photon）等。其中，所有非强子衰变产生的光子的总和称为直接光子（direct photon）。瞬时光子主要来自康普顿散射过程（$q+g \rightarrow q+\gamma$）或湮灭过程（$q+\overline{q} \rightarrow \gamma+g$），它携带着硬散射过程中初态部分子的信息。同时，瞬时光子在产生时，其周围一般没有同一硬过程产生的其他伴随粒子，是“孤立”的。而其他来源的光子则不同，周围是存在其他伴随粒子的，是非“孤立”的。实验上通过施加孤立性判据（isolation criteria）可有效筛选出瞬时光子，同时发现所选择的瞬时光子主要来自高能碰撞中的康普顿散射过程。因此，对孤立光子散射截面的测量可检测 pQCD 理论预言，提供一种获得质子中胶子的 PDF 的方法，特别是在其他测量可能获得信息较少的低 x 值下的胶子部分子分布函数（gluon PDF）具有独特约束作用。

欧洲核子研究中心（CERN）的大型强子对撞机（LHC）为目前世界最大粒子加速器，为强子–强子和核–核对撞（pp、Pb–Pb、p–Pb 和 Xe–Xe）提供了目前可用的最高质心系能量（$\sqrt{s}$），这对于探测基本粒子的基本相互作用和特性至关重要。大型强子对撞机上的实验组广泛测量了质子-质子 (pp) 对撞中各种粒子产生过程的横动量（p_{T}）微分截面。目前，ALICE（大型离子对撞机实验）、ATLAS（大型强子对撞机上超环面装置实验）和 CMS（LHC 上紧凑缪子螺线管装置实验）合作组的测量结果都与 pQCD 计算结果相吻合，进一步验证了理论框架。例如，对孤

立光子散射截面的精确测量改进了对胶子 PDF 的测定。此外，这些测量还促进了对部分子簇射（parton shower）演化以及微扰和非微扰 QCD 效应之间相互作用的研究。ATLAS 和 CMS 对孤立光子散射截面的测量优势在高横动量区间（高于 20 GeV/c），而中低横动量区间的测量受背景复杂性、探测器设计优先级和理论模型的限制，未能实现全面覆盖。而 ALICE 合作组，其电磁量能器（EMCal）可以提供高分辨率的能量测量，这对于在复杂的碰撞环境中高精度重建和识别光子、中性介子和电子至关重要。同时，ALICE 径迹系统包括一个高效的时间投影室（TPC）和内部径迹系统（ITS），能够精确实现对带电粒子径迹重建和背景剔除，以确保探测到的信号尽可能不受污染。此外，低动量跟踪能力允许在更宽能量范围产生的粒子进行更全面的分析，从而提高散射截面测量的总体精度。这些特点使得 ALICE 探测器特别适合分离和分析像孤立光子产生这类稀有过程。

本研究中，电磁量能器测量 ALICE 实验二期运行数据时面临两个关键性技术挑战：高能区伪光子信号的抑制和触发系统优化。ALICE 实验是首次实现 100 GeV 以上超高能区的光子测量，面临更大范围内伪信号的识别与处理。EMCal 采用铅-闪烁体夹层结构，整个探测器由 17664 个探测单元（cell）构成。光子能量主要沉积于单个单元及其邻近区域形成团簇（cluster），每个单元通过雪崩光电二极管（APD）将沉积能量转换为电信号。针对超高 p_{T}（$>$ 100 GeV/c）光子候选团簇的分析发现中子直接撞击 EMCal 结构体时 APD 产生的异常伪信号显著影响测量精度。此类伪信号会在 EMCal 主单元附近诱导出明显的电子学串扰信号，形成容易被误判成光子的能量分布。这种串扰信号只影响位于同一读出模块（2×8 单元矩阵）内的单元，而真实光子团簇在 80 GeV 时会在多个读出模块中沉积能量。基于此，本研究提出针对团簇的一个额外筛选条件：超过 80 GeV 的高能团簇的能量分布必须在至少两个读出模块中有响应。结果表明，添加这一筛选条件后高能区伪信号可以有效去除。电磁量能器作为触发探测器能够筛选出包含高能信号的事件，在 ALICE 二期运行阶段全程启用。系统研究触发器性能，建立基于数据采集周期的动态触发映射关系。数据质量验证发现，量能器不同区域响应特性存在显著差异且具有时间依赖性。为此展开对触发响应系统性研究，以定位并屏蔽量能器中的死区或异常活跃区（电子噪声，校准缺陷等）。通过应用这些屏蔽规则（所有 EMCal 相关分析均需采用），各区域的性能一致性得到了显著改善。

研究采用 ALICE 探测器于 2016 年至 2018 年采集的质心系能量 $\sqrt{s}$ = 13 TeV pp 碰撞数据样本，包括最小偏差（Minimum Bias，MB）事件样本以及电磁量能器（EMCal）触发的 EMCal L1 触发数据样本，所用数据样本的总积分亮度为 $\mathcal{L}_{\mathrm{int}} = 10.79\ \mathrm{pb}^{-1}$。基于 EMCal 上粒子能量沉积的团簇形状信息 (shower shape) 和能量沉积量鉴别出穿越 EMCal 探测器的光子。为有效抑制碎裂光子及中性介子衰变光子（例如 $\pi^0 \to \gamma\gamma$ 过程，其光子产额比直接光子高出一个数量级以上）的背景干扰，研究引入孤立判据：以光子候选粒子为中心轴构建半径 $R = 0.4$ 的锥形区域，

要求该区域内带电粒子的横向动量总和小于 1.5 GeV/c。该复合孤立判据可以优化瞬时光子的选择效率，实现对瞬时光子的可靠鉴别与精确测量。

基于 ALICE 实验数据，通过对探测器伪信号的去除和孤立光子的鉴别，本研究测量了质心系能量 $\sqrt{s}$ = 13 TeV pp 碰撞中孤立光子的微分散射截面。测量的孤立光子横动量区间为 $7 < p_{\mathrm{T}}^{\gamma} < 200$ GeV/c，对应 Bjorken-x 范围是 $1.1\times10^{-3} < x \approx x_{\mathrm{T}}^{\gamma} = 2p_{\mathrm{T}}^{\gamma}/\sqrt{s} < 30.8\times10^{-3}$。测量结果与次领头阶 pQCD 计算的一致性验证了 pQCD 计算的可靠性。相较于 ALICE 在 $\sqrt{s}$ = 7 TeV pp 碰撞中对孤立光子散射截面的测量（$10 < p_{\mathrm{T}}^{\gamma} < 60$ GeV/c，以及 $2.9\times10^{-3} < x_{\mathrm{T}}^{\gamma} < 17.1\times10^{-3}$），本研究将测量范围扩展至更宽区间。ALICE 实验组不同质心系能量下的散射截面比值与理论计算相吻合，进一步验证了 pQCD 计算的可靠性。与 ATLAS（$p_{\mathrm{T}}^{\gamma} > 125$ GeV/c）和 CMS（$p_{\mathrm{T}}^{\gamma} > 190$ GeV/c）实验组同能标下的测量范围相比，本研究向更低动量区间扩展了一个数量级。测量结果在误差范围内的互相吻合则体现了不同实验测量间的一致性。本研究首次在 LHC 能区实现 pp 碰撞中孤立光子横动量 7–10 GeV/c 散射截面的测量。研究还提供了迄今为止在中等快度（mid-rapidity）区间通过孤立光子测量到的最低 Bjorken-x。与不同 $\sqrt{s}$ 下，pp 和 p$\bar{\mathrm{p}}$ 碰撞中所有可用的孤立光子测量结果在统一标度 $(\sqrt{s})^{n=4.5}$ 下保持良好一致性，所测得的低 x 值将为胶子部分子分布函数（PDF）提供重要约束。

关键词：大型重离子对撞实验（ALICE）；质子-质子碰撞；孤立光子；散射截面；部分子分布函数；比约肯变量

Abstract

The Standard Model (SM) of Particle Physics is the theoretical framework for describing three of the four fundamental forces (the strong, electromagnetic and weak forces) of Nature and its elementary particles, including quarks and leptons, and the mediators of these three fundamental forces, gluons, photons, W, Z, and Higgs Bosons. Within the framework of the Standard Model of Particle Physics, Quantum Chromodynamics (QCD) is the fundamental theory describing the strong interactions between quarks and gluons. These interactions are characterized by two key properties: color confinement and asymptotic freedom. Color confinement dictates that quarks and gluons cannot be observed in isolation, they are confined within final state hadrons such as mesons and baryons. Conversely, asymptotic freedom implies that at very high energies, the interaction strength between quarks decreases, allowing them to behave almost as free particles. Extending to high-energy regimes, perturbative QCD (pQCD) provides a systematic framework for calculating scattering amplitudes and cross sections in processes where the interaction energy is much higher than the characteristic scale of the strong interaction. This approach relies on the fact that the coupling constant becomes small at high energies to allow for a perturbative expansion. Consequently, pQCD enables precise predictions for particle production rates, jet formation, and other high-energy phenomena, thereby providing a robust tool for probing the internal structure of hadrons and validating the theoretical underpinnings of QCD. The particle cross-section measurement is crucial for testing pQCD predictions and refining our understanding of parton (quark and gluon) distribution functions (PDFs) in nucleons and nuclei and parton fragmentation functions.

Photons are color-neutral particles and do not participate in the strong interaction. Among the photon sources, the direct prompt photons, which are produced directly from hard scattering processes involving quarks and gluons, carry information about these initial-state partons. Unlike quarks and gluons that fragment into hadrons during the hadronization process, direct prompt photons do not undergo fragmentation, making them a “clean” probe to tag the initial hard scattering process. This advantage allows for more direct tests of pQCD predictions and provides stringent constraints on PDFs. Direct prompt photons are produced “isolated” (no other particles produced nearby from the same hard process) if they originate from Compton or annihilation processes. They can also be produced “not isolated” if they originate from fragmentation processes (next-to-leading order). Applying isolation criteria, the selected direct prompt photons are mainly from the Compton scattering processes ($g + q \rightarrow \gamma + q$) in proton–proton (pp) high-energy collisions. Thus, the isolated photon cross-section measurement offers valuable insights into the not well-known gluon PDF in protons, owing to the isolated photon clean

experimental signature and direct connection to the initial-state partons.

The Large Hadron Collider (LHC) at CERN (European Organization for Nuclear Research) provides an unparalleled environment for high-energy physics experiments, offering the highest center-of-mass energies ($\sqrt{s}$) for hadronic collisions (pp, Pb–Pb, p–Pb, and Xe–Xe) currently available, which are essential for probing the fundamental interactions and properties of elementary particles. The different experimental results at the LHC have extensively measured the differential cross sections for various particles transverse momentum (p_{T}) distribution in pp collisions. Recent measurements by the ALICE (A Large Ion Collider Experiment), ATLAS (A Toroidal LHC Apparatus) and CMS (Compact Muon Solenoid) Collaborations have demonstrated excellent agreement with pQCD calculations, validating the theoretical framework even further. For instance, the precise measurement of isolated photon production cross-section has improved the determination of gluon PDF. Furthermore, these measurements have facilitated the study of parton shower evolution and the interplay between perturbative and non-perturbative QCD effects. While ATLAS and CMS continue to advance high-p_{T} photon studies (above 20 GeV/c), low-to-medium p_{T} measurements remain constrained by background complexity, detector design priorities, and theoretical ambiguities, necessitating future upgrades or complementary experiments for comprehensive coverage. With the ALICE experiment, the electromagnetic calorimeter (EMCal) provides high-resolution energy measurements, which is crucial for accurately reconstructing and identifying photons, neutral mesons and electrons amidst the complex collision environment. The ALICE tracking system, which includes a highly-efficient Time Projection Chamber (TPC) and Inner Tracking System (ITS), enables precise particle tracking and background rejection, ensuring that the detected signals are as free from contamination as possible. In particular, the low-momentum tracking capabilities allow for a more comprehensive analysis of particles produced at various energies, enhancing the overall precision of the scattering cross-section measurement. These features collectively make ALICE particularly well-suited for isolating and analyzing rare processes like isolated-photon production down to low p_{T}.

This work presents the measurement of the inclusive isolated-photon cross section in pp collisions at $\sqrt{s}$ = 13 TeV at mid-rapidity ($|\eta| < 0.67$) using a data sample collected by ALICE in years 2016, 2017, and 2018, with integrated luminosity $\mathcal{L}_{\mathrm{int}} = 10.79\ \mathrm{pb}^{-1}$. The photon measurement at high energy relies on the high-precision detection and triggering of the EMCal. The EMCal photon trigger dataset is utilized to enhance the statistical significance of the measurement. Photon candidates are identified through a combination of the particle deposited energy and spread information (shower shape) from the EMCal. Furthermore, an isolation criterion, the sum of the transverse momentum of charged particles

inside a cone centered on the photon candidate of angular size 0.4 rad must be smaller than 1.5 GeV/c, is implemented to suppress contributions not only from fragmentation photons but also from neutral meson decay photons (e.g., $\pi^0 \rightarrow \gamma\gamma$, the dominant photon source in the collision by more than one order of magnitude), thereby improving toward direct prompt photon selection. This approach ensures robust identification and selection of direct prompt photons.

Two main unexpected challenges were confronted in this measurement that require additional technical work in the ALICE-EMCal community. For the first time, photon energies above 100 GeV were reached and the treatment of already known fake signals needs further adjustment and improvements. This is part of my work during the PhD besides the physics analysis. The EMCal is segmented into cells: towers made of a lead-scintillator sandwich, 76 and 77 layers, respectively. A photon deposits most of its energy in a single cell plus several surrounding ones, forming a cluster. Each cell is coupled to an Avalanche Photodiode (APD) that transforms the deposited energy into an electronic signal that is recorded. Analyzing the signals of very high p_{T} photon candidate clusters ($p_{\mathrm{T}} > 100$ GeV/c), a significant contribution from anomalous pseudo-signals created by neutrons hitting directly the APDs of the EMCal towers was found. Such fake signals induce significant electronics cross-talk signals in nearby cells to the main one in the calorimeter, creating clusters with an energy spread that could be misidentified as photons. At such high energies, real photon signals create clusters spanning more than one readout card (2×8 cells), therefore, an additional novel selection of clusters was implemented for this work to remove the fake signals: high-energy clusters above 80 GeV must have an energy spread in at least two of the readout cards. In addition, the trigger performance was studied systematically, finding the good trigger map as a function of the periods the data was taken. During the data quality assurance checks, it was observed that different regions of the calorimeter exhibited varying responses, which also depended on the period of data collection. This triggered a careful study on the trigger activity to identify and mask dead or too active areas (electronic noise, imperfect calibration) in the calorimeter. With those masks, needed for all EMCal-related analyses, the agreement on the performance between regions was significantly improved.

The measured isolated photon p_{T}-differential cross section is performed in the photon transverse momentum range $7 < p_{\mathrm{T}}^{\gamma} < 200$ GeV/c and correspondingly $1.1 \times 10^{-3} < x_{\mathrm{T}}^{\gamma} < 30.8 \times 10^{-3}$. This study is done for the first time in the p_{T}^{γ} range of 7–10 GeV/c in any collision systems at the LHC and provides the lowest Bjorken-x probed with isolated photons at mid-rapidity to date. This is crucial for constraining the gluon PDF in protons at low Bjorken-x. The measured results are also compared with NLO pQCD calculations and the results at the same $\sqrt{s}$ from the ATLAS and CMS experiments, as well as with

measurements at other collision energies. The measurement and theory prediction are in agreement with each other within the experimental and theoretical uncertainties. The mutual agreement of the data with the theory supports the theoretical calculations and demonstrates the consistency of the different measurements.

Finally, this dissertation is structured as follows: First, an introductory Chapter 1 outlines the theoretical background relevant to this study, the physical context of direct prompt photons, and the existing experimental results. Chapter 2 details the ALICE experiment's detector system and its functionalities. Chapter 3 then shifts the focus to the particle reconstruction techniques, quality selection criteria, and calibration methods on the electromagnetic calorimeter, which are essential for precise photon energy measurements. The subsequent chapter (Chapter 4) delves into the methodologies for identifying direct prompt photons and presents detailed analysis procedures, and Chapter 5 discusses and evaluates the different sources of systematic uncertainties and their impacts on the measurement, ensuring the reliability and accuracy of the findings. The main measurement results are presented and discussed in depth in Chapter 6, and the entire experimental work conducted in this study is summarised in Chapter 7, which also offers perspectives on future research directions.

Keywords: ALICE; Proton-proton collision; Isolated photon; Cross section; PDF; Bjorken-*x*

Résumé

Dans le grand schéma de la Physique des Particules moderne, notre compréhension de la composition fondamentale de la matière et de ses interactions a fait des progrès remarquables. Le Modèle Standard (SM, accronyme en anglais) de la physique des particules constitue le cadre théorique permettant de décrire trois des quatre forces fondamentales (force forte, électromagnétique et faible) de la nature et de ses particules élémentaires, dont les quarks et les leptons, ainsi que les médiateurs des trois forces fondamentales, les gluons, les photons, les bosons W, Z, et de Higgs. Le SM est le fondement théorique central du domaine depuis le milieu du XXe siècle.

Dans le cadre du modèle standard de la physique des particules, la chromodynamique quantique (QCD, accronyme en anglais) est la théorie fondamentale décrivant les interactions fortes entre les quarks et les gluons. Ces interactions sont caractérisées par deux propriétés clés : le confinement de la couleur et la liberté asymptotique. Le confinement de la couleur dicte que les quarks et les gluons ne peuvent pas être observés isolément, ils sont confinés dans des particules composites telles que les protons et les neutrons. À l'inverse, la liberté asymptotique implique qu'à très haute énergie, la force d'interaction entre les quarks diminue, leur permettant de se comporter presque comme des particules libres. S'étendant aux régimes de haute énergie, la QCD perturbative (pQCD) fournit un cadre systématique pour calculer les amplitudes de diffusion et les sections efficaces dans les processus où l'énergie d'interaction est bien supérieure à l'échelle caractéristique de l'interaction forte. Cette approche repose sur le fait que la constante de couplage devient faible à haute énergie pour permettre une expansion perturbative. Par conséquent, la pQCD permet des prédictions précises sur les taux de production de particules, la formation de jets et d'autres phénomènes de haute énergie, fournissant ainsi un outil robuste pour sonder la structure interne des hadrons et valider les fondements théoriques de la QCD. La mesure de la section efficace des particules est cruciale pour tester les prédictions de la pQCD et affiner notre compréhension des fonctions de distribution des partons (quarks et gluons) (PDF, accronyme en anglais) dans les nucléons et les noyaux et des fonctions de fragmentation des partons.

Les photons sont particules de couleur neutre et ne participent pas à l'interaction forte. Parmi les sources de photons, les photons prompts, qui sont produits directement à partir de processus de diffusion dure impliquant des quarks et des gluons, portent des informations sur ces partons d'état initial. Contrairement aux quarks et gluons, qui se fragmentent en hadrons pendant le processus d'hadronisation, les photons prompts ne subissent pas l' hadronisation, ce qui en fait des sondes idéales pour marquer le processus initial de diffusion dure. Cet avantage permet des tests plus directs des prédictions

pQCD et fournit des contraintes strictes sur les PDF. Les photons prompts sont produits “isolés” (aucune autre particule produite à proximité du même processus dur) s’ils proviennent de processus Compton ou d’annihilation. Ils peuvent également être produits “non isolés” s’ils proviennent de processus de fragmentation (ordre suivant). En appliquant des critères d’isolement, les photons prompts sélectionnés proviennent principalement des processus de diffusion Compton (gluon–quark $\rightarrow$ γ–quark) dans les collisions proton–proton (pp) à haute énergie. Ainsi, la mesure de la section efficace des photons isolés offre des informations précieuses sur la PDF des gluons dans les protons, peu connue, en raison de la signature expérimentale propre des photons isolés et de la connexion directe avec les partons de l’état initial.

Le LHC (Large Hadron Collider) au CERN (Organisation européenne pour la recherche nucléaire) offre un environnement sans précédent pour les expériences de physique des hautes énergies, offrant les énergies de centre de masse ($\sqrt{s}$) les plus élevées pour les collisions hadroniques (pp, Pb–Pb, p–Pb et Xe–Xe) actuellement disponibles, qui sont essentielles pour sonder les interactions et propriétés fondamentales des particules élémentaires. Les différents résultats expérimentaux au LHC ont largement mesuré les sections efficaces différentielles d’impulsion transversale (p_{T}) pour divers processus de production de particules dans les collisions pp. Des mesures récentes effectuées par les collaborations ALICE (A Large Ion Collider Experiment), ATLAS (A Toroidal LHC Apparatus) et CMS (Compact Muon Solenoid) ont démontré une excellente concordance avec les calculs pQCD, validant encore davantage le cadre théorique. Par exemple, la mesure précise de la section efficace de production de photons rapides isolés a amélioré la détermination de la PDF des gluons. De plus, ces mesures ont facilité l’étude de l’évolution des gerbes de partons et de l’interaction entre les effets QCD perturbatifs et non perturbatifs. Alors qu’ATLAS et CMS continuent de faire progresser les études sur les photons à p_{T} élevé (supérieur à 20 GeV/c), les mesures de faible à moyen p_{T} restent limitées par la complexité du fond de particules, les priorités de conception des détecteurs et les ambiguïtés théoriques, ce qui nécessite de futures mises à niveau ou des expériences complémentaires pour une couverture complète. Dans l’expérience ALICE, le calorimètre électromagnétique EMCal fournit des mesures d’énergie à haute résolution, ce qui est essentiel pour reconstruire et identifier avec précision les photons, les mésons neutres et les électrons dans l’environnement complexe des collisions. Le système de suivi ALICE, qui comprend une chambre de projection temporelle (TPC) et un système de suivi interne (ITS) hautement efficaces, permet un suivi précis des particules et un rejet de l’arrière-plan, garantissant que les signaux détectés sont aussi exempts de contamination que possible. De plus, les capacités de suivi à faible impulsion permettent une analyse plus complète des particules produites à différentes énergies, améliorant ainsi la précision globale de la mesure de la section efficace de diffusion. Ces caractéristiques collectives rendent AL-

ICE particulièrement bien adapté à l'isolement et à l'analyse de processus rares comme la production de photons isolés.

Ce travail présente la mesure de la section efficace inclusive des photons isolés dans les collisions pp à $\sqrt{s}$ = 13 TeV à moyenne rapidité ($|\eta| < 0,67$) en utilisant un échantillon de données collectées avec ALICE au cours des années 2016, 2017 et 2018, avec une luminosité intégrée de $\mathcal{L}_{\text{int}} = 10.79$ pb^{-1}. Dans l'expérience ALICE, la mesure des photons à haute énergie repose sur la détection et le déclenchement de haute précision de l'EMCal. L'ensemble de données de déclenchement des photons EMCal est utilisé pour améliorer la signification statistique de la mesure. Les candidats photons sont identifiés grâce à une combinaison de l'énergie déposée des particules et des informations de propagation (forme de la gerbe) de l'EMCal. De plus, un critère d'isolement, la somme de l'impulsion transversale des particules chargées à l'intérieur d'un cône centré sur le photon candidat de taille angulaire 0.4 rad doit être inférieure à 1.5 GeV/c, est mis en œuvre pour supprimer les contributions non seulement des photons de fragmentation mais aussi des photons de désintégration de mésons neutres (par exemple, $\pi^0 \rightarrow \gamma\gamma$, la source de photons dominante dans la collision de plus d'un ordre de grandeur), améliorant ainsi la sélection directe des photons prompts. Cette approche garantit une identification et une sélection robustes des photons prompts directs.

Deux principaux défis inattendus ont été rencontrés dans cette mesure, ce qui a ajouté du travail technique supplémentaire nécessaire à la communauté ALICE-EMCal. Pour la première fois, des énergies de photons supérieures à 100 GeV ont été atteintes et le traitement des faux signaux déjà connus a nécessité des ajustements. L'EMCal est segmenté en cellules : des tours constituées d'un sandwich plomb-scintillateur, respectivement de 76 et 77 couches. Un photon dépose la majeure partie de son énergie dans une seule cellule plus plusieurs cellules environnantes, formant un cluster. Chaque cellule est couplée à une photodiode à avalanche (APD) qui transforme l'énergie déposée en un signal électronique qui est enregistré. En analysant les signaux des clusters de photons candidats à très haut p_{T} ($p_{\text{T}} > 100$ GeV/c), une contribution significative des pseudo-signaux anormaux créés par des neutrons frappant directement les APD des tours EMCal a été trouvée. De tels faux signaux induisent des signaux de diaphonie électronique importants dans les cellules proches de la principale du calorimètre, créant des clusters avec une dispersion d'énergie qui pourrait être identifiée à tort comme des photons. À des énergies aussi élevées, les vrais signaux de photons créent des clusters couvrant plus d'une carte de lecture (2×8 cellules), par conséquent, une nouvelle sélection supplémentaire de clusters a été mise en œuvre pour ce travail afin de supprimer les faux signaux : les clusters à haute énergie au-dessus de 80 GeV doivent avoir une dispersion d'énergie dans au moins deux des cartes de lecture. De plus, les

performances de déclenchement ont été étudiées systématiquement, en trouvant la bonne carte de déclenchement en fonction des périodes pendant lesquelles les données ont été prises. Lors des contrôles d'assurance qualité des données, il a été observé que différentes régions du calorimètre présentaient des réponses variables, qui dépendaient également de la période de collecte des données. Cela a déclenché une étude minutieuse de l'activité de déclenchement pour identifier et masquer les zones mortes ou trop actives (bruit électronique, étalonnage imparfait) dans le calorimètre. Avec ces masques, nécessaires pour toutes les analyses liées à EMCal, l'accord sur les performances entre les régions a été considérablement amélioré.

La mesure de la section efficace différentielle p_{T} du photon isolé est effectuée dans la gamme d'impulsions transverses du photon $7 < p_{\mathrm{T}}^{\gamma} < 200$ GeV/c et en conséquence $1.1 \times 10^{-3} < x_{\mathrm{T}}^{\gamma} < 30.8 \times 10^{-3}$. Cette étude est réalisée pour la première fois dans la gamme p_{T} de 7 à 10 GeV/c dans tous les systèmes de collision du LHC et fournit le Bjorken-x le plus bas sondé avec des photons isolés à moyenne rapidité à ce jour. Ceci est crucial pour contraindre la PDF du gluon dans les protons à faible Bjorken-x. Les résultats mesurés sont comparés aux calculs NLO pQCD et aux résultats aux mêmes $\sqrt{s}$ des expériences ATLAS et CMS, ainsi qu'aux mesures à d'autres énergies de collision. La mesure et la prédiction théorique concordent entre elles dans les limites des incertitudes expérimentales et théoriques. La concordance mutuelle des données avec la théorie soutient les calculs théoriques et démontre la cohérence des différentes mesures.

Enfin, cette thèse est structurée comme suit : tout d'abord, un Chapitre introductif 1 décrit le contexte théorique pertinent pour cette étude, le contexte physique des photons rapides et les résultats expérimentaux existants. Le Chapitre 2 détaille le système de détection de l'expérience ALICE et ses fonctionnalités. Le Chapitre 3 se concentre ensuite sur les techniques de reconstruction des particules, les critères de sélection de la qualité et les méthodes d'étalonnage du calorimètre électromagnétique, qui sont essentiels pour des mesures précises de l'énergie des photons. Le chapitre suivant (Chapitre 4) se penche sur les méthodologies d'identification des photons rapides directs et présente des procédures d'analyse détaillées, et le Chapitre 5 discute et évalue les différentes sources d'incertitudes systématiques et leurs impacts sur la mesure, garantissant la fiabilité et l'exactitude des résultats. Les principaux résultats de mesure sont présentés et discutés en profondeur au Chapitre 6, et l'ensemble du travail expérimental mené dans cette étude est résumé au Chapitre 7, qui offre également des perspectives sur les orientations de recherche futures.

Mots-clés: ALICE; Collisions proton-proton; Photons isolés; Section efficace; PDF; Bjorken-x

Contents

摘　要 I

Abstract IV

Résumé VIII

1 Introduction of high-energy particle physics 1

1.1 Theoretical description 2

1.1.1 The standard model of particle physics 2

1.1.2 Quantum Chromodynamics theory 3

1.1.3 Parton distribution functions 6

1.2 Prompt photon production in hadronic collisions 7

1.2.1 Photon sources 8

1.2.2 Direct prompt photon selection: the isolation method 9

1.2.3 Experimental results on prompt photons 12

2 Experimental setup 20

2.1 LHC introduction 20

2.2 ALICE detector description 24

2.2.1 V0 detector 25

2.2.2 Inner Tracking System, ITS 25

2.2.3 Time-Projection Chamber, TPC 26

2.2.4 Electromagnetic Calorimeter, EMCal 28

3 EMCal data selection, reconstruction and calibration 31

3.1 Data and Monte Carlo samples 31

3.2 Event selection 34

3.3 EMCal cluster reconstruction 34

3.3.1 EMCal shower shape definition 35

3.4 EMCal calibration 36

3.4.1 Cell energy calibration 36

3.4.2 Bad channel masking 38

3.4.3 Cell Time calibration 38

3.4.4 Cell temperature calibration 38

3.4.5 Cell cross-talk in data and emulation in simulation 38
3.5 EMCal cluster quality selection 40
3.5.1 Basic criteria 40
3.5.2 Track–cluster association 41
3.5.3 Exotic cluster 42
3.6 EMCal trigger performance 45
3.6.1 Trigger overview 45
3.6.2 Trigger quality assurance work: Supermodule by supermodule response 46
3.6.3 Trigger efficiency 52
3.6.4 Calorimeter triggered events rejection factor 54
4 Prompt photon identification and cross section 57
4.1 Photon identification via shower shape 57
4.2 Prompt photon identification via the isolation method 59
4.3 Efficiency 69
4.4 Purity 73
4.4.1 The ABCD method 73
4.4.2 Study of correlation in the ABCD regions 82
4.4.3 Purity fitting 94
4.5 Normalization 97
4.6 Cross section 98
5 Systematic uncertainties 100
5.1 Uncertainties associated to the purity 100
5.1.1 Shower shape range in background region 101
5.1.2 Isolation momentum range in background region 101
5.1.3 Signal-to-background ratio in the simulation 102
5.1.4 Total purity uncertainty 103
5.2 Uncertainties associated with the cross section 104
5.2.1 Neutral cluster selection 104
5.2.2 The shower shape description and its selection in signal region 109
5.2.3 Energy scale and material budget 110
5.2.4 Total uncertainty 110

6 Isolated photon measurement results and discussion 113
6.1 Isolated photon purity 113
6.2 Differential p_{T} cross section 115
6.3 x_{T}^{γ} distribution 121
7 Conclusion and outlook 123
Appendix A Isolation probability 134
A.1 The ratio of isolation fraction in data to simulation 134
A.1.1 The double ratio distribution and background fit range variation for $k = 1.0$ 134
A.1.2 The double ratio distribution and background fit range variation for $k = 0.0$ 137
A.1.3 The double ratio distribution and background fit range variation for $k = 0.5$ 140
A.1.4 The double ratio distribution and background fit range variation for $k = 1.5$ 143
A.1.5 The double ratio distribution and background fit range variation for $k = 2.0$ 146
A.2 Parameters obtained by fitting with a first order polynomial function to different R_f background ranges 149
A.2.1 Fit results of the background fit range variation 149
A.2.2 Constant parameter obtained by the multi-background range fitted function 152
A.2.3 Slope parameter obtained by the multi-background range fitted function 155
Appendix B Purity function fit range variable 158
Appendix C 博士论文中文简介 160
C.1 背景简介 160
C.2 探测器简介 161
C.3 孤立直接光子鉴别 162
C.4 孤立直接光子散射截面测量 163
C.5 结果讨论与展望 166
Appendix D Synthèse par chapitre en Français 168
D.1 Introduction à la physique des particules de haute énergie 168
D.2 Configuration expérimentale 170
D.3 Sélection, reconstruction et calibration des données EMCal 172
D.4 L'identification et mesure de la section efficace des photons prompt 176
D.5 Incertitudes systématiques 180
D.6 Résultats de mesures de photons isolés, conclusions et perspectives 180

Contributions on behalf of ALICE Collaboration 183

Acknowledgements 184

List of Figures

1.1 Elementary particles in the Standard Model of Particle Physics [4]. 2

1.2 Various measurements of α_s as a function of Q along with a fit function. Image from Ref. [10]. 4

1.3 Left: PDFs from HERAPDF2.0, which have been determined from charm data, jet data and low energy data as well as the HERA-I and II high energy inclusive data [16].Right: Maps of QCD evolution as a function of (Q,x). The evolution towards large Q^2 can be described by DGLAP, and that towards small (but not too small) x by BFKL. At very small x, where the gluon density is very high, non-linear effects become relevant, and other evolution equations (BK or JIMWLK) are necessary. 7

1.4 View of the various sources of photon production in pp collisions. 8

1.5 Feyman diagrams of prompt photon production. 9

1.6 NLO QCD predictions for the ratio $\gamma_{\text{prompt}}/\pi^0$ in proton-proton, proton-nucleus and nucleus-nucleus collisions at 200 GeV and 5.5 TeV. At $\sqrt{s}$ = 14 TeV in pp collision case, the CTEQ6 [27] structure functions are used for the NLO QCD predictions. For the prompt photon spectrum, the BFG [28] parametrization of fragmentation functions is used while the KKP [29] fragmentation functions are used for the NLO pQCD estimates of decay photons. The cross section is evaluated at 0 rapidity. Plot from Ref. [30]. 10

1.7 Left: Relative contributions of the quark-gluon Compton scattering, $q\overline{q}$ annihilation and fragmentation subprocesses in NLO prompt photon production at the LHC mid-rapidity in pp collision at $\sqrt{s}$ = 14 TeV obtained with JETPHOX (CTEQ6.6 PDF, $\mu = E_T^{\gamma}$, and BFG-II FFs). Right: same process but with an isolation radius $R = 0.4$ and a hadron fraction of the photon energy of $\varepsilon = 0.1$ inside the cone [33]. 11

1.8 Left: Measured isolated photon cross section at $\sqrt{s}$ = 7 TeV in pp collision with ALICE ratio to the JETPHOX calculations at NLO. Right: Comparison of ratio from the ATLAS [39] and CMS [42]. Results from Ref. [42]. 13

1.9 The ratio of various theoretical calculations over the measured isolated photon cross section from ATLAS in pp collisions at $\sqrt{s}$ = 13 TeV [36]. 13

1.10 The ratio of NLO JETPHOX calculations over the measured isolated photon cross section from CMS in pp collisions at $\sqrt{s}$ = 13 TeV [45]. 14

1.11 Nuclear modification factor R_{AA} for isolated photons at $\sqrt{s_{NN}}$ = 5.02 TeV for isolation cone radii R = 0.2 (black) and R = 0.4 (blue). Also, for charged hadrons [47] and pions [48] from ALICE and Z^0 bosons from CMS [49] (integrated p_T, point at boson mass). The bands correspond to pQCD calculations with JETPHOX for Pb–Pb collisions (nPDF) for 0–100% centrality over pp collisions (PDF). The width of each band corresponds to the scale and PDF uncertainties. The normalization uncertainties are represented as a red box centered at unity. Figures from Ref. [51]. 16

1.12 Data-over-theory ratio of isolated photon cross section as a function of p_T^γ for R = 0.2 (left) and R = 0.4 (right) in pp and Pb–Pb collisions at $\sqrt{s_{NN}}$ = 5.02 TeV. The bands centred at unity correspond to JETPHOX NLO pQCD calculations, their width represents the scale (blue) uncertainty and PDF (orange) uncertainty. The normalization uncertainties are shown as a grey box on the left of each frame around unity. Figures from Ref. [51]. 17

1.13 Nuclear modification factor R_{pA} of isolated prompt photon production in p–Pb collisions at $\sqrt{s_{NN}}$ = 5.02 TeV and 8.16 TeV. Ratio compared to JEPHOX NLO pQCD predictions for different nPDF. Figures from Ref. [52]. 17

1.14 The γ^{iso}-tagged fragmentation function for pp (red) and p–Pb data (blue) at $\sqrt{s_{NN}}$ = 5.02 TeV as measured by the ALICE detector. The boxes represent the systematic uncertainties while the vertical bars indicate the statistical uncertainties. The dashed green line corresponds to PYTHIA 8.2. Plot from Ref. [53]. 18

1.15 γ^{iso}–hadron correlations $I_{pQCD\ NLO}$ ratio, $D(z_T)$ measured in Pb–Pb collisions by ALICE for three centrality classes over pp collisions from NLO pQCD calculations, all at $\sqrt{s_{NN}}$ = 5.02 TeV. Plot from Ref. [54]. 19

2.1 Overview of accelerators and connected experiments at CERN, as in the year 2022 [56]. 20

2.2 Schematic overview of the ALICE detectors [65]. 24

2.3 Layout of the ALICE ITS [63]. 26

2.4 Schematic drawing of the ALICE TPC [71]. 27

2.5 The p_T resolution for standalone TPC and ITS–TPC matched tracks with and without constraint to the vertex. The vertex constrain significantly improves the resolution of TPC standalone tracks. For ITS–TPC tracks, it has no effect (green and blue squares overlap) [72]. 28

2.6 Schematic view of the EMCal (left) illustrating the module position on two approximately opposite locations in azimuth. The PHOS calorimeter inside the DCal is indicated in brown. The right figure shows a cross section of the ALICE barrel detectors. Figure from [74]. 29

2.7 EMCal full-size (SM) in the ($\eta - \varphi$) plane including visualizations of sub-components and their tower coverage. Figure adapted from Ref. [74]. 29

2.8 Geometric overview of the EMCal and DCal detectors in the $\eta - \varphi$ plane. The drawing outlines the full LHC Run 2 setup with all twenty SMs as well as the PHOS detector in the DCal gap. 30

3.1 Cluster energy distribution, per p_{T}-hard bin (colored lines) and the sum (black line) of all bins for γ–jet (left) and jet–jet triggered by decay photons with $p_{\mathrm{T}} > 7$ GeV/c (right) simulations after scaling the p_{T}-hard bins using Eq. (3.1). 33

3.2 Schematic view of cluster energy repartition in cells and the shower shape axes. The different colors indicate the amount of energy deposited in each cell, the darker the more energy. 35

3.3 Clusters σ^2_{long} distribution from data (black), pp collisions at $\sqrt{s} = 13$ TeV, or simulation, γ–jet + jet–jet PYTHIA processes, with different cross-talk (xTalk) emulation parameterizations (see Sec. 3.4.5 Tab. 3.4) and in different cluster p_{T} bins. Distributions normalised to the number of entries on each histogram. 37

3.4 Fraction of clusters with the number of cells contribute to cluster shower shape calculation, within the range $0.1 < \sigma^2_{\mathrm{long}} < 0.3$ per SM, in pp $\sqrt{s} = 13$ TeV L1-γ triggered data. Plot from Ref. [74]. Left, EMCal SMs (top SMs) and right DCal SMs (bottom). 39

3.5 Distance between a cluster and the closest projected track in η (top-left) or φ angle (top-right) versus the track momentum and for matched track-cluster pairs (bottom) in pp collisions at $\sqrt{s} = 13$ TeV collected with the minimum bias trigger. The black lines in the left and middle panels indicate the suggested selection criteria expressed in Eq. (3.9). From Ref. [74]. 42

3.6 Number of cells as a function of the cluster energy in pp collisions at $\sqrt{s} = 13$ TeV using the EMCal high threshold L1-γ trigger. The region below the lines is populated by exotic clusters. The distribution for each energy bin is normalized to its integral. Plot From Ref. [89]. 43

3.7 Left: "Exoticity" (F_+) as a function of the cluster energy in pp collisions at $\sqrt{s}$ = 13 TeV using the EMCal high threshold L1-γ trigger. The region above the line is populated by exotic clusters. The distributions are normalized to have an integral of unity for each energy bin. Plot from Ref. [89] slide 6. Right: Same distribution after the shower shape selection $\sigma^2_{\text{long}} > 0.1$ is applied (see definition in Sec. 3.3.1 and discussion on its use in Sec. 4.1). Plot from Ref. [89] slide 9. 44

3.8 Number of cells in the cluster in the same T-Card as the highest energy cell as a function of the number of cells in a different T-Card, for clusters between 100 and 200 GeV. In simulations that do not include cross-talk the same distribution is found but the bin at $n_{\text{cells, diff T-Card}} = 0$ is empty; this bin in data is populated by exotic clusters. From Ref. [74] 45

3.9 Top left: Semi-corrected narrow cluster ($0.1 < \sigma^2_{\text{long}} < 0.3$) p_{T} spectra by prompt γ efficiency ($N_\gamma^{\text{reconstructed}}/N_\gamma^{\text{generated}}$ within the analysis acceptance) in different acceptances within the calorimeter corresponding to supermodules acceptance or EMCal or DCal positive or negative η (even or odd SM numbers). The numerator of the ratio consists of: top right, spectra obtained for Full EMCal or DCal acceptance, of positive or negative eta SM of EMCal and DCal; bottom left, spectra obtained within each single EMCal SM; bottom right, spectra obtained within each single DCal SM. 47

3.10 Top left: Semi-corrected isolated narrow cluster ($0.1 < \sigma^2_{\text{long}} < 0.3$, $p_{\text{T}}^{\text{iso}} < 1.5$ GeV/c) p_{T} spectra by prompt γ efficiency ($N_\gamma^{\text{reconstructed}}/N_\gamma^{\text{generated}}$ within the analysis acceptance) in different acceptances within the calorimeter corresponding to supermodules acceptance or EMCal or DCal positive or negative η. The numerator of the ratio consists of: top right, spectra obtained for Full EMCal or DCal acceptance, of positive or negative eta SM of EMCal and DCal; bottom left, spectra obtained within each single EMCal SM; bottom right, spectra obtained within each single DCal SM. 48

3.11 Double ratio: neutral clusters ($\sigma^2_{\text{long}} > 0.1$) p_{T} spectra data/simulation per SM or group of SM divided by data/simulation for EMCal +DCal. Simulation is the addition of PYTHIA8 γ–jet and jet–jet events (biased). Ratios for different triggers, MB (top row), EMCal + DCal G2 trigger (middle row) and EMCal +DCal G1 trigger (bottom row). Each column corresponds to grouping in the numerator data/simulation ratio different SMs (left), only EMCal SMs (centre) or only DCal SMs (right). Simulation periods are reweighted by the trigger number of events. 49

3.12 Double ratio: isolated-narrow clusters ($0.1 < \sigma^2_{\rm long} < 0.3$, $p_{\rm T}^{\rm iso} < 1.5$ GeV/c) $p_{\rm T}$ spectra data/simulation per SM or group of SM divided by data/simulation for EMCal +DCal. Simulation is the addition of PYTHIA8 γ–jet and jet–jet events (biased). Ratios for different triggers, MB (top row), EMCal + DCal G2 trigger (middle row) and EMCal +DCal G1 trigger (bottom row). Each column corresponds to grouping in the numerator data/simulation ratio different SMs (left), only EMCal SMs (centre) or only DCal SMs (right). Simulation periods are reweighted by the trigger number of events. ····· 50

3.13 Averaged dispersion of the double ratios data/simulation shown in Figs. 3.11 and 3.12. Upper row for neutral clusters and lower for isolated narrow, left for MB trigger (and simulation periods weighted by MB number of events in data) middle for EMCal + DCal G2 triggers and right for EMCal + DCal G1 triggers (simulation periods reweighted by G1 number of events in data). ····· 51

3.14 Trigger efficiency for neutral (open square), narrow (open bullet) and isolated-narrow (full bullet) clusters in pp collisions at $\sqrt{s}$ = 13 TeV for the high (red) and low (black) L1-γ triggers. ····· 52

3.15 Left top panel, cross section $p_{\rm T}$ distribution obtained considering the trigger efficiency in the calculation or not, bottom panel, ratio of the two options. Right, associated relative uncertainty in %. We take half of the distribution as uncertainty. The red lines are the constant function fit at low $p_{\rm T}$ and the linear polynomial order 1 fit at intermediate $p_{\rm T}$. ·· 53

3.16 Top: The L1-γ low trigger rejection factor calculated with (blue square) and without (black dot) applying the trigger efficiency. The results of a constant fit to the rejection factor plateau regions are shown in the legend. Bottom: compared to the L1-γ low trigger, the L1-γ high trigger enhancement capability as a function of cluster $p_{\rm T}$ with (blue circle) and without (black cross) the trigger efficiency correction. The constant fit result with total uncertainty for the rejection factor plateau regions is shown in the legend. ····· 55

3.17 Cluster trigger rejection factors obtained by multiple fits changing the $RF^{\rm trig}$ $p_{\rm T}$ range of the fit, left is for G1/G2 per triggered event yield ratio and right for G2/MB per trigger event yield ratio. The histogram RMS is used as uncertainty. Distributions fitted to a Gaussian function and fit results are shown in the box, as a closure test. ····· 56

4.1 Distribution of the opening angle θ_{12} of two decay photons from π^0 (left) and η (right) mesons decays as a function of the meson energy obtained at generator level from an MC simulation. The horizontal lines indicate the opening angle corresponding to a width of approximately 1, 3 and 5 EMCal cells separating the two photons (1 cell = 0.0143 rad). Two photons completely merge into one cluster if they fall below the one cell distance, while they start merging at a width of approximately 3 cells, depending on the clusterizer. The colored vertical lines correspond to the energy limits where two photons could still be fully resolved by the clusterization described in Sec. 3.3 (blue) or by a clusterization that produces cluster splitting when more than one local maximum is found in the cluster (red). Plot from Ref. [74]. 57

4.2 (a) Cluster shower shape distribution σ^2_{long} as a function of the cluster p_{T} in data. The dashed lines correspond to the upper and lower selection limit values for single photon candidate clusters used in the analysis. (b) Projected shower shape distribution in two p_{T} intervals in data (black circles) and simulation (red crosses, PYTHIA 8 jet–jet and γ–jet events). For the simulation, the σ^2_{long} distribution for clusters with different particle origins are also shown as shaded areas except for prompt photons from γ–jet PYTHIA 8 processes that are presented with a blue histogram line. 58

4.3 Left: σ^2_{long} as a function of the exoticity parameter F_+ for $12 < E < 15$ GeV. Right: σ^2_{long} as a function of the cluster energy when the selection $F_+ < 0.97$ is not applied. Both distributions are shown for pp collisions at $\sqrt{s} = 13$ TeV using the EMCal L1-γ-high trigger. The clusterization algorithm used splits merged clusters, for this reason, the π^0 merged band in the right figure is less prominent than in Fig. 4.2(a)). Dashed lines located at $\sigma^2_{\text{long}} = 0.1$ (both figures) and $F_+ = 0.97$ (left figure). Figures from Ref. [74]. . 59

4.4 σ^2_{long} distribution for EMCal (black) and DCal (red) in different p_{T} range and its corresponding ratio EMCal/DCal in different photon cluster p_{T} bins. 60

4.5 Isolation momentum density in the isolation cone for data MB (left) and L1-γ (right) triggers estimated with different methods described in [51, 95]. Neutral clusters $p_{\text{T}} > 10$ GeV/c. 61

4.6 Isolation momentum density in the isolation cone for γ-jet simulation estimated with different methods described in [51, 95]. Neutral clusters $p_{\text{T}} > 10$ GeV/c. 62

4.7 EMCal charge only $p_{\text{T}}^{\text{iso, ch, UE}}$ distribution between data (black) and MC (red), and the corresponding ratio MC/Data in different photon cluster p_{T} bins. 63

4.8 $p_{\text{T}}^{\text{iso, ch, UE}}$ distribution for EMCal (black) and DCal (red) in different p_{T} range and its corresponding ratio EMCal/ DCal in different photon cluster p_{T} bins. 64

4.9 Isolated clusters ($p_{\mathrm{T}}^{\mathrm{iso,\ ch,\ UE}} < 1.5$ GeV/c, $R = 0.4$) σ^2_{long} distribution from data (black), pp collisions at $\sqrt{s} = 13$ TeV, or simulation, γ–jet + jet–jet PYTHIA processes, with different cross-talk (xTalk) emulation parameterizations (see Sec. 3.4.5 and Tab. 3.4) and in different cluster p_{T} bins. Distributions normalised to the number of entries on each histogram. 65

4.10 Top: Fraction of isolated-narrow clusters compared to the narrow clusters sample (f^{iso}) with and without UE subtraction, estimated with different methods described in [51, 95]. Bottom: Ratio of the f^{iso} for each UE subtraction method over no UE subtraction. Data L1-γ triggered sample (left) and γ–jet PYTHIA events (right). 66

4.11 Fraction of clusters with cells in more than one T-Card for different cluster selection criteria: Neutral, Narrow, Isolated and Isolated Narrow. Data, L1-γ high threshold. 67

4.12 Cluster time distribution, for the different cluster types and different p_{T} bins in data. All triggers combined, first frame only MB+L1-γ-low triggers. Distributions normalized to the integral between -50 and 50 ns. 67

4.13 Top, raw cluster spectrum after RF^{trig} normalization for each trigger sample. Bottom, ratio of each trigger spectra of the top plot to the combined spectrum. 68

4.14 Efficiency for prompt photon clusters generated with PYTHIA8 γ–jet simulation depending on the selection cuts chain: only reconstructed neutral clusters (green), plus shower shape cut of $0.1 < \sigma^2_{\mathrm{long}} < 0.3$ (red), and plus the isolation cut (blue). Black points correspond to the fraction of generated photons that pass the isolation cut at the generator level. 70

4.15 The total isolated-photon efficiency as a function of the reconstructed p_{T}^{γ}. The systematic uncertainty shown as boxes in the plot has been obtained from the "no MC tuning" uncertainty source related to the cross-talk emulation discussed in Sec. 5. 71

4.16 Prompt photon isolation efficiency at the generator level changing in PYTHIA the activation of MPI and FSR/ISR processes. Kindly produced by Florian Jonas. 72

4.17 Top: Isolation efficiency κ^{iso} at the generator level in PYTHIA for different collision energies: $\sqrt{s}$ = 5.02 [87], 7 [44], 8 [97, 98], and 13 TeV, and removing event-by-event the UE for $\sqrt{s}$ = 5, 8 and 13 TeV. The UE is removed event by event estimating the particle energy density in an η-band out of the isolation cone ($\sqrt{s}$ = 5 and 13 TeV) or perpendicular cones ($\sqrt{s}$ = 8 TeV). Bottom: Ratio of the κ^{iso} removing over not removing the UE. 72

4.18 Visualization of the ($p_{\mathrm{T}}^{\mathrm{iso,\ ch,\ UE}}$ and σ^2_{long}) phase space used to calculate the purity of the selected isolated photon clusters. 73

4.19 Isolated-photon purity by the data-driven method defined in Eq. (4.12) as a function of the photon p_{T}. 75

4.20 Purity MC correction factor as a function of the photon energy. 76

4.21 Purity of the isolated-photon sample as a function of p_{T}^{γ} calculated using Eq. (4.15). The statistical and systematic uncertainties have been evaluated as discussed in Sec. 5. The red and blue lines are the results of a fit to the measured purity using a two-sigmoid-function described by Eq. (4.19) for two different transverse momentum intervals. 77

4.22 Purity of the isolated-photon sample as a function of p_{T}^{γ} for simulations combining γ–jet and jet–jet PYTHIA samples. Different colour lines correspond to different σ^2_{long} cut. Each frame corresponds to a different isolation threshold $p_{\mathrm{T}}^{\mathrm{iso,\ ch,\ UE}} = 1.5$, 2.0 and open. 79

4.23 Purity of the isolated-photon sample as a function of p_{T}^{γ} for simulation combining γ–jet and jet–jet PYTHIA samples. The background only considers single decay photon clusters. Different colour lines correspond to different σ^2_{long} cut. Each frame corresponds to a different isolation threshold $p_{\mathrm{T}}^{\mathrm{iso,\ ch,\ UE}} = 1.5$, 2.0 and open. 80

4.24 Purity of the isolated-photon sample as a function of p_{T}^{γ} for simulation combining γ–jet and jet–jet PYTHIA samples. The background only considers merged photon clusters from π^0 decay. Different colour lines correspond to different σ^2_{long} cut. Each frame corresponds to a different isolation threshold $p_{\mathrm{T}}^{\mathrm{iso,\ ch,\ UE}} = 1.5$, 2.0 and open. 81

4.25 The distribution of the double ratio, R_f, as a function of cluster σ^2_{long}. Different linear function fits changing the fit range are displayed in different coloured lines. Clusters with $8 < p_{\mathrm{T}} < 9$ GeV/c (top) and $16 < p_{\mathrm{T}} < 18$ GeV/c (bottom). 83

4.26 The R_f distribution with cluster $p_{\mathrm{T}} = 8$–9 GeV/c, different linear fits changing the fit range are displayed in different coloured lines. With the scaling factor $k = 1$ (top) and $k = 2$ (bottom). 84

4.27 C_α from different scale factor k which is the γ–jet simulation scaling factor, the R_f background fit range is $0.4 < \sigma^2_{\mathrm{long}} < 2.0$. 85

4.28 α_{MC} from different scale factor k which is the γ–jet simulation scaling factor, the R_f background fit range is $0.4 < \sigma^2_{\mathrm{long}} < 2.0$. 85

4.29 Top panel: Purity for different α'_{MC} obtained varying the k scaling factor to calculate C_α. Bottom panel: The corresponding purity ratio to the default selection. Both R_f background fit range is $0.4 < \sigma^2_{\mathrm{long}} < 2.0$. 86

4.30 The constant parameters obtained by fitting a linear function to the different R_f background ranges as a function of the cluster p_{T}. Each coloured marker for a different σ^2_{long} fitting range indicated in the legend. The upper one is for $k = 1$ and the bottom is for $k = 2$. 87

4.31 The slope parameters obtained by fitting a linear function to the different R_f background ranges as a function of the cluster p_{T}. Each coloured marker for a different σ^2_{long} fitting range indicated in the legend. The upper one is for $k = 1$ and the bottom is for $k = 2$. 88

4.32 C_α distribution with parameters obtained by fitted linear function to different background ranges of the R_f. Each coloured marker for a different σ^2_{long} fitting range indicated in the legend. The upper one is for $k = 1$ and the bottom is for $k = 2$. 89

4.33 α_{MC} variations obtained from different R_f background range polynomial order 1 fit calibration factors C_α. Each coloured marker for a different σ^2_{long} fitting range indicated in the legend. The upper one is for $k = 1$ and the bottom is for $k = 2$. 90

4.34 Purity variations when α_{MC} is obtained from different R_f background range polynomial order 1 fit calibration factors C_α. Each coloured marker for a different σ^2_{long} fitting range indicated in the legend. The upper plot is for $k = 1$ and the bottom is for $k = 2$. 91

4.35 Ratio of purities from Fig. 4.34 obtained with different calibration factors C_α to the default obtained when changing the fitting range in R_f. Each coloured marker for a different σ^2_{long} fitting range indicated in the legend. The upper plot is for $k = 1$ and the bottom is for $k = 2$. 92

4.36 The relative uncertainty calculated comparing standard purity and the purity calculated with the C_α calibration for different R_f σ^2_{long} background fit ranges and the variations of the fit range. Each coloured marker for a different σ^2_{long} fitting range indicated in the legend. The signal simulation scale factor is $k = 2$. 93

4.37 C_α from different scale factor k which is the γ–jet simulation scaling factor, R_f background fit range $0.4 < \sigma^2_{\mathrm{long}} < 2.0$. 93

4.38 Ratio of the sigmoid fit functions results of Fig. 4.21 and the purity points. The fitting ranges are [7, 30] GeV/c and [20, 160] GeV/c for the low and high p_{T}. 95

4.39 Ratio of the purity points of Fig. 4.21 and sigmoid fit functions obtained with different fitting ranges. The fitting ranges are [7, 40] GeV/c and [20, 160] GeV/c for the low and high p_{T}. 95

4.40 Isolated photon purity and the two fitted sigmoid functions. The band indicating the fit uncertainty obtained varying the fit parameters within the fit errors. 96

4.41 Purity function fitting relative uncertainty. 96

4.42 Isolated-photon cross section in pp collisions at $\sqrt{s} = 13$ TeV, associated with statistical uncertainty only. 99

5.1 (a) Top panel, purity obtained for different background σ^2_{long} range variations. Bottom panel, ratio to the reference background σ^2_{long} range. (b) Associated relative uncertainty in % taking the average of the two variations, the red line is fit to a constant. 101

5.2 (a) Top panel, purity obtained for different background anti-isolation p_{T} ranges variations, fixing the minimum of the range at 2 GeV/c. Bottom panel, ratio to the reference range. (b) Associated relative uncertainty in % taking the average of all the possible variations discussed in the text, the red lines are the result of a fit to constant or linear functions. 102

5.3 (a) Top panel, purity obtained for different MC scale variations, $k = 0.5, 1.0, 1.5$. Bottom panel, ratio to the reference range, $k = 1.0$. (b) Associated relative uncertainty in % taking the average of the 2 variations, the red line is the constant function fit. 103

5.4 Purity uncertainty sources and total uncertainty (red line). 103

5.5 Relative uncertainty in % from the charged particle veto selection, the red line is a constant function fit between 7 and 160 GeV/c. 105

5.6 Relative uncertainty in % from the number of local maximum, the red line is a constant function fit between 7 and 50 GeV/c and a linear function fit between 50 and 100 GeV/c. 105

5.7 Relative uncertainty in % from the distance to masked channels, the red line is given by a constant function fit. 106

5.8 Relative uncertainty in % from F_+, the red line is a constant function fit between 7 and 50 GeV/c. 106

5.9 Fraction of isolated or not isolated narrow or wide cluster spectrum selected within a time window of 10 or 40 ns divided by the default 20 ns window. 107

5.10 Left: Data driven purity from Eq. (4.12) for different time windows $|t| < 10$, 20 or 40 ns. Right: ratio to $|t| < 20$ ns. 108

5.11 Relative uncertainty in % when comparing the time cut $|t| < 20$ ns to $|t| < 10$, 40 ns and their average. The average is fitted above 20 GeV/c by a constant resulting in 1.4%. 108

5.12 Uncertainty from the cross-talk emulation in %, the red line is a constant function fit used as uncertainty above 10 GeV/c. 109

5.13 (a) Top panel, cross-section p_{T} distribution obtained for different signal σ^2_{long} ranges variations. Bottom panel, ratio to the reference range. (b) Associated relative uncertainty in % taking the average of the 2 variations, the red lines are the constant function fit. ··· 110

5.14 Top, corrected isolated photon spectra scaled x axis by ±0.5% and fitted to power law function. Bottom, relative uncertainty from the energy scale for each variation. ····· 111

5.15 Cross section uncertainties, the black line is the total relative uncertainty and the coloured lines are the different uncertainty sources. ····· 111

6.1 Isolated-photon purity in pp collisions at $\sqrt{s}$ = 5.02, 7, 8, 13 TeV and 50–90% Pb–Pb collisions (peripheral collisions similar to pp collisions) at $\sqrt{s_{\mathrm{NN}}}$ = 5.02 TeV. All purities are shown for ALICE measurement (left) and PYTHIA MC (right) calculated as the ratio of prompt photons from γ–jet processes over prompt photons plus clusters from jet–jet processes all passing the isolation and shower shape selection criteria. Isolation energy ($p_{\mathrm{T}}^{\mathrm{iso}}$) changes from isolation using only charged particles (pp $\sqrt{s}$ = 13 TeV, 8 TeV and 5.02 TeV, and Pb–Pb $\sqrt{s_{\mathrm{NN}}}$ = 5.02 TeV) and using neutral (calorimeter) and charged particle information (pp $\sqrt{s}$ = 7 TeV), and subtracting the underlying event from the isolation energy (pp $\sqrt{s}$ = 5.02 TeV and 8 TeV, and Pb–Pb $\sqrt{s_{\mathrm{NN}}}$ = 5.02 TeV) and not subtracting it (pp $\sqrt{s}$ = 7 and 13 TeV). The cone size is R = 0.4 common to all systems. The charged particle veto selection (CPV) discussed in Sec. 3.5.2 is used in all the measurements except pp collisions at $\sqrt{s}$ = 5.02 TeV. The measured purity at $\sqrt{s}$ = 7 TeV in pp collision is from Ref. [44], at $\sqrt{s_{\mathrm{NN}}}$ = 5.02 TeV in pp and Pb–Pb collisions are from Ref. [51] and $\sqrt{s}$ = 8 TeV in pp collision is from Ref. [52]. ····· 114

6.2 Differential cross section of isolated-photons measured in pp collisions at $\sqrt{s}$ = 13 TeV. Vertical black lines and open boxes represent data statistical and systematic uncertainties, respectively. ····· 115

6.3 Top panel: Differential cross section of isolated-photons measured in pp collisions at $\sqrt{s}$ = 13 TeV. Vertical black lines and grey-filled boxes represent data statistical and systematic uncertainties, respectively. The blue boxes correspond to pQCD calculations with JETPHOX, open boxes for scale uncertainty and filled boxes for PDF uncertainty, respectively. Bottom panel: Ratio between the JETPHOX calculation results and data displayed in the blue boxes, vertical boxes size shows the theory scale and PDF uncertainties. Experimental uncertainties are shown here on the black points centered at unity. The normalization uncertainty of 1.5%, described in Sec. 4.5, is included only in the bottom panel and shown as a red box at 200 GeV/c. ····· 116

6.4 Ratios of theory to data using three PDF sets —NNPDF40 (cyan) [104], CT18 (red) [106], and MSHT20 (blue) [107] —as a function of p_{T}^{γ}. Experimental uncertainties are shown here on the black points centered at unity, and the experimental systematic uncertainties are represented as gray bands. The ratio between the JETPHOX NNPDF40 calculation results and data displayed in the blue boxes, vertical boxes size shows the theory scale and PDF uncertainties. The ratio between CT18 or MSHT20 and the data is only presented with statistical uncertainty. 117

6.5 Isolated-photon cross section measured with the photon EMCal in pp collision at $\sqrt{s}$ = 5.02 [51], 7 [44], 8 [52], and 13 [108] (this work) TeV. All cross sections p_{T} spectra are shown for ALICE measurement and NLO JETPHOX calculation with NNPDF40 and BFG II for the fragmentation function. The NLO calculations are scaled down by the partonic to hadronic isolation efficiency κ^{iso}. The isolation momentum threshold for each collision system is reported in the legend. The cone size is $R = 0.4$ common to all systems. 118

6.6 Ratio between theory predictions for the isolated-photon differential cross section and measurements for ATLAS [36], CMS [45], and ALICE [108]. The isolation required transverse energy for ATLAS is $E_{\mathrm{T}}^{\mathrm{iso}} < 4.2{\times}10^{-3}{\times}E_{\mathrm{T}}^{\gamma}{+}4.8$ GeV, for CMS is $p_{\mathrm{T}}^{\mathrm{iso,UE}} < 5$ GeV, and for ALICE, this work, is $p_{\mathrm{T}}^{\mathrm{iso,\ ch,\ UE}} < 1.5$ GeV. The isolation radii are $R = 0.4$ for the three. Theory predictions are obtained for ATLAS with NNLOJET [109] NNLO NNPDF3.1 PDFs [110], for CMS with JETPHOX NLO and NNPDF3.0 PDFs [111], and for ALICE with JETPHOX NLO and NNPDF4.0 PDFs [104]. Experimental uncertainties are shown here on the points centered at unity, for CMS and ATLAS statistical and systematic uncertainties are added in quadrature and shown as a vertical error bar. ALICE error bars are statistical uncertainties and boxes are systematic uncertainties. The colored boxes centered at the ratio indicate the theoretical uncertainty on the PDF and scales. The luminosity normalization uncertainty of each experiment is presented as an overall box around unity at the right of the figure centered at unity. 119

6.7 Isolated-photon cross-section ratio of pp collisions at $\sqrt{s}$ = 13 TeV (this work, as Ref. [108]) over $\sqrt{s}$ = 7 TeV from Ref. [44] (left) and $\sqrt{s}$ = 5.02 TeV from Ref. [51] in data and NLO calculation from JETPHOX for $R = 0.4$. Error bars and empty boxes are the data statistical and systematic uncertainties, respectively. Filled boxes represent the theory scale (orange) and PDF (pink) uncertainties. 120

6.8 Ratio of isolated-photon cross sections measured in pp collisions at $\sqrt{s}$ = 7 TeV (taken from Ref. [44]) over the one at $\sqrt{s}$ = 5.02 TeV from Ref. [51] compared to NLO calculations from JETPHOX shown as colored boxes. 121

6.9 ALICE data compared to previous measurements of isolated-photon spectra in pp and $p\bar{p}$ collisions as a function of x_T where the invariant cross sections have been scaled by $(\sqrt{s})^n$ with n = 4.5 (taken from Ref. [114]). For this comparison, only the results covering mid-rapidity are shown. 122

A.1 Isolation fraction double ratio (data to MC) R_f (Eq. 4.16) in different cluster p_T interval from 7 to 14 GeV/c, fit by a first order polynomial function in different background σ^2_{long} range. 134

A.2 Isolation fraction double ratio (data to MC) R_f (Eq. 4.16) indifferent cluster p_T interval from 14 to 35 GeV/c, fit by a first order polynomial function in different background σ^2_{long} range. 135

A.3 Isolation fraction double ratio (data to MC) R_f (Eq. 4.16) indifferent cluster p_T interval from 35 to 200 GeV/c, fit by a first order polynomial function in different background σ^2_{long} range. 136

A.4 Isolation fraction double ratio (data to MC) R_f (Eq. 4.16) indifferent cluster p_T interval from 7 to 14 GeV/c, fit by a first order polynomial function in different background σ^2_{long} range. 137

A.5 Isolation fraction double ratio (data to MC) R_f (Eq. 4.16) indifferent cluster p_T interval from 14 to 35 GeV/c, fit by a first order polynomial function in different background σ^2_{long} range. 138

A.6 Isolation fraction double ratio (data to MC) R_f (Eq. 4.16) indifferent cluster p_T interval from 35 to 200 GeV/c, fit by a first order polynomial function in different background σ^2_{long} range. 139

A.7 Isolation fraction double ratio (data to MC) R_f (Eq. 4.16) indifferent cluster p_T interval from 7 to 14 GeV/c, fit by a first order polynomial function in different background σ^2_{long} range. 140

A.8 Isolation fraction double ratio (data to MC) R_f (Eq. 4.16) indifferent cluster p_T interval from 14 to 35 GeV/c, fit by a first order polynomial function in different background σ^2_{long} range. 141

A.9 Isolation fraction double ratio (data to MC) R_f (Eq. 4.16) indifferent cluster p_T interval from 35 to 200 GeV/c, fit by a first order polynomial function in different background σ^2_{long} range. 142

A.10 Isolation fraction double ratio (data to MC) R_f (Eq. 4.16) in different cluster p_T interval from 7 to 14 GeV/c, fit by a first order polynomial function in different background σ^2_{long} range. 143

A.11 Isolation fraction double ratio (data to MC) R_f (Eq. 4.16) in different cluster p_T interval from 14 to 35 GeV/c, fit by a first order polynomial function in different background σ^2_{long} range. 144

A.12 Isolation fraction double ratio (data to MC) R_f (Eq. 4.16) in different cluster p_T interval from 35 to 200 GeV/c, fit by a first order polynomial function in different background σ^2_{long} range. 145

A.13 Isolation fraction double ratio (data to MC) R_f (Eq. 4.16) in different cluster p_T interval from 7 to 14 GeV/c, fit by a first order polynomial function in different background σ^2_{long} range. 146

A.14 Isolation fraction double ratio (data to MC) R_f (Eq. 4.16) in different cluster p_{T} interval from 14 to 35 GeV/c, fit by a first order polynomial function in different background σ^2_{long} range. ····· 147

A.15 Isolation fraction double ratio (data to MC) R_f (Eq. 4.16) in different cluster p_{T} interval from 35 to 200 GeV/c, fit by a first order polynomial function in different background σ^2_{long} range. ····· 148

A.16 R_f (Eq. 4.16) fitted by a first order polynomial function to different background intervals. The constant and slope parameters obtained by the fitted function and the corresponding mean values are in different colours and styles. Cluster p_{T} interval from 7 to 200 GeV/c, scale factor $k = 1$. ····· 150

A.17 R_f (Eq. 4.16) fitted by a first order polynomial function to different background intervals. The constant and slope parameters obtained by the fitted function and the corresponding mean values are in different colours and styles. Cluster p_{T} interval from 7 to 200 GeV/c, scale factor $k = 2$. ····· 151

A.18 The constant parameters obtained by fitting a first order polynomial function to different background ranges of the R_f (Eq. 4.16) and the corresponding mean values, cluster p_{T} interval from 7 to 200 GeV/c, scale factor $k = 1$. ····· 153

A.19 The constant parameters obtained by fitting a first order polynomial function to different background ranges of the R_f (Eq. 4.16) and the corresponding mean values, cluster p_{T} interval from 7 to 200 GeV/c, scale factor $k = 2$. ····· 154

A.20 The slope parameters obtained by fitting a first order polynomial function to different background ranges of the R_f (Eq. 4.16) and the corresponding mean values, cluster p_{T} interval from 7 to 200 GeV/c, scale factor $k = 1$. ····· 156

A.21 The slope parameters obtained by fitting a first order polynomial function to different background ranges of the R_f (Eq. 4.16) and the corresponding mean values, cluster p_{T} interval from 7 to 200 GeV/c, scale factor $k = 2$. ····· 157

B.1 Ratio, purity Sigmoid fit divided by points, fit range varied in each panel. ····· 158

B.2 Ratio, purity Sigmoid fit divided by points, fit range varied in each panel. ····· 159

List of Tables

2.1 Overview of ALICE data taking campaign until 2024. 23

3.1 Number of events collected with the minimum bias and L1 photon triggers in pp collisions at $\sqrt{s}$ = 13 TeV data per year and total. 31

3.2 The p_{T} usability range on the various JJ-triggered samples. 32

3.3 The list of p_{T}-hard bins of the jet–jet and γ–jet PYTHIA simulation sample generations. 33

3.4 Emulation parameters used to calculate the $E_{i,j}^{\mathrm{ind}}$ in the five surrounding cells to a given cell with signal in the T-Card depending on the SM number. Note that we allow also the inducing energy in cells two rows away, but only with F^{ind}=$F_{\mathrm{min}}^{\mathrm{ind}}$. Different parametrizations (Default or Std, More, EtaDep, Less) change the $F_{\mathrm{min}}^{\mathrm{ind}}$ parameter by a factor of 0.5 or 2 with respect to the default one. From Ref. [87] Sec. 6.1. 40

3.5 Setup of the EMCal triggers in various collision systems in LHC Run 2 (2015 - 2018). During Run 2, equivalent DCal triggers were enabled using the same thresholds. The L0 and L1-γ triggers are based on 2×2 FastORs. The patch size of the L1-jet triggers for EMCal is 16×16 FastORs, while DCal uses 8×8 FastORs in pp and p–Pb collisions. In Pb–Pb collisions the L1-jet trigger patch size is 8×8 FastORs for both parts of the calorimeter. Table from Ref. [74]. 46

3.6 Cluster rejection factors fitted value and its associated uncertainty, the last column is total uncertainty for G1/G2 and G2/MB. The final G1/MB (G2/MB · G1/G2) uncertainty is obtained combining G1/G2 and G2/MB uncertainties and is driven by G2/MB. 56

4.1 Variations of the purity sigmoid function parameters obtained from the fit. 95

4.2 The corresponding interaction cross section for years 2016, 2017, and 2018, in pp collisions at $\sqrt{s}$ = 13 TeV data. The last row corresponds to the weighted average of the years by the number of events. Weighted uncertainty calculated from the each year uncertainty and the uncertainty transfer rules. 97

4.3 Number of selected events, EMCal L1-γ trigger rejection factors, and luminosity per trigger. The luminosity uncertainty contains both the σ_{MB} and rejection factor uncertainties. 97

5.1 Summary of uncorrelated relative systematic uncertainties in per cent for selected p_{T} bins of the isolated photon measurement. The luminosity normalization uncertainty of 1.9% is not included in this table. ····· 112



博士学位论文

DOCTORAL DISSERTATION



1 Introduction of high-energy particle physics

Until the beginning of the 20th century, atoms were regarded as the fundamental, indivisible building blocks of all forms of matter. In the 1900s, it was discovered that atoms have a structure, it was found through the experiments of Rutherford [1] and others [2]. An atom consists of a dense central nucleus, which is comprised of protons and neutrons – collectively referred to as nucleons – orbited by electrons. Historically, protons, neutrons, and electrons were considered the fundamental particles of nature. However, the existence of other kinds of particles was evident via cosmic ray studies that led to the discovery of the positron, pion, muon, and others [3]. By the early 1960s, as accelerators that could accelerate protons or electrons to high energies and smash them into nuclei reached higher energies, a hundred or more types of particles were found.

In this chapter, I will give a brief overview of the background information relevant to my work. The main theoretical background is given in Sec. 1.1. The Standard Model of Particle Physics developed in the early 1970s has successfully explained almost all experimental results and precisely predicted a wide variety of phenomena, and is described at the beginning of this section. It successfully integrates the electromagnetic, weak, and strong forces through a unified theoretical framework. Among these forces, the strong interaction is described by Quantum Chromodynamics (QCD) which a brief introduction is given in Sec. 1.1.2. The parton distribution functions (PDFs) described in Sec. 1.1.3 are essential tools for predicting the behavior of hadrons in high-energy collisions. It quantifies the probabilities of finding quarks, antiquarks, and gluons – collectively known as partons – within hadrons at various momentum fractions. These distributions bridge the gap between the non-perturbative regime of QCD, where the strong coupling constant is large, and the perturbative domain accessible through collider experiments. As photons do not interact with the strong force, they are considered one of the “golden” probes for investigating phenomena governed by this interaction. The prompt photons produced directly in the hard-scattering process are valuable because they can provide precise measurements of PDFs and test predictions of pQCD. In Sec. 1.2, a more detailed exposition of the prompt photon in high-energy collisions will be presented, including the selection method and measurement results pertinent to the prompt photon.

1.1 Theoretical description

1.1.1 The standard model of particle physics

The Standard Model of Particle Physics encapsulates our understanding of the fundamental particles and the forces. It explains how the basic building blocks of matter interact, governed by three of the four fundamental forces in nature. Figure 1.1 presents the elementary particles in the standard model.

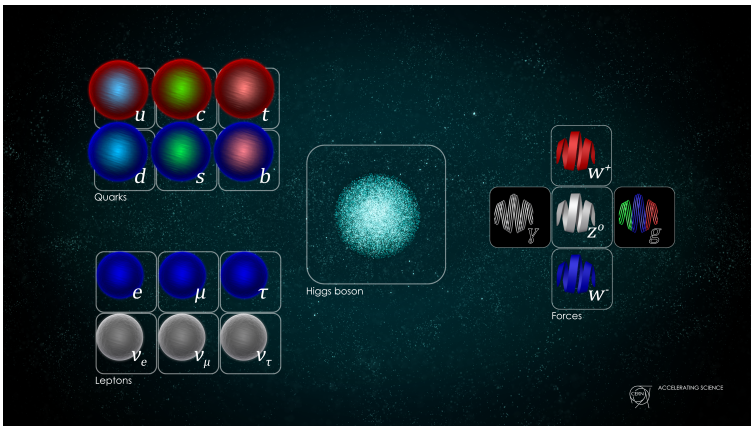

Figure 1.1: Elementary particles in the Standard Model of Particle Physics [4].

The fundamental particles, the basic building blocks of matter, are separated into two basic types: quarks and leptons, as presented on the left side in Fig. 1.1. Both quark and lepton are fermions with a spin of 1/2. Each group comprises six particles, which are related in "generations" or pairs. Quarks, q, have six types, divided into 3 "generations". The lightest and most stable particles make up the first generation, while the heavier and less stable particles belong to the second and third generations. All stable matter in the universe is made from particles that belong to the first generation; any heavier particles quickly decay into more stable ones. The three quark generations or pairs are: the "up quark (u)" and the "down quark (d)" from the first generation, followed by the "charm quark (c)" and "strange quark (s)" , then the "top quark (t)" and "bottom (or beauty) quark (b)" . Quarks also come in three different "colors" and only mix in such ways as to form colorless objects (hadrons). The six leptons are similarly arranged in three generations – the "electron (e)" and the "electron neutrino (ν_e)" , the "muon (μ)" and the "muon neutrino (ν_μ)" , and the "tau (τ)" and the "tau neutrino (ν_τ)" . The e, μ, τ all have an electric charge and a sizeable mass, whereas the neutrinos are electrically neutral and have very little mass.

The fundamental forces at work in the universe are the strong force, the weak force, the electromagnetic force, and the gravitational force. Three of those fundamental forces, the electromagnetic force,

the strong force, and the weak force, result from the exchange of force-carrier particles, which belong to a broader group called "bosons" with spin 0 or 1. Each of the fundamental forces has its boson – the photons γ, responsible for the electromagnetic interaction, the bosons $W^{\pm}$ and Z^{0}, carry the electro-weak interaction, and the gluons g carry the strong force. Those bosons are listed on the right side of Fig. 1.1. For gravity, the corresponding force-carrying particle has not been found yet, but it is so weak on the scale of those other three fundamental forces to be considered negligible and does not form part of the standard model of particle physics. Particles of matter transfer discrete amounts of energy by exchanging the force-carrying particles with each other.

The four fundamental "forces" have different strengths or intensities over distance ranges. Gravity is the weakest force that decreases with the distance. The electromagnetic force also decreases with the distance but is $\sim 10^{36}$ times stronger than gravity. The weak and strong forces are effective only over a very short range and dominate only at the level of subatomic particles. The weak force is much stronger than gravity but it is weaker than the strong force and the electromagnetic force. The strong force, as its name suggests, is the strongest of the four fundamental interactions. It is a very short-range force, acting only over distances of approximately one femtometre, which is about the size of a nucleon. At a distance of one femtometre, if the magnitude of the strong force is taken as 1, the magnitudes of the electromagnetic force, the weak force, and gravity would be 10^{-3}, 10^{-8} and 10^{-37}, respectively. As the distance is longer, the strong force becomes weaker and is eventually overtaken by electromagnetic force and gravity.

1.1.2 Quantum Chromodynamics theory

Each of these interactions is described by a Quantum Field Theory (QFT) [5, 6], which provides the mathematical framework to understand and quantify the interactions found in the standard model. In essence, QFT treats each particle as an excitation of a quantum field defined over all space and time. How and if a force is mitigated is determined by the properties of the boson and the QFT that is associated with the given interaction. For the electromagnetic interaction, the corresponding theory is known as Quantum Electro Dynamics (QED) [7] and the strong interaction is described by Quantum Chromodynamics (QCD) [8, 9]. Weak interactions are usually described within electro-weak theory, which allows a unified description of the electromagnetic- and weak forces.

QCD has two interesting properties that were discovered experimentally and predicted by theory. The first is asymptotic freedom – at very high energies or short distances, the strong force becomes weaker and particles can interact more freely. Gluons carry color charge, a property of the strong force analogous to the electric charge in electromagnetism, and interact with each other with their color charge.

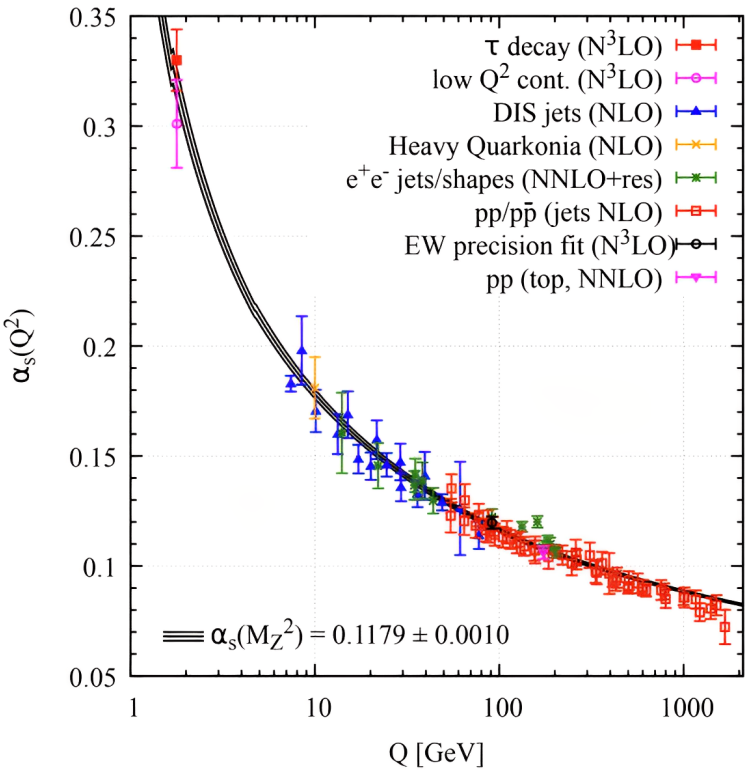

Figure 1.2: Various measurements of α_s as a function of Q along with a fit function. Image from Ref. [10].

Whereas photons carry no electric charge and do not interact with each other. This interaction causes the strong force to be weaker and weaker at short distances because the gluons effectively shield each other from their interactions. The second interesting property of QCD is confinement – quarks and gluons cannot exist in isolation but must exist in bound color-neutral states. Both properties can be seen in the measurements of α_s, the QCD coupling constant which describes the strength of the strong interaction as a function of Q^2, the energy scale. The relationship between α_s and Q is shown in Fig. 1.2. At low Q, corresponding to large distances, the α_s seems to approach infinity asymptotically. If two partons are pulled apart, the α_s will continue to increase with the distance until it is energetically more favorable for a quark-antiquark to be produced out of the vacuum. When Q increases, the distance between the partons decreases, and the strength of the strong force diminishes, which leads to the asymptotic freedom mentioned above. The coupling constant can be written as a function of the energy scale as

$$\alpha_s(Q^2) = \frac{4\pi}{(11 - (2/3)N_f)\ln(Q^2/\Lambda_{\mathrm{QCD}})} \tag{1.1}$$

where N_f is the number of quarks, and Λ_{QCD} is a constant that roughly indicates the scale at which the perturbatively defined coupling would diverge [10].

The interaction between quarks and gluons is complex due to the strong couplings, and the strong

interactions described by QCD are highly nonlinear. This makes solving the QCD equation directly almost impossible. Concurrently, in the high-energy region, where Q^2 is large, the QCD shows asymptotic freedom, which means that the α_s becomes sufficiently small, thereby enabling the application of perturbation theory. That is to say, perturbative quantum chromodynamics (pQCD) can be employed for calculations. The pQCD provides a way to treat strong interactions at high energies by progressively approximating the actual physical phenomena through an order expansion.

The calculation of the cross section of QCD processes in hadron–hadron collisions presents a significant challenge, given that not all aspects of the collision can be treated within the framework of pQCD. To still obtain predictions for such cross sections, we can employ the factorization theorems [11], which allow us to separate the various energy scales involved in the collision in a systematic way. By factorization, one can obtain a cross section which is a convolution of the perturbatively treatable hard parton–parton scattering and process independent descriptions of the non-perturbative regimes in the initial and final state. Such independent treatment of different regimes is possible since the hard scattering occurs on a much shorter timescale than the processes in the initial and final state. Since hadrons are bound objects, the fluctuations inside them must be smaller than the confinement scale $\Lambda_{QCD} \approx 200$ MeV, and most virtual fluctuations inside the hadron occur on a timescale of $\approx 1/\Lambda_{QCD}$. The scattering partons interact on a much shorter timescale $1/Q \ll 1/\Lambda_{QCD}$ and therefore "see" a frozen-in-time snapshot of the initial state [12].

The scattering cross section $\sigma_{\mathrm{NN}\to\mathrm{h+X}}$ for a process of two colliding nucleons N which produce a hadron h is expressed after factorization as

$$\frac{d^3\sigma_{NN\to h}}{dp^3} = \sum_{a,b,c} \underbrace{f_a(x_a,\mu_f^2)\otimes f_b(x_b,\mu_f^2)}_{\text{PDFs}} \otimes \underbrace{\frac{d^3\sigma_{ab\to c+X}}{d\hat{p}^3}}_{\text{partonic cross section}} \otimes \underbrace{D_{c\to h}(z,\mu_f^2)}_{\text{fragmentation}} , \tag{1.2}$$

which can be seen as a convolution of three main parts: Parton Distribution Functions (PDFs) $f_i(x_i,\mu_f^2)$, partonic cross section $\sigma_{ab\to c+X}$ and fragmentation function $D_{c\to h}(z,\mu_f^2)$. The PDFs describe the initial state of the interaction which gives the probability density to find a parton, a or b in Eq. (1.2), within a nucleon/nucleus (N in Eq. (1.2)). The probability density is a function of the momentum fraction x_i (usually called Bjorken-x) and the factorization scale μ_f which the hadron is probed. The partonic cross section describes a hard scattering of two partons a and b to produce an outgoing parton c. Since there is sufficient large transfer momentum, it can be calculated with pQCD to a given order, commonly Next-to-Leading Order (NLO) or Next-to-next-to-leading Order (NNLO). The probability of finding the incoming partons a and b from the colliding hadrons is contained in the PDFs, then the cross section

describes the production of parton c. The fragmentation function is the fraction of the momentum carried by the hadron h, which can be observed in the detector, from the outgoing parton c. It is associated with the hadronization process in the final state. Providing constraints to the PDF is one of the motivations for the measurements presented in this work, and I will introduce this in detail in Sec. 1.1.3.

1.1.3 Parton distribution functions

The PDFs′ evolution with μ_f is treatable with pQCD using evolution equations such as DGLAP [13] and BFKL [14]. The choice is frequently made to align the μ_f with the momentum transfer Q of the scattering process [15]. This means that once a PDF is constrained by experimental data within a certain region of x and Q, the evolution equations can be employed to extrapolate the PDF to other regions of the phase space. Precise knowledge of PDFs is crucial, as any uncertainties present in the PDF will propagate to the uncertainties of theory predictions for physics observables. These, in turn, are used in various measurements performed at the experiment. In addition to their role in a variety of measurements, PDFs themselves represent our understanding of the substructure of protons and neutrons: the ongoing endeavor of constraining PDFs over a wide phase space in x and Q directly corresponds to probing the proton in different regimes and testing our understanding of QCD evolution over scales spanning several orders of magnitude.

The PDFs are universal, they can be determined from deep inelastic scattering (DIS), such as H1 and ZEUS at HERA [16], and those can be used to calculate cross sections of hard processes at the experiments [17]. The PDFs from HERAPDF2.0 are shown in the left panel of Fig. 1.3 as an example. The DGLAP evolution equations are valid at moderate to large Q^2 and moderate to large x, where the parton densities are not too large. For intermediate values of Q^2 but small values of x, the BFKL equations [14], are expected to describe the evolution. In small enough x, the large number of soft gluons resulting from gluon splitting leads to high enough parton densities, so that parton recombination, in particular gluon fusion, will be significant. In this regime, the QCD evolution is non-linear and can be described by the JIMWLK [18] or approximated by the BK [19] equations.

Measurements of hadronic observables, such as jet production, offer high constraining power for the gluon density. Jets are defined as collimated sprays of particles resulting from the fragmentation of partons. In particular, measurements of inclusive jet, dijet, and trijet production at the LHC allowed providing constraints for quarks and gluons at $x \geq 0.005$, as well as the possibility to measure the strong coupling α_s (Q) in the TeV regime [20].

The hard scattering processes in pp collisions play a pivotal role in probing the proton's internal

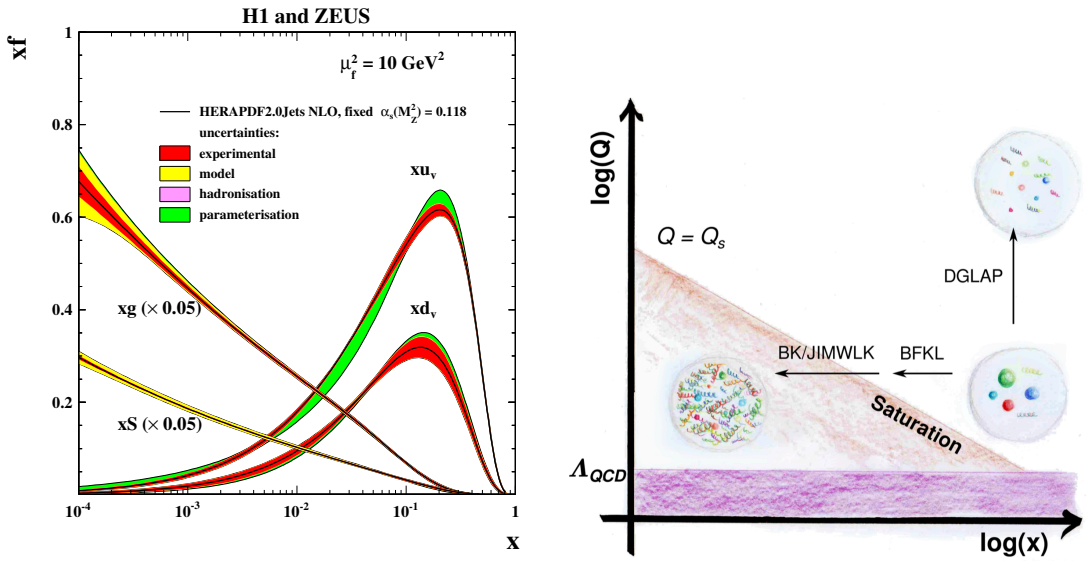

Figure 1.3: Left: PDFs from HERAPDF2.0, which have been determined from charm data, jet data and low energy data as well as the HERA-I and II high energy inclusive data [16].Right: Maps of QCD evolution as a function of (Q,x). The evolution towards large Q^2 can be described by DGLAP, and that towards small (but not too small) x by BFKL. At very small x, where the gluon density is very high, non-linear effects become relevant, and other evolution equations (BK or JIMWLK) are necessary.

structure. This is because the probability of a hard scattering event increases significantly when one or more partons carry a small fraction of the proton's momentum, corresponding to the low x regime [21]. Moreover, certain hard scattering processes, such as those producing prompt photons via the $qg \rightarrow q\gamma$ process, provide a way to get the gluon PDF in the proton, especially at low x values where other measurements may be less informative [22].

The work, measurement of the prompt photon production, enables the probe of the gluon density at low-x. It will be introduced in more detail in Sec. 1.2. For a comprehensive overview of the processes relevant to PDF analyses, as well as their kinematic coverage, please refer to, for example, Tab. 18.1 in Ref. [10] and Fig. 1 in Ref. [23].

1.2 Prompt photon production in hadronic collisions

Photons are produced in all stages of a collision and are a unique probe because they do not interact with strong interactions. This allows them to carry information about their production time unaltered by final-state effects until their detection in the experimental apparatus. Among the different photon sources, direct prompt photons produced in the quark-gluon Compton process are sensitive to the gluon PDF, which is one of the least constrained PDFs and cannot be directly accessed via DIS measurements.

This section will commence with a short introduction to the various photon sources, followed by the direct prompt photon selection. Finally, it will present the existing results.

1.2.1 Photon sources

Photons can be produced in multiple ways at different stages of the collision [24]. The majority of photons produced in pp collisions originate from hadron decays, mostly $\pi^0 \rightarrow \gamma\gamma$. Photons that do not originate in hadronic decays are called direct photons. In direct photons, we can find two different origins, prompt photons produced in the initial stage of a hard scattering process, and thermal photons, radiated by the QGP in nucleus-nucleus collisions. At the leading order (LO) of pQCD, prompt photons are produced by Compton ($qg \rightarrow \gamma q$, dominant process), annihilation ($q\overline{q} \rightarrow \gamma g$) and by double photon production (very small cross section), in the following, we denominate those photons "direct prompt photons". At the NLO of pQCD, prompt photons are also produced in the fragmentation of one of the outgoing partons in its hadronization process, those are then called "fragmentation photons". The distinction between the two sources is not so simple, the collinear part of such processes has been shown to contribute effectively at LO [25]. A schema describing those photon sources in pp collision is shown in Fig. 1.4, and the Feynman diagrams of the Compton and annihilation processes are presented in Fig. 1.5.

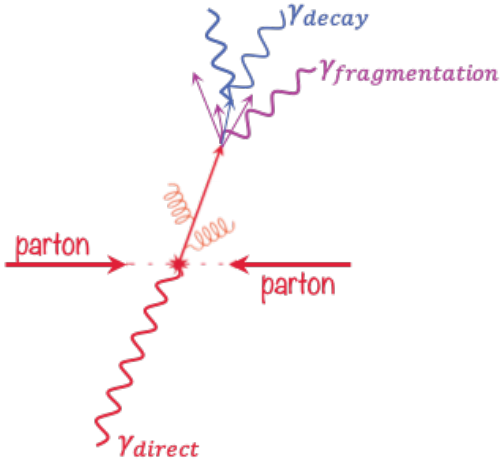

Figure 1.4: View of the various sources of photon production in pp collisions.

The NLO corrections come from subprocesses like $qg \rightarrow \gamma gg$ and $q\overline{q} \rightarrow \gamma gg$. Thermal photons are produced by interactions between the constituents of the thermalized quark–gluon plasma or hadron gas produced in heavy-ion collisions, and thus contain information about the plasma such as its temperature and collective flow [26]. The measurement of direct prompt photons is the main motivation for this work.

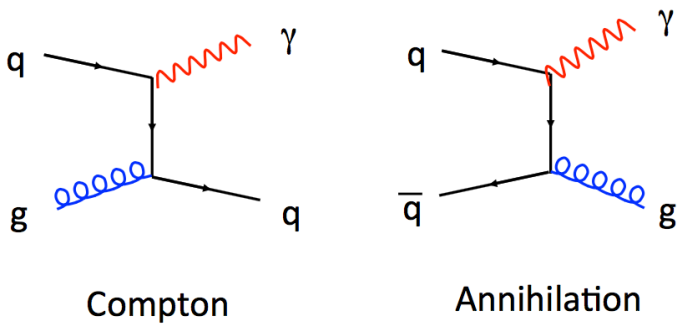

Figure 1.5: Feyman diagrams of prompt photon production.

The production ratio of prompt photon and π^0 in NLO pQCD prediction at different collision energies and types is shown in Fig. 1.6. At $\sqrt{s}$ = 14 TeV in pp collision case, the CTEQ6 [27] structure functions are used for the NLO QCD predictions. For the prompt photon spectrum, the BFG [28] parametrization of fragmentation functions is used while the KKP [29] fragmentation functions are used for the NLO pQCD estimates of decay photons. The cross section is evaluated at 0 rapidity [30]. One can observe that the ratio is significantly below unity with a strong p_{T} dependence of this ratio, ranging from 0.005 at 7 GeV/c to 0.1 at 100 GeV/c. In any case, given the small value of the ratio, for prompt photon measurements, one needs to find a selection procedure to reject hadronic decay photons.

1.2.2 Direct prompt photon selection: the isolation method

Prompt photons are produced in Compton and annihilation processes, due to their (at LO) point–like connection to the incoming partons. The inclusive cross section of prompt photon production $\sigma(p_\gamma)$ is

$$\sigma(p_\gamma) = \sum_{a=q,\bar{q},g} \int_0^1 \underbrace{\frac{dz}{z}\hat{\sigma}^a\left(\frac{p_\gamma}{z};\mu_R,\mu,\mu_f\right)\cdot D_a^\gamma(z,\mu_f)}_{\text{fragmentation}} + \underbrace{\hat{\sigma}^\gamma(p_\gamma;\mu_R,\mu,\mu_f)}_{\text{direct}} \tag{1.3}$$

which contains the fragmentation and the direct parts. In the equation, the $\hat{\sigma}^a$ and $\hat{\sigma}^a$ are the partonic cross sections for the production of a parton a and a photon (γ) which both already contain the convolution with the PDFs for the initial-state partons a coming from the colliding projectiles, the $D^\gamma_{q/g}$ is the parton-to-photon fragmentation function [31]. Thus far, the partonic cross section has been calculated up to NNLO [32].

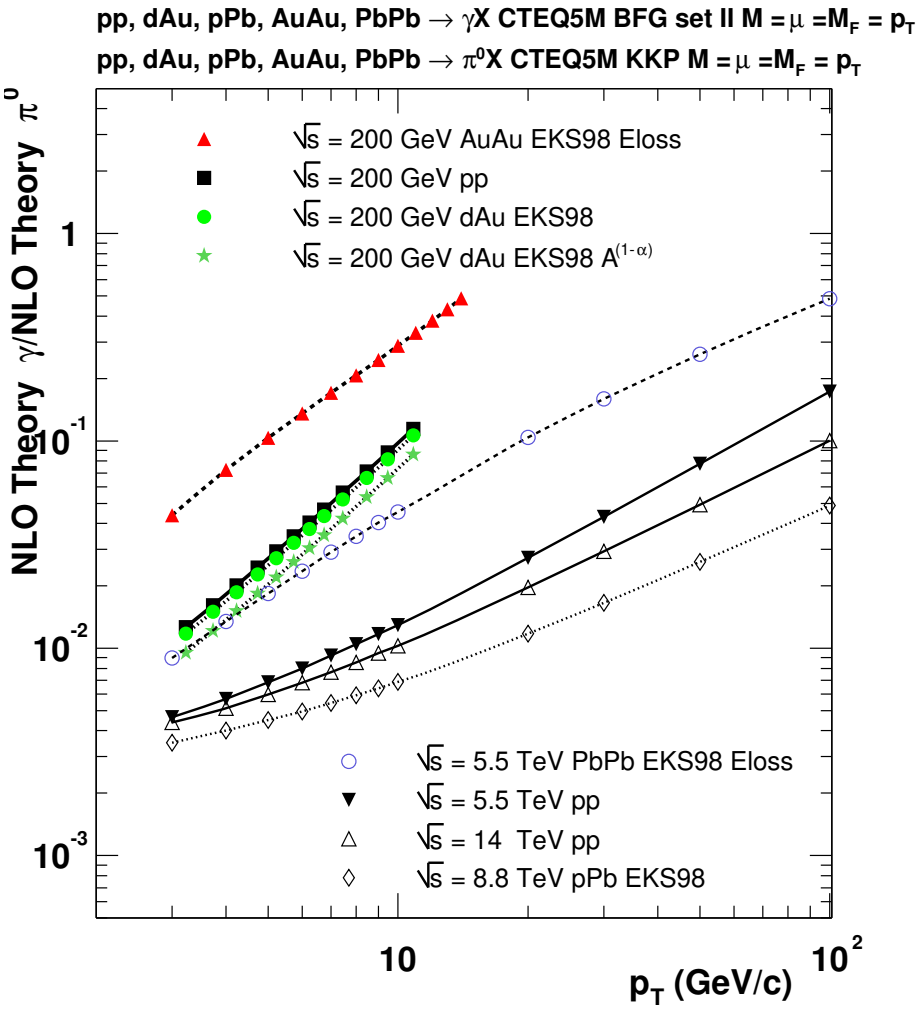

Figure 1.6: NLO QCD predictions for the ratio $\gamma_{\text{prompt}}/\pi^0$ in proton-proton, proton-nucleus and nucleus-nucleus collisions at 200 GeV and 5.5 TeV. At $\sqrt{s}$ = 14 TeV in pp collision case, the CTEQ6 [27] structure functions are used for the NLO QCD predictions. For the prompt photon spectrum, the BFG [28] parametrization of fragmentation functions is used while the KKP [29] fragmentation functions are used for the NLO pQCD estimates of decay photons. The cross section is evaluated at 0 rapidity. Plot from Ref. [30].

The three subprocesses (Compton, annihilation, and fragmentation) production ratio to the prompt photon at the LHC mid-rapidity ($y = 0$) in pp collision at $\sqrt{s} = 14$ TeV as a function of the photon E_{T} is shown in Fig. 1.7. They have been obtained by selecting the corresponding Feynman diagrams at

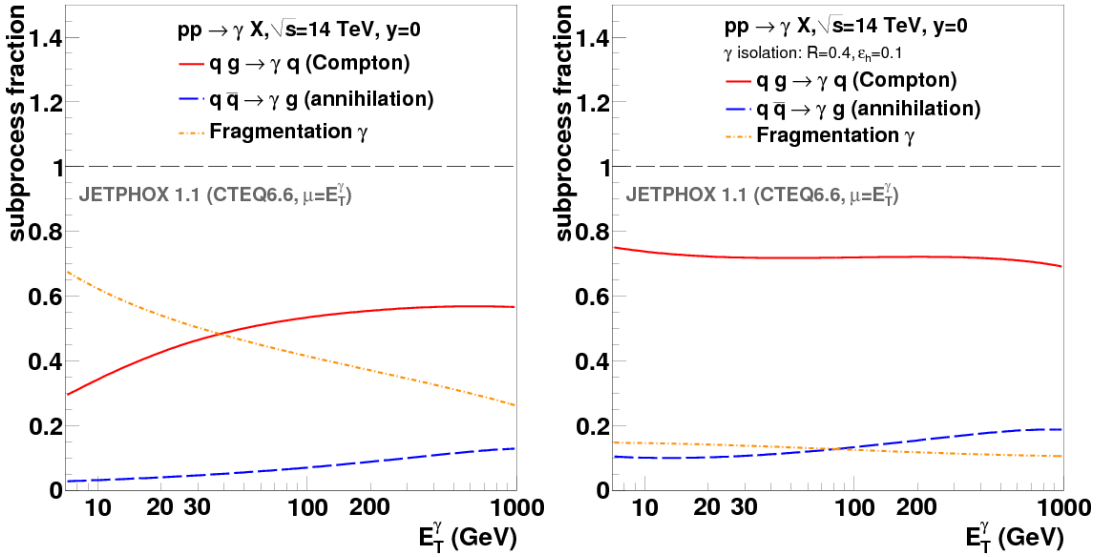

Figure 1.7: Left: Relative contributions of the quark-gluon Compton scattering, $q\bar{q}$ annihilation and fragmentation subprocesses in NLO prompt photon production at the LHC mid-rapidity in pp collision at $\sqrt{s} = 14$ TeV obtained with JETPHOX (CTEQ6.6 PDF, $\mu = E_T^{\gamma}$, and BFG-II FFs). Right: same process but with an isolation radius $R = 0.4$ and a hadron fraction of the photon energy of $\varepsilon = 0.1$ inside the cone [33].

NLO with the JETPHOX MC, setting all scales to $\mu = E_{\mathrm{T}}^{\gamma}$, and using the CTEQ6.6 parton densities and the BFG-II parton-to-photon FFs for the fragmentation photons [33]. In the left panel, one can see that the fraction of fragmentation photon decreases as the photon E_{T}. Nevertheless, its fraction is still comparable to the prompt photon at approximately 200 GeV. A clean separation of the different prompt photon sources experimentally is difficult and only the sum can be calculated with pQCD. Still, one can suppress the contribution of fragmentation and bremsstrahlung, which are accompanied by other parton fragments, via the selection of "isolated photons".

The isolation method is a way to select the direct prompt photons based on the fact that they are produced with low hadronic activity around them, but decay and fragmentation photons are not. As shown on the right side of Fig. 1.7, the fragmentation photons are effectively rejected after applying the isolated criteria. The isolation criteria here are as follows: within the isolation cone radius $R = 0.4$, only select photons where the accompanying hadronic energy is less than 10% of the photon energy. For more details, please see Ref. [33]. One can also find that after the isolation criteria are applied, the majority of prompt photons come from the Compton hard scattering process.

The momentum fraction x (x_i in eq.(1.2)) in a $2 \rightarrow 2$ hard scattering that produces a prompt photon (at LO) with p_{T}^{γ} and η_{γ} from kinematics can be estimated as:

$$x = \frac{p_{\mathrm{T}}}{\sqrt{s}} \left(e^{\pm\eta_a} + e^{\pm\eta_\gamma}\right) \overset{\eta_a \approx \eta_\gamma}{\approx} \frac{2p_{\mathrm{T}}}{\sqrt{s}} e^{\pm\eta_\gamma} \tag{1.4}$$

where η_a is the pseudorapidity of the other parton produced in the scattering process and $\sqrt{s}$ is the center-of-mass energy of the collision. Hence, at mid-rapidity($y \approx 0$), $x \approx x_{\mathrm{T}} = 2p_{\mathrm{T}}/\sqrt{s}$.

1.2.3 Experimental results on prompt photons

1.2.3.1 Production in pp collisions

Over the past few decades, measurements related to prompt photon production have been made, with center-of-mass system energies ranging from $\sqrt{s} \approx 20$ GeV [34] to $\sqrt{s} = 13$ TeV [35–37]. The available inclusive isolated prompt photon data was compiled in 2012 by d'Enterria and Rojo in Ref. [38] and compared the results to the NLO calculations. It includes the data of p–$\overline{\mathrm{p}}$ collisions collected at Tevatron and Sp$\overline{\mathrm{p}}$S, as well as the early LHC data available at the time of the review, i.e. the measurements in pp collisions at $\sqrt{s} = 2.76$ TeV and 7 TeV performed by ATLAS [39, 40] and CMS [41–43].

Figure 1.8 presents the ratio of isolated-photon measured cross section to theoretical prediction in pp collisions at $\sqrt{s} = 7$ TeV with ALICE [44] on the left side. The isolation criterion for this measurement is that the sum of the p_{T} of charged and neutral particles within an isolation cone of radius $R = 0.4$ is less than 2 GeV/c. It covers the p_{T} range between 10 to 60 GeV/c and shows an agreement within the uncertainties. The right-hand side of the figure presents a comparison with the similar measurement made by ATLAS [39] and CMS [42], shows that the ratio is consistent in different Collaborations. Note that the isolation cone size was the same in the three experiments but the isolation momentum selection criteria are higher than in the ALICE measurement, the hadronic energy in the cone must be smaller than 3 and 5 GeV/c for ATLAS and CMS measurements, respectively. Therefore, the comparison with ALICE results can only be done via the ratio to theory.

Similar measurements at $\sqrt{s} = 13$ TeV in pp collisions at mid-rapidity have been done by ATLAS and CMS. Figure 1.9 shows the ratio of theory to measured from ATLAS [36] with the p_{T} range being 125 to 2000 GeV/c. One can find that the various theoretical calculations can describe the data within the uncertainties. In more detail, the JETPHOX NLO (blue) underestimates the data in all p_{T} ranges, and this kind of underestimation decreases when considering NNLO (black). The ratio from CMS [45] at mid-rapidity is presented in Fig. 1.10 within $190 < p_{\mathrm{T}} < 1000$ GeV/c, which also shows agreement between the NLO JETPHOX calculations and the data. This work studies the same measurement with data obtained by ALICE and tries to extend the p_{T} reach (down to 125 GeV/c by ATLAS) and x_{T} ($\sim 3 \times 10^{-2}$ in

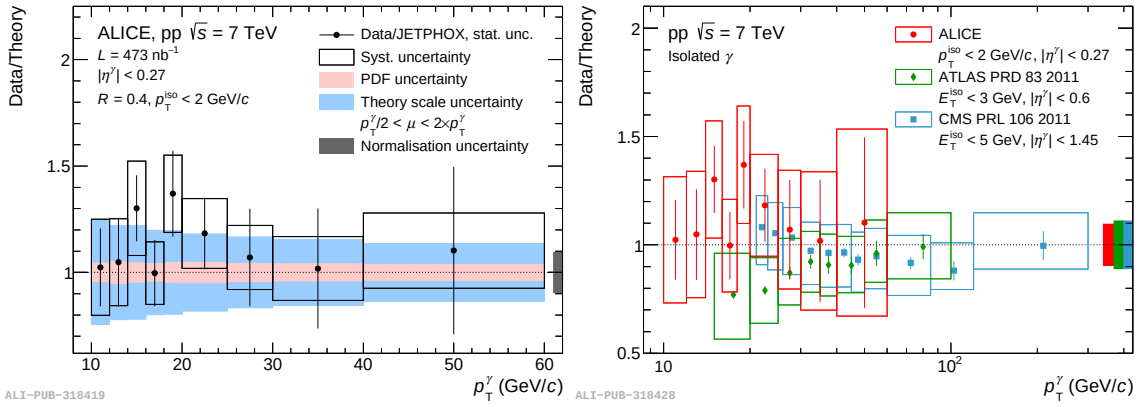

Figure 1.8: Left: Measured isolated photon cross section at $\sqrt{s}$ = 7 TeV in pp collision with ALICE ratio to the JETPHOX calculations at NLO. Right: Comparison of ratio from the ATLAS [39] and CMS [42]. Results from Ref. [42].

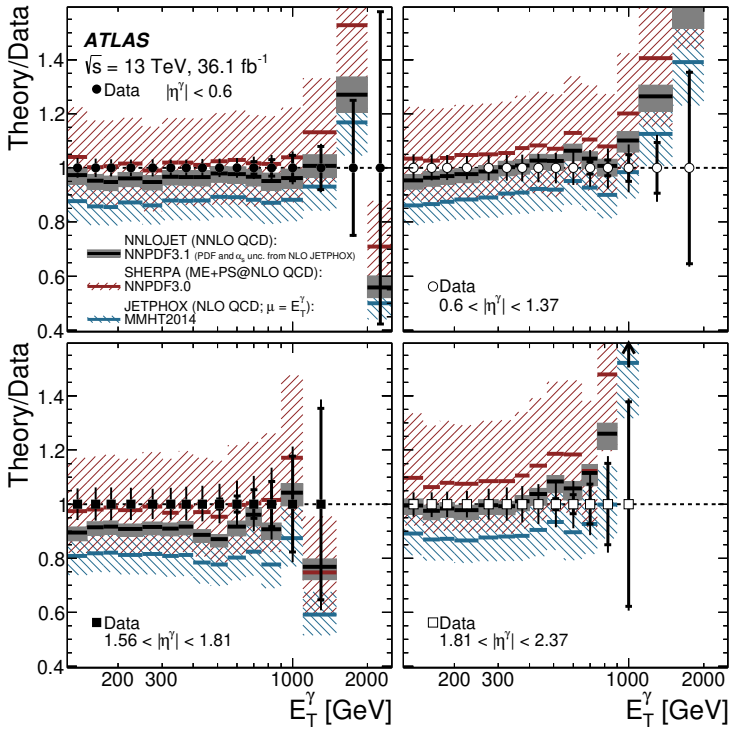

Figure 1.9: The ratio of various theoretical calculations over the measured isolated photon cross section from ATLAS in pp collisions at $\sqrt{s}$ = 13 TeV [36].

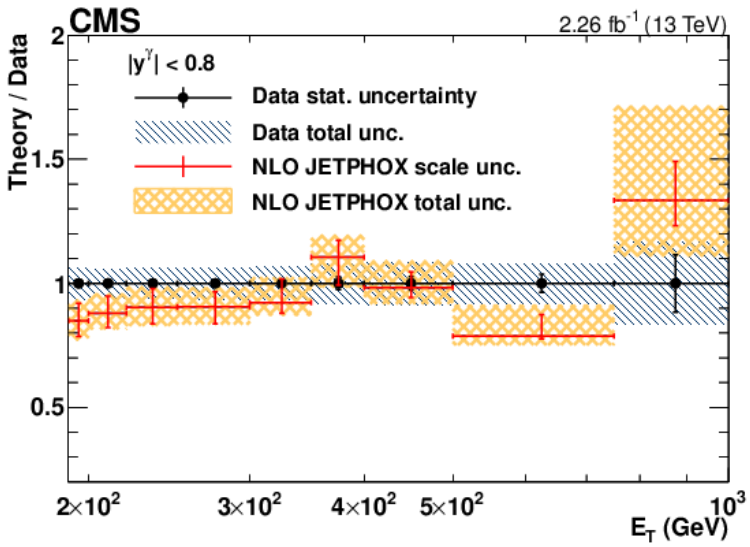

Figure 1.10: The ratio of NLO JETPHOX calculations over the measured isolated photon cross section from CMS in pp collisions at $\sqrt{s}$ = 13 TeV [45].

ALICE) to a lower range.

In conclusion, the measurements of isolated photon cross section in pp collisions at the LHC show that the theoretical calculations give a description consistent with the isolated photon data which is in agreement with the measurement at lower collision energies. The calculations performed at NLO are slightly underestimated and can be improved by including corrections beyond NLO.

1.2.3.2 Production in Pb–Pb and p–Pb collisions

The study of collisions involving heavy ions, such as lead, offers unique opportunities for probing various fundamental aspects of QCD in extreme conditions. These collisions involve very high-energy densities for which a new state of matter is formed – the so-called Quark-Gluon Plasma (QGP). In this soup-like state, quarks and gluons are found as quasi-free particles no longer confined within hadrons. This new state of matter is also of cosmological importance since it is expected to have existed only a few microseconds after the Big Bang. Partons created in the initial stages of the collision will lose their energy when traversing the QGP. This effect is known as “jet-quenching”. This effect is expected in heavy-ion nucleus-nucleus collisions but not a priori on proton-nucleus or proton-proton collisions that are considered a reference to observe modifications in the hadron production measurements as a function of p_{T} due to the presence of a QGP. However, some effects expected in the presence of the QGP have been observed, such as flow, in such smaller collision systems [46], which questions the use of pp collisions as reference.

Since photons do not interact strongly with the QGP, their production is not expected to be modified when comparing pp and Pb-Pb collisions. This comparison is done via the nuclear modification factor defined as the ratio of the particle transverse momentum yield between AA and pp collisions

$$R_{\mathrm{AA}} = \frac{1}{\langle N_{\mathrm{coll}} \rangle} \frac{\mathrm{d}^2\sigma_{\mathrm{Pb-Pb}}/(\mathrm{d}p_{\mathrm{T}}\,\mathrm{d}\eta)}{\mathrm{d}^2\sigma_{\mathrm{pp}}/(\mathrm{d}p_{\mathrm{T}}\,\mathrm{d}\eta)}, \tag{1.5}$$

where N_{coll} is the number of collisions between nucleons and $\mathrm{d}^2\sigma_{\mathrm{Pb-Pb(pp)}}/(\mathrm{d}p_{\mathrm{T}}\,\mathrm{d}\eta)$ is the measured particle cross section in heavy-ion or pp collisions.

The isolated photon R_{AA} in Pb–Pb collisions at $\sqrt{s_{\mathrm{NN}}} = 5.02$ TeV measured by ALICE for five Pb–Pb centrality intervals and two cone sizes are shown in Fig. 1.11. The R_{AA} of charged particles [47] and charged pions [48] from ALICE and Z^0 bosons from CMS [49] are also shown. The collision centrality is related to the collision impact parameter (distance between the two colliding nuclei), and is defined as the percentile of the hadronic cross-section for which more than a given energy or multiplicity threshold is produced, where a lower percentile corresponds to a more central/head-on collision [50]. In the figure, 0–10% are the more central collisions and 70–90% are the more peripheral collisions. The more central the collision is, the more suppressed the hadron spectrum becomes. The hadron suppression is due to the jet-quenching that shifts down in p_{T} the spectrum of particles originated from parton fragmentation, since the parton loses energy in the presence of the QGP. One also observes that R_{AA} for isolated photons for both cone sizes ($R = 0.2$ is in black and 0.4 in blue) and Z^0 bosons (orange) is compatible with unity for all the centrality classes, which means that there is no modification of the electroweak bosons yield due to the QGP since they do not interact strongly. The figure also shows the theoretical calculation of the ratio of spectra including nuclear over proton PDF, independent of centrality. This ratio expects a moderate suppression below 40 GeV/c due to cold nuclear matter effects like saturation and shadowing, the result is also in agreement with this prediction within the uncertainties.

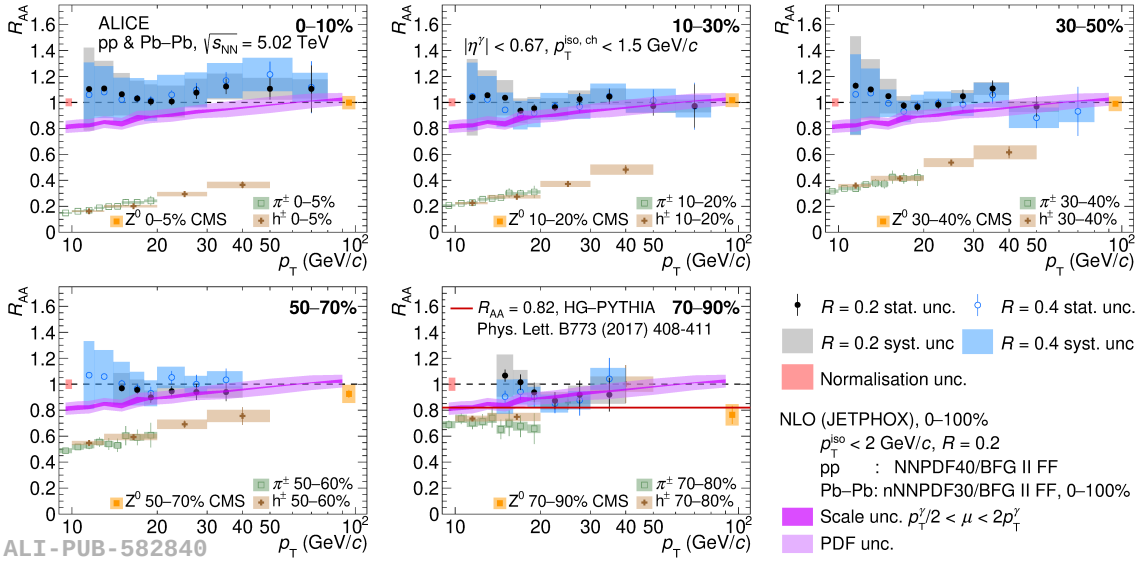

Figure 1.11: Nuclear modification factor R_{AA} for isolated photons at $\sqrt{s_{NN}}$ = 5.02 TeV for isolation cone radii R = 0.2 (black) and R = 0.4 (blue). Also, for charged hadrons [47] and pions [48] from ALICE and Z^0 bosons from CMS [49] (integrated p_T, point at boson mass). The bands correspond to pQCD calculations with JETPHOX for Pb–Pb collisions (nPDF) for 0–100% centrality over pp collisions (PDF). The width of each band corresponds to the scale and PDF uncertainties. The normalization uncertainties are represented as a red box centered at unity. Figures from Ref. [51].

Figure 1.12 presents the ratio of the measured isolated photon cross section in pp and Pb–Pb collisions at $\sqrt{s_{NN}}$ = 5.02 TeV in ALICE over JETPHOX pQCD NLO calculation, the calculation scaled by N_{coll}. One can see that for both isolation cone sizes and collision systems, the ratio between data and theory is around 1 within the uncertainties, with a particularly good agreement for central Pb–Pb collisions, which supports further the nPDF prescription of the theoretical calculation.

Figure 1.13 shows the ratio equivalent to R_{AA} but changing the Pb–Pb collision by p–Pb collisions at $\sqrt{s_{NN}}$ = 5.02 TeV and 8.16 TeV [52]. Like the R_{AA} this measured ratio is compatible with unity as expected, although in this case there are hints of a suppression below 20 GeV/c as predicted by theory due to cold nuclear matter effects.

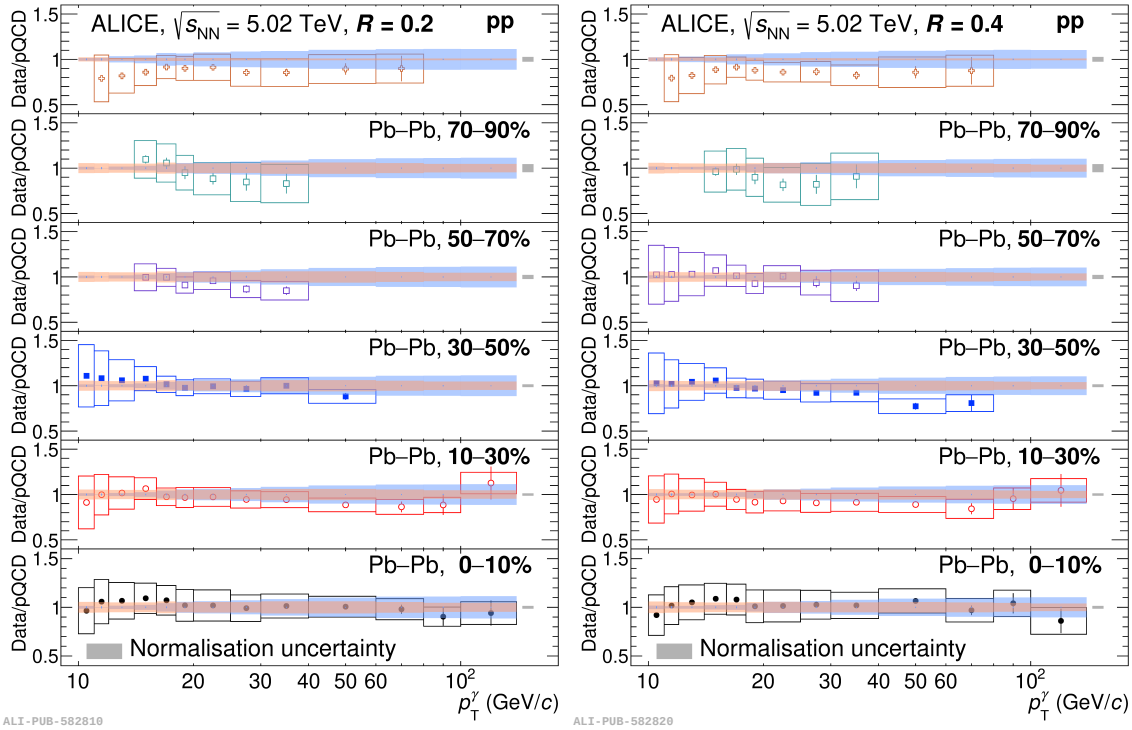

Figure 1.12: Data-over-theory ratio of isolated photon cross section as a function of p_T^γ for R = 0.2 (left) and R = 0.4 (right) in pp and Pb–Pb collisions at $\sqrt{s_{NN}}$ = 5.02 TeV. The bands centred at unity correspond to JETPHOX NLO pQCD calculations, their width represents the scale (blue) uncertainty and PDF (orange) uncertainty. The normalization uncertainties are shown as a grey box on the left of each frame around unity. Figures from Ref. [51].

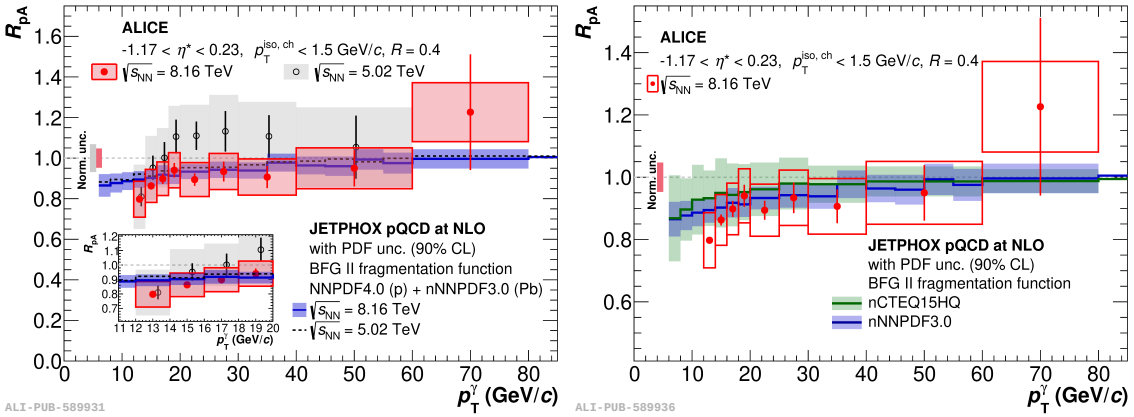

Figure 1.13: Nuclear modification factor R_{pA} of isolated prompt photon production in p–Pb collisions at $\sqrt{s_{NN}}$ = 5.02 TeV and 8.16 TeV. Ratio compared to JEPHOX NLO pQCD predictions for different nPDF. Figures from Ref. [52].

1.2.3.3 Isolated photon–hadron correlation measurements

Even if isolated photons are not modified by the QGP, the correlation between isolated photons and a hadronic observable, such as a jet or a single hadron, can be used to study the medium-induced partonic energy loss mechanism. The photon and parton produced in the same hard-scattering process will be emitted at a back-to-back azimuth angle. The photon p_{T} reflects the initial energy of the parton before any medium-induced energy loss and fragmentation into a jet. Therefore, the distribution of the opposite side hadron with the momentum fraction $z_{\mathrm{T}} = p_{\mathrm{T}}^{\mathrm{h}}/p_{\mathrm{T}}^{\gamma}$ represents the parton fragmentation function. One can extract a similar measurement to the R_{AA} using $\mathrm{I}_{AA} = \mathrm{Y}_{\mathrm{AA}} \ / \ \mathrm{Y}_{\mathrm{pp}}$, where Y is the particle yield in opposite direction to the photon as a function of z_{T} in which case $\mathrm{I}_{AA} \approx D_{\mathrm{AA}}(z_{\mathrm{T}})/D_{\mathrm{pp}}(z_{\mathrm{T}})$.

Figure 1.14-top presents the γ^{iso}-tagged $\mathrm{D}(z_{\mathrm{T}})$ distribution at $\sqrt{s_{\mathrm{NN}}} = 5.02$ TeV in pp and p–Pb collisions measured in ALICE [53]. It can be observed that there is an agreement within uncertainties between pp, p-Pb, and the PYTHIA 8.2 Monash Tune, which as expected jet-quenching is not expected to be present in p–Pb collisions. The bottom figure shows the ratio between p–Pb and pp, indicating no significant difference between the two.

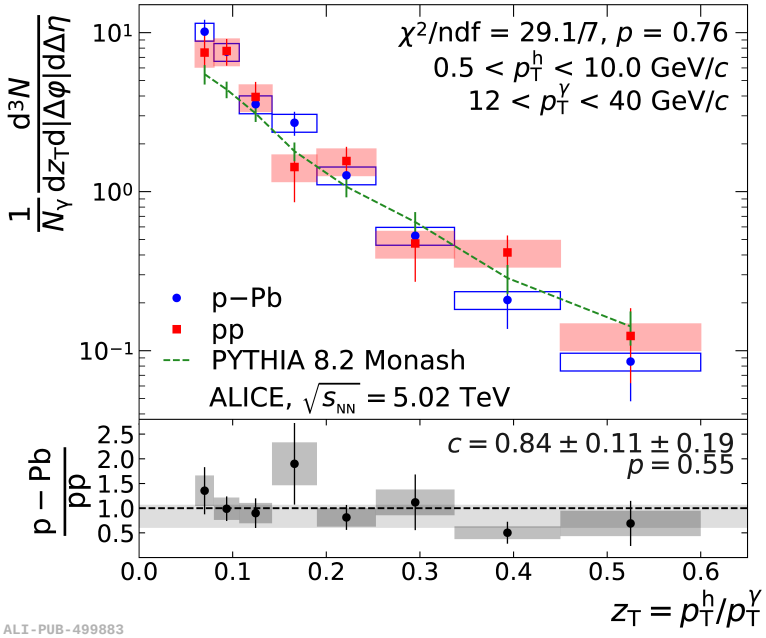

Figure 1.14: The γ^{iso}-tagged fragmentation function for pp (red) and p–Pb data (blue) at $\sqrt{s_{\mathrm{NN}}} = 5.02$ TeV as measured by the ALICE detector. The boxes represent the systematic uncertainties while the vertical bars indicate the statistical uncertainties. The dashed green line corresponds to PYTHIA 8.2. Plot from Ref. [53].

Figure 1.15 provides the ratio of isolated photon-hadron correlation $D(z_T)$ distribution between Pb–Pb collisions measured in ALICE and pp collisions from an NLO pQCD calculation at $\sqrt{s_{NN}} = 5.02$ TeV, $I_{\text{pQCD NLO}}$, for three centrality classes [54]. One can see that there is more suppression in the hadron yield emitted opposite to the isolated photon in 0–30% central Pb–Pb collisions than in 50–90% peripheral Pb–Pb collisions (agreement with pQCD), suppression which has the same origin as what is observed in the hadron R_{AA} in Fig. 1.11, the jet-quenching.

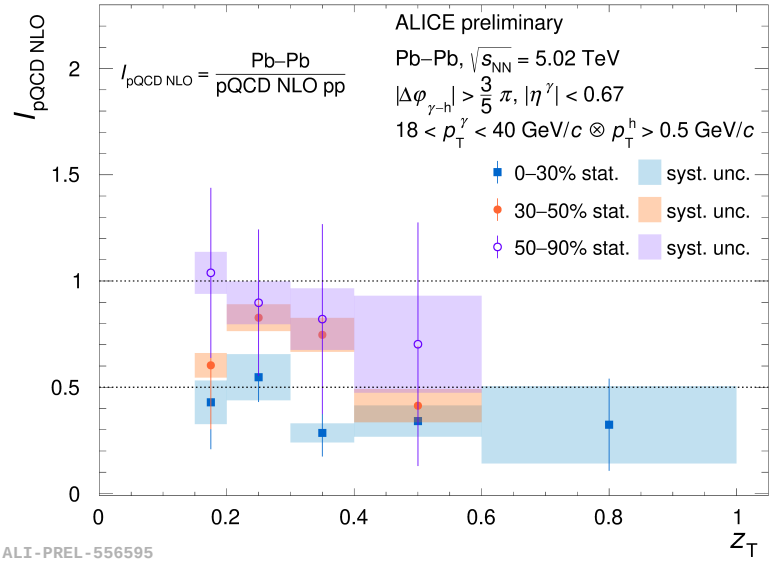

Figure 1.15: γ^{iso}–hadron correlations $I_{\text{pQCD NLO}}$ ratio, D(z_T) measured in Pb–Pb collisions by ALICE for three centrality classes over pp collisions from NLO pQCD calculations, all at $\sqrt{s_{NN}} = 5.02$ TeV. Plot from Ref. [54].

2 Experimental setup

2.1 LHC introduction

The Large Hadron Collider (LHC) [55] is the world's largest and most powerful particle accelerator at present, built by the European Organization for Nuclear Research (CERN) below the French-Swiss border near the city of Geneva. The LHC consists of a 27-kilometer ring of superconducting magnets with several accelerating structures to boost the energy of the particles along the way. The LHC beams are produced and pre-accelerated in the CERN accelerator chain, so-called LHC injectors. Inside the accelerator, two high-energy particle beams travel at close to the speed of light before they are made to collide. The overview of CERN accelerator complex as of 2022 is presented in Fig. 2.1.

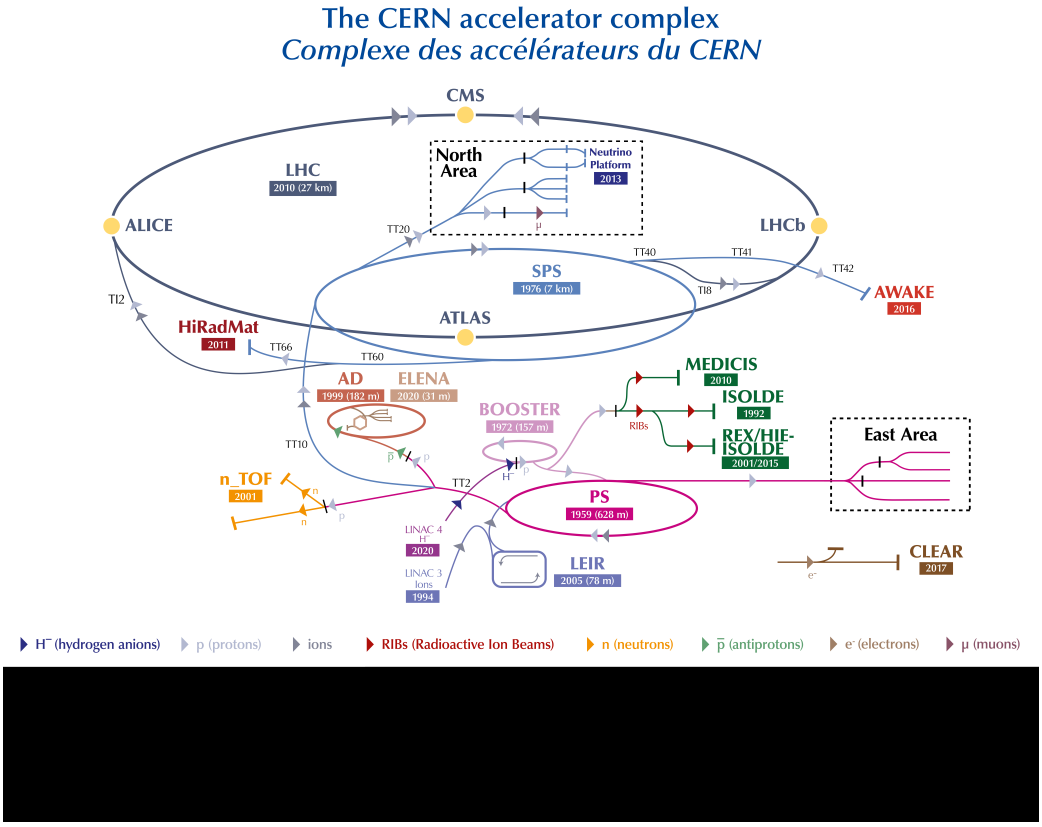

Figure 2.1: Overview of accelerators and connected experiments at CERN, as in the year 2022 [56].

The LHC, as its name implies, is designed for the collision of hadrons, with the majority of its operational time each year dedicated to proton-proton (pp) collisions. And also, the LHC can be used as an ion collider, like collision of lead ions (Pb–Pb), as well as asymmetric collisions of protons and

lead ions (p–Pb or Pb–p). Although the LHC regularly conduces Pb–Pb or p–Pb as part of its heavy-ion program for approximately one month each year, it is still possible to accelerate other ion species at the LHC, like it was done with xenon in year 2017 and it is foreseen and under discussion with oxygen, neon or argon in Run 3 and 4. Before reaching the LHC, protons or heavy ions undergo pre-acceleration through a series of stages. This process entails a progressive increase in their energy levels, thereby preparing them for injection into the LHC.

For pp collisions, the LHC aims to accelerate and collide proton beams at an energy of 7 TeV, which gives a total center-of-mass energy of 14 TeV, and 2.75 TeV/nucleon Pb beams lead to a center-of-mass energy of 5.5 TeV.

A crucial metric for an accelerator is the luminosity ($\mathscr{L}$) at the interaction points. The luminosity is the number of collision events per second $\mathrm{d}N_{\text{event}}/\mathrm{d}t$ for a given event with cross-section σ_{event} is given by

$$\frac{\mathrm{d}N_{\text{collision}}}{\mathrm{d}t} = \mathscr{L}\sigma_{\text{event}} \,. \tag{2.1}$$

A high luminosity is crucial to study rare processes such as the production of a Higgs boson or physics beyond the standard model. The luminosity is mainly contingent upon the number of particles present in each colliding beam, their rotational frequency, and the degree to which the beam can be focused at the interaction point. In addition, the two beams must be collided at a crossing angle at the interaction point, which reduces the luminosity but enables the delivery of luminosity at each four interaction points to be steered individually and also suppresses the collision outside the collision point that are unwanted.

The proton and heavy-ion beams are divided into thousands and hundreds of bunches, respectively, to facilitate acceleration. A beam at the LHC is comprised of up to 2808 so-called bunches, each containing up to 1.7×10^{11} protons, with a nominal bunch spacing of 25 nanoseconds (ns). In 2017, the LHC delivered peak luminosities of more than 2×10^{34} $\mathrm{cm}^{-2}\mathrm{s}^{-1}$ in proton-proton operation, exceeding its design value by a factor of two [31, 57]. At present, the LHC has reached the center–of–mass energies at $\sqrt{s}$ = 13.6 TeV in proton-proton (pp) collisions, $\sqrt{s_{\mathrm{NN}}}$ = 8.16 TeV for proton-lead (p–Pb) collisions, and $\sqrt{s_{\mathrm{NN}}}$ = 5.36 TeV for lead-lead (Pb–Pb) collisions.

There are four principal interaction points at which accelerated particles are collided. At each interaction point, the dedicated LHC experiments particle detectors are located: ATLAS, CMS, ALICE and LHCb, each one with different physics programs. The ATLAS (A Toroidal LHC Apparatus) [58]

detector is 46 metres in length and 25 metres in diameter, and the complete CMS (Compact Muon Solenoid) [59] detector is 21 metres long, 15 metres wide and 15 metres high. They have a broad physics programme ranging from the study of the Standard Model (including the Higgs boson) to the search for extra dimensions and particles that could make up dark matter, and also the heavy-ion Physics program. The design of the sub-systems enables ATLAS and CMS to play an important role in the search for the Higgs boson, which was finally discovered in 2012 [31, 60, 61]. The discovery of the Higgs boson furthermore illustrates the synergy of ATLAS and CMS, where the observation of Higgs decays by both experiments, positioned on opposite sides of the LHC, serves as an important cross check for the discovery and improves its statistical significance. Both ATLAS and CMS are particularly well-suited for the measurement of highly energetic particles, this is also reflected in the magnetic fields where, for example, the 4 T superconducting solenoid of CMS provides sufficient bending power to unambiguously determine the charge of the muon for momenta up to $\approx$ 1 TeV [59]. For more details on the sub-detectors and their characteristics, please have a look at Refs. [58] and [59].

The LHCb (Large Hadron Collider beauty) experiment [62] is dedicated to the investigating of the slight differences between matter and antimatter by studying the “b quark” and related decays. To detect the b quarks, LHCb has developed sophisticated movable tracking detectors close to the path of the beams circling in the LHC. The 5600-tonne LHCb detector is made up of a forward spectrometer and planar detectors. The apparatus measures 21 metres in length, 10 metres in height and 13 metres in width. The LHCb experiment comprises a single-arm, located on one side of the collision vertex and surrounding the beampipe. This decision is motivated by the fact that highly energetic b quarks, and thus, b hadrons are dominantely produced in the same cone, either in forward or backward direction. This layout allows the LHCb detector to cover forward pseudorapidities of $2 < \eta < 5$ for both charged- and neutral particles, where a silicon based tracking system enables a momentum resolution of 0.4% to 0.5% and the ECAL and HCAL provide electromagnetic- and hadronic calorimetry, respectively [31].

ALICE (A Large Ion Collider Experiment) [63] is a multipurpose experiment dedicated to the heavy-ion physics at the LHC, but also has a dedicated pp collisions program to compare to the heavy-ion collisions as a reference and in general to test QCD predictions. It has a length of 26 metres, a height of 16 metres, a width of 16 metres and a mass of 10,000 tonnes. ALICE is designed to study the physics of strongly interacting matter at extreme energy densities. Its physics program necessitates robust particle identification, as well as wide covered transverse momentum range for hadrons, electrons, photons, and muons, even in the high-multiplicity environment of Pb–Pb collisions, where up to 10,000 particles are produced at mid-rapidity. These capabilities are provided by 19 subsystems, which are shown in

the schematic overview of the ALICE detector given in Fig. 2.2. One can group the systems into two distinct parts: the majority of subdetectors are located inside the L3 solenoid magnet (No.10, shown in red), which provides a nominal magnetic field of 0.5 T that bends the tracks of charged particles, allowing one to determine their momentum. These detectors are referred to as the central barrel. The forward muon spectrometer is located outside the L3 magnet and placed behind an absorber to shield the muon arm from the high multiplicities of unwanted particles, such as electrons and hadrons, exploiting the in comparison low interaction rate of muons with the traversed material.

In 2009, ALICE commenced its inaugural data-taking period, which was conducted in pp collisions at $\sqrt{s}$ = 0.9 TeV. ALICE recorded data from the first lead-lead collisions at the LHC in 2010. In 2014, the collaboration started a major program of consolidation and upgrades that were completed during the Long Shutdown 2 (LS2) of LHC in 2019–2021. Then the data taking is divided into 3 periods, Run 1 (2009–2013), Run 2 (2015–2018) and Run 3 (2022–2026). Currently, ALICE is engaged in data acquisition during the LHC Run 3 program, which started in July 2022. Table 2.1 lists the collisions and energies accumulated by ALICE up to the present.

Table 2.1: Overview of ALICE data taking campaign until 2024.

Year	System	$\sqrt{s_{\mathrm{NN}}}$ (TeV)	Year	System	$\sqrt{s_{\mathrm{NN}}}$ (TeV)	Year	System	$\sqrt{s_{\mathrm{NN}}}$ (TeV)
2009	pp	0.9	2015	pp	13	2022	pp	13.6
	pp	2.36		pp	5.02		Pb-Pb	5.36
2010	pp	0.9		Pb-Pb	5.02	2023	pp	13.6
	pp	7.0	2016	**pp**	**13**		Pb-Pb	5.36
	Pb-Pb	2.76		p-Pb	5.02	2024	pp	5.36
2011	pp	2.76		p-Pb	8.16		pp	13.6
	pp	7.0	2017	**pp**	**13**		Pb-Pb	5.36
	Pb-Pb	2.76		Xe-Xe	5.44			
2012	pp	8	2018	**pp**	**13**			
	p-Pb	5.02		Pb-Pb	5.02			
2013	p-Pb	5.02	Long Shutdown 2					
	pp	2.76						
Long Shutdown 1								

This work, the study of isolated prompt photon production in pp collisions, mainly uses the ALICE detector in the central barrel which is explained in detail in the following sections.

2.2 ALICE detector description

The ALICE central barrel system has multiple detector systems for measuring charged and neutral particles. The central tracking system covering a pseudorapidity of $|\eta| < 0.9$ consists of the Inner Tracking System (ITS), Time-Projection Chamber (TPC), Transition Radiation Detector (TRD) and Time Of Flight (TOF). In the central region, ALICE includes two electromagnetic calorimeter systems: the PHOton Spectrometer (PHOS) and the Electro Magnetic Calorimeter (EMCal).

The forward regions contain the T0 detector, V0 detector and Forward Multiplicity Detector (FMD) [64]. The main task of T0, with a pseudorapidity range of $-3.3 < \eta < -2.9$ and $4.5 < \eta < 5.0$, is to supply fast-timing signals used in the L0 trigger for ALICE, to provide a wake-up call for TRD, and to deliver collision time reference for TOF. The V0 main functionality is to provide the trigger for ALICE and I will describe this detector in the following section (Sec. 2.2.1). The FMD provides the charged particle multiplicity information within the pseudorapidity range $-3.4 < \eta < -1.7$ and $1.7 < \eta < 5.0$. In conjunction with the ITS, the FMD will provide charged particle multiplicity distributions for all collision types within the range $-3.4 < \eta < 5.0$.

In this analysis, photon reconstruction is performed using the EMCal, while charged particles used in the photon isolation selection criteria are reconstructed with the combination of the ITS and the TPC. This section introduces the individual sub-systems, with a focus on those used in this analysis, and discusses their respective physical performance.

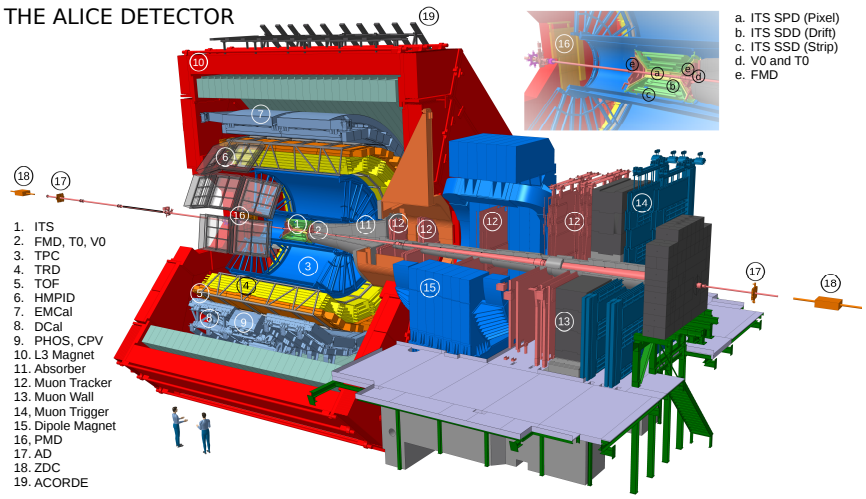

Figure 2.2: Schematic overview of the ALICE detectors [65].

2.2.1 V0 detector

The ALICE V0 detector, labeled as 2 in Fig. 2.2, consists of two arrays of 32 plastic scintillators at asymmetric positions, one on each side of the interaction point. The coverage is $2.8 < \eta < 5.1$ (V0A) and $-3.7 < \eta < -1.7$ (V0C) [66].

The V0 detector is capable of providing the minimum-bias trigger for inelastic pp collisions to ALICE detectors, which aims to acquire inelastic events with as little bias as possible. This trigger requires a coincident signal on both sides of the V0 detector ("V0AND" trigger logic). This requirement reduces a substantial amount of background events such as interactions of the beam with residual gas inside the beam pipe or with mechanical structures of the beam line. As the number of measured particles on the V0 arrays and the number of primary emitted particles are proportional to each other, the V0 can serve as an indicator of the centrality of the collision based on the multiplicity measured in V0 in the event. In addition to its core function as a trigger source, the V0 system is also used to monitor LHC beam conditions, reject beam-induced backgrounds and measure basic physics quantities such as luminosity, particle multiplicity, centrality and event plane direction in nucleus-nucleus collisions.

2.2.2 Inner Tracking System, ITS

The ITS [67] which is marked as 1 in Fig. 2.2, is the most central detector surrounding the beampipe. As Fig. 2.3 illustrates, the ITS is composed of six cylindrical layers of silicon detectors with full azimuthal acceptance and surrounds the interaction point. The two innermost layers consist of the Silicon Pixel Detector (SPD), whose fine granularity provides high-spatial precision for tracking close to the primary vertex. Those layers are positioned at radial distances of 3.9 cm and 7.6 cm from the beam line. They are surrounded by the two layers of the Silicon Drift Detector (SDD) at 15.0 cm and 23.9 cm, and by those of the Silicon Strip Detector (SSD) at 38.0 cm and 43.0 cm. While the two SPD layers cover a pseudorapidity of $|\eta| < 2$ and $|\eta| < 1.4$, respectively, the SDD and the SSD subtend $|\eta| < 0.9$ and $|\eta| < 1.0$, respectively.

The ITS is used to measure and identify charged particles, which leave signals when traversing the six ITS layers. Those signals are combined to reconstruct the trajectory of a given particle, which is known as "tracking". The proximity of the ITS to the interaction point enables the reconstruction of the position at which a collision occurred (the primary vertex), as well as the determination of the impact parameter of secondary tracks originating from decays of strange, charm and beauty particles that live long enough to travel a few cm away from the interaction point before decaying (secondary vertices).

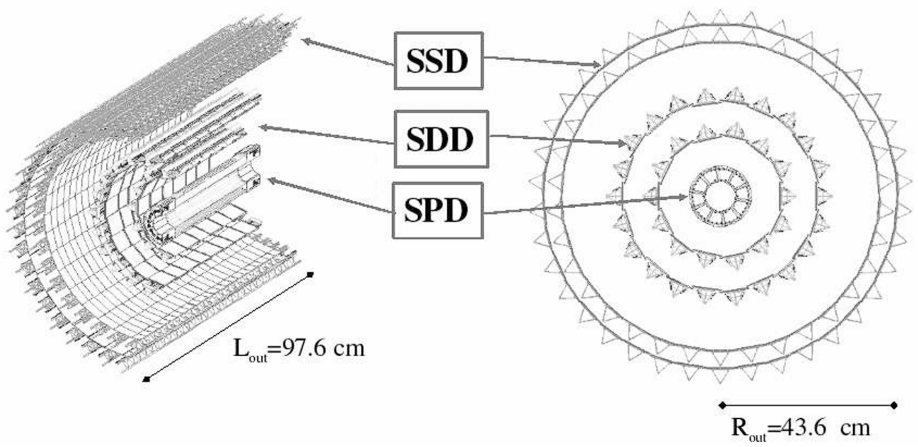

Figure 2.3: Layout of the ALICE ITS [63].

Furthermore, the additional space points provided by the ITS close to the primary vertex allow the tracking and the identification of particles with low-momentum. Tracking of high-p_{T} particles also profits from the ITS when used together with the TPC, where the additional space-points improve the overall momentum resolution, as discussed in the next section (Sec. 2.2.3).

During the second long LHC shutdown (LS2), the ITS has been upgraded in preparation for the significantly increased interaction rate in Run 3 (starting 2022) [68]. The upgrade focussed on increasing the readout-rate capabilities of the ITS, as well as improving its tracking capabilities, thereby reinforcing the ALICE's heavy-flavor physics program. The completely revised geometry, segmentation and read-out, as well as a reduction of the beampipe diameter by about 40%, will allow for an expected increase in read-out rate from previously 1 kHz up to 100 kHz in Pb–Pb collisions, as well as an improvement of impact parameter resolution by a factor 3 and 5 in the r, φ, and z coordinates, respectively [68, 69].

2.2.3 Time-Projection Chamber, TPC

The TPC [70] is the main device in the ALICE 'central barrel' for tracking charged particles and particle identification. The ALICE TPC was designed to cope with the highest conceivable charged particle multiplicities produced in central Pb–Pb collisions at LHC energies. A schematic overview of the TPC is given in Fig. 2.4. The TPC is a large (≈ 85 m^3) cylindrical drift detector filled with a gas mixture, it covers $|\eta| < 0.9$ over the full azimuth angle, with a maximum of 159 reconstructed space points along the track path.

The charged particles traverse the gas volume of the TPC, leaving a track of ionization electrons along their path. The freed electrons are accelerated toward the readout chambers via a uniform 100

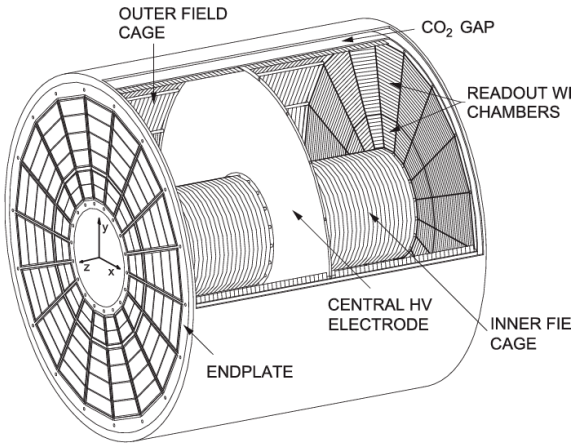

Figure 2.4: Schematic drawing of the ALICE TPC [71].

kV electric field, which is applied between the end caps and the electrodes located at the center of the detector. After the drift time, a maximum of approximately 90 µs, the freed electrons reach the readout chamber, which is comprised of Multi-Wire Proportional Chambers (MWPCs) with pad readout, enabling the determination of a two-dimensional projection of the charged particle's trajectory within the detector. By measuring the drift time of the freed electrons, one can calculate the third spatial coordinate, thus obtaining the three-dimensional measurement of the charged particle's trajectory.

The trajectory measurement happens at discrete space points, given by the spacing of the wires in the radial direction and the precision of the drift time measurement. Consequently, the trajectory must be reconstructed by connecting the individual signals to a continuous line, a process known as track reconstruction. The tracking performance of the TPC is illustrated in Fig. 2.5, which depicts the p_{T} resolution of standalone TPC tracks. Furthermore, the figure also shows the p_{T} resolution of the track using the combined tracking information of ITS and TPC, as well as the impact of further constraints derived from the reconstructed primary vertex. It can be observed that TPC standalone tracks with $p_{\mathrm{T}} > 1$ GeV/c exhibit a precision of less than one percent and be further improved when including information from the ITS and the reconstructed primary vertex [72].

The readout rate of the TPC during Run 1 and Run 2 of the LHC operation was mainly constrained to a few kHz in Pb–Pb collisions due to the triggered operation of a gating grid. This grid is transparent to electrons after an interaction trigger but then is closed to block ions from entering the active detector area after the electrons have passed through. For Run 3, a novel readout chamber was installed, which has intrinsic ion-blocking capabilities that allow for TPC operation with continuous readout, enabling readout rates of up to 50 kHz in Pb–Pb collisions [73].

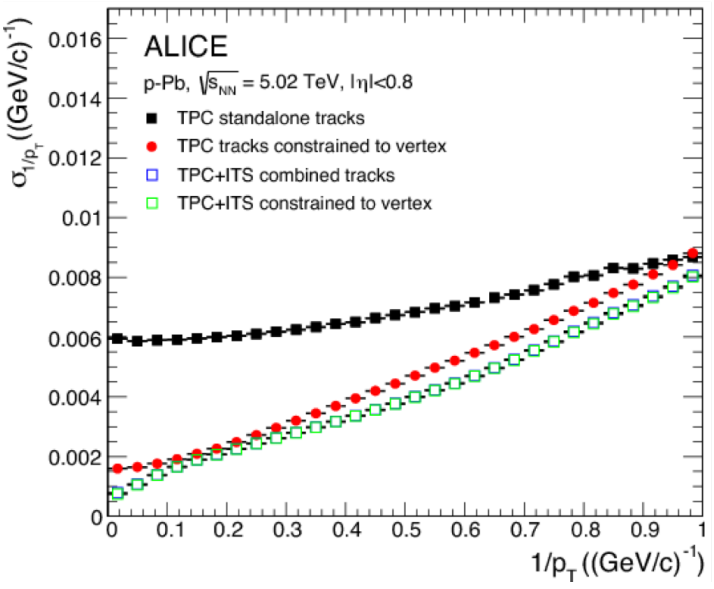

Figure 2.5: The p_T resolution for standalone TPC and ITS–TPC matched tracks with and without constraint to the vertex. The vertex constrain significantly improves the resolution of TPC standalone tracks. For ITS–TPC tracks, it has no effect (green and blue squares overlap) [72].

2.2.4 Electromagnetic Calorimeter, EMCal

The EMCal [74] is a layered lead (Pb)-scintillator (Scint) sampling calorimeter used to measure photons, electrons, and the neutral part of jets via the electromagnetic showers that the different particles produce in cells of the calorimeter. The scintillation light is collected by optical fibres coupled to Avalanche Photo Diodes (APD) that amplify the signal. The energy resolution is $\sigma_E/E = A \oplus B/\sqrt{E} \oplus C/E$ with $A = (1.4 \pm 0.1)\%$, $B = (9.5 \pm 0.2)\%$, $C = (2.9 \pm 0.9)\%$, and energy E in units of GeV.

The EMCal was installed at a radial distance of 4.28 m from the ALICE interaction point and covered two separate ranges in azimuth, as illustrated in Fig. 2.6 [74]. The lower component, in which the PHOS is embedded within a gap, is referred as the Di-Jet Calorimeter (DCal). The basic unit of the calorimeter is the tower (cell). Each cell has a transverse size of 6×6 cm^2 which corresponds to $\Delta\varphi \times \Delta\eta = 0.0143 \times 0.0143$ rad, approximately twice the Molière radius. Thus, most of the energy of a single photon is deposited in a single cell plus the adjacent ones. The total number of installed cells is 17664. An important unit for the EMCal is the module which consists of 2×2 cells. A group of 2×8 cells is covered by a readout T-Card and 2 adjacent T-Card (4×8) form the FEE-Card. The groups are illustrated in Fig. 2.7.

During the period in which the analysed dataset was collected, the EMCal consisted of twenty

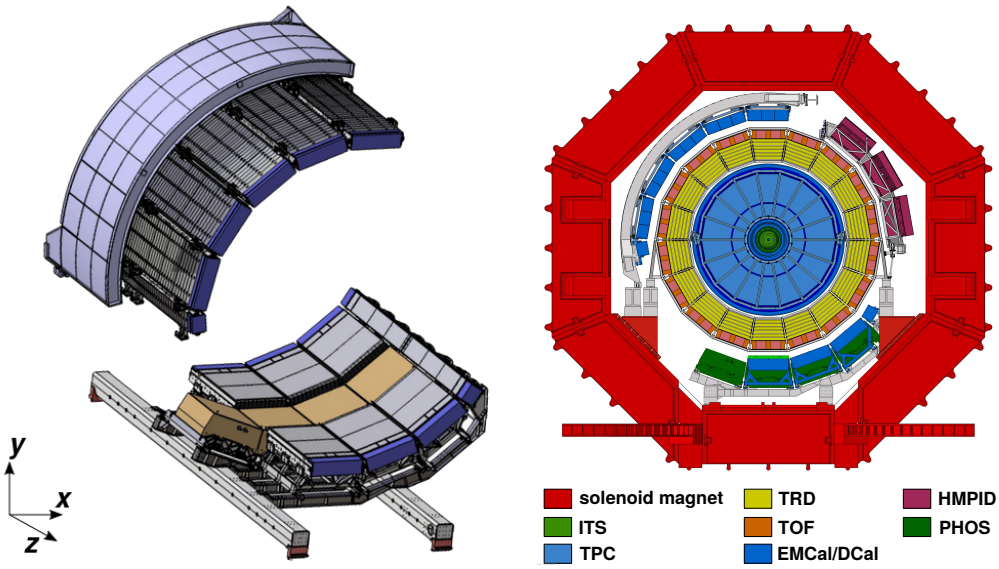

Figure 2.6: Schematic view of the EMCal (left) illustrating the module position on two approximately opposite locations in azimuth. The PHOS calorimeter inside the DCal is indicated in brown. The right figure shows a cross section of the ALICE barrel detectors. Figure from [74].

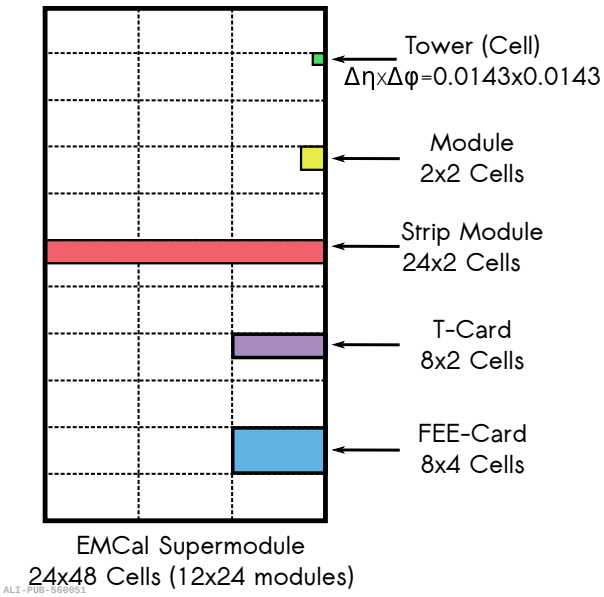

Figure 2.7: EMCal full-size (SM) in the ($\eta - \varphi$) plane including visualizations of sub-components and their tower coverage. Figure adapted from Ref. [74].

supermodules (SMs). The supermodules have different sizes and are subdivided into 24 × 48 (along $\varphi \times \eta$) cells for "full SM", 24 × 32 cells for "2/3 SM", and 8 × 48 cells for "1/3 SM". The EMCal (top SMs) has ten "full SM" and two "1/3 SM", a total of 12288 cells, which are installed with a total aperture of $|\eta| < 0.7$ in pseudorapidity and $80° < \varphi < 187°$ in azimuthal angle. The DCal (bottom SMs) is comprised of six "2/3 SM" and two "1/3 SM". Six "2/3 SM", a total of 5376 cells, are located

facing the "full SM" at $260° < \varphi < 320°$ with $0.22 < |\eta| < 0.7$, with a gap at $|\eta| < 0.22$ covered by the PHOS detector [75] at $|\eta| < 0.13$ (not used in this analysis) plus mechanical and electronics services. The remaining two "1/3 SM" are located at $320° < \varphi < 327°$ with $|\eta| < 0.7$. The EMCal and DCal $\eta - \varphi$ geometric overview is shown in Fig. 2.8.

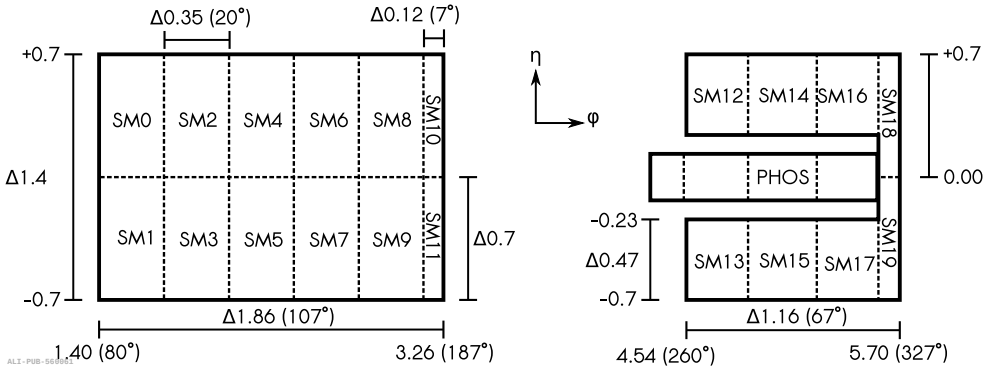

Figure 2.8: Geometric overview of the EMCal and DCal detectors in the $\eta - \varphi$ plane. The drawing outlines the full LHC Run 2 setup with all twenty SMs as well as the PHOS detector in the DCal gap.

Both EMCal and DCal provide inputs to the Level-0 (L0) and Level-1 (L1) trigger decisions in ALICE, the trigger logic is discussed in Ref. [76]. The trigger subsystem resides in specific hardware boards that deliver FastOR signals corresponding to digital sums of 2×2 cells. The Trigger Region Unit (TRU) [77] is used to digitize, at the machine bunch crossing rate (40.08 MHz), the FastOR signals provided by the FEE and to compute and generate the local L0 triggers [76], the first level trigger. Upon receipt of an accepted L0 trigger from the Central Trigger Processor (CTP), the digitized 2×2 cell sums from each TRU are passed to the Summary Trigger Unit (STU). In the STU the 4×4 overlapping cell sums are formed again, but across TRU boundaries over the full acceptance to provide an improved L1 high-energy shower trigger referred to as L1-γ trigger [76]. At the same time, cell sums over a 16×16 or 32×32 cells are also formed to provide a L1-jet trigger. Both L1 triggers allow the definition of two thresholds for the event selection, referred to as high and low threshold. More technical details about the trigger implementation can be found in [78].

3 EMCal data selection, reconstruction and calibration

In this chapter, I present the data taken with the EMCal and how it was reconstructed, calibrated and selected. First, a brief introduction of the data sample used in the analysis and the event selection. Then the EMCal reconstruction and calibration procedures are presented followed by the EMCal cluster selection criteria. Finally, the EMCal trigger performance is discussed.

3.1 Data and Monte Carlo samples

The analysis uses the pp collisions at $\sqrt{s}$ = 13 TeV data collected with ALICE in years 2016, 2017, and 2018, which are listed in bold in Tab. 2.1. The data were taken with a minimum bias interaction trigger (MB) and EMCal L1 photon dedicated triggers (L1-γ). The MB trigger was based on the response of the V0 detector, two EMCal L1-γ triggers were used, consisting in energy depositions larger than 4 GeV (L1-γ-low, labeled as G2) or 9 GeV (L1-γ-high, labeled as G1) in 4×4 adjacent cells, in addition to the MB trigger condition and an EMCal L0 trigger at 2.5 GeV, see detailed description of the EMCal triggers in Sec. 3.6 and Refs. [74, 76]. Table 3.1 lists the number of analyzed events collected with the different triggers in each year. The final row is the cumulative total events from the years for different triggers.

Table 3.1: Number of events collected with the minimum bias and L1 photon triggers in pp collisions at $\sqrt{s}$ = 13 TeV data per year and total.

Year	Number of events per trigger		
	MB	G2 ($E_{\text{trig}} > 4$ GeV)	G1 ($E_{\text{trig}} > 9$ GeV)
2016	3.90×10^8	4.10×10^7	2.62×10^7
2017	5.37×10^8	5.06×10^7	3.53×10^7
2018	6.61×10^8	4.40×10^7	3.20×10^7
Total	1.59×10^9	1.36×10^8	9.35×10^7

Given the different trigger thresholds, the data samples are combined depending on the measured photon spectrum transverse momentum: for $p_{\text{T}} < 12$ GeV/c the MB and the L1 photon G2 data samples are used, for higher transverse momenta, all the data samples are used.

This analysis covers the EMCal and DCal full acceptance range as explained in Sec. 2.2.4, the acceptance used is $81.2° < \varphi < 185.8°$ so $\Delta\varphi = 104.6°$ and $|\eta| < 0.67$ so $\Delta\eta = 1.34$ and the lower part (referred as DCal) of $261.2° < \varphi < 318.8°$ so $\Delta\varphi = 57.6°$ and $0.25 < |\eta| < 0.67$ so $\Delta\eta = 0.42$ and $321.2° < \varphi < 325.8°$ so $\Delta\varphi = 4.6°$ and $|\eta| < 0.67$.

The detector response is modelled by Monte Carlo (MC) simulations reproducing the detector conditions of the data-taking period. The MC events are obtained using PYTHIA 8 (version 8.210 [79] using the Monash 2013 tune [80]) as particle generator. Two kinds of PYTHIA 8 processes are generated in intervals of the transverse momentum of the hard scattering for this analysis: on the one hand, 2→2 Compton and annihilation hard processes emitting a photon and a parton, leading to so-called γ–jet events (GJ): these are used here to reproduce a direct photon signal. Photons were selected at the generator level to fall into the acceptance of the EMCal and DCal to reduce the output size; On the other hand, hard processes resulting in the emission of two opposite partons, leading to jet–jet events (JJ), the event is accepted when at least one jet produces a high-p_{T} photon originating from a hadron decay in the EMCal acceptance. This is done to enhance the number of such photons, which are the main background in this analysis. In order to enhance the high-energy π^0 and η mesons in the particle population, the jet–jet simulation has been performed with "triggers" selecting high-energy decay photons falling into the acceptance of EMCal and DCal. Three trigger thresholds were considered: 3.5 GeV/c (JJ low), 7 GeV/c (JJ high) and 28 GeV/c (JJ additional). Finally, the transport of the generated particles in the detector material is done using GEANT3 [81] and, to reproduce the effective conditions of data taking used here. The detector conditions during the data taking were considered in the simulated samples.

Each of the JJ–triggered samples is used for corrections in different spectra p_{T} ranges so that the statistical limitations of each sample at high p_{T} are reduced. The p_{T} range usability depends on the lower limit of applicability of the JJ sample, usually near 2 times the p_{T} trigger threshold, which roughly corresponds to the neutral meson lower p_{T} that was triggered. Table 3.2 provides a summary of the p_{T} range for each JJ-triggered sample.

Table 3.2: The p_{T} usability range on the various JJ-triggered samples.

Sample	p_{T} threshold	Usability range
JJ low	3.5 GeV/c	$7 < p_{\mathrm{T}} < 14$ GeV/c
JJ high	7 GeV/c	$14 < p_{\mathrm{T}} < 80$ GeV/c
JJ additional	28 GeV/c	$80 < p_{\mathrm{T}} < 200$ GeV/c

To cumulate more statistics for high p_{T} particles in collisions, the simulation events are generated with several p_{T} hard bins, which are the transverse momentum bins of the outgoing partons produced in the 2→2 process. Thereby ensuring a reasonable statistic over a wide spectrum energy range. The p_{T} hard bins for the different production processes are listed in Tab. 3.3.

Table 3.3: The list of p_{T}-hard bins of the jet–jet and γ–jet PYTHIA simulation sample generations.

Sample	N^{bin}	p_{T} hard bin interval (GeV/c)
GJ	6	[5, 11], [11, 21], [21, 36], [36, 57], [57, 84], [> 84]
JJ low	6	[5, 7], [7, 9], [9, 12], [12, 16], [16, 21], [> 21]
JJ high	8	[8, 10], [10, 14], [14, 19], [19, 26], [26, 35], [35, 48], [48, 66], [> 66]
JJ additional	1	[> 66]

However, in order to compare to the data, the p_{T} hard bins have to be weighted to provide a realistic description of photon production. The weights are calculated using:

$$\omega_{p_{\mathrm{T}}}^{\mathrm{hard}} = \frac{\sigma_{\mathrm{hard}}}{N_{\mathrm{trial}} \times N_{\mathrm{evt}}}, \tag{3.1}$$

where the σ_{hard} is the average hard process cross section, N_{trial} is the number of trials needed to produce the hard process, and N_{evt} is the number of generated events [82]. Figure 3.1 shows the energy distribution of EMCal clusters from particles (see cluster definition in Sec. 3.3) for a γ–jet and jet–jet production after scaling for each of the p_{T}-hard bins and adding them.

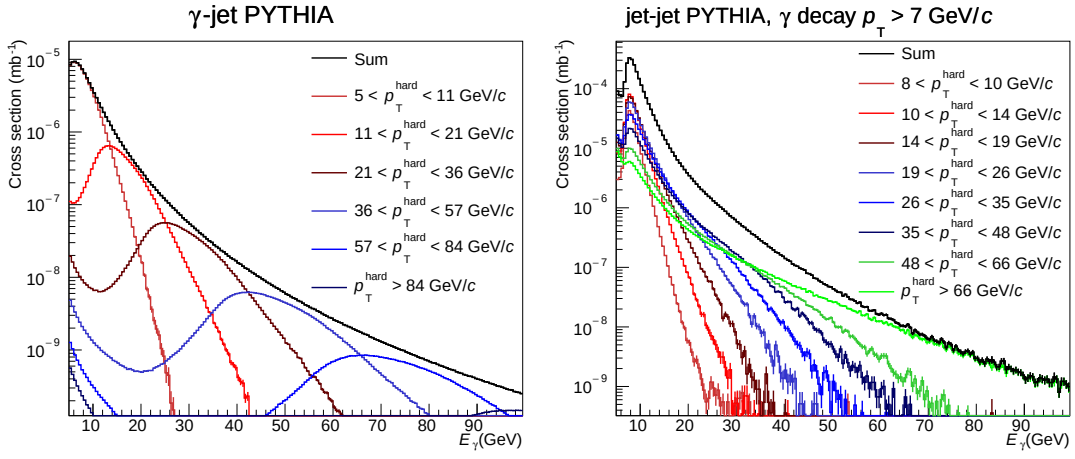

Figure 3.1: Cluster energy distribution, per p_{T}-hard bin (colored lines) and the sum (black line) of all bins for γ–jet (left) and jet–jet triggered by decay photons with $p_{\mathrm{T}} > 7$ GeV/c (right) simulations after scaling the p_{T}-hard bins using Eq. (3.1).

3.2 Event selection

All events with more than one reconstructed primary vertex were rejected in the analysis to exclude pileup events within the same bunch crossing [72]. Also, only events with a primary vertex position along the beam direction within ±10 cm from the centre of the apparatus were considered in this analysis.

The same event cuts were used in data and simulation. In jet–jet simulations, an additional event cut is considered, to remove event outliers on the generated p_{T}-hard bins, events with generated level jet p_{T} large compared to the generated p_{T}-hard bin are rejected, namely when $p_{\mathrm{T}}^{\mathrm{jet,\ gen}}$ / p_{T}-hard >2.

3.3 EMCal cluster reconstruction

Particles deposit most of their energy in a single cell in EMCal, and the rest in several neighbouring cells. One wants to form a "cluster" of cells where a given particle deposited energy, although depending on the energy, granularity, clusterization algorithm, or event type, those clusters might have contributions from different particles [74]. Clusters ideally represent the energy a particle deposited in the calorimeter, particularly for photons and electrons. The clusterization method defines what cells belong to a cluster. Details about how the clusterizers work in EMCal can be found in Ref. [74].

There are several clusterization methods available for the EMCal. The selection of the clusterization method depends on the goal of the analysis. The basic EMCal clusterization algorithm used here builds clusters starting from the highest energetic cell in a region, referred to as the seed cell, with energy above $E_{\mathrm{seed}} = 500$ MeV, and associate cells in the vicinity that share a common side with cells already in the cluster. Cells are aggregated into the cluster in case their energy is above the aggregation threshold at $E_{\mathrm{agg}} = 100$ MeV. This algorithm allows the merging of clusters originated from particles produced not too far away in the calorimeter.

Once the cluster is formed, its energy E can be calculated as the sum of the energies of the cell that belongs to the cluster ($E_{\mathrm{cell},\,i}$),

$$E = \sum_i E_{\mathrm{cell},\,i}, \tag{3.2}$$

where i indicates a cell that belongs to the cluster. The cluster position is given by a weighted average of the cell's position (x_i, y_i, z_i)

$$\langle x \rangle = \sum_i \frac{w_i x_i}{w_{\mathrm{tot}}}, \quad \langle y \rangle = \sum_i \frac{w_i y_i}{w_{\mathrm{tot}}}, \quad \langle z \rangle = \sum_i \frac{w_i z_i}{w_{\mathrm{tot}}}, \quad \text{with} \quad w_{\mathrm{tot}} = \sum_i w_i \tag{3.3}$$

where w_i is given from the cell energies,

$$w_i = \mathrm{Max}\left(0,\ w_{\mathrm{max}} + \ln\left(\frac{E_{\mathrm{cell},\,i}}{E}\right)\right), \tag{3.4}$$

the $w_{\max}$ set as 4.5 [83] to exclude cells with energy smaller than 1.1% of the cluster energy [74].

Other parameters related to particle identification can be extracted from the cluster: the shower shape, discussed in the section, and the "number of local maxima". When two clusters from different particles are close, they can have overlapping cells when the distance between the centroids is not too small. In such cases, one can find two cells with the highest energy surrounded by several lower energy cells, in such cases we have two local maxima. In data, we observe clusters of cases with one, two and many local maxima. We are interested in those clusters with one maximum (single particles) or with at most two local maxima (neutral mesons decay photons with small opening angle) as discussed in Sec. 4.1.

3.3.1 EMCal shower shape definition

The distribution of energy within a cluster, referred to as "shower shape", is described using a parametrization of the shower surface ellipse axes. More details can be found in Ref. [84]. The shower surface is defined by the intersection of the cone containing the shower with the front plane of the calorimeter, as displayed schematically in Fig. 3.2.

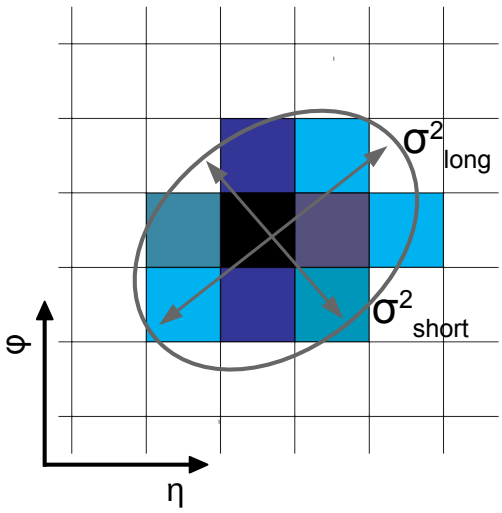

Figure 3.2: Schematic view of cluster energy repartition in cells and the shower shape axes. The different colors indicate the amount of energy deposited in each cell, the darker the more energy.

The energy distribution along the η (pseudorapidity) and φ (azimuth) directions is represented by a covariance matrix with terms $\sigma^2_{\varphi\varphi}$, $\sigma^2_{\eta\eta}$ and $\sigma^4_{\eta\varphi}$,

$$\delta^2_{\alpha\beta} = \sum_i \frac{w_i \alpha_i \beta_i}{w_{\text{tot}}} - \sum_i \frac{w_i \alpha_i}{w_{\text{tot}}} \sum_i \frac{w_i \beta_i}{w_{\text{tot}}}, \text{ with } \alpha \text{ and } \beta = \eta \text{ or } \varphi \tag{3.5}$$

which are calculated using logarithmic energy weights w_i in Eq. (3.4) [83]. The shower shape parameters σ^2_{long} (long axis) and σ^2_{short} (short axis) are defined as the eigenvalues of the covariance matrix, and are calculated as

$$\sigma^2_{\text{long}} = (\sigma^2_{\varphi\varphi} + \sigma^2_{\eta\eta})/2 + \sqrt{(\sigma^2_{\varphi\varphi} - \sigma^2_{\eta\eta})^2/4 + \sigma^4_{\eta\varphi}}\,, \tag{3.6}$$

$$\sigma^2_{\text{short}} = (\sigma^2_{\varphi\varphi} + \sigma^2_{\eta\eta})/2 - \sqrt{(\sigma^2_{\varphi\varphi} - \sigma^2_{\eta\eta})^2/4 + \sigma^4_{\eta\varphi}}. \tag{3.7}$$

This is one of the main parameters of this analysis for the photon identification. For neutral particles, the σ^2_{long} has a clear discrimination power to identify particles, while the σ^2_{short} is not as effective [74]. For this, we use the parameter σ^2_{long} in this analysis to identify neutral particles that the cluster belongs to. The parameter units are cell sizes, but for simplicity, this parameter is reported without units.

Figure 3.3 presents the cluster σ^2_{long} distribution in data and simulation, for different parameterizations on the simulation discussed in Sec. 3.4.5, clusters calibrated and selected following the criteria discussed in Secs. 3.4 and 3.5. A clear main peak centred at 0.25 is observed populated by single photon clusters or very merged particle clusters at high energy, followed by another maximum at higher σ^2_{long} populated by not too overlapped particle clusters. The complete discussion on the particle discrimination power of the shower shape is done in Sec. 4.1.

3.4 EMCal calibration

The EMCal calibration is an essential step to ensure accurate measurement of the energy deposited by these particles. There are different types of calibrations performed on the EMCal to obtain accurate measurements. Here I explain part of the calibration procedures, further technical or performance details regarding the ALICE EMCal can be found in the EMCal performance paper [74].

3.4.1 Cell energy calibration

The objective of cell energy calibration is to calculate the calibration coefficients for each cell in a way that all cells report the same energy when given the same input. The cell energy calibration is performed by using $\pi^0 \to \gamma\gamma$ decays. Measuring the invariant mass distribution of π^0 meson candidates for which one of the two decay photons has the cluster centroid (see Eq. (3.5)) located in the cell being calibrated. The cluster centroid is the central cell in the cluster. The distribution is then fit by the sum of a Gaussian (for the π^0 peak) and a second-order polynomial (for the combinatorial background). The calibration coefficient c_i is obtained from the ratio of the known π^0 mass $M^{\text{PDG}}_{\pi^0}$ and the mean of the fitted Gaussian μ^{fit}_i: $c_i = \left(M^{\text{PDG}}_{\pi^0}/\mu^{\text{fit}}_i\right)^n$, with $n = 1.5$ [75]. Both decay photons were required to be in the same super module to avoid effects from the misalignment in the EMCal super modules in the

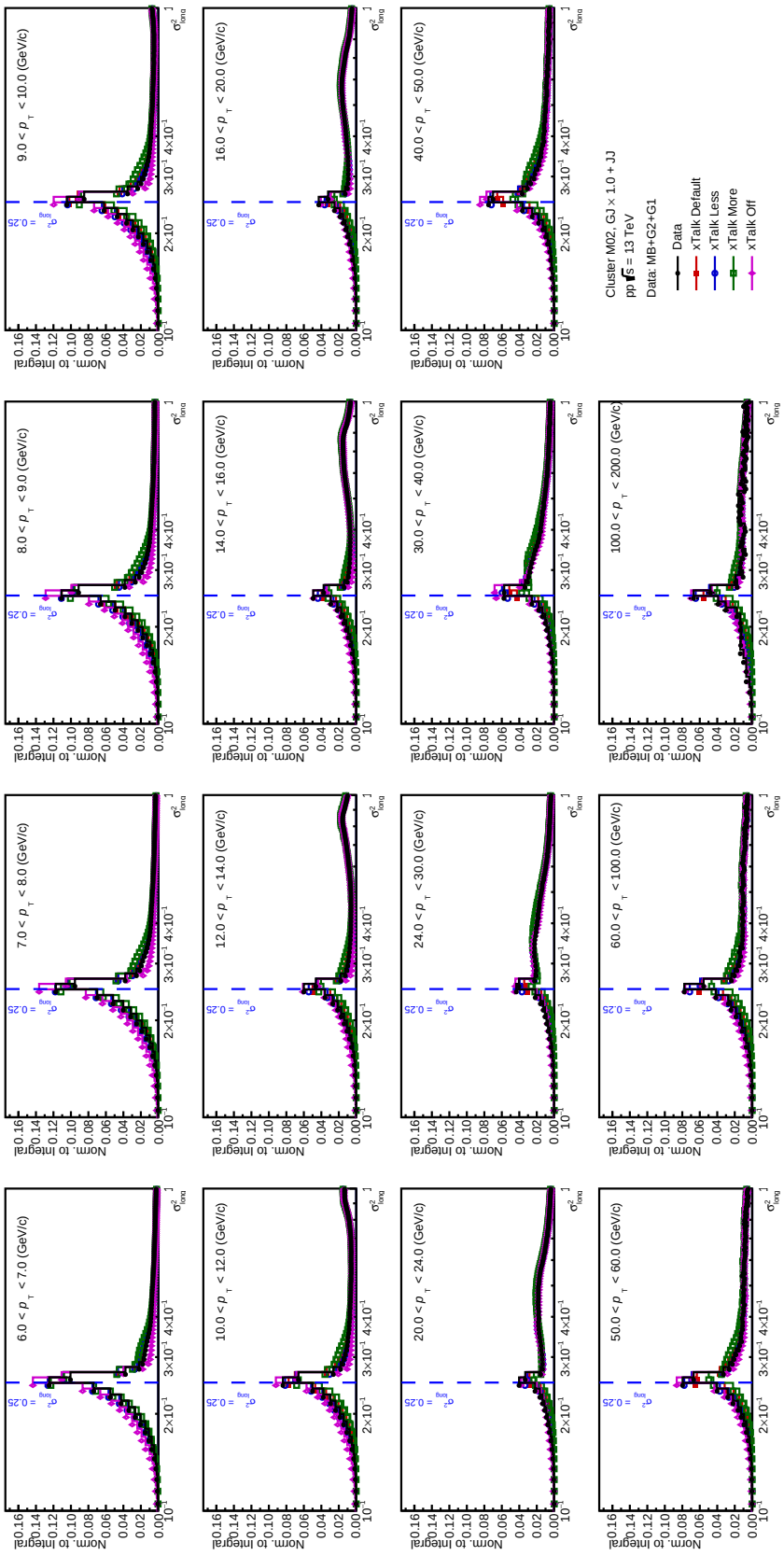

Figure 3.3: Clusters σ^2_{long} distribution from data (black), pp collisions at $\sqrt{s} = 13$ TeV, or simulation, γ–jet + jet–jet PYTHIA processes, with different cross-talk (xTalk) emulation parameterizations (see Sec. 3.4.5 Tab. 3.4) and in different cluster p_{T} bins. Distributions normalised to the number of entries on each histogram.

z-direction. Few iterations are needed since the cluster contains more cells that need calibration, and also we pair with uncalibrated clusters, more details can be found in Sec. 5.2 of Ref. [74].

3.4.2 Bad channel masking

In some instances, channels within the calorimeter may exhibit an improper response to a hit. These channels are noisy or have a discontinuous energy spectrum, for example. These so-called bad channels must be masked and excluded from any data analysis. To identify these channels, we used two observables: the mean energy per channel and the number of hits recorded by a channel. Certain cells might give a bad response only in certain energy ranges, so the two variables are evaluated independently of each other over various energy slices. The assumption that the number of hits per channel should only differ statistically is used to weed out noisy, hot, cold, dead, or otherwise improper channels.

3.4.3 Cell Time calibration

The cell time calibration aims to correct the cell time information by the average of the cell measured time over a long period, which can be as long as one data taking period or a whole year. The calibration corrects for the cable length, electronic response time, and time shifts due to clock phase differences. Cluster time distributions after calibration can be found in Sec. 4.2 Fig. 4.12.

3.4.4 Cell temperature calibration

The temperature calibration is necessary because the gain of the APD is linearly dependent on the temperature. Since the temperature can fluctuate during the runs, a correction to the gain is applied offline. There are LEDs and temperature sensors installed near the APDs at various locations. The LED pulses are monitored throughout the runs as a function of time for the different EMCal strips. The average temperature from the temperature sensors was used to calibrate the data. More technical or performance details can be found in Ref. [74].

3.4.5 Cell cross-talk in data and emulation in simulation

Early analysis showed that the shower shape distribution (defined in sec. 3.3.1) mean peak (photons peak) is broader in the data than in the simulation with default settings as shown in Fig. 3.3. Broader cluster shapes can be due to additional material in front of the detector, but investigations excluded this option and found that the largest contribution arises from problems at the hardware level [74], in particular, cell cross-talk: a signal in a given cell affects the energy and time distribution of the adjacent cells, and thus, will modify the cluster shower shape.

Due to the cell cross talk, some energy can leak from a sufficiently high-energy cell to neighbouring cells with low energy, which can cause the neighbouring cells to exceed the clusterization threshold, and therefore, have potentially broader shape than in ideal conditions. It was found that the effect depends on the SM and even on the pseudorapidity location inside the SM. The most affected SMs are SM 3 and 7, followed by SMs 1 and 10 (see their location in Fig. 2.8). This can be observed by counting the number of cells contributing to the shower shape calculation (pass the w_0 limit), and is shown in Fig. 3.4 where the fraction of clusters with more than 4 cells in the shower shape calculation is shown. In this figure, SM 3 and 7 have a particularly higher fraction compared to other SMs.

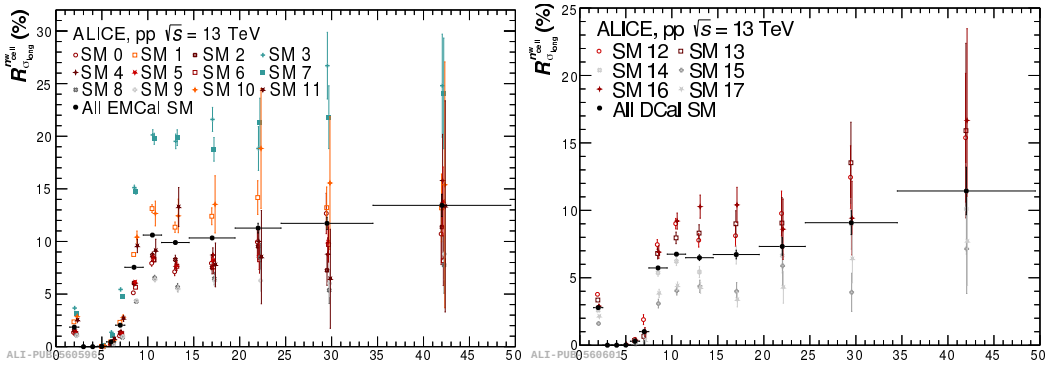

Figure 3.4: Fraction of clusters with the number of cells contribute to cluster shower shape calculation, within the range $0.1 < \sigma^2_{\text{long}} < 0.3$ per SM, in pp $\sqrt{s}$ = 13 TeV L1-γ triggered data. Plot from Ref. [74]. Left, EMCal SMs (top SMs) and right DCal SMs (bottom).

To emulate the observed features in the simulations, the following assumptions were made [74, 85, 86]:

- The problem is purely a cross-talk between cells inside a T-Card;
- It affects all cells in the calorimeter;
- Given a signal in a cell, the cells around are affected, and possibly those 2 rows away;
- It can depend on the cell energy;
- It can depend on the SM number but not on rapidity or azimuth.

The last assumption on the rapidity independence is not entirely correct, because the cable lengths affect the region near $|\eta| = 0$, but we will average the effect on the full SM. Considering this, the algorithm emulation at simulation level is as follows: inspect all the cells with signal in the simulation, and per each cell with energy E_{cell}, add to the surrounding 5 cells in the same T-Card an induced energy $E^{\text{ind}}_{i,j}$

$$E^{\text{ind}}_{i,j} = F^{\text{ind}} E_{\text{cell}}\ , \quad with\ F^{\text{ind}} = \mu_1 + \mu_2\ E_{\text{cell}}, \tag{3.8}$$

where i and j indicate the column and row with respect to the selected cell, and the parameters μ_1 and μ_2 are found comparing data and simulation and can be different per SM and even per induced cell location (i, j) [74, 85, 86]. Finally, the total induced energy in the nearby T-Card cells is subtracted from the main signal cell, $E^{\text{final}}_{\text{cell}} = E_{\text{cell}} - \sum E^{\text{ind}}_{i,j}$, so that the energy scale is preserved.

Figure 3.3 also presents the σ^2_{long} distribution for simulation with different cross-talk emulation parameters listed in Tab. 3.4. The "Default" or "Less" parametrizations are closer to the data distributions, but still not a perfect reproduction. We will use as systematic uncertainty half of the difference between no emulation and "Default" emulation.

Table 3.4: Emulation parameters used to calculate the $E^{\text{ind}}_{i,j}$ in the five surrounding cells to a given cell with signal in the T-Card depending on the SM number. Note that we allow also the inducing energy in cells two rows away, but only with F^{ind}=$F^{\text{ind}}_{\text{min}}$. Different parametrizations (Default or Std, More, EtaDep, Less) change the $F^{\text{ind}}_{\text{min}}$ parameter by a factor of 0.5 or 2 with respect to the default one. From Ref. [87] Sec. 6.1.

	group 1	group 2	group 3	group 4
SM EMCal	3, 7	1, 10	0, 2, 4, 5, 6, 11	8, 9
SM DCal	-	-	12, 13, 16	14, 15, 17, 18, 19
$F^{\text{ind}}_{\text{min}}$				
– Default-Std	0.6%	0.5%	0.45%	0.35%
– More ($\lvert\eta\rvert < 0.7$) or EtaDep ($\lvert\eta\rvert < 0.2$)	0.9%	0.75%	0.68%	0.52%
– Less	0.3%	0.25%	0.235%	0.175%
$F^{\text{ind}}_{\text{max}}$	1.8%	1.6%	1.6%	1.6%
μ_1	1.2%	1.2%	1.15%	0.8%
μ_2 (GeV^{-1})	-0.11%	-0.11%	-0.11%	-0.11%
σ_{ind}	0.5%	0.5%	0.5%	0.5%
$E^{\text{ind}}_{\text{min}}$ (GeV)	$E^{\text{cell}}_{\text{min}}$	$E^{\text{cell}}_{\text{min}}$	$E^{\text{cell}}_{\text{min}}$	$E^{\text{cell}}_{\text{min}}$

3.5 EMCal cluster quality selection

3.5.1 Basic criteria

A cluster must contain at least two cells to guarantee a minimum cluster size and to remove single-cell electronic noise fluctuations. Also, the highest-energy cell must be at a distance d_{mask} of at least two cells away from a known misbehaving cell to avoid possible electronic influence between channels, or from a dead cell to avoid holes in the cell energy spread of the clusters. To limit energy leakage at the SM borders, a distance of at least one cell of the highest-energy cell in the cluster to the SM border is required, except at the SM border at $\eta = 0$ where two SMs are adjacent and clusters can be shared between SMs. To ensure the selection of clusters from the main bunch crossing, the measured time of

the highest-energy cell in the clusters relative to the main bunch crossing has to satisfy $\Delta t < 20$ ns. Finally, clusters can contain more than one or two local maxima cells, no cluster splitting is performed.

The energy response of the EMCal is not linear due to losses in the cell limits and electronics saturation. An energy non-linearity correction derived from electron test beam data [74] is applied to the reconstructed cluster energy. It amounts to about 6% at $E = 1$ GeV decreasing to approximately 2% between 20 and 100 GeV and increasing to approximately 3% at 200 GeV due to signal saturation. Since the simulation does not exactly reproduce the energy linearity, an extra correction factor is applied to match the π^0 mass obtained in simulations to the corresponding measurements in data. The value of this correction is 1.025 at $E = 1$ GeV, decreasing to 0.975 above 7 GeV. After the corrections, the energy scale uncertainty of the EMCal is considered to be 0.5%.

3.5.2 Track–cluster association

The EMCal is designed with the purpose of measuring the energy of photons and electrons. It should be noted, hadrons are also capable of depositing energy in the EMCal. In instances where the distinction between showers originating from charged and neutral particles is necessary, clusters are associated with charged-particle tracks.

Contamination of the cluster sample by charged particles is suppressed by a charged particle veto (CPV). Tracks of charged particles are reconstructed in a hybrid approach using ITS and TPC, which reduces local inefficiencies potentially caused by non-functioning elements of the ITS. Two distinct track classes are accepted in this method [72]: (i) tracks containing at least three hits in the ITS, including at least one hit in the SPD, with momentum determined from a Kalman-filter fit to the hits attached to the track, and (ii) tracks containing less than three hits in the ITS or no hit in the SPD, with the primary vertex included in the momentum determination. Class (ii) is used only when SPD modules along the particle trajectory are inactive. Class (i) contributes 90% and class (ii) 10% of all accepted tracks, independently of p_{T}. Charged-particle tracks are selected to have a distance of closest approach to the primary vertex smaller than 2.4 cm in the plane transverse to the beam, and smaller than 3.0 cm in the beam direction. Figure 3.5 shows the angular correlation between tracks and clusters observed in data.

EMCal clusters originating from charged particles are tagged by applying a selection on the separation of the position of the track extrapolated to the EMCal surface from the cluster position, which must fulfil:

$$\Delta\eta^{\mathrm{residual}} < 0.010 + (p_{\mathrm{T}}^{\mathrm{track}} + 4.07)^{-2.5} \text{ and } \Delta\varphi^{\mathrm{residual}} < 0.015 + (p_{\mathrm{T}}^{\mathrm{track}} + 3.65)^{-2} \text{ rad} \tag{3.9}$$

where $\Delta\eta^{\mathrm{residual}} = |\eta^{\mathrm{track}} - \eta^{\mathrm{cluster}}|$, $\Delta\varphi^{\mathrm{residual}} = |\varphi^{\mathrm{track}} - \varphi^{\mathrm{cluster}}|$, and the track transverse momentum

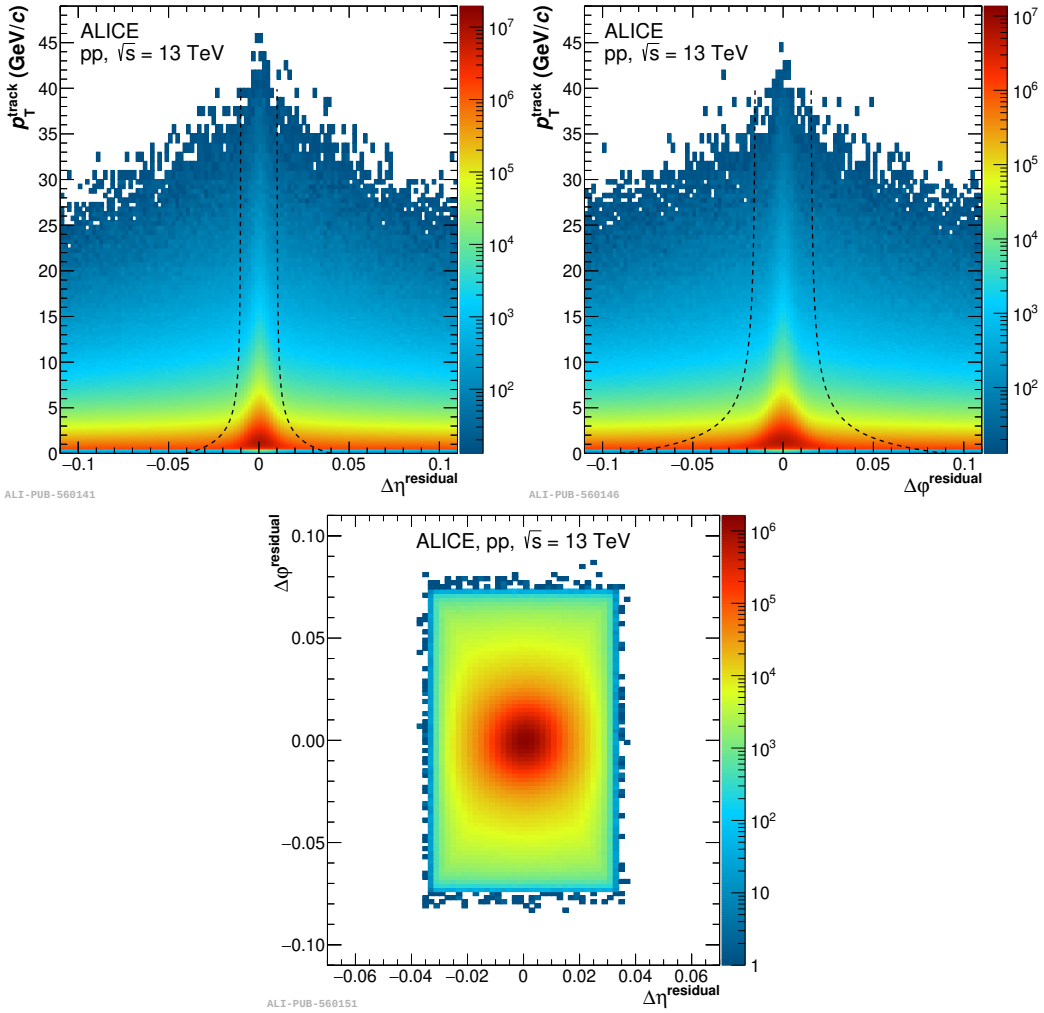

Figure 3.5: Distance between a cluster and the closest projected track in η (top-left) or φ angle (top-right) versus the track momentum and for matched track-cluster pairs (bottom) in pp collisions at $\sqrt{s} = 13$ TeV collected with the minimum bias trigger. The black lines in the left and middle panels indicate the suggested selection criteria expressed in Eq. (3.9). From Ref. [74].

($p_{\mathrm{T}}^{\mathrm{track}}$) is in GeV/$c$ units. This condition is applied if the ratio of cluster energy over track momentum is smaller than 1.7, used to reduce the amount of fake vetoes, if larger, no cluster–track association is considered [74]. The track-to-cluster matching efficiency amounts to about 92% for primary charged hadrons and electrons at cluster energies of $E \simeq 1$ GeV, and increases up to 96% for clusters of 10 GeV.

From now on, clusters that are not matched to any charged-particle track are called “neutral clusters”.

3.5.3 Exotic cluster

Nuclear interactions occurring in the APD, in particular those involving neutrons, induce an abnormal signal [74, 88]. Such a signal is most frequently observed as a single high-energy cell with no

or few surrounding low-energy cells, this latter case being mostly caused by cell cross-talk (details in Sec. 3.4.5) or overlaps of the underlying event particles and this abnormal signal in the measurement.

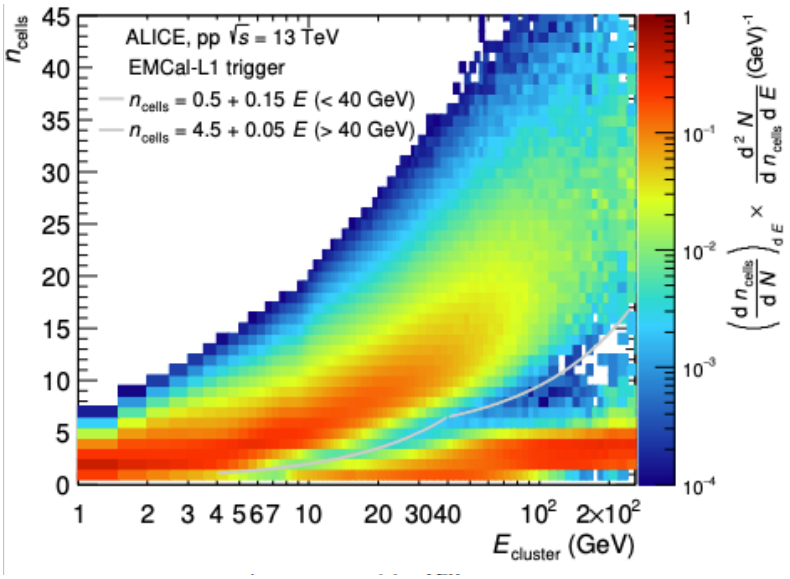

Figure 3.6: Number of cells as a function of the cluster energy in pp collisions at $\sqrt{s}$ = 13 TeV using the EMCal high threshold L1-γ trigger. The region below the lines is populated by exotic clusters. The distribution for each energy bin is normalized to its integral. Plot From Ref. [89].

Exotic clusters are defined as reconstructed clusters with too high energy in a single channel with respect to the secondary cells in the cluster [74, 90]. Such exotic clusters can be directly observed in EMCal data when looking at the number of cells in the cluster as a function of the energy as in Fig. 3.6, two clear populations are observed, the one with low number of cells and high energy is due to exotic clusters. However, the corresponding response is not implemented in the simulation, mainly due to the missing description of the APD behavior.

The degree of the homogeneity of the energy partition within the cluster is estimated via the parameter F_+, defined as follows

$$F_+ = 1 - E_+/E_{\text{cell}}^{\text{max}}, \tag{3.10}$$

where $E_{\text{cell}}^{\text{max}}$ is energy of the cell with highest energy and E_+ is the sum of the energy of the four cells with common side to the maximum energy cell [74, 85]. Figure 3.7 shows the F_+ as a function of the cluster energy, the exotic clusters populate the region above 0.97 from low to high energy, this limit is good to clean the cluster sample without cutting on real signal (similar figures on simulation without cross talk do not show this cluster population above 0.97) and is used in the analysis.

For very high-energy cluster ($E_{\text{cluster}} > 50$ GeV), the leading energy cell leaks via cross-talk a signif-

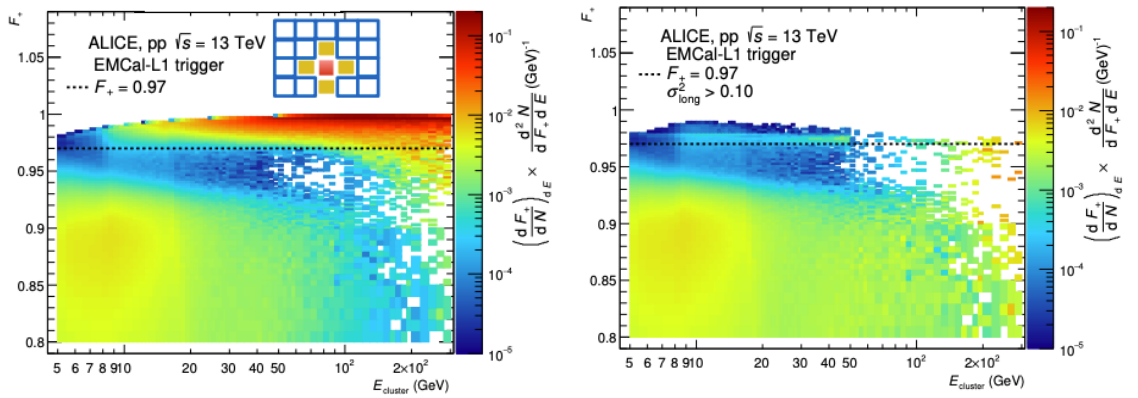

Figure 3.7: Left: "Exoticity" (F_+) as a function of the cluster energy in pp collisions at $\sqrt{s}$ = 13 TeV using the EMCal high threshold L1-γ trigger. The region above the line is populated by exotic clusters. The distributions are normalized to have an integral of unity for each energy bin. Plot from Ref. [89] slide 6. Right: Same distribution after the shower shape selection $\sigma^2_{\text{long}} > 0.1$ is applied (see definition in Sec. 3.3.1 and discussion on its use in Sec. 4.1). Plot from Ref. [89] slide 9.

icant amount of energy to the neighbouring cells. Those neighbouring cells, in turn, have enough signal to induce a significant cross-talk to other adjacent cells. This contributes to a relatively larger value of the shower shape parameter, leading to a significant contamination in the photon candidate population even selecting clusters with $F_+ < 0.97$ (see Sec. 4.1 Fig. 4.3). This was one important finding of this analysis, that triggered my study of the high-energy exotic clusters. At such high energies, photons produce clusters that cover more than one T-Card. Simulations without exotics and cross-talk emulation show that above 50 GeV, less than one per mil of clusters cover just one T-Card, except those whose highest energy cell sits in a border, which is usually removed from most of the analyses [74]. But this is clearly not what was found in the data and shown in Fig. 3.8, many high-energy clusters have their secondary cells in a single T-Card. Clusters just sitting on a single T-Card at such energies can only be due to exotic clusters and must be removed. Consequently, an additional requirement is used: the cluster must contain at least one cell in a different T-Card to the one where the highest energy cell is located for clusters with $E \geq 80$ GeV in this analysis.

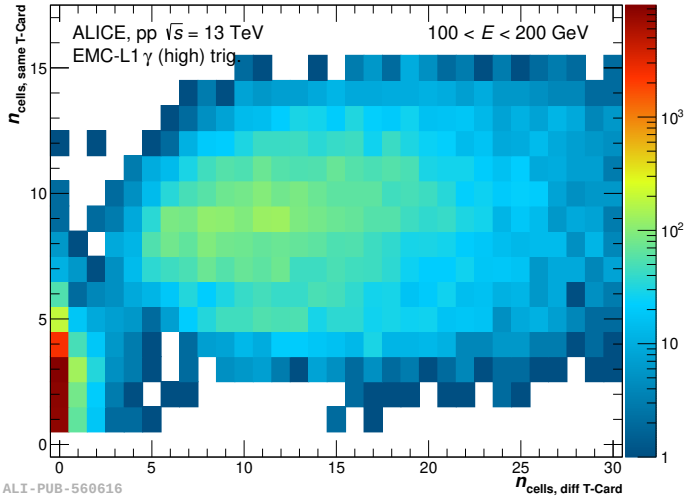

Figure 3.8: Number of cells in the cluster in the same T-Card as the highest energy cell as a function of the number of cells in a different T-Card, for clusters between 100 and 200 GeV. In simulations that do not include cross-talk the same distribution is found but the bin at $n_{\text{cells, diff T-Card}} = 0$ is empty; this bin in data is populated by exotic clusters. From Ref. [74]

Note that those exotic clusters are "isolated" and can have an important impact on the final result of this analysis if they are not removed. For that, at very high p_{T}, only using $F_{+} < 0.97$ is not sufficient to reject them and the additional condition on the number of cells in different T-Cards is imperative. See also Figs. 4.3 and 4.11 and the dedicated discussion in Secs. 4.1 and 4.2 to see the effect of exotic clusters on the shower shape distribution and final result.

3.6 EMCal trigger performance

3.6.1 Trigger overview

As explained in Sec. 2.2.4, the EMCal (and DCal) have several levels of hardware triggers to enhance the statistics of high-p_{T} observables, like photons, electrons or jets. Table 3.5 lists the trigger configurations for the datasets collected in pp, p–Pb, and Pb–Pb collisions during LHC Run 2 at a variety of $\sqrt{s}$. This analysis is based on data collected using both minimum bias interaction (MB) and EMCal L1 photon-dedicated (L1-γ) triggers. The use of the L1-γ trigger significantly enhances the integrated luminosity inspected and the number of EMCal clusters reconstructed.

The enhancement of the triggered sample to the MB sample is quantified via the "trigger rejection factor" (marked as RF^{trigger}), which is also used to correctly calculate the luminosity in Sec. 4.5. However, studies of the trigger efficiency show that the EMCal γ triggers do not become fully efficient at high p_{T} and that kinematic biases may lead to residual slopes in the plateau region. For these distortions and inefficiencies, a trigger efficiency is estimated in the simulation and discussed in Sec. 3.6.3.

Table 3.5: Setup of the EMCal triggers in various collision systems in LHC Run 2 (2015 - 2018). During Run 2, equivalent DCal triggers were enabled using the same thresholds. The L0 and L1-γ triggers are based on 2×2 FastORs. The patch size of the L1-jet triggers for EMCal is 16×16 FastORs, while DCal uses 8×8 FastORs in pp and p–Pb collisions. In Pb–Pb collisions the L1-jet trigger patch size is 8×8 FastORs for both parts of the calorimeter. Table from Ref. [74].

System	Energy	Year	Energy threshold (GeV)				
			L0	γ High	γ Low	Jet High	Jet Low
pp	$\sqrt{s}$ = 5.02 TeV	2015	2.5	-	-	-	-
		2017	2.5	-	4	-	16
	$\sqrt{s}$ = 13 TeV	2015 - 2018	2.5	9	4	20	16
p-Pb	$\sqrt{s_{\mathrm{NN}}}$ = 8.16 TeV	2016	3	8	5.5	23	18
Pb-Pb	$\sqrt{s_{\mathrm{NN}}}$ = 5.02 TeV	2015	-	10	-	20	-
		2018	2.5	10	5	20	-

3.6.2 Trigger quality assurance work: Supermodule by supermodule response

I observed a difference in the EMCal and DCal performance in the isolated-photon raw spectrum. This triggered my study discussed in the next lines. Studying the origin of this difference, at first two problems were found:

- We were using when analyzing the γ–jet simulations a $p_{\mathrm{T}}^{\mathrm{hard}}$ outlier event cut that was biasing the event selection, suppressing photons at large η. The cut was comparing reconstructed cluster momentum and generated momentum: $p_{\mathrm{T}}^{\text{reco from }\gamma}/p_{\mathrm{T}}^{\mathrm{hard}} > 2$. Removing this cut, we fixed mainly the efficiency and most of the discrepancy observed between large and small η.
- The shower shape cross-talk emulation assumed no η dependence although it was observed that at central rapidity the showers tended to be larger in data and not in MC, see [85] appendix C and meeting presentations [91, 92]. Even if this is not clear to be a cross-talk/hardware effect, we have used the cross-talk emulation framework to account for this effect. A new parametrization of the cross-talk emulation to the 1/3 more central part of the supermodules $|\eta| < 0.22$ was introduced. The lost energy cannot be lower than a fixed value that is increased for the central part of the detector by 50%. This new parametrization improves the description at large η of the σ^2_{long} and reduces the differences between central to outer rapidity regions, but it was still not enough to fix the discrepancy between the two calorimeters. Since the effect is small, we stick with the default parametrization of the cross-talk without η dependence.

After fixing these, the discrepancy remained and we decided to look in detail at the performance at

the supermodule (SM) level. Figures 3.9 and 3.10 show the cluster p_{T} spectra variation per supermodule or groups of supermodules compared to the cluster p_{T} spectra of EMCal + DCal. Figure 3.9 for narrow clusters ($0.1 < \sigma^2_{\mathrm{long}} < 0.3$) corrected only by prompt-photon reconstruction efficiency, Fig. 3.10 for isolated-narrow clusters (isolation condition discussed in Sec. 4.2) corrected by prompt photon reconstruction efficiency (no isolation). Within EMCal and DCal, the supermodules behaved differently, independent of the isolation and the purity correction.

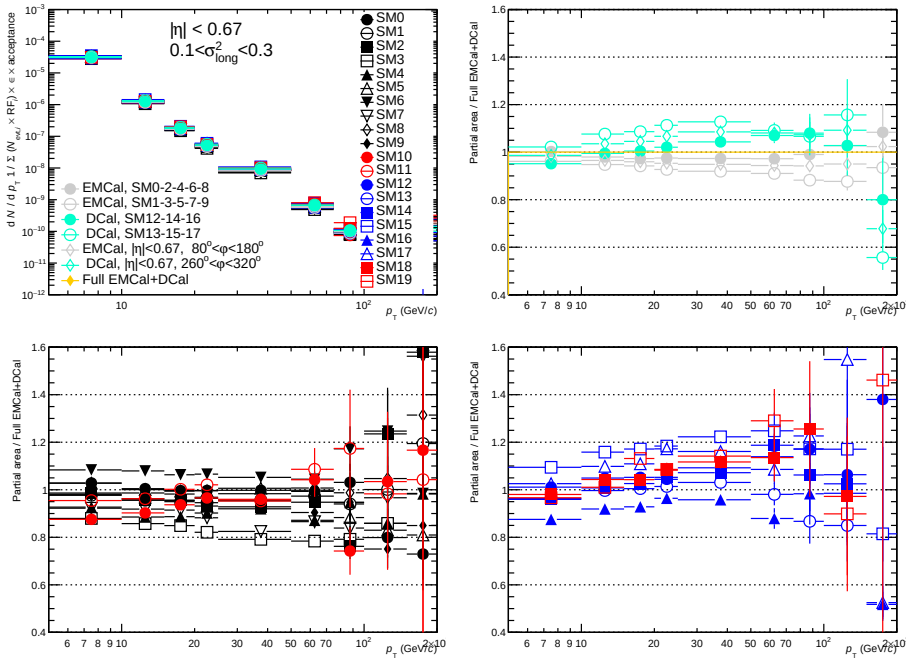

Figure 3.9: Top left: Semi-corrected narrow cluster ($0.1 < \sigma^2_{\mathrm{long}} < 0.3$) p_{T} spectra by prompt γ efficiency ($N_{\gamma}^{\mathrm{reconstructed}}/N_{\gamma}^{\mathrm{generated}}$ within the analysis acceptance) in different acceptances within the calorimeter corresponding to supermodules acceptance or EMCal or DCal positive or negative η (even or odd SM numbers). The numerator of the ratio consists of: top right, spectra obtained for Full EMCal or DCal acceptance, of positive or negative eta SM of EMCal and DCal; bottom left, spectra obtained within each single EMCal SM; bottom right, spectra obtained within each single DCal SM.

We needed to look even more in detail to understand the problem, so we checked similar plots per year (2016, 2017 and 2018) and even per period. Finally, we observed that the difference depends strongly on the triggered sample and much less on the MB sample, and that year 2016 is particularly bad compared to the other years. The trigger masks vary strongly per year and period, and these masks were not considered in the simulation analysis, and therefore, when comparing semi-corrected triggered cluster yields measured in EMCal and DCal. Key cluster acceptance plots can be found in Ref. [92] (ALICE internal). In particular, slides 65 to 67 to check the evolution per year and the effect of using trigger masks.

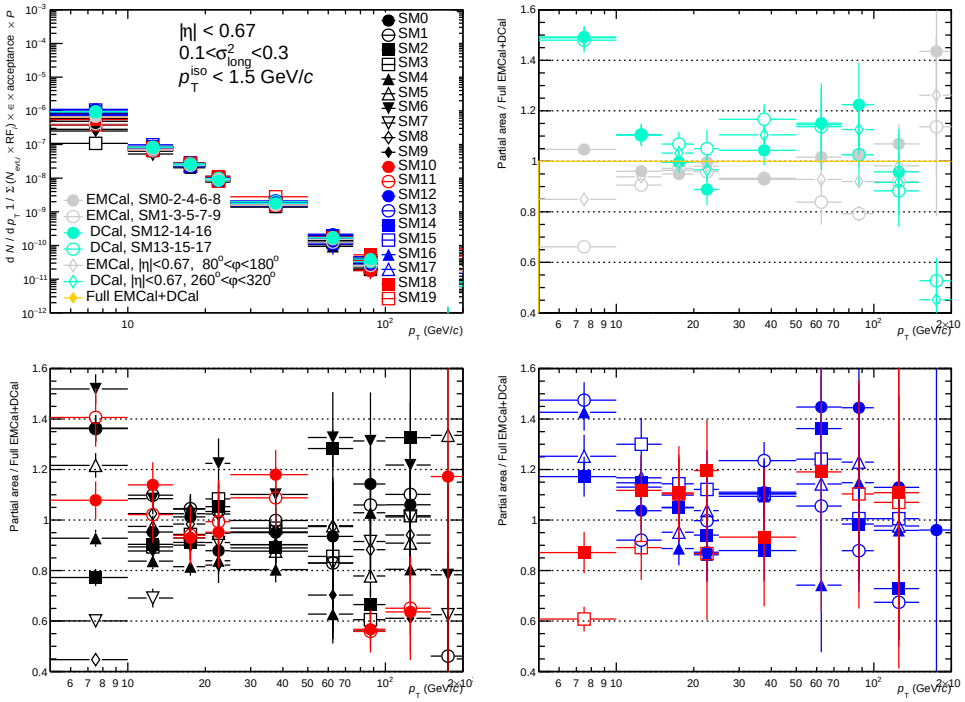

Figure 3.10: Top left: Semi-corrected isolated narrow cluster ($0.1 < \sigma^2_{\text{long}} < 0.3$, $p_{\text{T}}^{\text{iso}} < 1.5$ GeV/c) p_{T} spectra by prompt γ efficiency ($N_{\gamma}^{\text{reconstructed}}/N_{\gamma}^{\text{generated}}$ within the analysis acceptance) in different acceptances within the calorimeter corresponding to supermodules acceptance or EMCal or DCal positive or negative η. The numerator of the ratio consists of: top right, spectra obtained for Full EMCal or DCal acceptance, of positive or negative eta SM of EMCal and DCal; bottom left, spectra obtained within each single EMCal SM; bottom right, spectra obtained within each single DCal SM.

In summary, what was found and done to fix as much as possible the discrepancies was:

- Most of the discrepancy appears in the first periods of year 2016 where the DCal trigger was heavily masked and our studies found that more regions needed to be masked. The years 2017 and 2018 looked better, but still, a disagreement was observed.
- A careful check per period was done to implement masks in under-performing TRUs① in data. And also, many smaller isolated regions per period were identified and masked.
- The simulation periods anchoring relied on the MB trigger number of events. When studying calorimeter triggers and merging full years and periods, one has to rely on the number of events of the calorimeter trigger for the simulation, if not, one risks giving more weight to periods where a strong mask was applied. Without the proper event weighting in simulation SM15 and SM16 (heavily masked in the first part of the year) misbehave, but not with the proper event weighting.

① A TRU covers 1/3 of the acceptance of a full SM, a TRU covers full SM azimuth and 1/3 in rapidity, except for the smaller SMs (10, 11, 18, 19) where a TRU covers the full SM.

Figures 3.11 and 3.12 show the double ratio data/simulation per SM (or group of SM) over data/simulation over the full EMCal + DCal neutral clusters or isolated narrow clusters spectra, respectively, when the trigger emulation (simulation) and decision recalculation (data and simulation) was applied with the trigger masks found and proper event weighting applied. If the data and simulation had the same performance, the ratios should be at 1, and we can see that this is mostly the case, there is still a remaining dispersion that we will use as a systematic uncertainty.

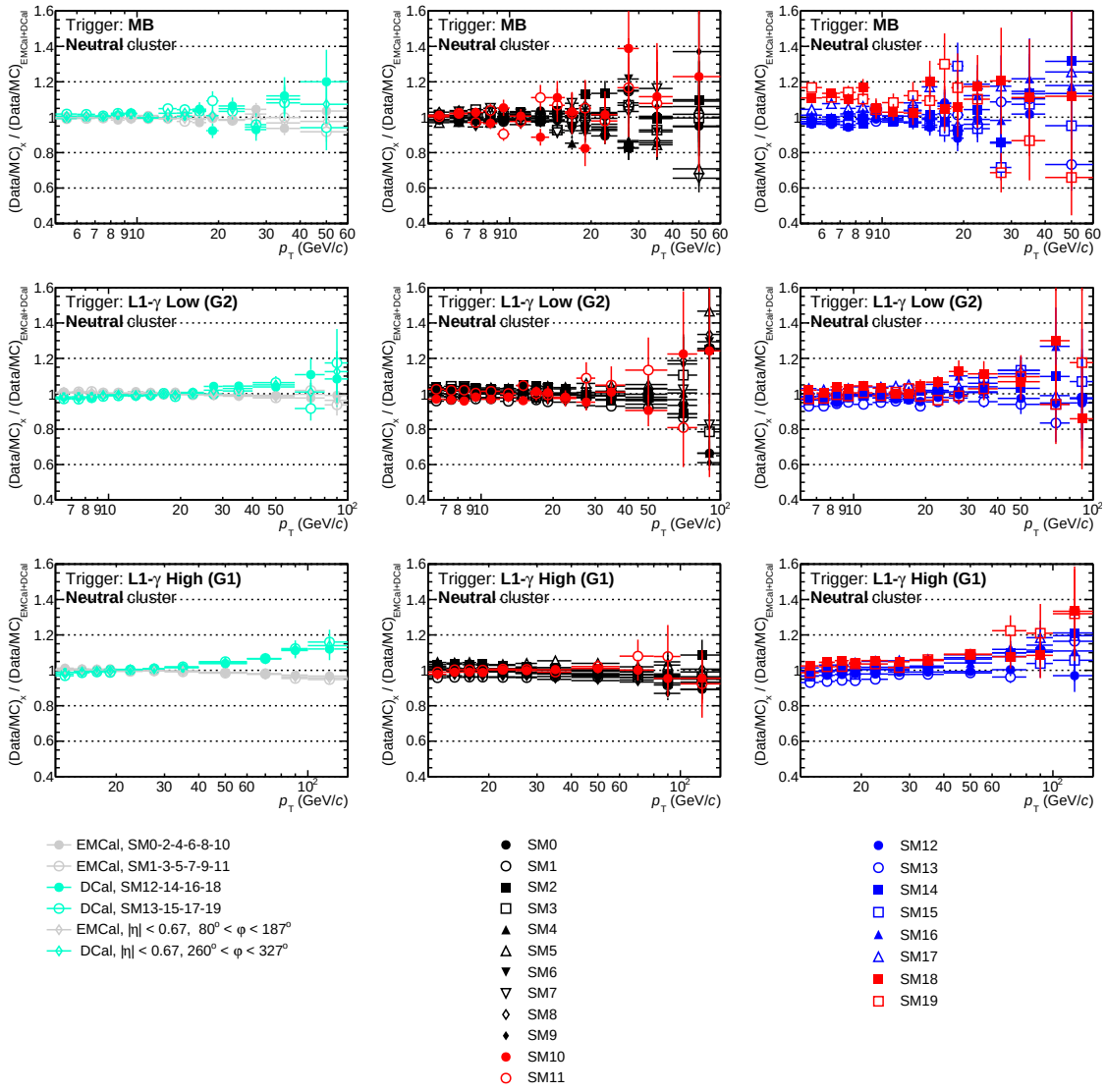

Figure 3.11: Double ratio: neutral clusters ($\sigma^2_{\text{long}} > 0.1$) p_{T} spectra data/simulation per SM or group of SM divided by data/simulation for EMCal +DCal. Simulation is the addition of PYTHIA8 γ–jet and jet–jet events (biased). Ratios for different triggers, MB (top row), EMCal + DCal G2 trigger (middle row) and EMCal +DCal G1 trigger (bottom row). Each column corresponds to grouping in the numerator data/simulation ratio different SMs (left), only EMCal SMs (centre) or only DCal SMs (right). Simulation periods are reweighted by the trigger number of events.

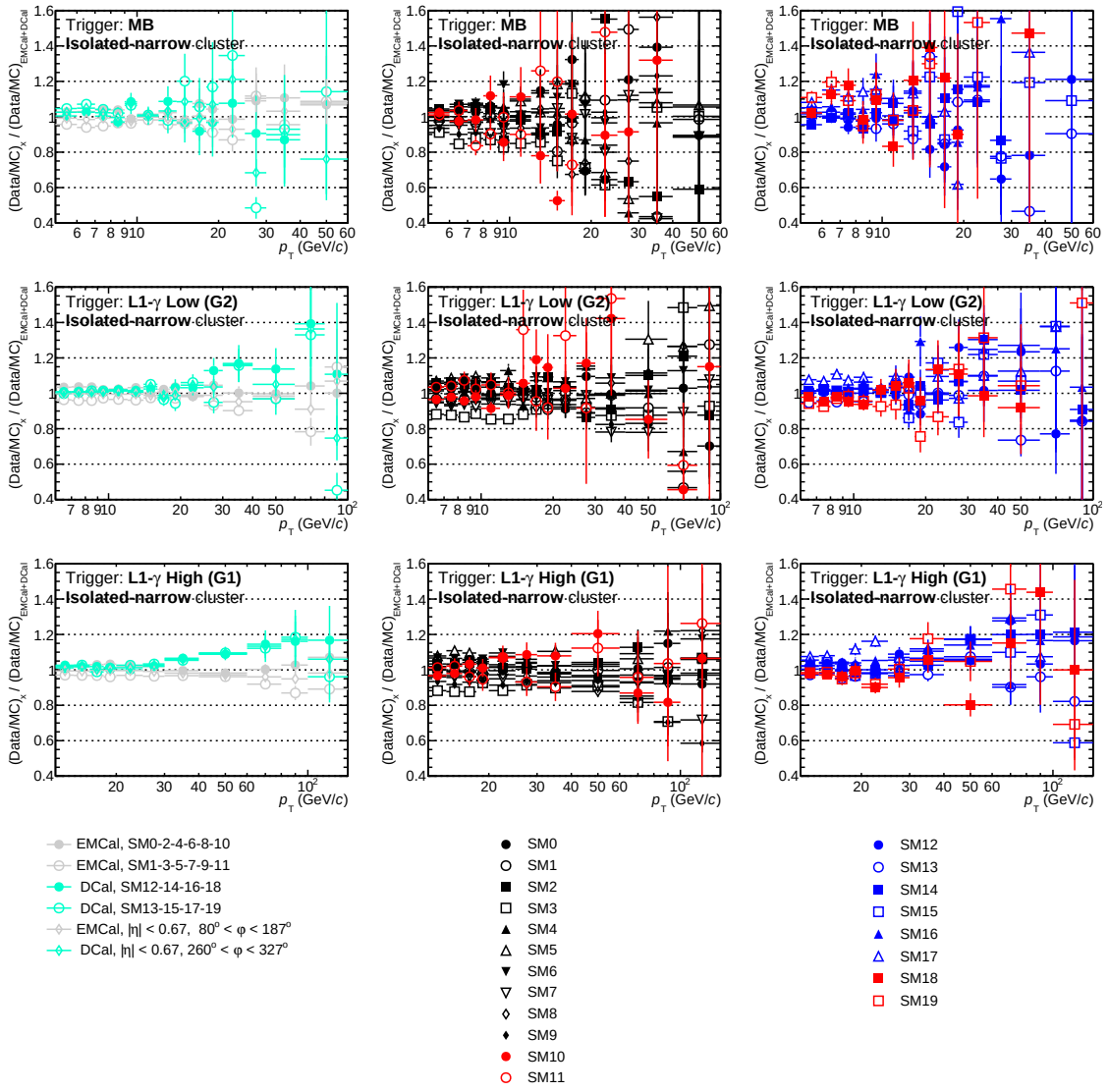

Figure 3.12: Double ratio: isolated-narrow clusters ($0.1 < \sigma^2_{\text{long}} < 0.3$, $p_{\text{T}}^{\text{iso}} < 1.5$ GeV/c) p_{T} spectra data/simulation per SM or group of SM divided by data/simulation for EMCal +DCal. Simulation is the addition of PYTHIA8 γ–jet and jet–jet events (biased). Ratios for different triggers, MB (top row), EMCal + DCal G2 trigger (middle row) and EMCal +DCal G1 trigger (bottom row). Each column corresponds to grouping in the numerator data/simulation ratio different SMs (left), only EMCal SMs (centre) or only DCal SMs (right). Simulation periods are reweighted by the trigger number of events.

We considered the variation (σ(SM)) per supermodule as

$$\sigma_i(\mathrm{SM}) = |1 - \mathrm{r}_{\mathrm{SM,i}}/\mathrm{r}_{\mathrm{EMCal+DCal}}| \tag{3.11}$$

where r is the cluster spectra ratio in data and simulation (PYTHIA8 γ–jet + jet–jet), shown in Fig. 3.11 and we calculated the systematic uncertainty due to the different performance at the SM level as

$$\Delta = \sqrt{\Sigma\sigma_i^2(\mathrm{SM})/\mathrm{n}_{\mathrm{SM}}}, \tag{3.12}$$

where n_{SM} is the number of SM used in the analysis. The resulting dispersion is shown in Fig. 3.13. For neutral clusters, there is about a 4.8% (MB) to 3% (G1, G2) dispersion depending on the trigger. For isolated-narrow clusters, it increases by 8.6% to 5.1%, the increase is partly a reflection of the decrease in statistics, especially in the MB sample, but the difference comes mostly from the shower shape cross-talk modelling already accounted in a separate uncertainty discussed in the previous section. Thus, we rely on the dispersion observed for neutral clusters, to decouple from any cross-talk systematic effect. We then decided to take a common constant systematic uncertainty for the MB and calorimeter triggers of 4%. At high p_{T}, there seems to be a linear increase of the dispersion, the kicking off p_{T} of this trend seems to depend on the trigger type and the type of cluster correlated with the number of clusters, the lower the statistics the lower the p_{T} this linear increase starts, we suspect this is a reflection of the poor statistics and thus we do not consider to have a higher systematic at high p_{T}.

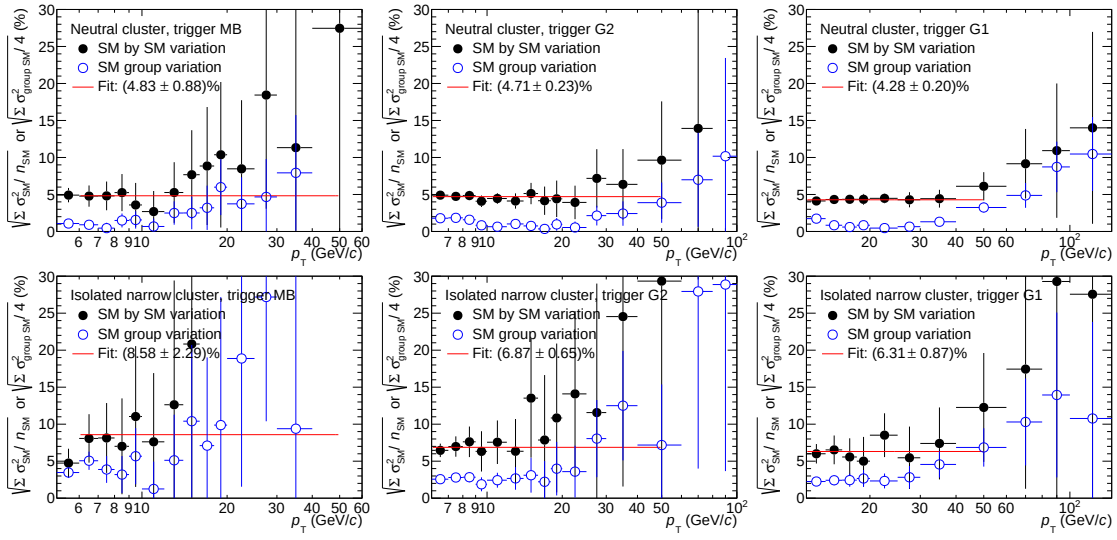

Figure 3.13: Averaged dispersion of the double ratios data/simulation shown in Figs. 3.11 and 3.12. Upper row for neutral clusters and lower for isolated narrow, left for MB trigger (and simulation periods weighted by MB number of events in data) middle for EMCal + DCal G2 triggers and right for EMCal + DCal G1 triggers (simulation periods reweighted by G1 number of events in data).

3.6.3 Trigger efficiency

The trigger efficiency depends partly on the masked calorimeter regions discussed in the previous section, and thus, the inspected calorimeter acceptance, and the trigger threshold. The efficiency is estimated, in the simulation, as the ratio of the selected cluster spectrum in events accepted by the trigger emulation and selection tools over all the generated clusters, as a function of the cluster p_{T}. The trigger emulation takes into account the masked areas over time obtained for this measurement.

Figure 3.14 presents the trigger efficiency for neutral (defined earlier at Sec. 3.5.2), narrow (small shower shape parameter value to select photon clusters, see next chapter) and isolated narrow clusters in this analysis, all obtained by mixing the combined jet–jet and γ–jet simulation samples.

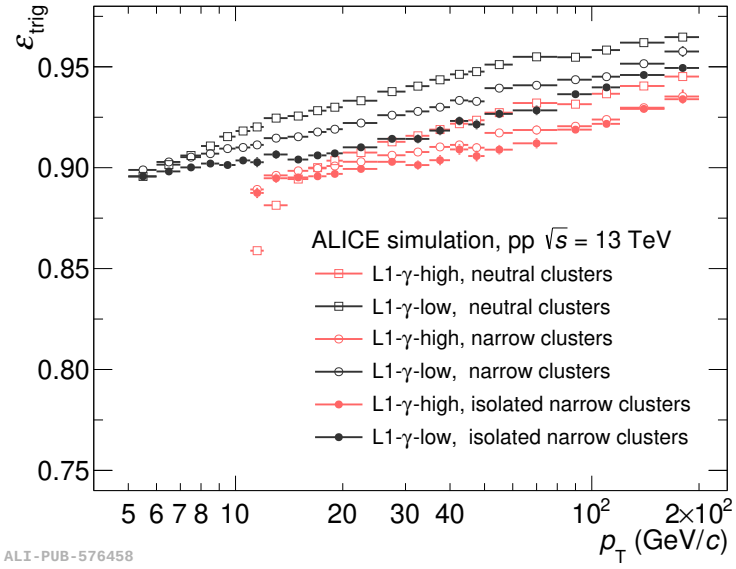

Figure 3.14: Trigger efficiency for neutral (open square), narrow (open bullet) and isolated-narrow (full bullet) clusters in pp collisions at $\sqrt{s}$ = 13 TeV for the high (red) and low (black) L1-γ triggers.

We can see that: (i) The efficiency is higher for the lower trigger threshold ($\approx$ 90% to 96% compared to $\approx$ 89% to 94%). But it does not reach unity even for the highest covered p_{T}. This can be explained by the fact that the masked FastORs resulted in a loss of trigger acceptance. (ii) Compared to narrow and isolated narrow clusters efficiency, the neutral clusters efficiency is higher by 1-2%, because wide clusters (two-photon merged clusters) cover more cells and therefore trigger better when moving away from the trigger threshold. We also observe that there is a clear slope in the efficiency distribution above the trigger threshold. Like if a cluster falls within a region of masked FastORs, the trigger condition can still be fulfilled by energy deposition from particles in the vicinity of the cluster [31]. This becomes increasingly probable as the cluster energy increases, resulting in the observed slope.

We apply in this analysis two different trigger efficiencies: 1) For reconstructed clusters, which is used for the rejection factor calculation, is corrected by using the neutral cluster trigger efficiency. 2) For the final cross section calculation, the uncorrected isolated photon spectrum is corrected by the corresponding isolated-narrow trigger efficiency.

The uncertainty of the trigger efficiency is half the ratio of the spectra corrected by the trigger efficiency and the corresponding rejection factor compared to the corrected spectra only with the rejection factor, which is also not corrected by the trigger efficiency. Figure 3.15 shows the two kinds of corrected spectra, their ratio, and the uncertainty of the trigger efficiency. For the trigger efficiency uncertainty at a low p_{T} interval (7–12 GeV/c) for which the dataset used is the MB sample combined with G2 triggered sample, we fit it with a constant function. For the intermediate p_{T} interval, 12 to 100 GeV/c, which uses a combined dataset of MB, G2 triggered as well as G1 triggered, a linear function is used to fit the uncertainty. For the highest interval, we use the points in the plot directly. Thus, the relative uncertainty for the region covered by the G2+MB trigger is of the order of 0.25% and for higher p_{T} it ranges from 0.5% at 12 GeV/c to close to 1.5% at 200 GeV/c.

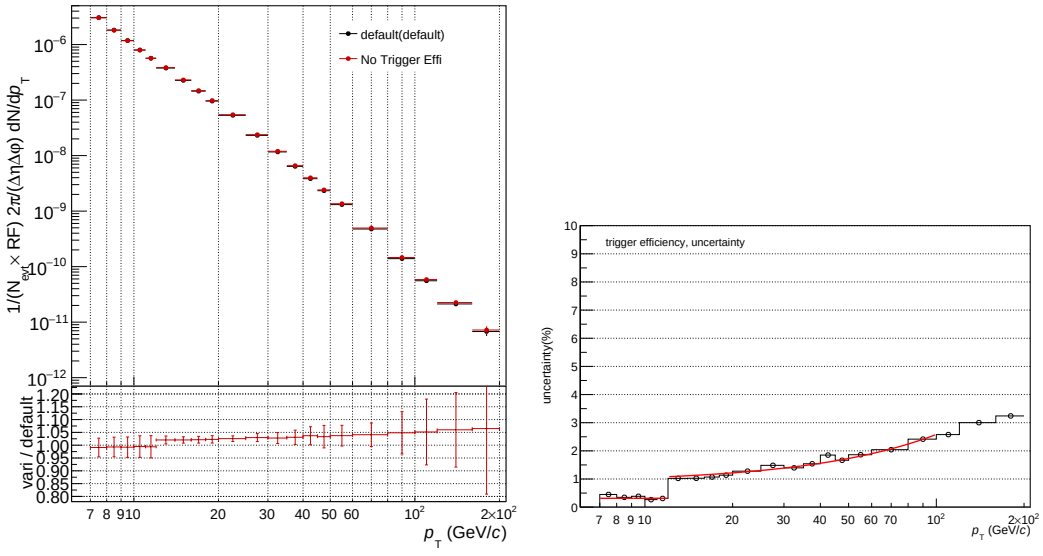

Figure 3.15: Left top panel, cross section p_{T} distribution obtained considering the trigger efficiency in the calculation or not, bottom panel, ratio of the two options. Right, associated relative uncertainty in %. We take half of the distribution as uncertainty. The red lines are the constant function fit at low p_{T} and the linear polynomial order 1 fit at intermediate p_{T}.

3.6.4 Calorimeter triggered events rejection factor

The rejection factor, RF^{trigger} also marked as RF^{trig}, is determined by studying event-normalized EMCal cluster spectra in each trigger class and calculating the ratio to the MB baseline, as Eq. (3.13).

$$RF^{\text{trig}} = \left(\frac{1}{N_{\text{evt}}^{\text{trig}}} \frac{\mathrm{d}N_{\text{cluster}}^{\text{trig}}}{\mathrm{d}p_{\text{T}}} \right) \Big/ \left(\frac{1}{N_{\text{evt}}^{\text{MB}}} \frac{\mathrm{d}N_{\text{cluster}}^{\text{MB}}}{\mathrm{d}p_{\text{T}}} \right) \tag{3.13}$$

The ratio should become constant at high p_{T}. It reflects the trigger improvement ability, simply put, it accounts for how many MB events are needed to obtain such a triggered event. For the RF^{trig} calculation, one has to take into account the effect of the trigger efficiency that is not constant with p_{T}, as seen in the previous section, and apply this correction to the triggered spectrum so that we get an ideally perfectly triggered cluster spectrum. Then, the formula becomes:

$$RF^{\text{trig}} = \left(\frac{1}{N_{\text{evt}}^{\text{trig}}} \frac{\mathrm{d}N_{\text{cluster}}^{\text{trig}}}{\mathrm{d}p_{\text{T}}} \frac{1}{\varepsilon_{\text{trig}}} \right) \Big/ \left(\frac{1}{N_{\text{evt}}^{\text{MB}}} \frac{\mathrm{d}N_{\text{cluster}}^{\text{MB}}}{\mathrm{d}p_{\text{T}}} \right) \tag{3.14}$$

Due to the limited statistics at high p_{T} in the MB sample, we can calculate the rejection factor in steps. Calculating the relative ratio to the next lower trigger and then gradually build up until it contains the ratio compared to the MB sample.

Figure 3.16 shows the cluster rejection factor distribution with and without the trigger efficiency applied in this analysis, the distribution is flatter as we expect after trigger efficiency is applied. Considering that the trigger is not fully efficient around the energy threshold, the fit starts at 9 GeV/c for the G2/MB and 15 GeV/c for G1/G2. Due to the large statistical bias at high p_{T}, the fit range is [9, 20] GeV/c for G2/MB and [15, 80] GeV/c for G1/G2. Both RF^{trig}s fittings are presented in the plot's color line, and the fitted values in the legend.

For the uncertainty of RF^{trig}, we consider two sources, the uncertainty from the fit which is related to the statistic, and the bias from the fit range selection. The fitting statistical uncertainty is the fitted parameter uncertainty obtained from fitting the RF^{trig} with the constant function. The fit results in this analysis are $RF^{\text{trig,G1/G2}} = 12.65 \pm 0.08$; $RF^{\text{trig,G2/MB}} = 471.14 \pm 48.95$. To estimate the uncertainty from the fitting range, considered as a systematic uncertainty, we follow the same approach as in the previous analysis [93]: refit the plateau region of the RF^{trig} with different fitting ranges, the fit range being all possible combinations with at least three points and a 5 GeV/c width, changing the lower and

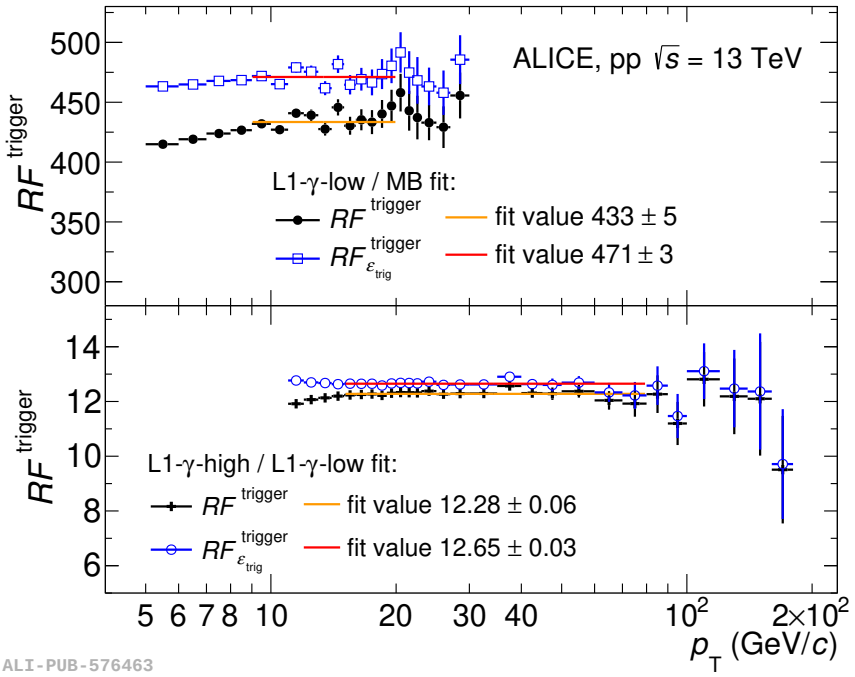

Figure 3.16: Top: The L1-γ low trigger rejection factor calculated with (blue square) and without (black dot) applying the trigger efficiency. The results of a constant fit to the rejection factor plateau regions are shown in the legend. Bottom: compared to the L1-γ low trigger, the L1-γ high trigger enhancement capability as a function of cluster p_{T} with (blue circle) and without (black cross) the trigger efficiency correction. The constant fit result with total uncertainty for the rejection factor plateau regions is shown in the legend.

higher fit limits. Then, all constant fitted results are filled as a histogram. The RMS of this filled histogram is treated as the uncertainty of the fitting p_{T} range. In this analysis, the various fit ranges are chosen to have a minimum width of 5 GeV/c and more than two p_{T} intervals are used to fit. The absolute ranges are [6, 27] GeV/c for the G2/MB case and [12, 90] GeV/c for the G1/G2 case. The histogram filled by multi-range constant fitted results in this analysis is presented in Fig. 3.17, the left one is for G1/G2 and the right is for G2/MB. The fitted Gaussian function, as a closure check, is the red line shown in both plots and the results are present in the corresponding panel. Finally, we can obtain the EMCal L1-γ trigger rejection factor with its total uncertainty for the analysis, as listed in Tab. 3.6 which also contains the corresponding statistical and systematic uncertainties.

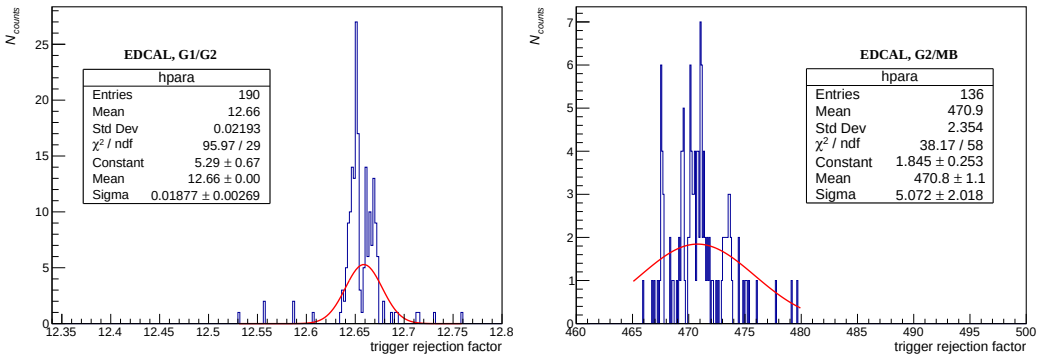

Figure 3.17: Cluster trigger rejection factors obtained by multiple fits changing the RF^{trig} p_{T} range of the fit, left is for G1/G2 per triggered event yield ratio and right for G2/MB per trigger event yield ratio. The histogram RMS is used as uncertainty. Distributions fitted to a Gaussian function and fit results are shown in the box, as a closure test.

Table 3.6: Cluster rejection factors fitted value and its associated uncertainty, the last column is total uncertainty for G1/G2 and G2/MB. The final G1/MB (G2/MB · G1/G2) uncertainty is obtained combining G1/G2 and G2/MB uncertainties and is driven by G2/MB.

RF^{trigger}	Fitted value	Stat. unc. (%)	Sys. unc. (%)	Total unc. (%)
G1/G2	12.65	0.14	0.17	0.22
G2/MB	471.14	0.34	0.50	0.60
G1/MB	5959.6	-	-	0.64

4 Prompt photon identification and cross section

In this chapter, we describe the different steps needed to measure the isolated-photon cross section. First, I describe the additional cluster selection criteria applied to the neutral clusters to obtain a raw sample of prompt photons: the shower shape and the isolation cut. More details can be found in [74]. Then, the different steps to correct the raw selected yield, efficiency and purity, and the normalization scaling factors to get the cross-section.

4.1 Photon identification via shower shape

The π^0 meson decay photon is known as the main background of the direct prompt photons. The opening angle between two decay photons from a π^0 as a function of the π^0 p_{T} is shown in Fig. 4.1 (left). The η meson has similar decay properties as the π^0 meson, which is also presented in Fig. 4.1 (right).

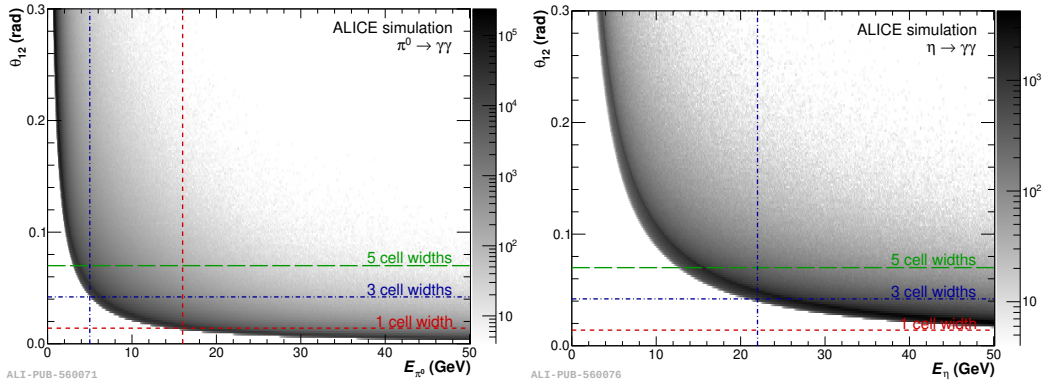

Figure 4.1: Distribution of the opening angle θ_{12} of two decay photons from π^0 (left) and η (right) mesons decays as a function of the meson energy obtained at generator level from an MC simulation. The horizontal lines indicate the opening angle corresponding to a width of approximately 1, 3 and 5 EMCal cells separating the two photons (1 cell = 0.0143 rad). Two photons completely merge into one cluster if they fall below the one cell distance, while they start merging at a width of approximately 3 cells, depending on the clusterizer. The colored vertical lines correspond to the energy limits where two photons could still be fully resolved by the clusterization described in Sec. 3.3 (blue) or by a clusterization that produces cluster splitting when more than one local maximum is found in the cluster (red). Plot from Ref. [74].

The opening angle is such that the outer cells of the photon clusters can overlap at energies greater than 5 GeV for π^0 (22 GeV for η). Above 16 GeV for π^0 mesons and 60 GeV for η mesons the minimum opening angle is close to or smaller than the cell size [74], the two decay photons are too close to be resolved by the clusterization algorithm.

The neutral-cluster σ^2_{long} distributions as a function of the cluster p_{T} is shown in Fig. 4.2(a) for data, and the comparison with simulation distribution is presented in Fig. 4.2(b). Most of the pure single

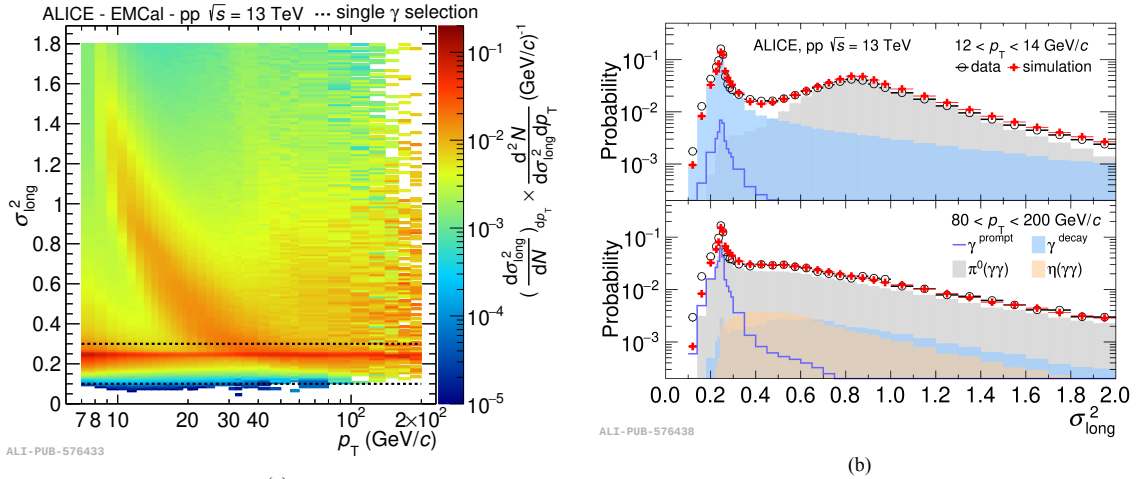

Figure 4.2: (a) Cluster shower shape distribution σ^2_{long} as a function of the cluster p_{T} in data. The dashed lines correspond to the upper and lower selection limit values for single photon candidate clusters used in the analysis. (b) Projected shower shape distribution in two p_{T} intervals in data (black circles) and simulation (red crosses, PYTHIA 8 jet–jet and γ–jet events). For the simulation, the σ^2_{long} distribution for clusters with different particle origins are also shown as shaded areas except for prompt photons from γ–jet PYTHIA 8 processes that are presented with a blue histogram line.

photons are reconstructed as clusters with $\sigma^2_{\text{long}} \approx 0.25$, other cases contribute to higher values, as seen in Fig. 4.2(b). Above the higher limit in σ^2_{long}, defined by the dashed line in Fig. 4.2(a), a clear p_{T}-dependent band is observed. This band is populated by two π^0-decay photons contributing to a single cluster as we explained before and can be deduced from Fig. 4.1. Figure 4.2(b) also shows different particle contributions to the shower shape distribution for two neutral-cluster p_{T} intervals in simulation. The dominant contributions to the narrow shower shape region are from single photons (at low p_{T}) or merged photons from neutral meson decays (at high p_{T}). Another more faint band appears in Fig. 4.2(a) for $p_{\text{T}} > 40$ GeV/c due to merged clusters from η meson decays, as it can be seen from the simulations reported on the lower panel of Fig. 4.2(b). The value of σ^2_{long} for merged photon clusters from meson decays decreases with increasing p_{T}, which leads to an almost full overlap of the π^0-decay photon band with the single photon shower band for about $p_{\text{T}} > 40$ GeV/c.

The lower limit at $\sigma^2_{\text{long}} = 0.1$ is set to clean the cluster sample from a few anomalous high-energy depositions that still pass the F_+ selection as it is shown in Fig. 4.3 where the correlation between σ^2_{long} and F_+ is shown. The σ^2_{long} as a function of the cluster energy is also shown when the $F_+ < 0.97$ selection is not applied, showing a clear exotic cluster population for $\sigma^2_{\text{long}} < 0.1$ that crosses over at high-p_{T} which can be further cleaned applying the condition on having clusters having cells in more than one T-Card as discussed in Sec. 3.5.3.

In this analysis, "photon candidates" refer to clusters with a narrow shape defined by $0.1 < \sigma^2_{\text{long}} <$

0.3.

Figure 4.4 shows a comparison of the σ^2_{long} distribution for the two upper and lower sections of the calorimeter, to check the common performance on the different areas of the detector, showing the agreement between them. Residual differences can be expected because of the different cross-talk in certain SM and the missing central region in the DCal calorimeter, but the distributions seem not to be significantly different.

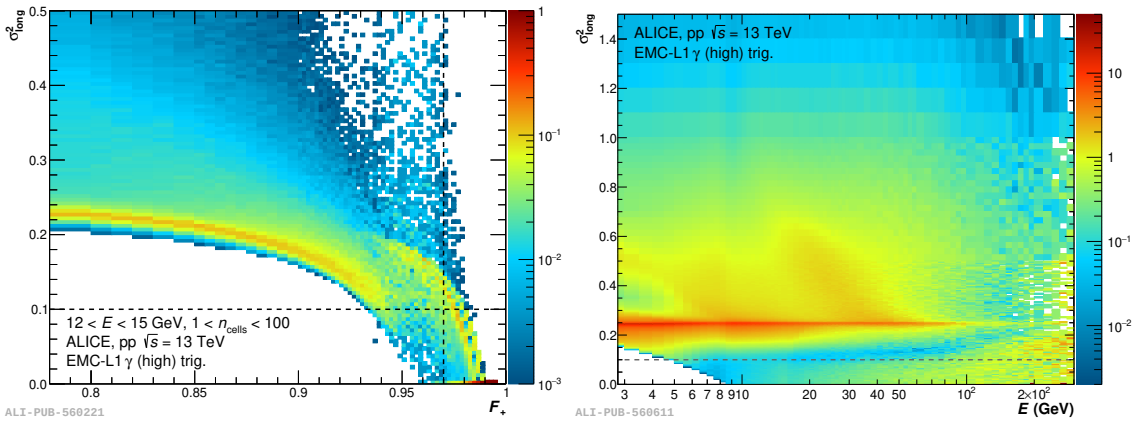

Figure 4.3: Left: σ^2_{long} as a function of the exoticity parameter F_+ for $12 < E < 15$ GeV. Right: σ^2_{long} as a function of the cluster energy when the selection $F_+ < 0.97$ is not applied. Both distributions are shown for pp collisions at $\sqrt{s} = 13$ TeV using the EMCal L1-γ-high trigger. The clusterization algorithm used splits merged clusters, for this reason, the π^0 merged band in the right figure is less prominent than in Fig. 4.2(a)). Dashed lines located at $\sigma^2_{\text{long}} = 0.1$ (both figures) and $F_+ = 0.97$ (left figure). Figures from Ref. [74].

4.2 Prompt photon identification via the isolation method

Direct prompt photons are mostly isolated, i.e. have no hadronic activity in their vicinity except for the underlying event of the collision, in contrast to other photon sources like photons from parton fragmentation or decays of hadrons which have a high probability to be accompanied by other fragments [33]. An isolation criterion is applied to the photon candidate to suppress the contribution by fragmentation and decay photon production. An equivalent isolation criterion is commonly included in theoretical calculations to account for the suppression of the fragmentation contribution to the total prompt photon cross section.

The isolation criterion is based on the so-called "isolation momentum" $p_{\text{T}}^{\text{iso}}$, i.e. the transverse momentum sum of all particles measured inside a cone of radius R around the photon candidate, located at η^γ and φ^γ. A particle of coordinates η and φ in angular space is inside the cone when

$$\sqrt{(\eta - \eta^\gamma)^2 + (\varphi - \varphi^\gamma)^2} < R. \tag{4.1}$$

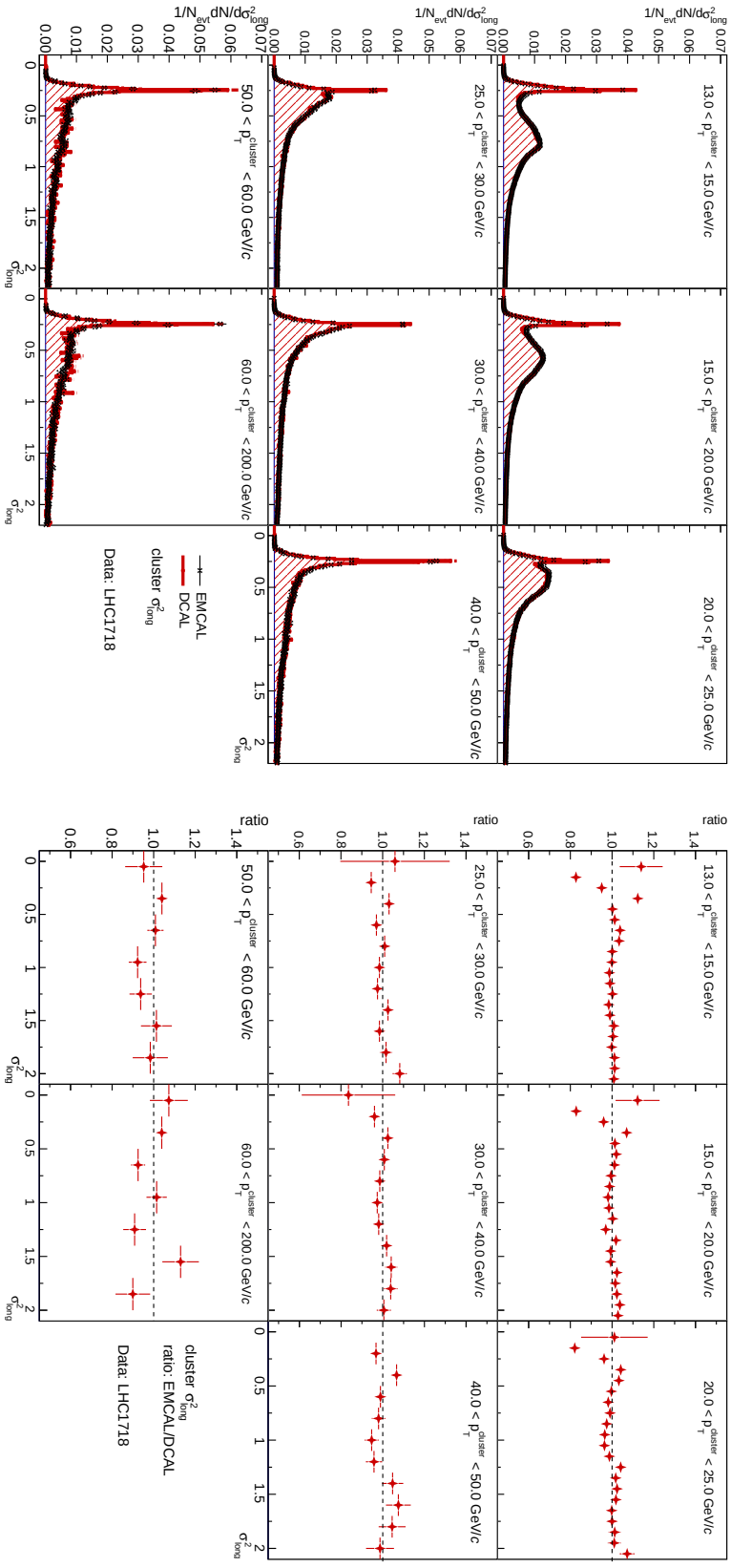

Figure 4.4: σ^2_{long} distribution for EMCal (black) and DCal (red) in different p_{T} range and its corresponding ratio EMCal/DCal in different photon cluster p_{T} bins.

The cone radius $R = 0.4$ is chosen as it contains the dominant fraction of the jet energy [94]. The isolation momentum is the sum of all the particles that fall into the cone excluding the trigger particle. Depending on the candidate-associated particle type in the isolation cone, there are three possibilities: only consider charged particles (tracks), only neutral particles (calorimeter clusters), and the sum of both. Also, one can consider estimating and removing the contribution from the underlying event energy density (ρ_{UE}), needed in Pb–Pb and p–Pb collisions, not so much in pp collisions as discussed below. Depending on the option used, we have different isolation momentum definitions:

$$\begin{aligned} p_{\mathrm{T}}^{\mathrm{iso,\ UE}} &= \sum p_{\mathrm{T}}^{\mathrm{cluster}} + \sum p_{\mathrm{T}}^{\mathrm{track}}, \text{used in pp measurement at } \sqrt{s} = 7 \text{ TeV [44]}; \\ p_{\mathrm{T}}^{\mathrm{iso,\ ch,\ UE}} &= \sum p_{\mathrm{T}}^{\mathrm{track}}, \text{ used in this analysis;} \\ p_{\mathrm{T}}^{\mathrm{iso,\ ch}} &= \sum p_{\mathrm{T}}^{\mathrm{track}} - \rho_{\mathrm{UE}} \cdot \pi \cdot R^2. \end{aligned} \tag{4.2}$$

The third option is used in pp, p–Pb and Pb–Pb measurements at $\sqrt{s_{\mathrm{NN}}} = 8$ and 5.02 TeV [51, 52, 95]. The tracks considered in this and all analyses are the same hybrid tracks used for the cluster-track association described in section 3.5.2.

Figure 4.5 shows the isolation energy density ρ_{UE} for pp collisions at $\sqrt{s} = 13$ TeV in data for different UE estimator methods described in [51, 95]. The density is found to be on average of the order of 1–1.5 GeV/(c rad), thus the correction to the $p_{\mathrm{T}}^{\mathrm{iso,\ ch,\ UE}}$ is smaller than 1 GeV/c on average. Therefore, it is considered that this subtraction is not strictly necessary and the same approach without UE subtraction as in the $\sqrt{s} = 7$ TeV measurement [44] but not adding the neutral energy, is considered in this analysis. Candidate clusters are considered isolated when $p_{\mathrm{T}}^{\mathrm{iso,\ ch,\ UE}} < 1.5$ GeV/c, equivalent to

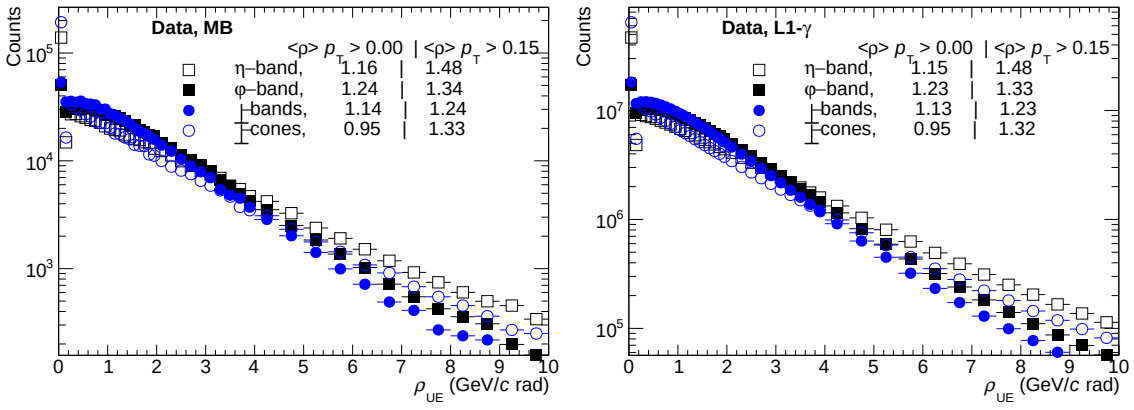

Figure 4.5: Isolation momentum density in the isolation cone for data MB (left) and L1-γ (right) triggers estimated with different methods described in [51, 95]. Neutral clusters $p_{\mathrm{T}} > 10$ GeV/c.

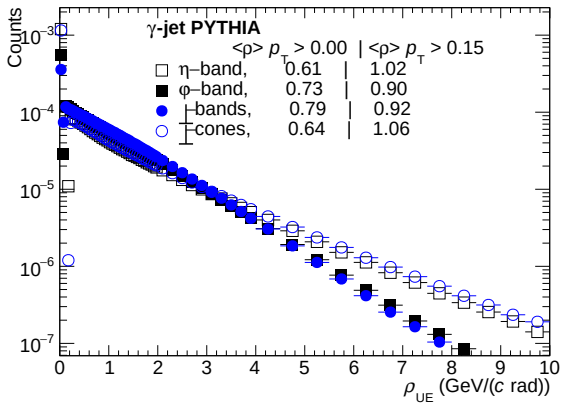

Figure 4.6: Isolation momentum density in the isolation cone for γ-jet simulation estimated with different methods described in [51, 95]. Neutral clusters $p_T > 10$ GeV/c.

the 2 GeV/c threshold used in the $\sqrt{s} = 7$ TeV measurement considering only charged particles in the cone. The ρ_{UE} distribution for signal γ-jet simulation is shown in Fig. 4.6, the mean of the distribution is smaller than in data.

Figure 4.7 shows the $p_T^{iso,\ ch,\ UE}$ distributions in data and MC. The agreement is not perfect, as observed in other pp collisions analyses in ALICE, but considered not an issue as discussed in Sec. 4.4.2. The comparison between EMCal and DCal trigger clusters in the isolation cone is shown in Fig. 4.8, to check the stability of the analysis in different regions. Thanks to the trigger masking work done for this analysis no significant difference was observed.

Figure 4.9 presents the cluster σ^2_{long} distribution that passes isolation cut between data and simulation with different cross-talk emulation parameters on the simulation like in Fig. 3.3. One can appreciate the suppression of the background tail and bump with respect to the photon peak due to the isolation cut comparing the two figures.

The fraction of narrow clusters isolated is shown in Fig. 4.10 for data and signal γ–jet simulation, a strong suppression of the narrow cluster yield is induced by the isolation in data, not as much in the signal simulation as expected. In data, the consideration or not of the UE subtraction in the isolation cone has an effect on this fraction of 10 to 25% decreasing the cluster p_T, without UE subtraction more clusters are rejected due to the random particles from the collision not originating in the hard process entering the cone. In the signal simulation, the effect is 4 to 8%.

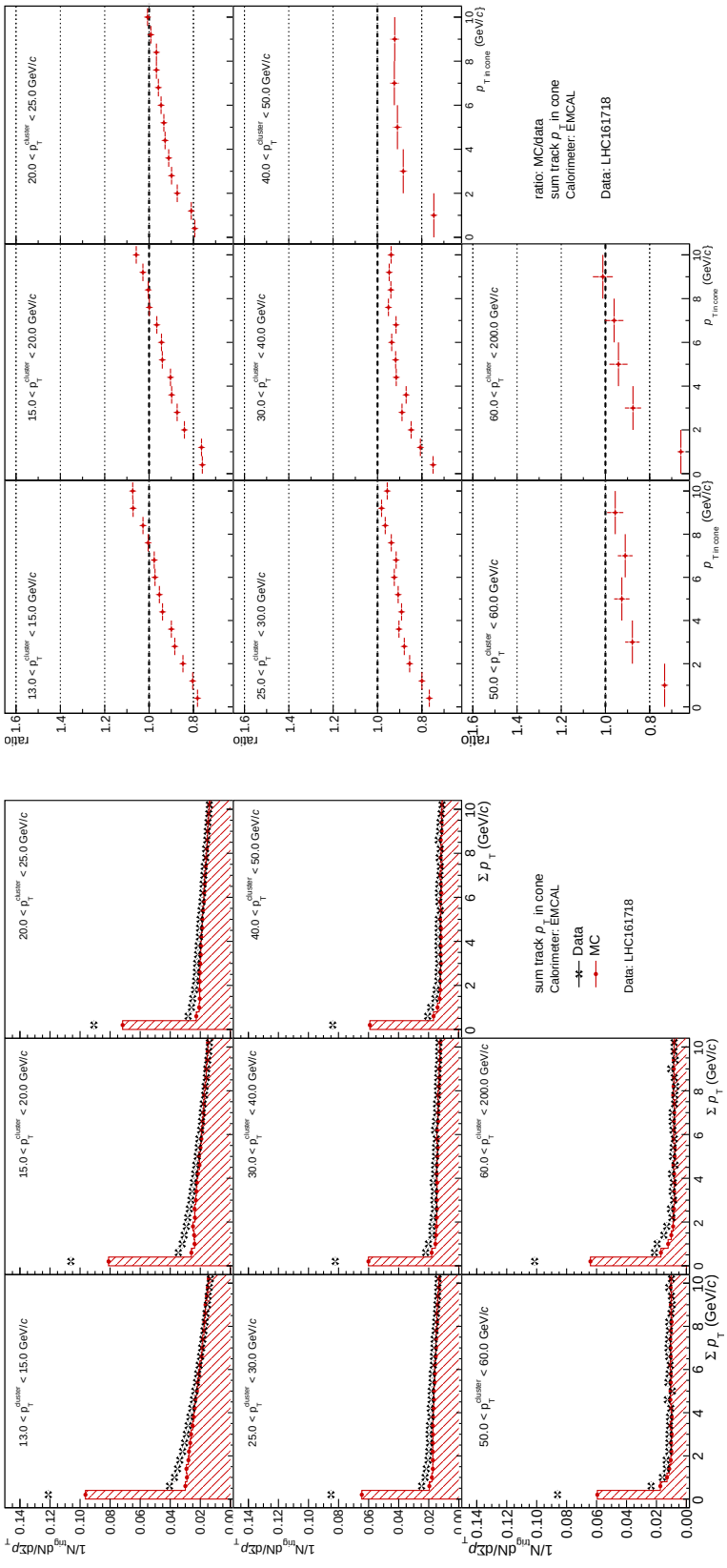

Figure 4.7: EMCal charge only $p_T^{iso,\,ch,\,UE}$ distribution between data (black) and MC (red), and the corresponding ratio MC/Data in different photon cluster p_T bins.

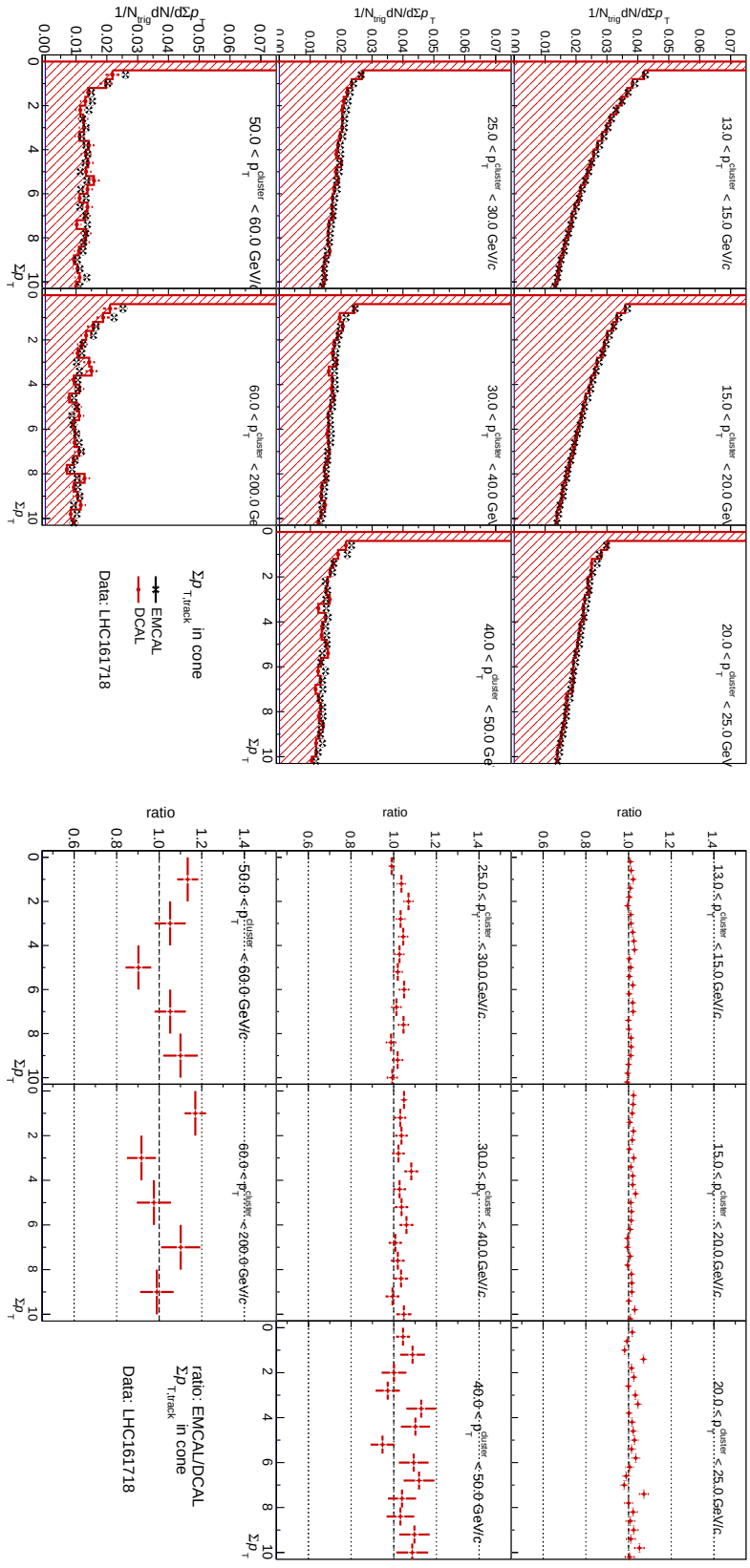

Figure 4.8: $p_{\mathrm{T}}^{\mathrm{iso,\ ch,\ UE}}$ distribution for EMCal (black) and DCal (red) in different p_{T} range and its corresponding ratio EMCal/ DCal in different photon cluster p_{T} bins.

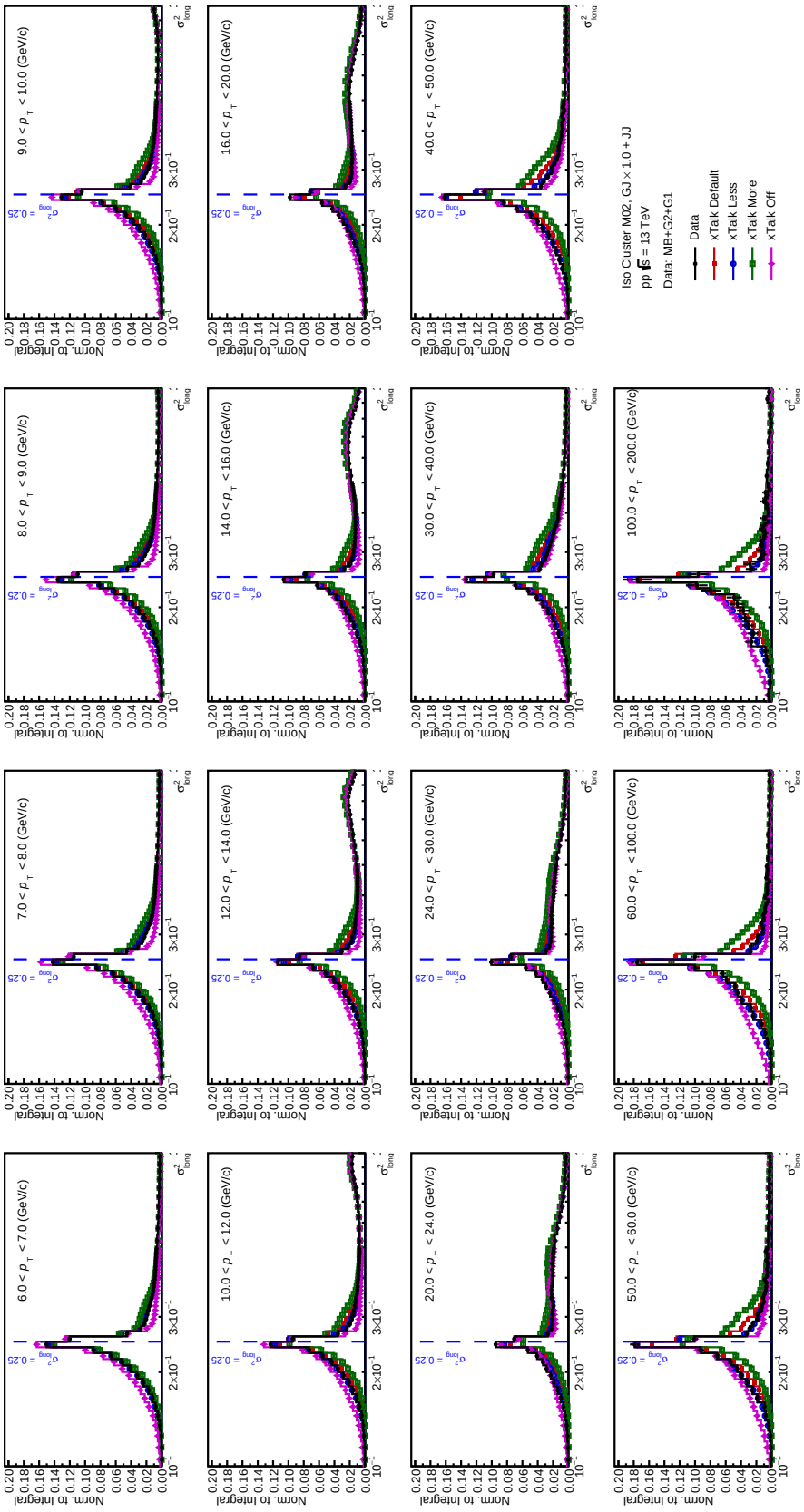

Figure 4.9: Isolated clusters ($p_{\mathrm{T}}^{\mathrm{iso,\,ch,\,UE}} < 1.5$ GeV/c, $R = 0.4$) σ^2_{long} distribution from data (black), pp collisions at $\sqrt{s} = 13$ TeV, or simulation, γ–jet + jet–jet PYTHIA processes, with different cross-talk (xTalk) emulation parameterizations (see Sec. 3.4.5 and Tab. 3.4) and in different cluster p_{T} bins. Distributions normalised to the number of entries on each histogram.

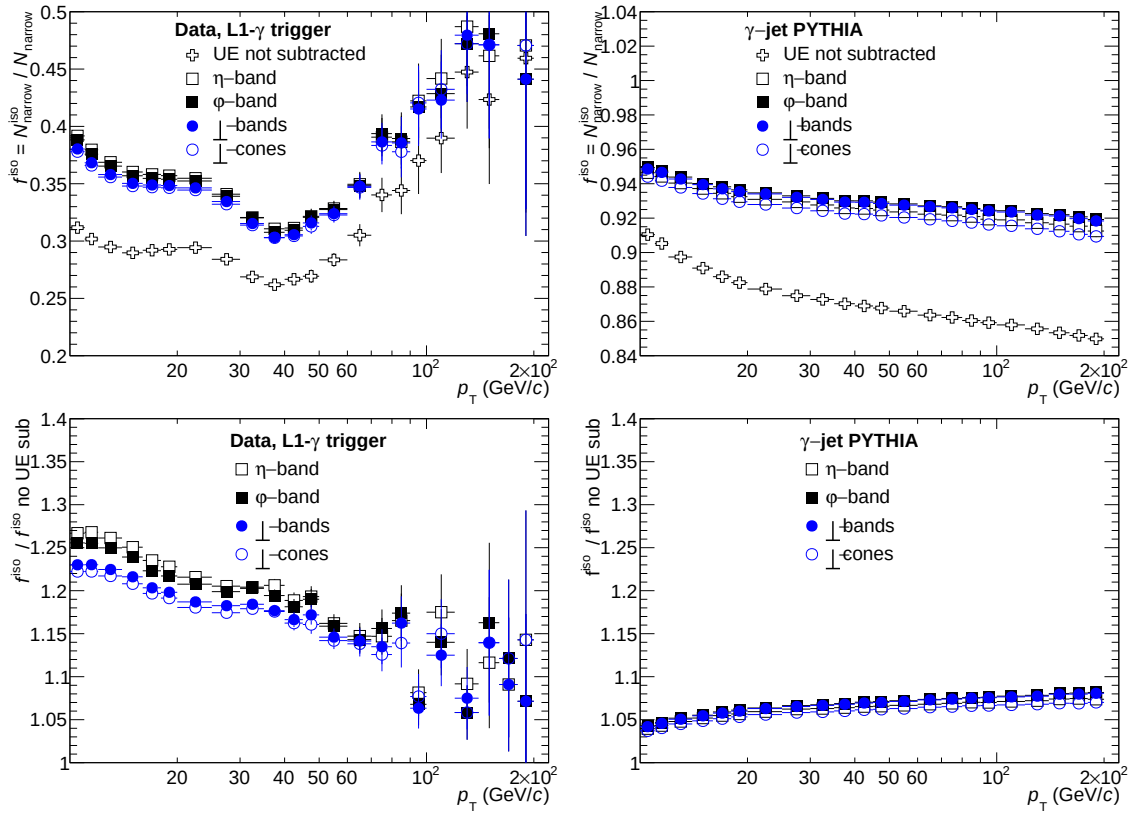

Figure 4.10: Top: Fraction of isolated-narrow clusters compared to the narrow clusters sample (f^{iso}) with and without UE subtraction, estimated with different methods described in [51, 95]. Bottom: Ratio of the f^{iso} for each UE subtraction method over no UE subtraction. Data L1-γ triggered sample (left) and γ–jet PYTHIA events (right).

The exotic cells (that are basically isolated and narrow) combined with the cross talk have a large impact at very high energies, their σ^2_{long} value increases and contributes to the photon band. For this reason, the rejection of clusters with energy larger than 80 GeV containing cells from only one T-Card was implemented, as discussed in Sec. 3.5.3. Figure 4.11 shows how many clusters survive this selection in EMCal-triggered higher threshold data. One can see that this selection has a significant impact above 140 GeV, less for neutral clusters, 15% at 160–200 GeV, but once the shower shape and/or the isolation criteria are used the rejection is stronger, up to 40% in the last p_T bin.

Figure 4.12 shows the cluster time distribution in different p_T bins for wide and narrow, isolated and not isolated clusters. One can see that the distribution is well centered at 0 and within the selection window at $|t| < 20$ ns and most of the peak is even within 10 ns. There seems to be some kind of plateau below the Gaussian distribution ending at $|t| < 25$–30 ns that might get more significant increasing the p_T, in particular for narrow clusters between 12 and 40 GeV, this could be due to remaining exotic clusters. Above 40 GeV, isolated-wide clusters have a significant wide distribution, which we cannot

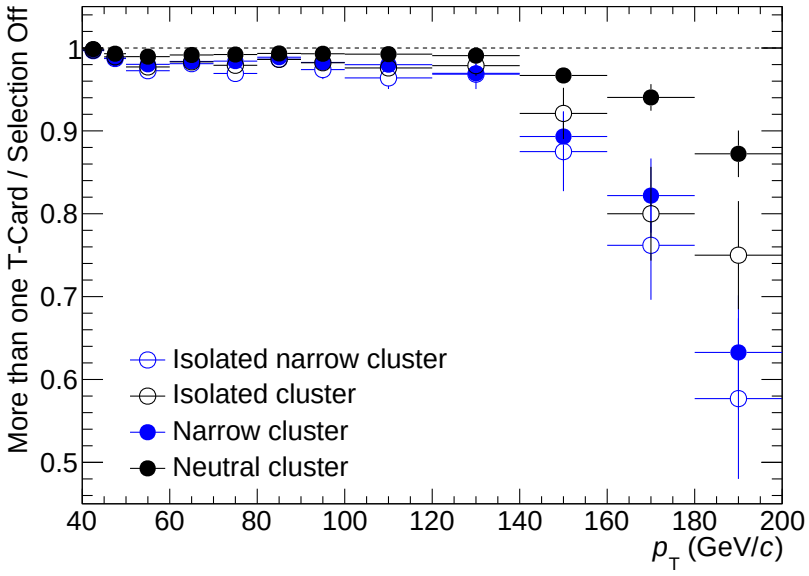

Figure 4.11: Fraction of clusters with cells in more than one T-Card for different cluster selection criteria: Neutral, Narrow, Isolated and Isolated Narrow. Data, L1-γ high threshold.

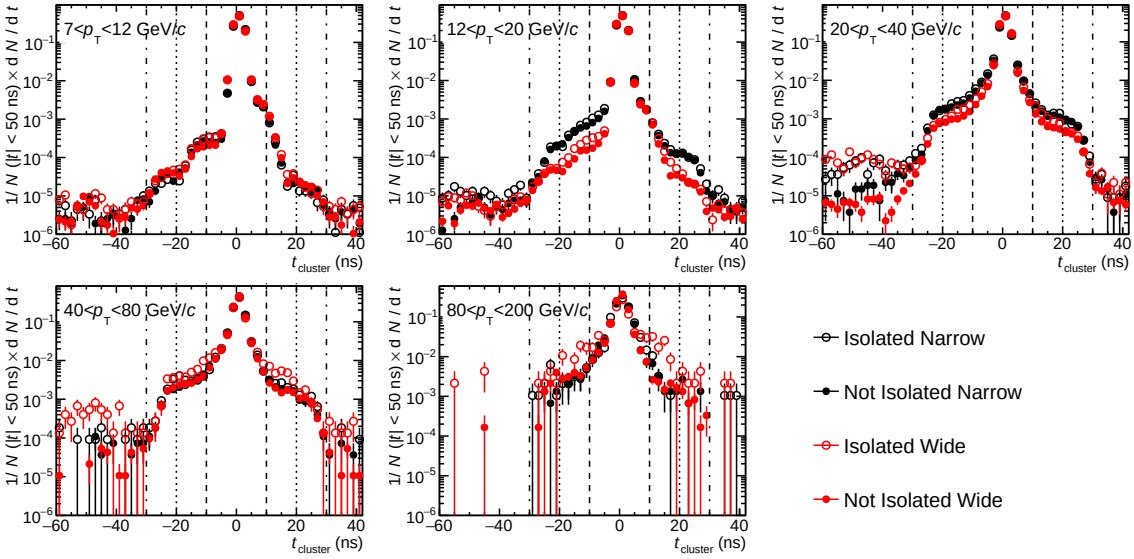

Figure 4.12: Cluster time distribution, for the different cluster types and different p_T bins in data. All triggers combined, first frame only MB+L1-γ-low triggers. Distributions normalized to the integral between -50 and 50 ns.

explain. Since this plateau seems significant, a variation of the time cut will be used as uncertainty, see Sec. 5.2.1.

With the shower shape and the isolation selection criteria applied, the raw isolated photon spectrum can be obtained for each triggered sample. The combination of the MB and triggered samples is done

with

$$\frac{1}{N_{\rm evt}}\frac{{\rm d}^2N_{\rm n}^{\rm iso}}{{\rm d}p_{\rm T}^{\gamma}\,{\rm d}\eta} = \frac{1}{\sum_i N_{\rm evt}^{i}\times RF^{{\rm trig},\,i}}\left(\sum_i \frac{{\rm d}^2N_{\rm n}^{{\rm iso},\,i}}{{\rm d}p_{\rm T}^{\gamma}\,{\rm d}\eta}\times\frac{1}{\varepsilon_{\rm trig}^{{\rm iso},\,i}}\right) \tag{4.3}$$

where $RF^{\rm trig}$ and $\varepsilon_{\rm trig}^{\rm iso}$ were described in Sec. 3.6.3 and Sec. 3.6.4, the $N_{\rm evt}$ is the number of selected events, i is an index depending on the data trigger, and $N_{\rm n}^{\rm iso}$ is the number of isolated and narrow clusters. For the MB sample, the $RF^{\rm trig}$ and $\varepsilon_{\rm trig}^{\rm iso}$ are 1. Due to the trigger thresholds, we can only combine the triggered samples in their available interval. In this analysis, the combined sample is taken from the MB and G2 triggered samples when $7 < p_{\rm T} < 12$ GeV/c, and all samples (MB, G2 triggered, and G1 triggered) are combined above 12 GeV/c. The spectrum distribution for each normalized sample and the combined spectrum of the three triggers are shown in the top panel of Fig. 4.13, and the ratio of each of the normalized spectra to the combined is at the bottom panel, one can see that the ratios are compatible with unity. The final cross section will be obtained by correcting the combined spectra of Fig. 4.13 top with the efficiency and purity discussed in the following sections.

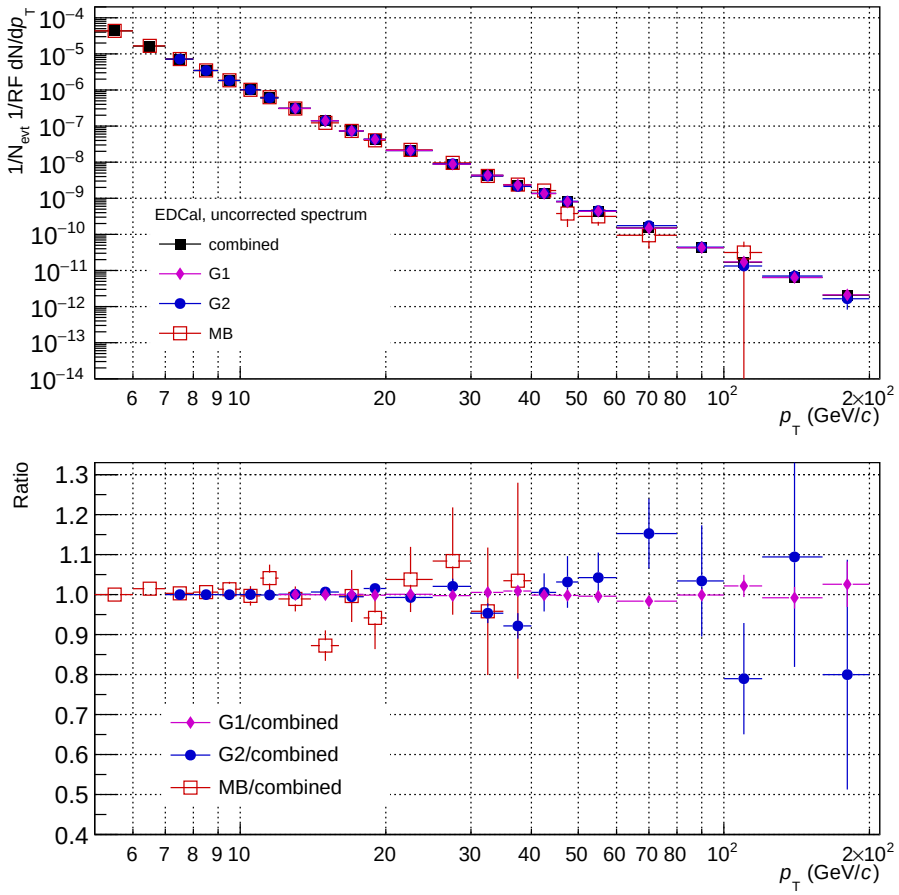

Figure 4.13: Top, raw cluster spectrum after $RF^{\rm trig}$ normalization for each trigger sample. Bottom, ratio of each trigger spectra of the top plot to the combined spectrum.

4.3 Efficiency

Due to detector performances, not all photons can be measured, and some are lost in the various selection steps during the reconstruction, identification, and isolation criteria. One has to evaluate the so-called "efficiency" to reconstruct and identify such particles. This can be achieved through the use of PYTHIA8 [79, 80, 96] γ-jet simulations, which are employed to reproduce the signal of interest. The number of measured isolated photons is then compared to the number of those which were originally generated within the acceptance of the analysis. This accounts for potential acceptance losses due to masked or dead regions in EMCal where isolated photons can be reconstructed and detector resolution effects. We define, therefore, a global efficiency $\varepsilon_{\gamma}^{\mathrm{iso}}$ for this analysis used to correct the spectra as:

$$\varepsilon_{\gamma}^{\mathrm{iso}} = \frac{\mathrm{d}\, N_{\gamma_{\mathrm{iso}}}^{\mathrm{rec}}}{\mathrm{d}\, p_{\mathrm{T}}^{\mathrm{rec}}} \Big/ \frac{\mathrm{d}\, N_{\gamma_{\mathrm{iso}}}^{\mathrm{gen}}}{\mathrm{d}\, p_{\mathrm{T}}^{\mathrm{gen}}} \tag{4.4}$$

the $\mathrm{d}N_{\gamma_{\mathrm{iso}}}^{x}/\mathrm{d}p_{\mathrm{T}}^{x}$ in the equation represent the reconstructed (x = rec) or generated (x = gen) isolated photon p_{T} distribution. The different analysis selection criteria determine the overall efficiency of the analysis. They are calculated as the ratio of spectra, where the denominator is the number of generated photons $\mathrm{d}N_{\gamma}^{\mathrm{gen}}/\mathrm{d}p_{\mathrm{T}}^{\mathrm{gen}}$, and the factors in the numerator are the reconstructed spectra after different selection criteria, $\mathrm{d}N_{\mathrm{cut}}^{\mathrm{rec}}/\mathrm{d}p_{\mathrm{T}}^{\mathrm{rec}}$. Then the efficiency in this analysis can be calculated as:

$$\varepsilon_{\gamma}^{\mathrm{iso}} = \frac{\mathrm{d}N_{\mathrm{n,\,iso}}^{\mathrm{rec}}}{\mathrm{d}p_{\mathrm{T}}^{\mathrm{rec}}} \Bigg/ \frac{\mathrm{d}N_{\gamma,\,\mathrm{iso}}^{\mathrm{gen}}}{\mathrm{d}p_{\mathrm{T}}^{\mathrm{gen}}} \equiv \frac{\varepsilon^{\mathrm{rec}} \times \varepsilon^{\mathrm{id}} \times \varepsilon^{\mathrm{iso}}}{\kappa^{\mathrm{iso}}}, \tag{4.5}$$

where each factor is:

- $\varepsilon^{\mathrm{rec}}$: the fraction of neutral clusters that can be reconstructed;
- $\varepsilon^{\mathrm{id}}$: the fraction of clusters that satisfy the photon identification (shower shape selection);
- $\varepsilon^{\mathrm{iso}}$: the fraction of photon candidates passing the isolation cut;
- κ^{iso}: the fraction of generated photons that satisfy the isolation selection criteria.

Figure 4.14 presents the efficiency decomposed into the different listed categories. It can be observed that the pure reconstruction efficiency of photons, $\varepsilon^{\mathrm{rec}}$, is approximately 50% (green squares). This efficiency loss is primarily due to excluded regions in the calorimeter, particularly the requirement of $d_{\mathrm{mask}} > 2$ and the exclusion of clusters in close proximity to the border of EMCal supermodules. The efficiency is reduced by 10–20% as a consequence of the photon identification (shower shape selection), resulting in an efficiency, $\varepsilon^{\mathrm{rec}} \times \varepsilon^{\mathrm{id}}$ of approximately 35–45% (red crosses). Furthermore, the efficiency is also decreased by the isolation criterion, reaching an efficiency, $\varepsilon^{\mathrm{rec}} \times \varepsilon^{\mathrm{id}} \times \varepsilon^{\mathrm{iso}} \approx$ 30–40% (blue diamonds). In addition, the black-filled circle in the figure depicts the efficiency at the generator level called κ^{iso}. A dedicated discussion on this fraction can be found at the end of this section.

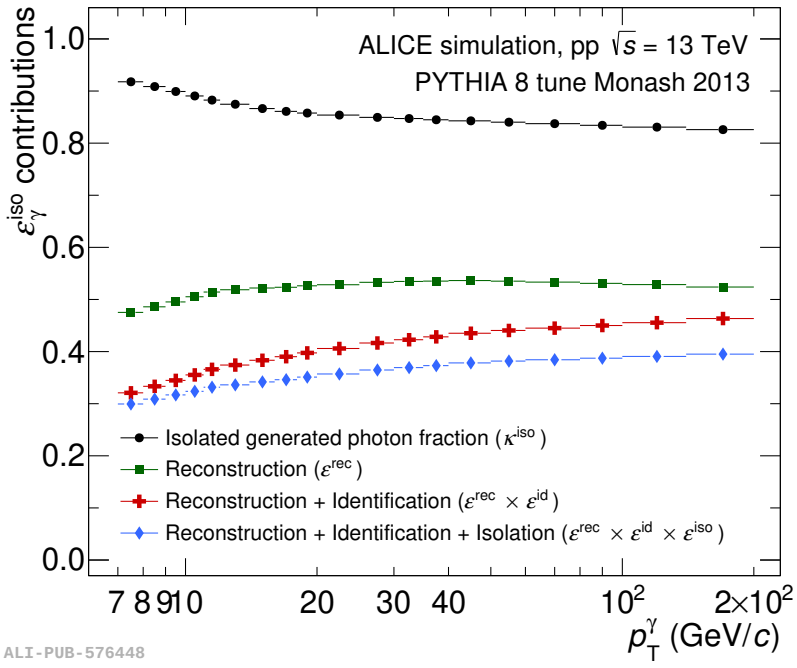

Figure 4.14: Efficiency for prompt photon clusters generated with PYTHIA8 γ–jet simulation depending on the selection cuts chain: only reconstructed neutral clusters (green), plus shower shape cut of $0.1 < \sigma^2_{\text{long}} < 0.3$ (red), and plus the isolation cut (blue). Black points correspond to the fraction of generated photons that pass the isolation cut at the generator level.

The total isolated-photon efficiency as a function of the reconstructed p_{T}^{γ} is shown in Fig. 4.15. One can see that the efficiency is p_{T} dependent due to the σ^2_{long} selection because the photon peak is wider at lower p_{T}, as shown in Fig. 4.2(b) in Sec. 4.1.

The isolation fraction at the generator level, κ^{iso}, accounts for the effect of the underlying event of the collision (UE) in the isolation cone. This can be seen in Fig. 4.16 where this efficiency is calculated with different PYTHIA options, with and without the activation in PYTHIA of MPI (multiple parton interactions, related to UE) and FSR/ISR (initial or final state radiation) processes. From the plots, we can observe that most of this efficiency not being at unity is due to the MPI processes, while FSR/ISR have about a 3% effect at 200 GeV/c smaller than 1% below 20 GeV/c when the MPI option is off. This factor is used in the cross-section definition Eq. (4.23) in Sec. 4.6 to correct for the UE bias in the measurement and be able to compare to other $\sqrt{s}$ measurements and theoretical calculations that do not include such UE contribution, neglecting any possible bias introduced by the remaining ISR/FSR processes that might also be included on NLO calculations.

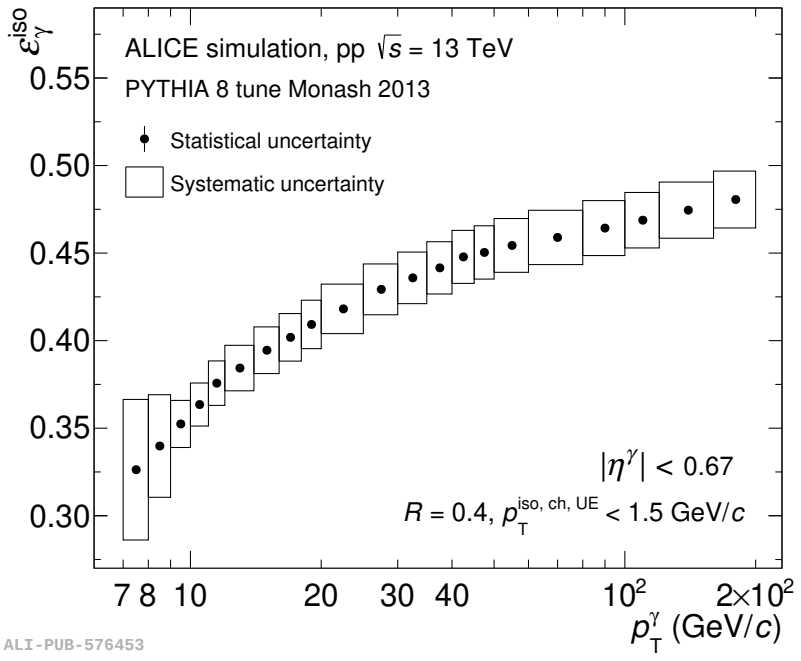

Figure 4.15: The total isolated-photon efficiency as a function of the reconstructed p_{T}^{γ}. The systematic uncertainty shown as boxes in the plot has been obtained from the "no MC tuning" uncertainty source related to the cross-talk emulation discussed in Sec. 5.

Figure 4.17 shows the κ^{iso} for different $\sqrt{s}$, one can appreciate that this efficiency is closer to unity for the smaller $\sqrt{s}$, in principle due to the lower UE. Also, this figure shows the effect of removing the UE from the cone event by event [87], the value of κ^{iso} is reduced significantly for $\sqrt{s}$ = 13 TeV, almost no effect for $\sqrt{s}$ = 5.02 TeV.

In other isolated photon measurements, in particular those in p–Pb and Pb–Pb collisions, the UE is significant and must be removed when calculating $p_{\mathrm{T}}^{\mathrm{iso,\,ch}}$. This is not strictly necessary in pp collisions measurements, since we found the UE contribution was on average below the isolation threshold in Fig. 4.5. In Fig. 4.17 we can see the effect of the removal of the UE in the κ^{iso}, it gets closer to unity moving from 85% to 92% at 20 GeV. The remaining difference from unity comes from estimation UE fluctuations and FSR/ISR effects.

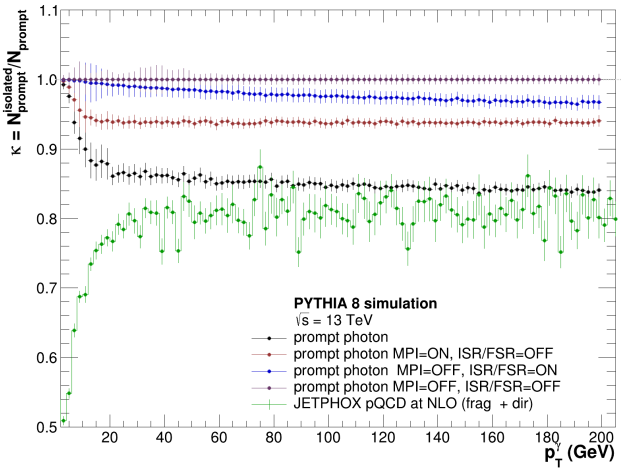

Figure 4.16: Prompt photon isolation efficiency at the generator level changing in PYTHIA the activation of MPI and FSR/ISR processes. Kindly produced by Florian Jonas.

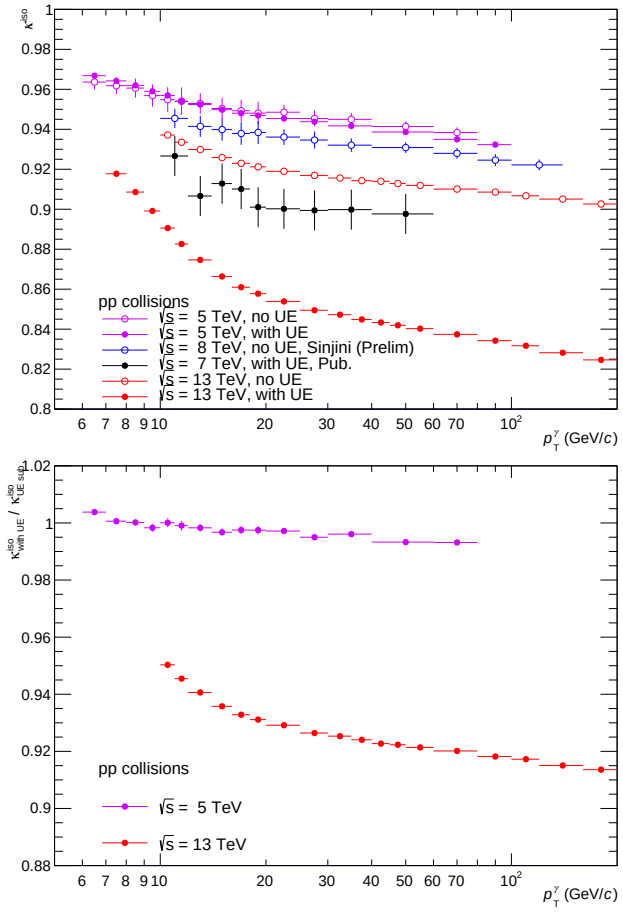

Figure 4.17: Top: Isolation efficiency κ^{iso} at the generator level in PYTHIA for different collision energies: $\sqrt{s}$ = 5.02 [87], 7 [44], 8 [97, 98], and 13 TeV, and removing event-by-event the UE for $\sqrt{s}$ = 5, 8 and 13 TeV. The UE is removed event by event estimating the particle energy density in an η-band out of the isolation cone ($\sqrt{s}$ = 5 and 13 TeV) or perpendicular cones ($\sqrt{s}$ = 8 TeV). Bottom: Ratio of the κ^{iso} removing over not removing the UE.

4.4 Purity

The isolated photon purity, P, is defined as the ratio of reconstructed isolated photons that were actually signal photons over all the candidate photons after the different selection criteria are applied. As the number of reconstructed isolated photons still has a non-negligible contribution from background clusters, mainly from neutral-meson decay photons, a good estimation of the purity of the selected cluster sample is crucial.

4.4.1 The ABCD method

The ABCD purity calculation method has been used in several publications, such as the measurement of isolated prompt production in pp collisions at $\sqrt{s}$ = 7 TeV by ATLAS [39, 40], CMS [42] and ALICE [44], the measurement in pp and Pb-Pb collisions at $\sqrt{s_{\rm NN}}$ = 5.02 TeV by ALICE [51, 95]. It creates a phase space based on the momentum measured inside the isolation cone, $p_{\rm T}^{\rm iso,\ ch,\ UE}$, and on the cluster shower shape, $\sigma^2_{\rm long}$. Depending on the signal selection analysis cuts ($p_{\rm T}^{\rm iso,\ ch,\ UE} < 1.5$ GeV/c and $0.1 < \sigma^2_{\rm long} < 0.3$), the phase space can be divided into 4 regions (𝔸, 𝔹, ℂ, and 𝔻), as shown in Fig. 4.18.

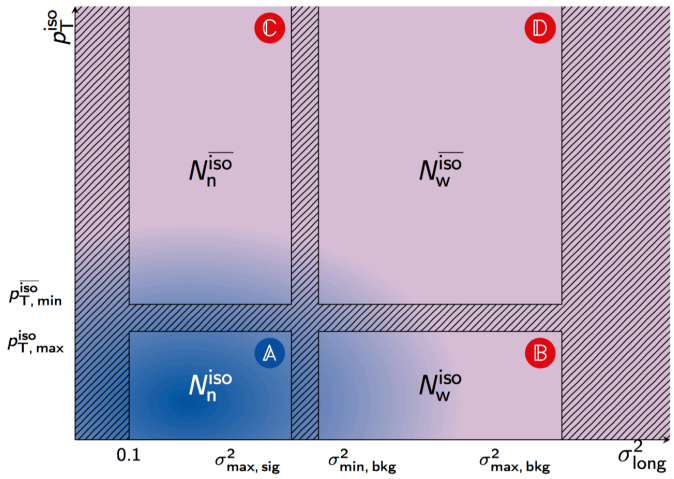

Figure 4.18: Visualization of the ($p_{\rm T}^{\rm iso,\ ch,\ UE}$ and $\sigma^2_{\rm long}$) phase space used to calculate the purity of the selected isolated photon clusters.

Each region is populated by clusters from different origins:

- 𝔸: the isolated and narrow (i.e. circular) cluster which corresponds to where most of our signal is present, denoted by $N_{\rm n}^{\rm iso}$;
- 𝔹: the isolated and wide (i.e. elliptic) clusters, denoted by $N_{\rm w}^{\rm iso}$, containing mostly background;
- ℂ: the anti-isolated and narrow clusters, denoted by $N_{\rm n}^{\overline{\rm iso}}$, containing mostly background ;

- $\mathbb{D}$: the anti-isolated and wide clusters, denoted by $N_{\mathrm{w}}^{\overline{\mathrm{iso}}}$, containing mostly background.

Therefore, region $\mathbb{A}$ is referred to as the signal region and regions $\mathbb{B}$, $\mathbb{C}$ and $\mathbb{D}$ are called the background regions. The background regions ($\mathbb{B}$, $\mathbb{C}$ and $\mathbb{D}$) are separated from the signal region ($\mathbb{A}$) by a gap in terms of $p_{\mathrm{T}}^{\mathrm{iso,\ ch,\ UE}}$ and σ^2_{long} (hatched cross area). This is intended to avoid edge effects in the measurement of each population, and any signal leakage into the background regions. We define an anti-isolation cut at $p_{\mathrm{T}}^{\mathrm{iso,\ ch,\ UE}} = 2.5$ GeV/c, above which a cluster belongs to regions $\mathbb{C}$ or $\mathbb{D}$, as well as a background shower shape lower cut $\sigma^2_{\mathrm{long}} = 0.4$, above which a cluster is part of regions $\mathbb{B}$ or $\mathbb{D}$. Note that an upper limit ($\sigma^2_{\mathrm{long}} = 2.4$, $p_{\mathrm{T}}^{\mathrm{iso,\ ch,\ UE}} = 10$ GeV/c) is also set for these regions to exclude regions not well reproduced by the simulation. In addition, having a gap between the different regions allowed us to vary the corresponding values to determine the associated systematic uncertainties in the purity and cross section measurements, as explained in Sec. 5.

As explained, there is a background in the signal region, e.g. induced by neutral mesons decay photons, which counts as contamination to the signal. One cannot directly use this region total population $N_{\mathrm{n}}^{\mathrm{iso}}$ as the isolated photon pure signal but has to consider this population as follows:

$$N_{\mathrm{n}}^{\mathrm{iso}} = S_{\mathrm{n}}^{\mathrm{iso}} + B_{\mathrm{n}}^{\mathrm{iso}} \tag{4.6}$$

where $S_{\mathrm{n}}^{\mathrm{iso}}$ is the direct photon signal we want to extract and $B_{\mathrm{n}}^{\mathrm{iso}}$ is the background cluster population in region $\mathbb{A}$. The ABCD method's main interest is to evaluate $B_{\mathrm{n}}^{\mathrm{iso}}$ in a data-driven way. Thus, we introduce the contamination term C, which is defined as

$$C = \frac{B_{\mathrm{n}}^{\mathrm{iso}}}{N_{\mathrm{n}}^{\mathrm{iso}}}. \tag{4.7}$$

The isolated photon purity is then

$$P \equiv 1 - C = 1 - \frac{B_{\mathrm{n}}^{\mathrm{iso}}}{N_{\mathrm{n}}^{\mathrm{iso}}}. \tag{4.8}$$

The determination of the $B_{\mathrm{n}}^{\mathrm{iso}}$ background contribution is based on two strong hypotheses on the properties of clusters in background regions $\mathbb{B}$, $\mathbb{C}$, and $\mathbb{D}$:

1. Direct photons negligibly contribute to background regions. In such cases:

$$N_{\mathrm{w}}^{\mathrm{iso}} = B_{\mathrm{w}}^{\mathrm{iso}},\ N_{\mathrm{n}}^{\overline{\mathrm{iso}}} = B_{n}^{\overline{\mathrm{iso}}},\ \text{and}\ N_{\mathrm{w}}^{\overline{iso}} = B_{\mathrm{w}}^{\overline{\mathrm{iso}}}; \tag{4.9}$$

2. Clusters induced by background particles have the same probability of passing the isolation threshold $p_{\mathrm{T,\ max}}^{\mathrm{iso,\ ch,\ UE}}$ whether they have a narrow (low σ^2_{long} values, regions $\mathbb{A}$ and $\mathbb{C}$) or a wide (high σ^2_{long} values, regions $\mathbb{B}$ and $\mathbb{D}$) shape; this hypothesis mathematically translates into the following

$$\frac{B_{\mathrm{n}}^{\mathrm{iso}}}{B_{\mathrm{n}}^{\overline{\mathrm{iso}}}} = \frac{B_{\mathrm{w}}^{\mathrm{iso}}}{B_{\mathrm{w}}^{\overline{\mathrm{iso}}}}. \tag{4.10}$$

By Eq. (4.10), we can have the background contribution $B_{\mathrm{n}}^{\mathrm{iso}}$ in the signal region, and then in combination with Eq. (4.9), $B_{\mathrm{n}}^{\mathrm{iso}}$ can be calculated as

$$B_{\mathrm{n}}^{\mathrm{iso}} = \frac{N_{\mathrm{w}}^{\mathrm{iso}}}{N_{\mathrm{w}}^{\overline{\mathrm{iso}}}} \times N_{\mathrm{n}}^{\overline{\mathrm{iso}}}. \tag{4.11}$$

Substituting this formulation into Eq. (4.8) gives the expression for the data-driven (dd) isolated photon purity we want to estimate, denoted as

$$P_{\mathrm{dd}} = 1 - \frac{N_{\mathrm{w}}^{\mathrm{iso}} \times N_{\mathrm{n}}^{\overline{\mathrm{iso}}}}{N_{\mathrm{w}}^{\overline{\mathrm{iso}}} \times N_{\mathrm{n}}^{\mathrm{iso}}}. \tag{4.12}$$

Figure 4.19 shows the isolated-photon purity by the data-driven method. The purity exhibits an increasing trend with the isolated photon p_{T}, from about 0.2 at $p_{\mathrm{T}} = 10$ GeV/c to 0.75 at $p_{\mathrm{T}} = 80$ GeV/c.

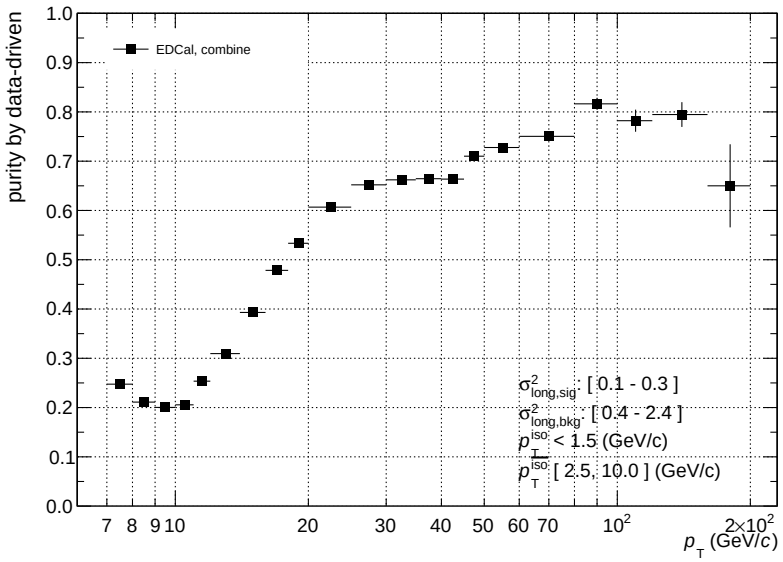

Figure 4.19: Isolated-photon purity by the data-driven method defined in Eq. (4.12) as a function of the photon p_{T}.

The ABCD method would allow the extraction of the purity in a purely data-driven way if the assumptions were exactly true. We can test at the MC level, whether the hypotheses hold via the double ratio in MC

$$\alpha_{\mathrm{MC}} = \left(\frac{B_{\mathrm{n}}^{\mathrm{iso}} / N_{\mathrm{n}}^{\overline{\mathrm{iso}}}}{N_{\mathrm{w}}^{\mathrm{iso}} / N_{\mathrm{w}}^{\overline{\mathrm{iso}}}} \right)_{\mathrm{MC=GJ+JJ}}, \tag{4.13}$$

where the MC simulation is a combination of the γ–jet (S) and jet–jet (B) PYTHIA simulations. If α_{MC} is not at unity, the hypotheses do not hold. This term is called the MC correction factor.

Figure 4.20 shows the α_{MC} distribution as a function of p_{T}. The figure shows that the α_{MC} is

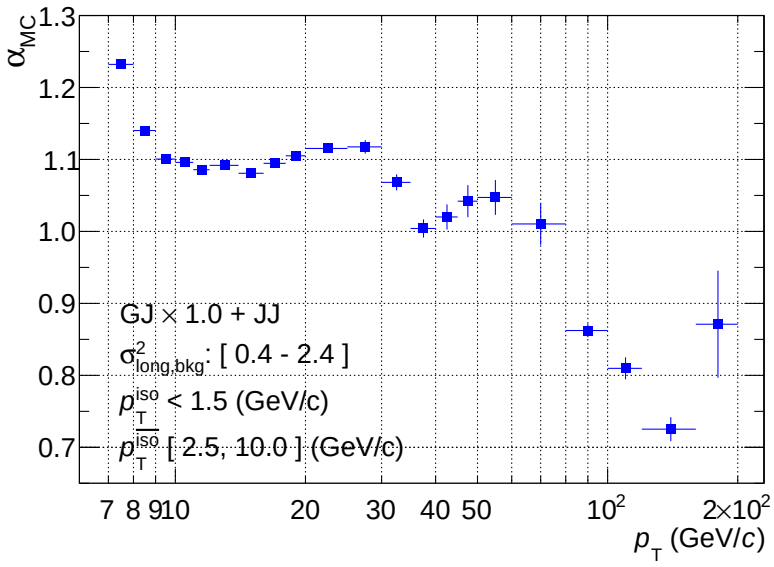

Figure 4.20: Purity MC correction factor as a function of the photon energy.

lower (greater) than unity at low (high) p_T, proving that the background estimation in region 𝔸 is not in agreement with the real background from γ–jet + jet–jet in PYTHIA8 simulation. Thus, the purity estimation method needs to be corrected because the two hypotheses are not entirely correct. Among the two hypotheses, the second one given by Eq. (4.10) is primarily responsible for the need for correction in this method.

Since these deviations from unity are purely due to particle kinematics and detector response, the simulation can be used to estimate the bias considering that

$$\left(\frac{B_n^{iso}/B_n^{\overline{iso}}}{B_w^{iso}/B_w^{\overline{iso}}}\right)_{data} = \left(\frac{B_n^{iso}/B_n^{\overline{iso}}}{B_w^{iso}/B_w^{\overline{iso}}}\right)_{MC}. \tag{4.14}$$

Weighting the contamination term in the purity calculation formula by the α_{MC}, the expression of the corrected isolated-photon purity P becomes

$$\begin{aligned} P &= 1 - \left(\frac{N_w^{iso}\times N_n^{\overline{iso}}}{N_w^{\overline{iso}}\times N_n^{iso}}\right)_{data} \times \alpha_{MC} \\ &= 1 - \left(\frac{N_w^{iso}\times N_n^{\overline{iso}}}{N_w^{\overline{iso}}\times N_n^{iso}}\right)_{data} \times \left(\frac{B_n^{iso}/N_n^{\overline{iso}}}{N_w^{iso}/N_w^{\overline{iso}}}\right)_{MC}. \end{aligned} \tag{4.15}$$

Figure 4.21 presents the corrected purity distribution, showing one strong rise till 20 GeV/c a plateau till 40–50 GeV/c, and then, another rise till 80–100 GeV/c, and finally, another plateau. The p_T^γ dependence of the purity is caused by an interplay of physics and detector effects. Most of the contamination

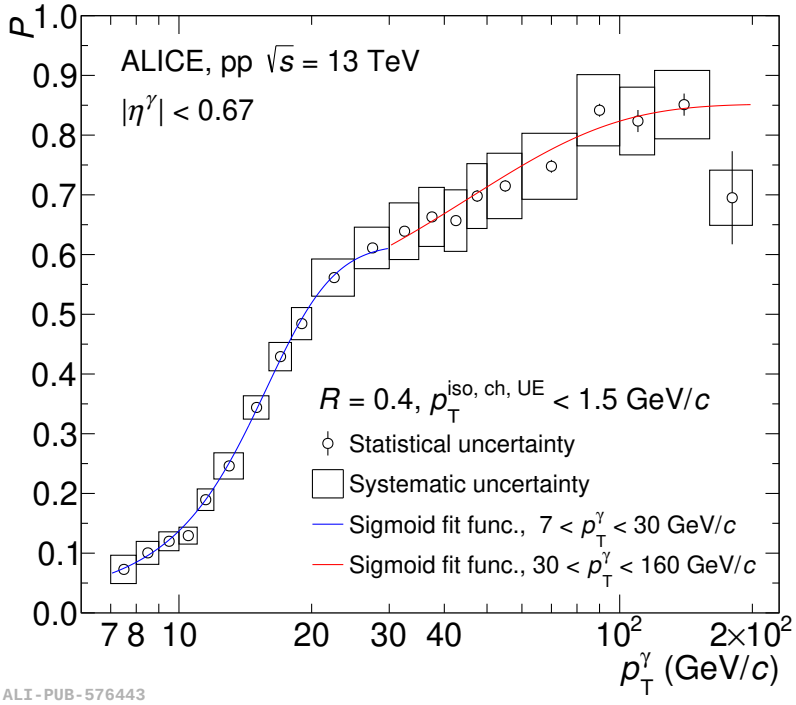

Figure 4.21: Purity of the isolated-photon sample as a function of p_{T}^{γ} calculated using Eq. (4.15). The statistical and systematic uncertainties have been evaluated as discussed in Sec. 5. The red and blue lines are the results of a fit to the measured purity using a two-sigmoid-function described by Eq. (4.19) for two different transverse momentum intervals.

is due to π^0-decay photons. On the one hand, the p_{T} spectra of prompt photons are harder than those of neutral pions, mainly because the latter undergo fragmentation, as also was found in pQCD calculations [30, 84]. For this reason, the $N_{\gamma_{2\to2}}/N_{\gamma(\pi^0)}$ yield ratio rises with p_{T}^{γ}, and the photon purity increases as well. Also, the probability of tagging a photon as isolated varies with p_{T}^{γ}. At higher decay-photon p_{T}^{γ}, isolation is less probable for a fixed isolation momentum. On the other hand, the rejection of clusters from π^0 and η decays at high p_{T} becomes less effective due to the decreasing decay-photon opening angle when increasing the meson p_{T}. Below 18 GeV/c, the contamination is dominated by single (i.e. unmerged) decay photons from π^0 mesons, the remaining contributors being mainly photons from η meson decays. Above 18 GeV/c, a large fraction of the $\pi^0 \to \gamma\gamma$ decays produces two photons with narrow opening angle and gives rise to merged clusters in the EMCal with a narrow shower shape that satisfies the condition for the single photon signal, as can be appreciated in Fig. 4.2(a). In the PYTHIA 8 jet–jet simulations, at p_{T} = 14–16 GeV/c approximately 6% of reconstructed clusters in the narrow shower shape region come from π^0 clusters, then at p_{T} = 20–25 GeV/c, they are more than 30% and above 60 GeV/c this contribution rises to about 80%. The clusters produced by merged photons from η-meson decays contribute to the narrow shower shape region for $p_{\mathrm{T}} > 60$ GeV/c but these remain subdominant compared to merged π^0-decay clusters. Instead, in the range $40 < p_{\mathrm{T}} < 60$ GeV/c, most

of the merged η-decay clusters have wide shower shapes, which is in part the reason for the increase of purity in this p_{T}^{γ} region since the contribution of single photon clusters from η decays to the narrow clusters decreases. The combined effect of these mechanisms leads to the rise of the purity at low p_{T}, saturation for $18 < p_{\mathrm{T}}^{\gamma} < 40$ GeV/c, then rise above 40 GeV/c, and finally, saturation above 80 GeV/c.

To support this, we checked at the simulation level what is the expected shape of the purity distribution even if the physics in PYTHIA is not exactly the same as in the data but close enough. We calculated the purity as the ratio of the isolated narrow clusters from signal (γ–jet) over signal+background (γ–jet + jet–jet). Figure 4.22 presents the purity in the simulation for clusters with different isolation and shower shape selections from tight to completely open. As illustrated in the figure, the purity continues to increase even in a very open shower shape cut, and the shower shape effectively removes the background from 6 to 40 GeV/c, above 40 GeV/c it does not cut much. Isolation criteria enhance the purity in comparison to the open cut parameter. Therefore, the shape of purity distribution depends on the shower shape rejection power and spectra shape.

Since π^0 is the main background we wanted to check what happens if we remove the other sources and distinguish between merged and unmerged photon decay clusters as shown in Figs. 4.23 and 4.24, respectively. The same cut variation as in Fig. 4.22 is used. Comparing the three figures, one can conclude that the shower shape cut is most efficient up to 20 GeV/c to discriminate between single and merged clusters, causing the strong rise between 10 and 20 GeV/c. Above 20 GeV/c, the merged clusters from π^0 mesons get less and less rejected and cause the flat purity till ~50 GeV/c. From 40 GeV/c we likely start rejecting merged η decays but their contribution to the rise in the purity from 60 to 80 GeV/c is marginal, being the isolation and the fraction of prompt photons over π^0 the driving factors of the final rise and plateau.

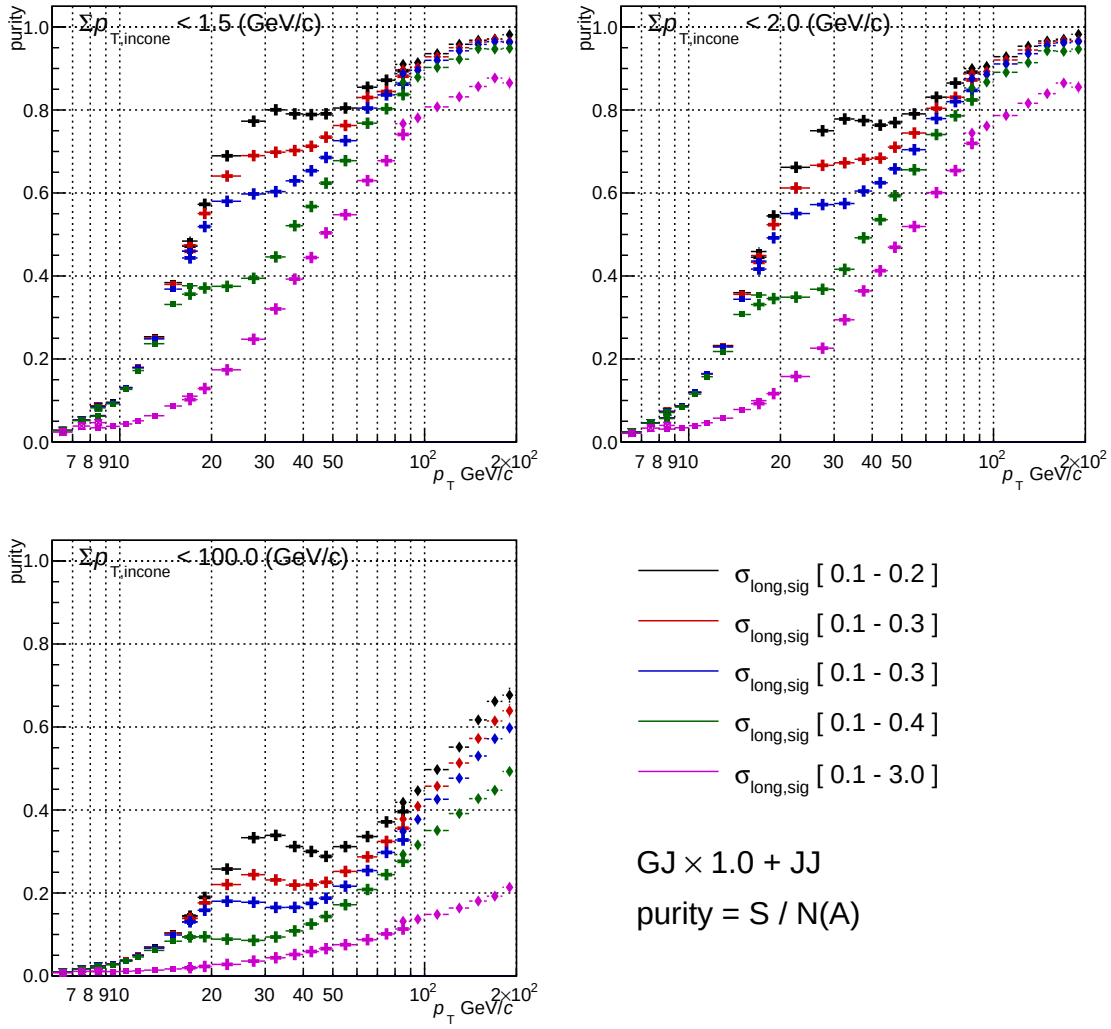

Figure 4.22: Purity of the isolated-photon sample as a function of p_T^{γ} for simulations combining γ–jet and jet–jet PYTHIA samples. Different colour lines correspond to different σ^2_{long} cut. Each frame corresponds to a different isolation threshold $p_T^{iso,\ ch,\ UE}$ = 1.5, 2.0 and open.

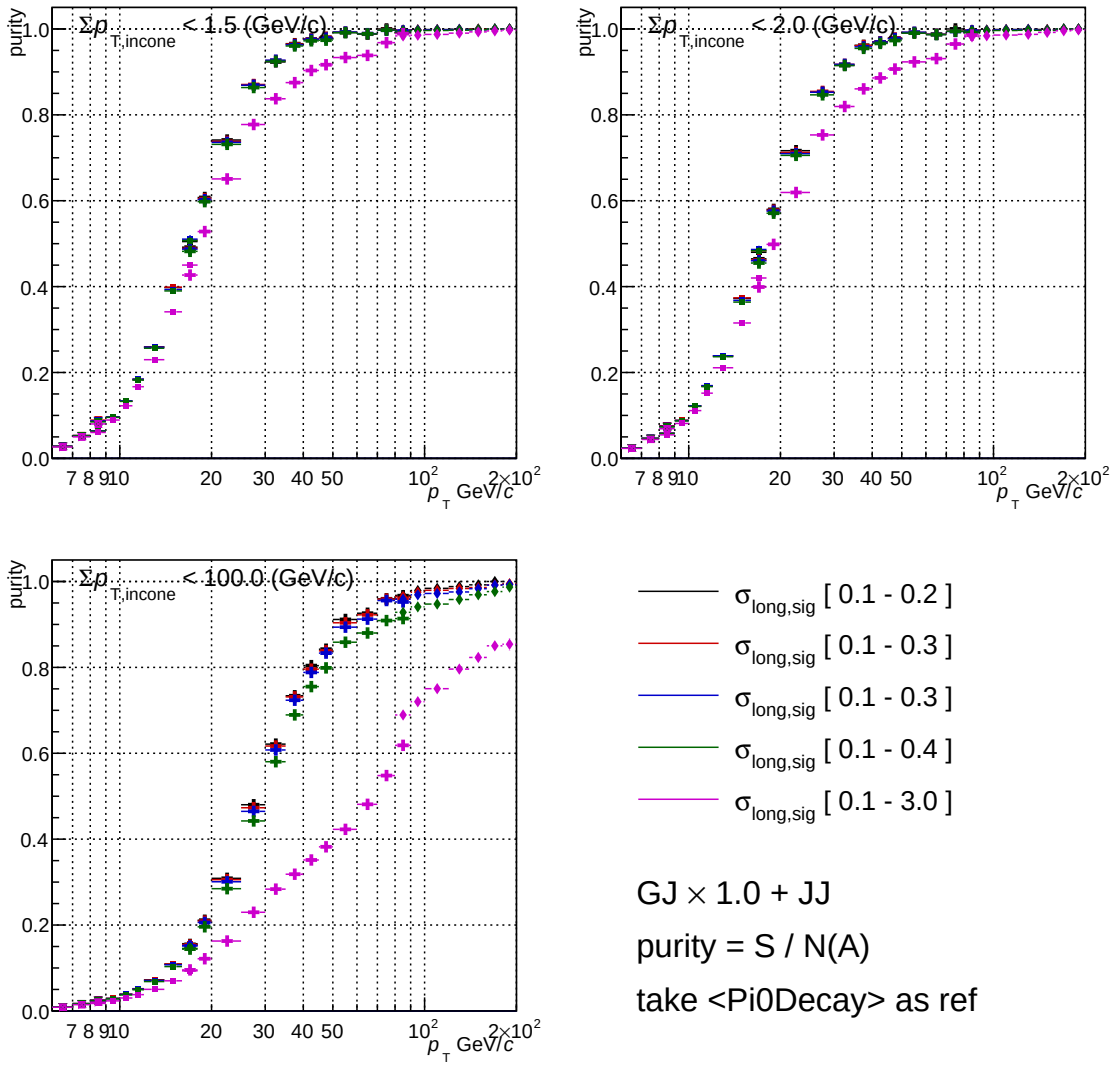

Figure 4.23: Purity of the isolated-photon sample as a function of p_{T}^{γ} for simulation combining γ–jet and jet–jet PYTHIA samples. The background only considers single decay photon clusters. Different colour lines correspond to different σ^2_{long} cut. Each frame corresponds to a different isolation threshold $p_{\mathrm{T}}^{\mathrm{iso,\ ch,\ UE}} = 1.5$, 2.0 and open.

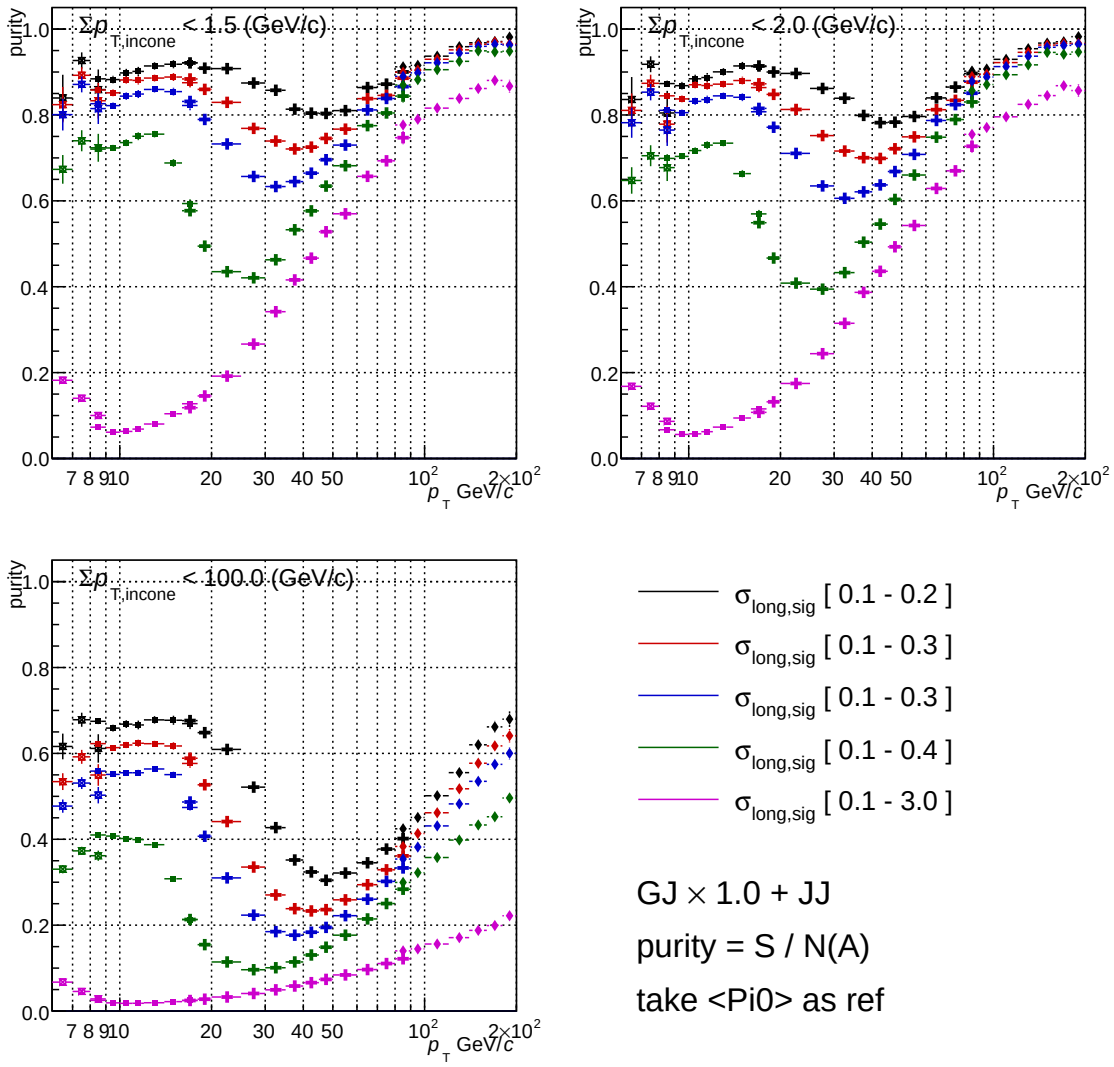

Figure 4.24: Purity of the isolated-photon sample as a function of p_T^{γ} for simulation combining γ–jet and jet–jet PYTHIA samples. The background only considers merged photon clusters from π^0 decay. Different colour lines correspond to different σ^2_{long} cut. Each frame corresponds to a different isolation threshold $p_T^{iso,\ ch,\ UE}$ = 1.5, 2.0 and open.

4.4.2 Study of correlation in the ABCD regions

The difference between the degree of the correlation between isolation momentum and shower shape distribution in data and simulation is another potential source of bias, as it influences the validity of Eq. (4.14). To check this, the dependence of the double ratio

$$\frac{\left(N^{\text{iso}}/N^{\overline{\text{iso}}}\right)^{\text{data}}}{\left(N^{\text{iso}}/N^{\overline{\text{iso}}}\right)^{\text{MC}}} = R_f, \tag{4.16}$$

where $N^{\text{iso}(\overline{\text{iso}})}$ represents the population of clusters that pass (do not pass) the isolation cut on $p_{\text{T}}^{\text{iso, ch, UE}}$. For simplicity, we define isolation fraction $f^{\text{i}} = (N^{\text{iso}}/N^{\overline{\text{iso}}})^{\text{i}}$, where i is data or simulation, so that $R_{\text{f}} = f_{\text{data}}/f_{\text{MC}}$.

The shower shape width σ^2_{long} is studied in a region where the signal contribution is expected to be negligible. If the correlation between the two variables is correctly reproduced in the simulation, the double ratio is independent of σ^2_{long}, i.e. it would be the same for wide and narrow clusters. Figure 4.25 shows the R_f as a function of the cluster σ^2_{long}, the upper plot anchored the clusters with $8 < p_{\text{T}} < 9$ GeV/c and bottom for $16 < p_{\text{T}} < 18$ GeV/c. Appendix A.1.1 shows the isolation fractions f_{data} and f_{MC} as a function of the cluster σ^2_{long} in data and simulation, and the corresponding R_f in different cluster p_{T} bins used in this analysis.

The double ratio was found to be above unity, indicating a larger isolation probability in data than in simulations. This is mainly due to an imperfect calibration of charged particle tracks which leads to some discrepancy between data and simulations in the estimate of the isolation energy from charged particles. However, since the correction introduced in Eq. (4.15) relies on a narrow-over-wide ratio, the overall normalisation in the double ratio of Eq. (4.16) does not enter the correction. It is also noted that the double ratio, R_f, has a small slope depending on σ^2_{long} which changes for the different p_{T}-intervals of the measurement. A possible bias can be estimated via extrapolations by linear fits of the dependence on σ^2_{long}.

The trend of the R_f distribution at high σ^2_{long} (background region) can be used to extrapolate down to the signal region for estimating how much we potentially miss in the signal purity calculation.

The polynomial order one function was used to fit the shape of R_f along σ^2_{long} in the background region, then, the fitted function is used to extrapolate the σ^2_{long} signal region. The possible double ratio discrepancy observed between the signal and background regions can be quantified as the ratio of a given modelling function expressed for the signal over the same expressed for the background.

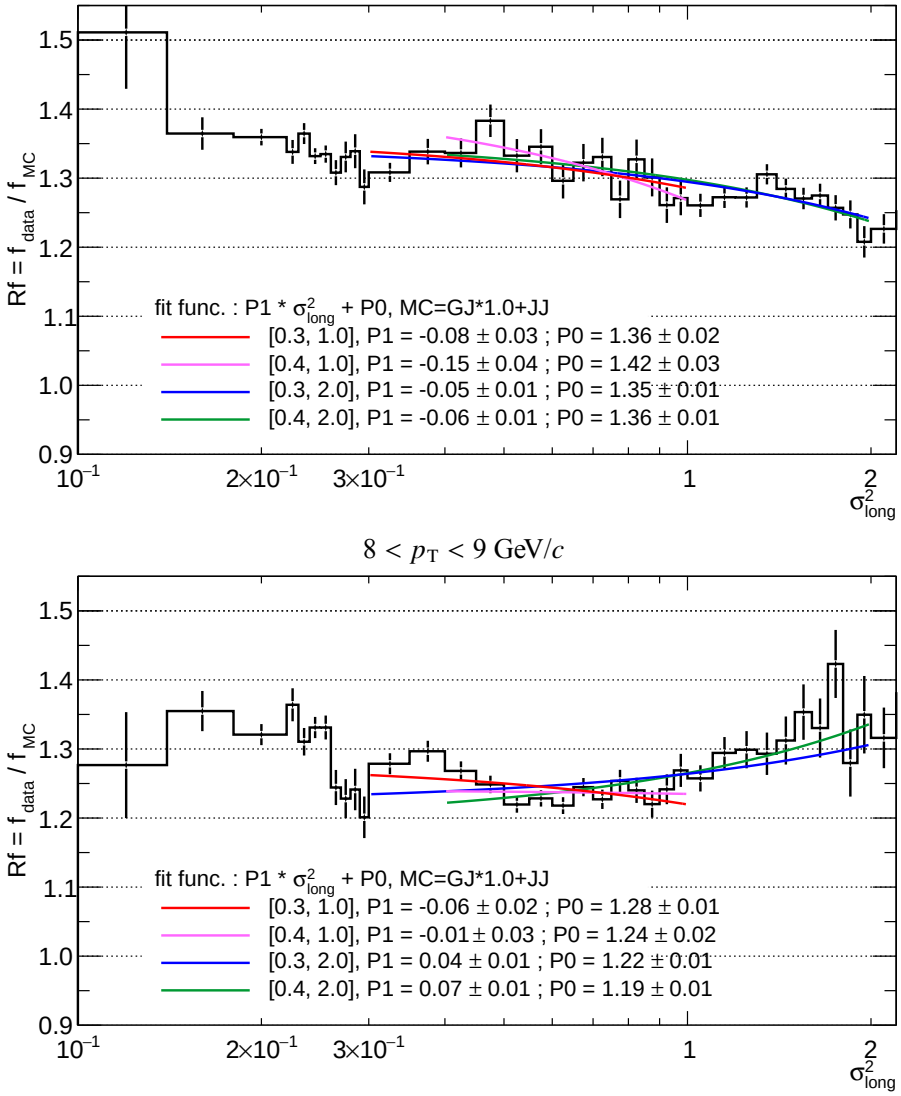

Figure 4.25: The distribution of the double ratio, R_f, as a function of cluster σ^2_{long}. Different linear function fits changing the fit range are displayed in different coloured lines. Clusters with $8 < p_T < 9$ GeV/c (top) and $16 < p_T < 18$ GeV/c (bottom).

A variable, C_α, is defined to describe this possible double ratio discrepancy:

$$C_\alpha = \left(\frac{p_0 + \sigma^2_{\text{long,n}} \cdot p_1}{p_0 + \sigma^2_{\text{long,w}} \cdot p_1} \right), \tag{4.17}$$

where $\sigma^2_{\text{long,n}}$ and $\sigma^2_{\text{long,w}}$ are the median values of the neutral-cluster σ^2_{long} distribution in the narrow and wide ranges, respectively, and p_0 and p_1 are the constant and slope parameters of the linear fit of the double ratio. Treated as a "calibration" term to be applied to the α_{MC}

$$\alpha_{\text{MC}} \longmapsto \alpha_{\text{MC}} \times C_\alpha, \tag{4.18}$$

In order to differentiate between these two α_{MC} factors, the calibrated one is labelled as α'_{MC}.

To determine the C_α distribution, we examine two factors related to the isolation fraction: the MC scale factor k (discussed in Sec. 5.1.3) and the shower shape fit range in the background region. In consideration of the MC scale factor, the variations are as $k = 0.5, 1.5, 2.0$. Figure 4.26 shows the

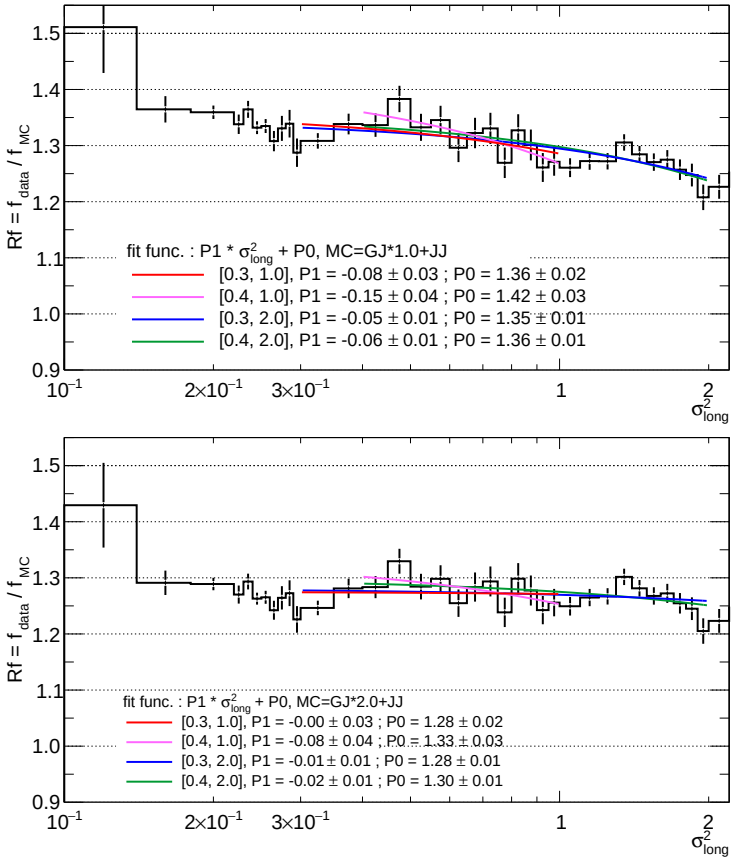

Figure 4.26: The R_f distribution with cluster p_{T} = 8–9 GeV/c, different linear fits changing the fit range are displayed in different coloured lines. With the scaling factor $k = 1$ (top) and $k = 2$ (bottom).

R_f distribution when $k = 1.0$ and $k = 2.0$ when cluster p_{T} = 8–9 GeV/c. More R_f distributions for

the analysis p_{T} bins are provided in Appendix A.1.1and A.1.5, which also contain the corresponding isolation fraction distribution for both data and simulation. Same plots for $k = 0.0, 0.5, 1.5$ also can be found in Appendix A.1.

To study the effect of the k variation, fitting range was fixed to $0.4 < \sigma^2_{\mathrm{long}} < 2.0$. The distribution of C_α, as a function of cluster p_{T}, for varying k values, is illustrated in Fig. 4.27. One can see that C_α is slightly closer to unity for $k = 2$ which could imply a better reproduction of the MC of the data behaviour below 40 GeV/c. Considering the different k values, α'_{MC} is calculated and shown in Fig. 4.28.

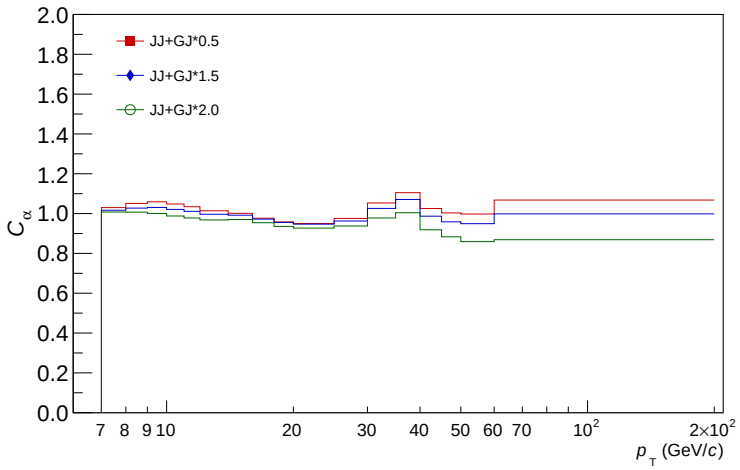

Figure 4.27: C_α from different scale factor k which is the γ–jet simulation scaling factor, the R_f background fit range is $0.4 < \sigma^2_{\mathrm{long}} < 2.0$.

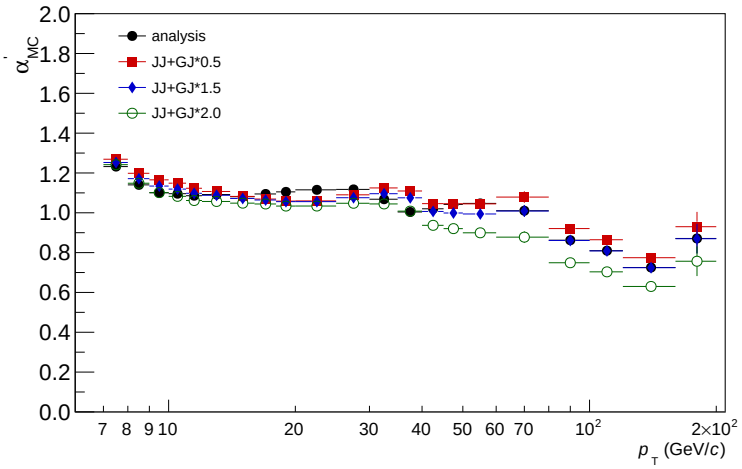

Figure 4.28: α_{MC} from different scale factor k which is the γ–jet simulation scaling factor, the R_f background fit range is $0.4 < \sigma^2_{\mathrm{long}} < 2.0$.

Figure 4.29 presents a comparison of the purity calculated with the $\alpha'_{\mathrm{MC}}(\alpha_{\mathrm{MC}})$ derived from Fig. 4.28, and the ratio of the varied purity to the standard purity. One can find that the difference is large at low p_{T} and negligible at high p_{T} and that the variation is smaller for $k = 2$.

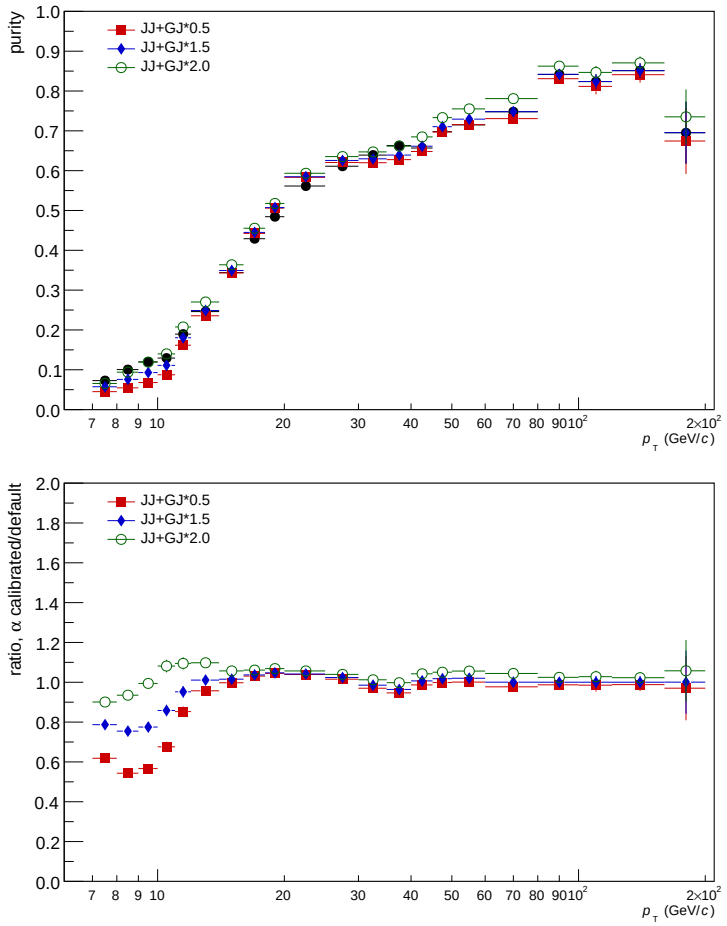

Figure 4.29: Top panel: Purity for different α'_{MC} obtained varying the k scaling factor to calculate C_{α}. Bottom panel: The corresponding purity ratio to the default selection. Both R_f background fit range is $0.4 < \sigma^2_{\mathrm{long}} < 2.0$.

The polynomial order one fit result in the R_f background region depends rather strongly on the σ^2_{long} fitting range as can be seen in Fig. 4.25 and Appendix A.1. The σ^2_{long} background fitting range for R_f was varied in reasonable ranges, the lower limit was set not too far from the signal region higher limit which at $\sigma^2_{\mathrm{long}} = 0.3$, and the higher limit not too close to the lower limit: the lower limits considered were 0.3, 0.35 and 0.4; and the upper limits considered were 1.0, 1.2, 1.4, 1.6, 1.8 and 2.0. Multiple sets of constant p_0 and slope p_1 parameters were obtained and are shown in appendix A.2 for both signal simulation scale parameters $k = 1$ and $k = 2$.

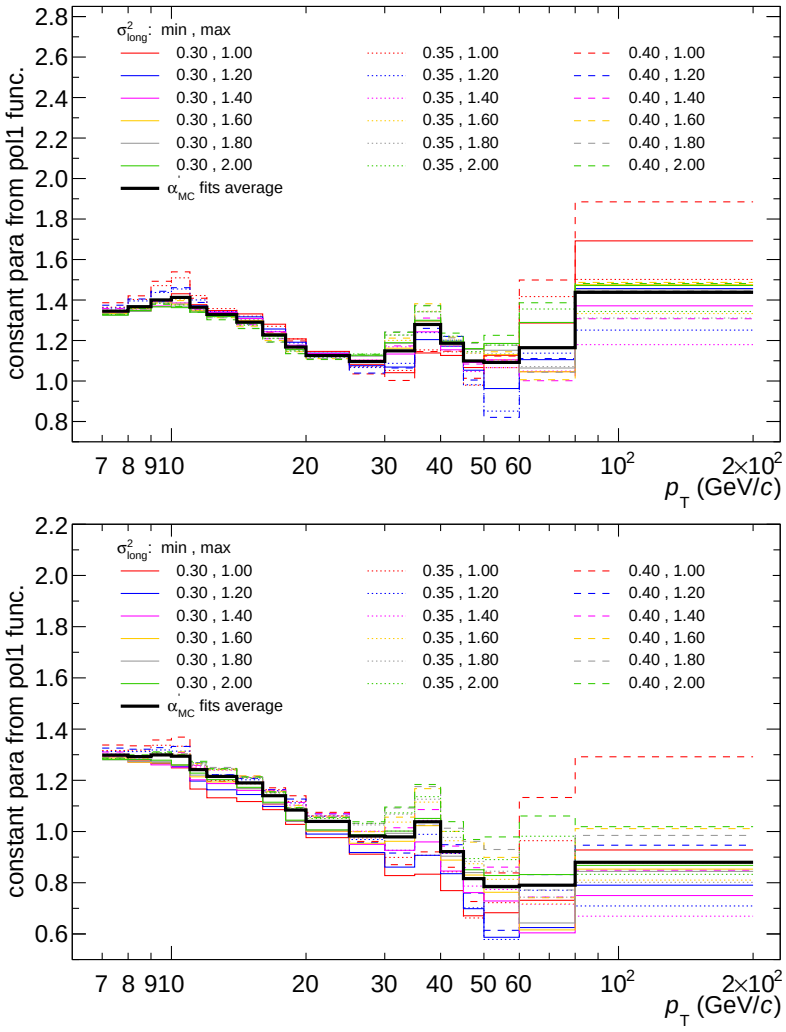

Figure 4.30: The constant parameters obtained by fitting a linear function to the different R_f background ranges as a function of the cluster p_T. Each coloured marker for a different σ^2_{long} fitting range indicated in the legend. The upper one is for $k = 1$ and the bottom is for $k = 2$.

Figure 4.30 and Fig. 4.31 show the constant and slope parameters for the different background ranges of the R_f as a function of cluster p_T, the upper plots are for scale factor $k = 1$ and the bottom are for $k = 2$. The average of each parameter of all the fits is also shown in the plots as a black line. Applying the multiple parameters obtained to Eq. (4.17), the sets of C_α for both scale factor cases are presented in Fig. 4.32. The black line in these figures shows the average of all constant or slope parameters. One can see significant variations at low $p_T < 11$ GeV/c and at high $p_T > 30$ GeV/c: at high p_T, the statistical limitations for the smaller ranges can drive the larger differences, in particular above 50 GeV/c; At low p_T, the structures that can be observed in the R_f in $0.3 < \sigma^2_{long} < 1$, a kind of maximum changing with p_T, drive strongly the smaller high limit fits driving the deviations. Figure 4.33 shows the α_{MC} after

calibration compared to the default one in the analysis. The black bullets in the plots are the ones used in the analysis without any C_α correction and a black discontinuous line is obtained using the average fit parameters value.

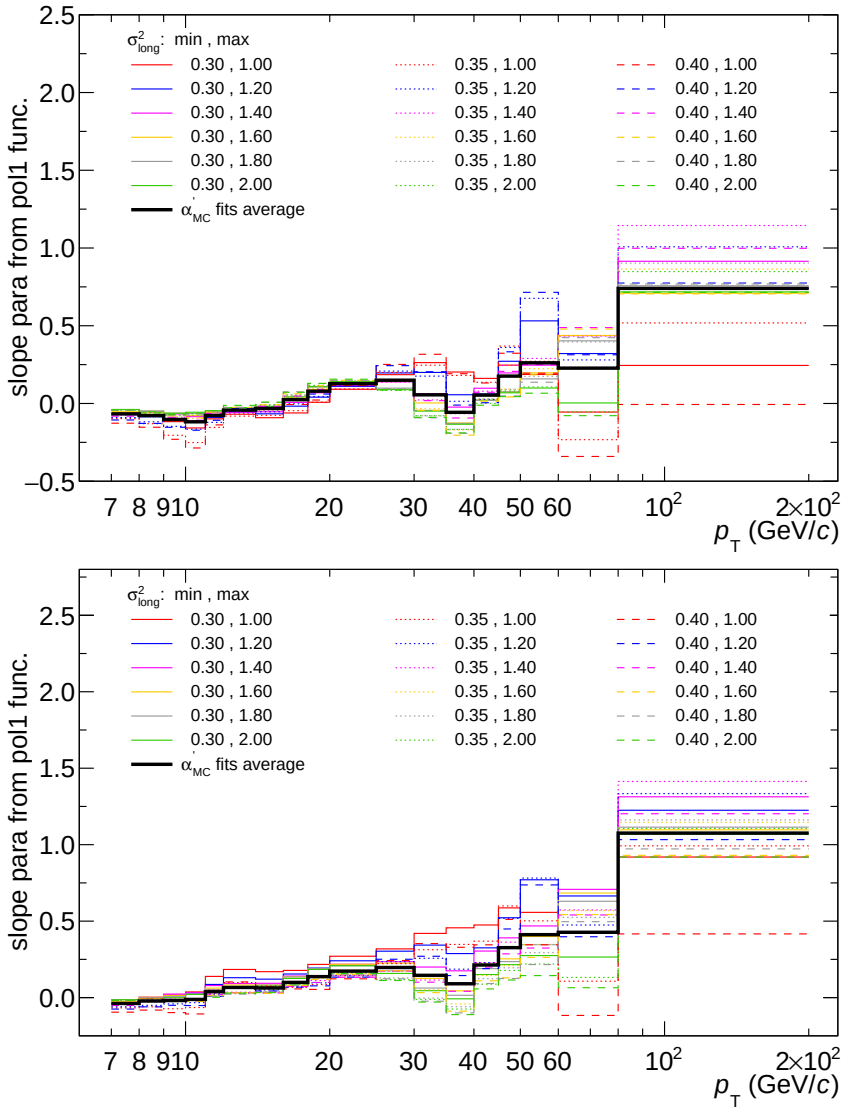

Figure 4.31: The slope parameters obtained by fitting a linear function to the different R_f background ranges as a function of the cluster p_{T}. Each coloured marker for a different σ^2_{long} fitting range indicated in the legend. The upper one is for $k = 1$ and the bottom is for $k = 2$.

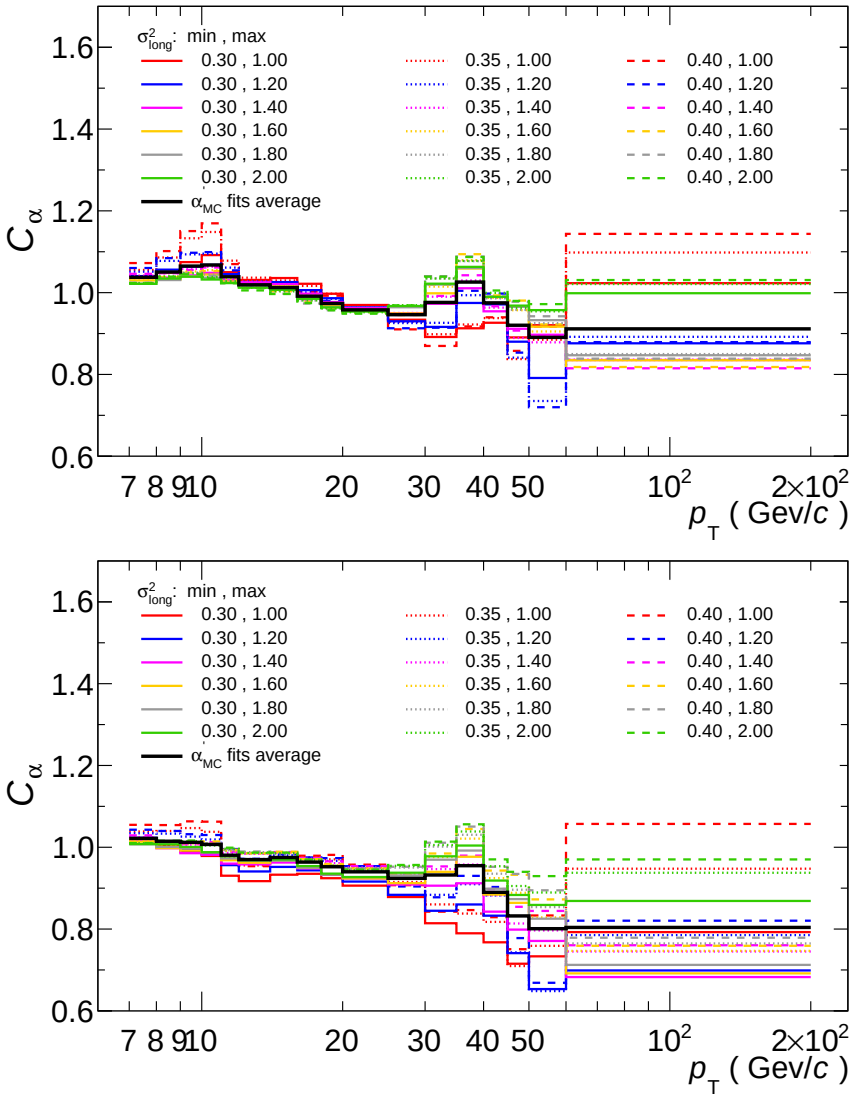

Figure 4.32: C_α distribution with parameters obtained by fitted linear function to different background ranges of the R_f. Each coloured marker for a different σ^2_{long} fitting range indicated in the legend. The upper one is for $k = 1$ and the bottom is for $k = 2$.

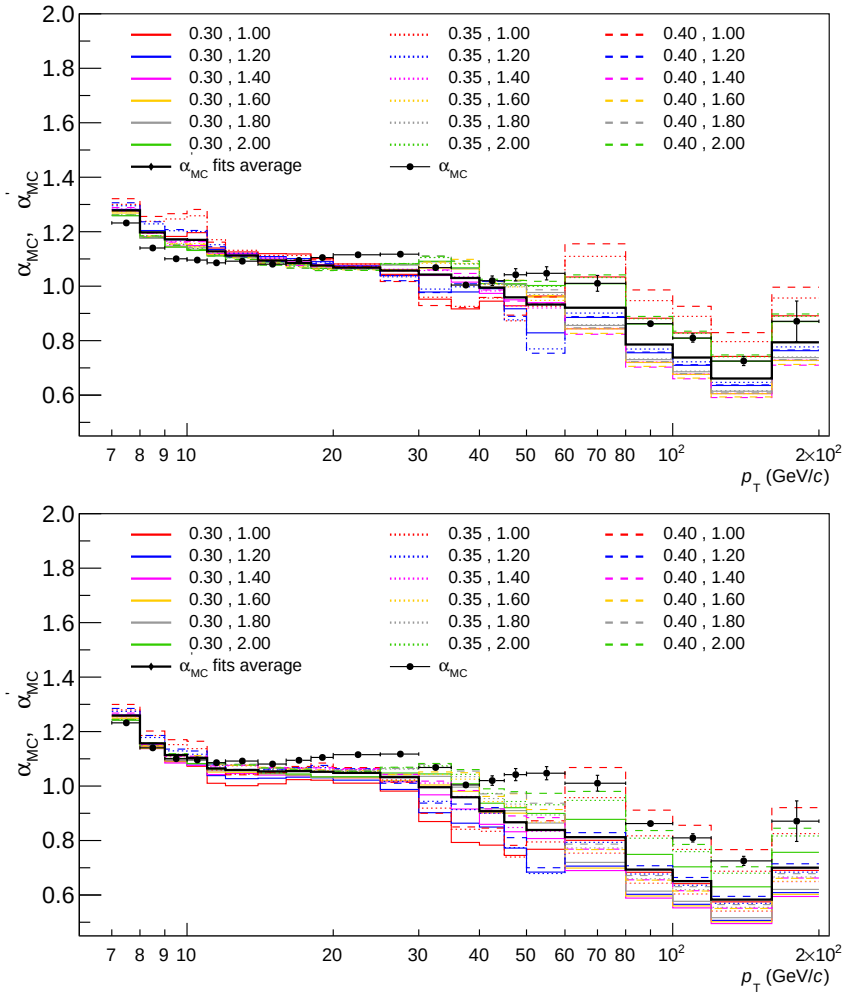

Figure 4.33: α_{MC} variations obtained from different R_f background range polynomial order 1 fit calibration factors C_α. Each coloured marker for a different σ^2_{long} fitting range indicated in the legend. The upper one is for $k = 1$ and the bottom is for $k = 2$.

The purity obtained from different C_α corrections using different fit ranges on R_f and the standard purity is compared in Fig. 4.34, and the ratio to the standard purity is shown in Fig. 4.35. One can find that the difference is small above 12 GeV/c, but below and especially when using a lower maximum background fit range ($\sigma^2_{\text{long}} = 1$) the difference becomes large. Looking more in detail at the plots in Fig. 4.25, 4.26 and in Appendix A.1, one can observe that at the lower p_{T} bins, the points in the region $\sigma^2_{\text{long}} = 0.4$ to 0.8 tend to fluctuate and even there seems to be a maximum from $\sigma^2_{\text{long}} = 0.8$ to 1, which affects strongly the fits restricted to $\sigma^2_{\text{long}} = 1$ as higher limit.

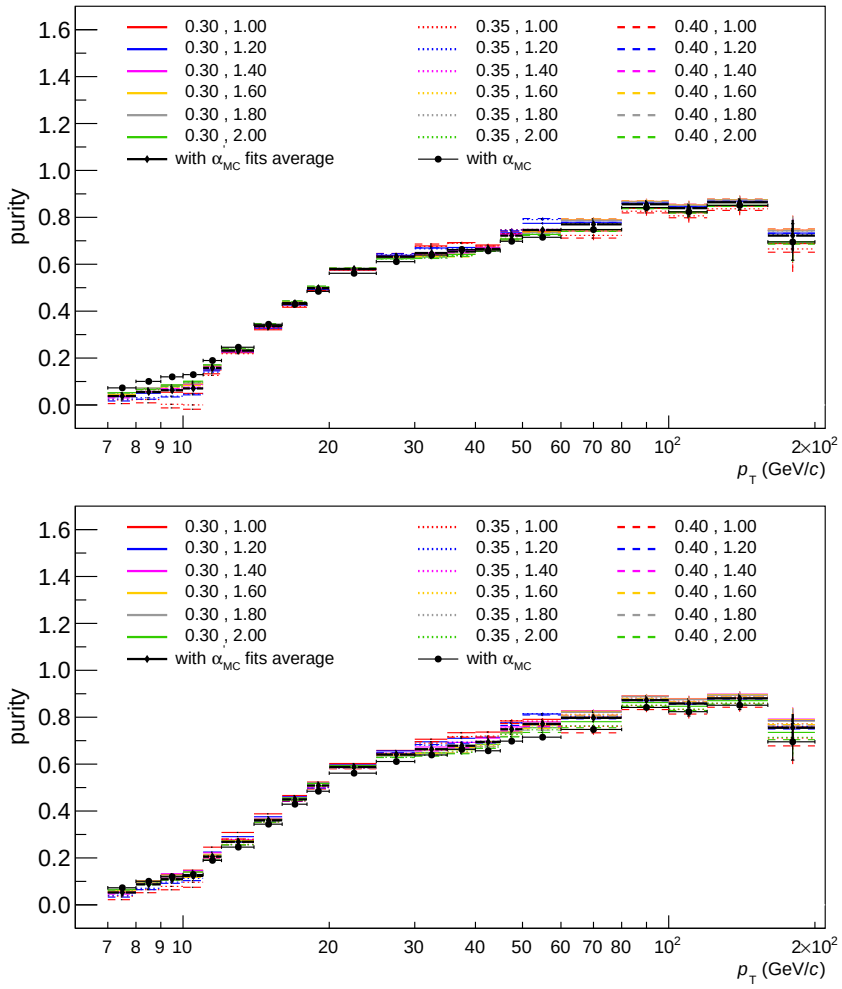

Figure 4.34: Purity variations when α_{MC} is obtained from different R_f background range polynomial order 1 fit calibration factors C_α. Each coloured marker for a different σ^2_{long} fitting range indicated in the legend. The upper plot is for $k = 1$ and the bottom is for $k = 2$.

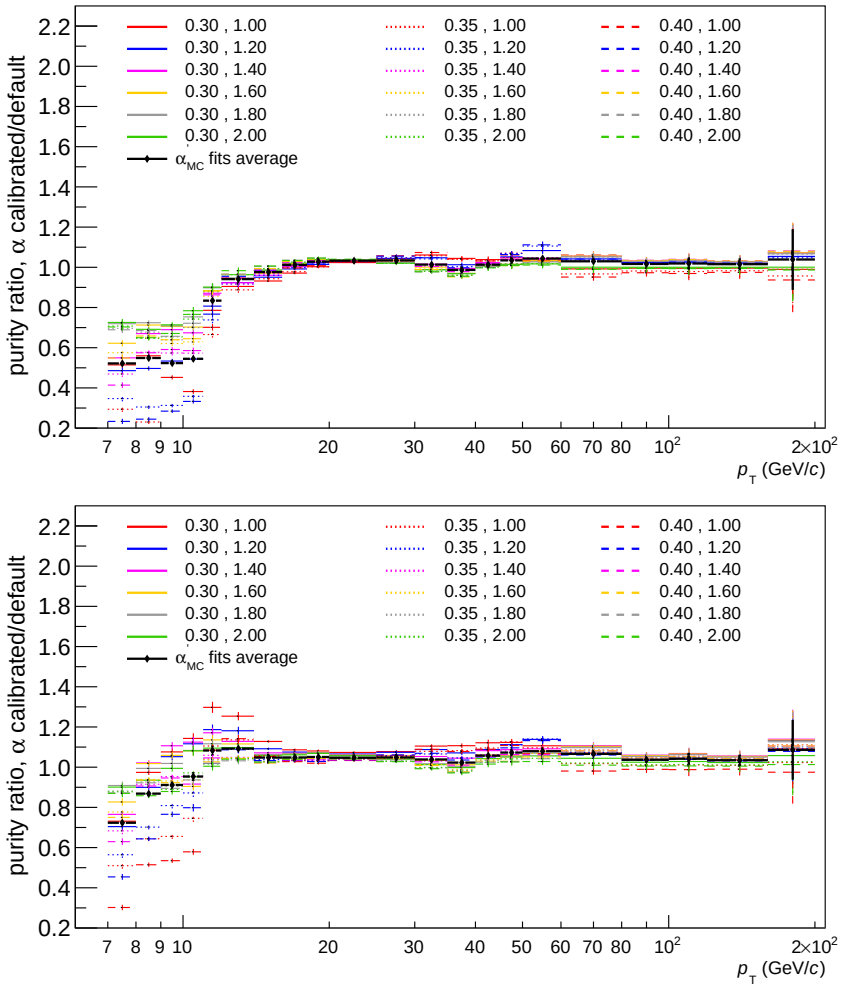

Figure 4.35: Ratio of purities from Fig. 4.34 obtained with different calibration factors C_α to the default obtained when changing the fitting range in R_f. Each coloured marker for a different σ^2_{long} fitting range indicated in the legend. The upper plot is for $k = 1$ and the bottom is for $k = 2$.

Figure 4.36 shows the relative variation in % for each of the fits for $k = 2$ with respect to the standard purity. Above $p_{\text{T}} > 12$ GeV/c, the variation fluctuates around 5% for any of the cases, below we have strong variations. Since there is no obvious optimal fitting range, we decided to take the average of the fit parameters of the selected ranges as the reference (bottom panel, black diamond in Fig. 4.33). Also, the R_f seems flatter with the scale mixing factor $k = 2$ so we take this value to estimate the systematic uncertainty.

The final uncertainty (the black line in Fig. 4.36) is shown and fitted in Fig. 4.37. We take the points as they are below 9 GeV/c (27% at 7 GeV/c and 13% at 8 GeV/c), then, to get rid of fluctuations and smooth the points, we take a constant fit from 9 to 14 GeV/c at 8% and then another constant fit above, getting close to 5% (fits are green lines).

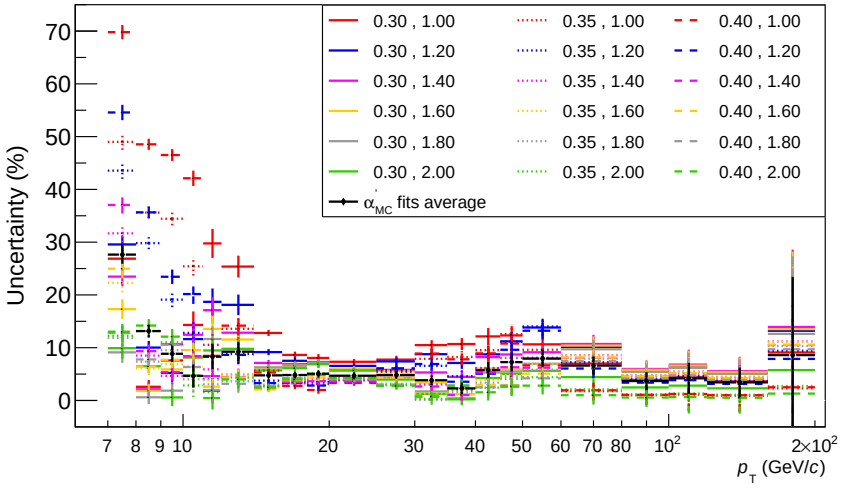

Figure 4.36: The relative uncertainty calculated comparing standard purity and the purity calculated with the C_α calibration for different R_f σ^2_{long} background fit ranges and the variations of the fit range. Each coloured marker for a different σ^2_{long} fitting range indicated in the legend. The signal simulation scale factor is $k = 2$.

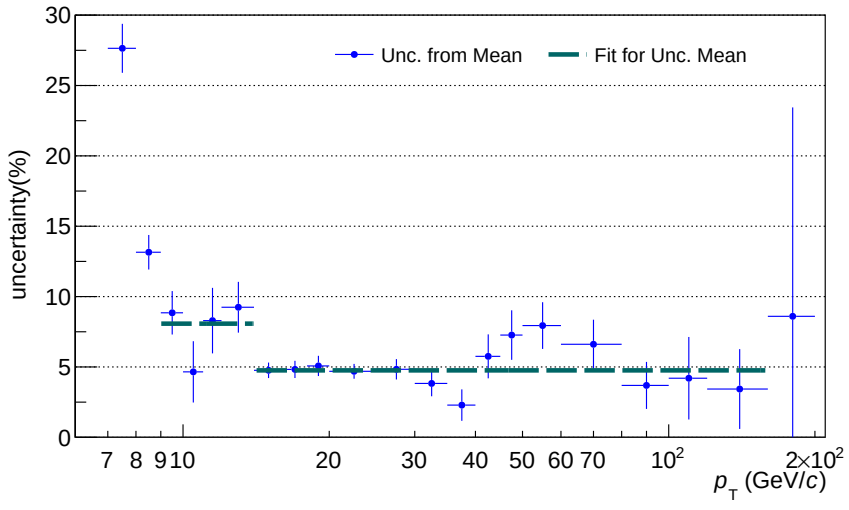

Figure 4.37: C_α from different scale factor k which is the γ–jet simulation scaling factor, R_f background fit range $0.4 < \sigma^2_{\text{long}} < 2.0$.

4.4.3 Purity fitting

The purity distribution is compatible with two overlapping plateaus as seen in Fig. 4.21 and corroborated with the simulation checks. To reduce the point-to-point statistical fluctuations in the purity used to correct the isolated-photon raw yield, the distribution is fitted by two sigmoid functions to reproduce the trend of the distribution with p_{T}^{γ}

$$f_{i,\ \mathrm{fit-sig}}(p_{\mathrm{T}}^{\gamma}) = \frac{a_i}{1+\exp(-b_i \times (p_{\mathrm{T}}^{\gamma} - c_i))}, \tag{4.19}$$

where i indicates the different fitting ranges, and a, b, c are the free fit parameters of the sigmoid function.

In this analysis, the first fit is done from $p_{\mathrm{T}}^{\gamma} = 7$ to 30 GeV/c with fit parameters obtained being $a_1 = 0.617 \pm 0.003$, $b_1 = 0.292 \pm 0.002$, and $c_1 = 14.28 \pm 0.05$. The second fit is done from $p_{\mathrm{T}}^{\gamma} = 20$ to 160 GeV/c with parameters $a_2 = 0.852 \pm 0.014$, $b_2 = 0.034 \pm 0.003$, and $c_2 = 2.4 \pm 1.0$. The results of the aforementioned fits are presented in Fig. 4.21, while the ratio of the fitted function to the calculated purity points is shown in Fig. 4.38. Within the overlapping fit ranges of these two fit functions, 20 to 30 GeV/c, the ratios are very similar. Additionally, the fitting range was varied, with each fit parameter obtained to ascertain whether the ratio was better to that observed previously. Figure 4.39 presents the ratio when the fit range is [7, 40] and [20, 160] GeV/c, the ratio for other fit range combinations can be found in the appendix B. It can be observed that the point-to-point fluctuations are larger than the variations provided by the fit range. This indicates that the fit is stable. In order to perform the cross-section calculation, it is necessary to ensure that the purity is a continuous function. Therefore, the values of purity from the fitted functions have been taken to be the ranges [7, 25] and [25, 200] GeV/c, respectively.

As mentioned before, Eq. (4.19) has three free parameters, a, b and c. For each parameter, the fitted value and its associated error from the fitting process can be obtained. Since this function is used to fit two p_{T} ranges, $a0$, $b0$, $c0$ are the low p_{T} range fit parameter values, $ea0$, $eb0$, $ec0$ are the corresponding fit value errors, and $a1$, $b1$, $c1$, $ea1$, $eb1$, $ec1$ are the high p_{T} range parameter and errors. To assign a systematic uncertainty to the fit, the function parameters were varied in the way provided in Tab. 4.1. The variation functions are shown as a band in Fig. 4.40. We take the largest variation as the purity fit uncertainty, and it is shown in Fig. 4.41. For the low-p_{T}^{γ} part of the fitting function, the uncertainty decreases from 3% to 0.5% from 7 to 30 GeV/c, and for the high-p_{T}^{γ} part, the uncertainty decreases from 4.5% to 2% from 30 to 200 GeV/c.

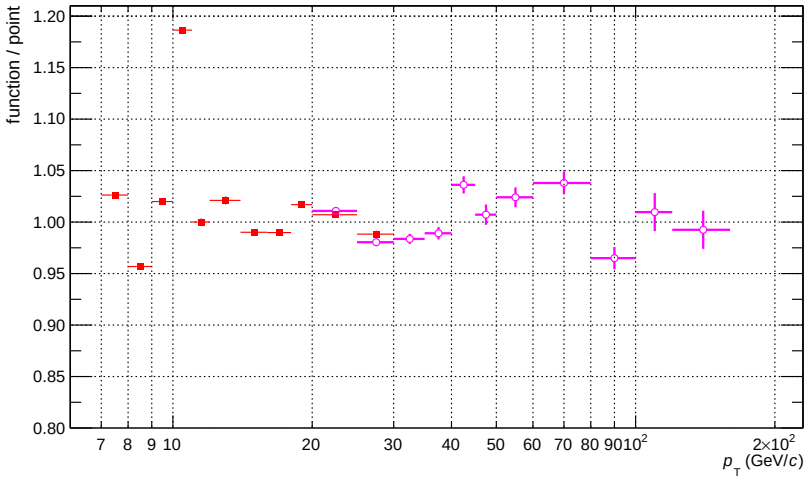

Figure 4.38: Ratio of the sigmoid fit functions results of Fig. 4.21 and the purity points. The fitting ranges are [7, 30] GeV/c and [20, 160] GeV/c for the low and high p_{T}.

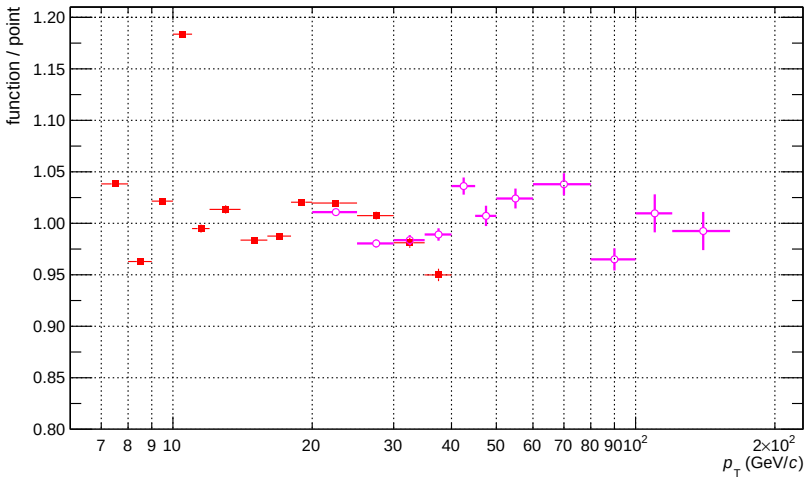

Figure 4.39: Ratio of the purity points of Fig. 4.21 and sigmoid fit functions obtained with different fitting ranges. The fitting ranges are [7, 40] GeV/c and [20, 160] GeV/c for the low and high p_{T}.

Table 4.1: Variations of the purity sigmoid function parameters obtained from the fit.

fit result	default	variable
$a0 \pm ea0$	$a0$	$a0 + ea0$, $a0 - ea0$
$b0 \pm eb0$	$b0$	$b0 + eb0$, $b0 - eb0$
$c0 \pm ec0$	$c0$	$c0 + ec0$, $c0 - ec0$
$a1 \pm ea1$	$a1$	$a1 + ea1$, $a1 - ea1$
$b1 \pm eb1$	$b1$	$b1 + eb1$, $b1 - eb1$
$c1 \pm ec1$	$c1$	$c1 + ec1$, $c1 - ec1$

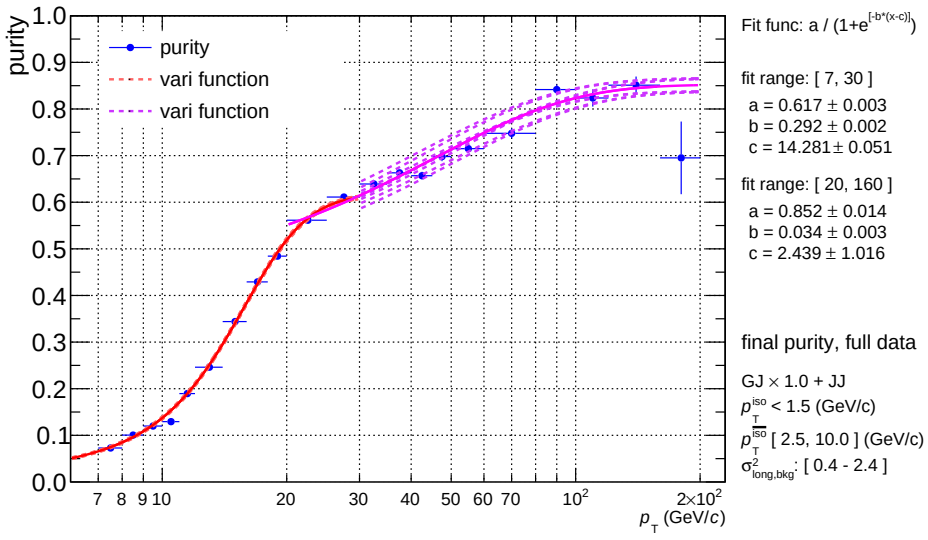

Figure 4.40: Isolated photon purity and the two fitted sigmoid functions. The band indicating the fit uncertainty obtained varying the fit parameters within the fit errors.

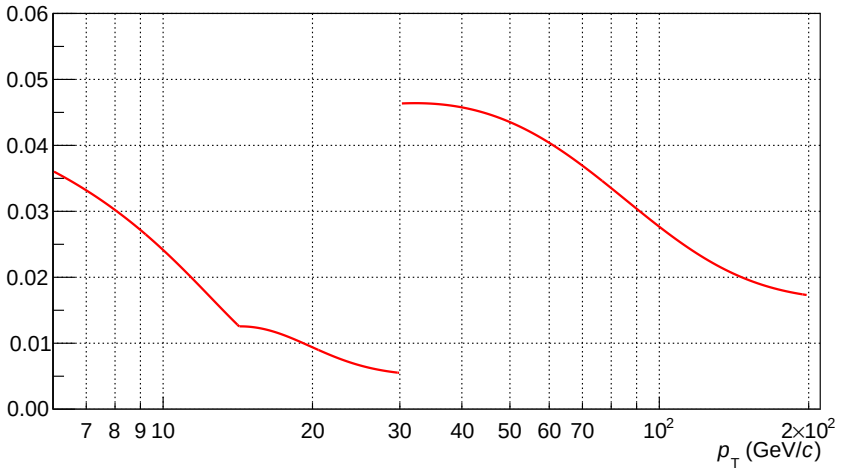

Figure 4.41: Purity function fitting relative uncertainty.

4.5 Normalization

The interaction cross section and uncertainty are provided year by year from Refs [99, 100]. The average interaction cross-section is calculated by weighting the number of events per year, where the number of events is the sum of events for each trigger scaled by the rejection factor in Sec. 3.6.4. Table 4.2 shows the interaction cross section and its associated uncertainty for each year, and the average interaction cross section and its corresponding uncertainty. The resulting interaction cross section averaged over the three data-taking years is $\sigma_{\mathrm{MB}}^{\mathrm{average}} = 58.05 \pm 0.90$ mb.

Table 4.2: The corresponding interaction cross section for years 2016, 2017, and 2018, in pp collisions at $\sqrt{s} = 13$ TeV data. The last row corresponds to the weighted average of the years by the number of events. Weighted uncertainty calculated from the each year uncertainty and the uncertainty transfer rules.

Year	σ_{MB} (mb)	Rel. unc. (%)
2016	58.44	1.9
2017	58.10	2.7
2018	57.52	2.1
Weighted average	58.05	1.5

The integrated luminosity collected with each of the used triggers ($\mathscr{L}_{\mathrm{int}}^{\mathrm{trigger}}$) has been determined using the expression

$$\mathcal{L}_{\mathrm{int}}^{\mathrm{trigger}} = \frac{N_{\mathrm{evt}}^{\mathrm{trigger}} \times RF^{\mathrm{trigger}}}{\sigma_{\mathrm{MB}}^{\mathrm{average}}}. \tag{4.20}$$

The corresponding values of the RF^{trigger} and integrated luminosity per trigger are presented in Tab. 4.3.

Table 4.3: Number of selected events, EMCal L1-γ trigger rejection factors, and luminosity per trigger. The luminosity uncertainty contains both the σ_{MB} and rejection factor uncertainties.

Trigger	$N_{\mathrm{evt}}^{\mathrm{trigger}}$	RF^{trigger}	$\mathscr{L}_{\mathrm{int}}^{\mathrm{trigger}}$
MB	1.587×10^9		27.34 ± 0.42 nb^{-1}
L1-γ-low	1.356×10^8	471 ± 3	1.13 ± 0.02 pb^{-1}
L1-γ-high	9.354×10^7	5960 ± 40	9.63 ± 0.16 pb^{-1}

The final production cross section is measured as a function of p_{T}, thus, the different triggers are combined depending on the trigger threshold. The L1-γ-high trigger threshold is at $E = 9$ GeV but it is not fully efficient until few GeV after, so it was decided to combine the three triggers above $p_{\mathrm{T}} = 12$ GeV/c. Hence, the distribution below $p_{\mathrm{T}} = 12$ GeV/c is a combination of MB and L1-γ-low triggers and above is the combination of the three triggers. The resulting sampled luminosity of the current

measurement is calculated as

$$\begin{aligned}\mathcal{L}_{\text{int}}(p_{\text{T}} > 12\ \text{GeV}/c) &= \mathcal{L}_{\text{int}}^{\text{MB}} + \mathcal{L}_{\text{int}}^{\text{L1}-\gamma-\text{low}} + \mathcal{L}_{\text{int}}^{\text{L1}-\gamma-\text{high}},\\ \mathcal{L}_{\text{int}}(p_{\text{T}} < 12\ \text{GeV}/c) &= \mathcal{L}_{\text{int}}^{\text{MB}} + \mathcal{L}_{\text{int}}^{\text{L1}-\gamma-\text{low}}\end{aligned} \tag{4.21}$$

resulting in

$$\begin{aligned}\mathscr{L}_{\text{int}}(p_{\text{T}} > 12\ \text{GeV}/c) &= 10.79 \pm 0.16\ \text{pb}^{-1},\\ \mathscr{L}_{\text{int}}(p_{\text{T}} < 12\ \text{GeV}/c) &= 1.160 \pm 0.018\ \text{pb}^{-1}.\end{aligned} \tag{4.22}$$

The luminosity normalisation uncertainty is found to be 1.5% at both low and high p_{T}, and is regarded as the uncertainty in the spectrum normalisation. The dominant contributor to this uncertainty is the $\sigma_{\text{MB}}^{\text{average}}$ uncertainty, with the $RF_{\varepsilon_{\text{trig}}}^{\text{trigger}}$ uncertainty representing a comparatively minor contribution (0.6%).

4.6 Cross section

The quantities involved in the calculation of the isolated photon differential cross-section have thus far been obtained and discussed. In this section, the aforementioned quantities are assembled to compute the observable following the equation:

$$\frac{\mathrm{d}^2\sigma_{\gamma}^{\text{iso}}}{\mathrm{d}p_{\text{T}}^{\gamma}\,\mathrm{d}\eta} = \sigma_{\text{MB}}^{\text{average}} \times \frac{1}{\sum_i N_{\text{evt}}^i \times RF^i} \sum_i \frac{\mathrm{d}^2 N_{\text{n}}^{\text{iso},\,i}}{\mathrm{d}p_{\text{T}}^{\gamma}\,\mathrm{d}\eta} \times \frac{1}{\varepsilon_{\text{trig}}^{\text{iso},\,i}} \times \frac{P}{\varepsilon_{\gamma}^{\text{iso}} \times \kappa^{\text{iso}} \times \text{Acc}} \tag{4.23}$$

where:

- $\sigma_{\text{MB}}^{\text{average}}$: the average of the minimum bias cross section obtain from Sec. 4.5;
- $\frac{1}{\sum_i N_{\text{evt}}^i \times RF^i} \sum_i \frac{\mathrm{d}^2 N_{\text{n}}^{\text{iso},\,i}}{\mathrm{d}p_{\text{T}}^{\gamma}\,\mathrm{d}\eta}$: uncorrected isolated photon spectra, see in Sec. 4.2 and 3.6.4;
- $\varepsilon_{\text{trig}}$: trigger efficiency obtained in Sec. 3.6.3;
- $\varepsilon_{\gamma}^{\text{iso}}$: isolated photon global efficiency obtained in Sec. 4.3;
- κ^{iso}: isolated photon efficiency at the generator level obtained in Sec. 4.3;
- P: isolated photon corrected purity determined in Sec. 4.4;

and i is an index depending on the data trigger, $\text{Acc} = \Delta\eta \times \Delta\varphi/2\pi$ is the acceptance area of the analysis. The cross-section formula includes a κ^{iso} dividing term (see definition and discussion in Sec. 4.3) to take into account the bias induced by the collision underlying event not present in NLO calculations. It is found that multi-particle interaction processes cause most of the deviation from unity, and only at the highest p_{T}^{γ} a small contribution from initial and final state radiation effects induces a deviation from unity by up to 3%. Note that if the UE is subtracted from the isolation cone, the κ^{iso} factor is not needed.

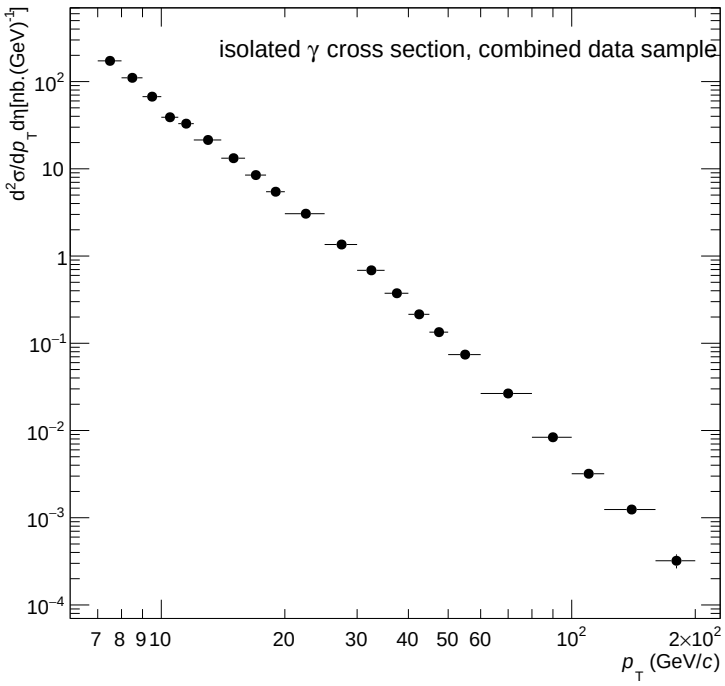

Figure 4.42: Isolated-photon cross section in pp collisions at $\sqrt{s}$ = 13 TeV, associated with statistical uncertainty only.

The isolated-photon cross section can be calculated with all the ingredients presented before using Eq. (4.23) and it is shown in Fig. 4.42. As a reminder, the purity fit function evaluated at the center of bin is used instead of the purity points.

5 Systematic uncertainties

As presented in the previous chapter of this thesis, this measurement is based on a number of selection criteria. Even though these were determined based on physical motivations, they can potentially give rise to fluctuations or uncertainties if they vary even slightly. To take this possibility into account, I investigate the various sources of systematic uncertainties that are likely to affect our measurement in this chapter. This process is a prerequisite to any comparison of the isolated photon cross section with theoretical predictions.

I will now explain how each of the uncertainties associated with the different sources has been evaluated. As common features of some of those evaluations, it should be noted that to avoid statistical fluctuations, some "re-binning" has been used as well as some fits. Those techniques are used when the systematic errors do not exhibit a notable p_{T} dependence and are justified by the fact that the size of the systematic errors is often smaller or (of the same size) than the statistical errors associated with their determination.

For most of the sources considered, the systematic uncertainty is calculated considering the relative variations in %

$$\Delta_{\mathrm{vari}}(x) = \frac{|x_{\mathrm{ref}} - x_{\mathrm{vari}}|}{x_{\mathrm{ref}}} \times 100, \tag{5.1}$$

where the $\Delta_{\mathrm{vari}}(x)$ represents the uncertainty due to the variable, and x is either the purity or the cross section (depending on the parameter varied), both as a function of p_{T}. We take the average of all variations as an uncertainty if there are several variations for one source.

We consider separating the sources of systematic uncertainties into two categories, those related to purity and those related to cross section. The total purity uncertainty is also a source of uncertainty in the cross section.

5.1 Uncertainties associated to the purity

The following uncertainty sources discussed in this section were considered for the purity:

- Shower shape σ^2_{long} background range (wide clusters);
- Isolation momentum $p_{\mathrm{T}}^{\mathrm{iso,\ ch,\ UE}}$ background range;
- Signal-to-background ratio in simulation, "MC signal amount";
- Effect of correlations on ABCD regions affecting the α_{MC} correction factor, "isolation probability", which was already presented in Sec. 4.4.2;

- Purity fit error, which was previously discussed in Sec. 4.4.3.

5.1.1 Shower shape range in background region

The uncertainty due to the choice of the background region range (wide showers, i.e. large values of σ^2_{long}) is investigated by moving the corresponding σ^2_{long} interval, $0.4 < \sigma^2_{\text{long}} < 2.4$, to $0.37 < \sigma^2_{\text{long}} < 2.37$ and $0.43 < \sigma^2_{\text{long}} < 2.43$.

The purity obtained for each of the σ^2_{long} variations and the two ratios to the reference purity range are shown in Fig. 5.1(a) top and bottom, respectively. The relative uncertainty in % obtained from the average of the two ratios is shown in Fig. 5.1(b). As the points fluctuate, we take the result of a constant fit from 10 to 100 GeV/c as systematic uncertainty above 10 GeV/c which is displayed as a red line in Fig. 5.1(b). From this figure, one can conclude that the uncertainty of the background σ^2_{long} range varies between 1-3% below 10 GeV/c and 0.4% above.

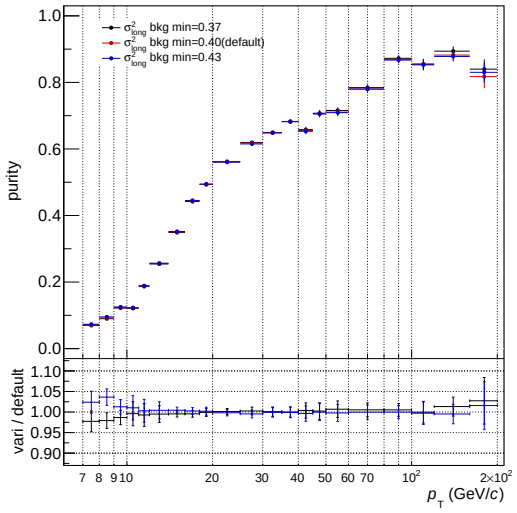

(a)

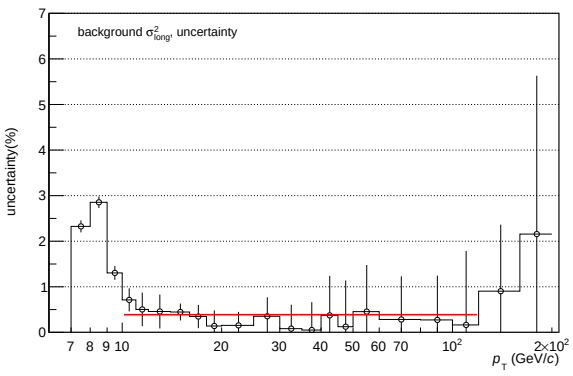

(b)

Figure 5.1: (a) Top panel, purity obtained for different background σ^2_{long} range variations. Bottom panel, ratio to the reference background σ^2_{long} range. (b) Associated relative uncertainty in % taking the average of the two variations, the red line is fit to a constant.

5.1.2 Isolation momentum range in background region

The $p_{\text{T}}^{\text{iso, ch, UE}}$ background range, labelled as the "anti-$p_{\text{T}}^{\text{iso, ch, UE}}$", is also varied, with the minimum limit from 2 to 5 GeV/c and the maximum from 6 to 20 GeV/c. The average of the differences due to these variations is used to estimate the uncertainty.

Figure 5.2(a) shows the purity for the different maxima compared to the default when the minimum

is fixed at 2 GeV/c, and at the bottom is the ratio to the default range. The uncertainty after averaging all the ratios for all the combinations min-max range is shown in Fig. 5.2(b). The red lines are the result of two fits to the points in different p_{T} ranges, linear function fit in the p_{T} range [7, 12] GeV/c and a constant function fit for the rest of the interval, resulting in an uncertainty of 15% at 7 GeV/c decreasing to 0.8% at 12 GeV/c from where it remains constant.

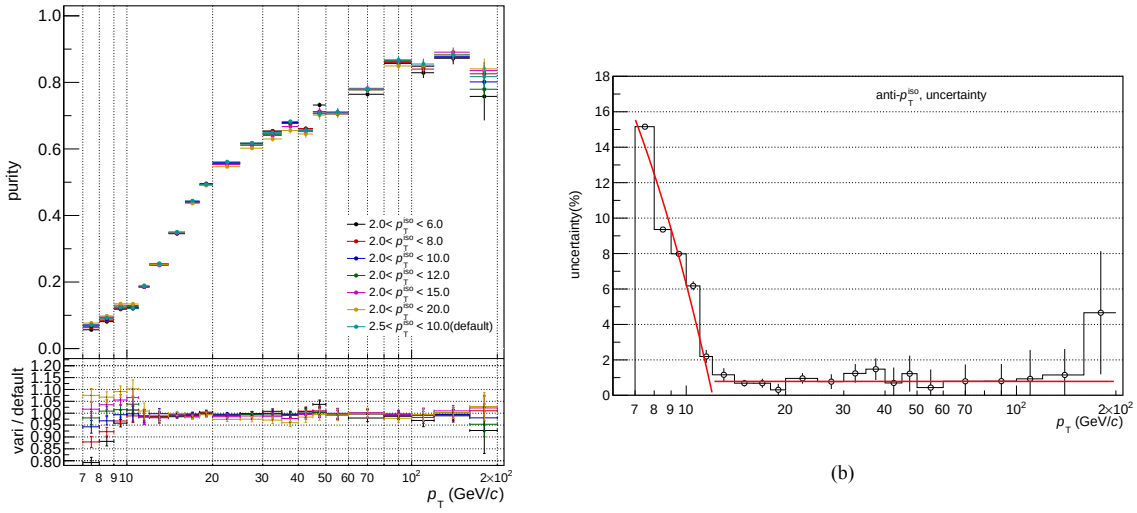

(a) (b)

Figure 5.2: (a) Top panel, purity obtained for different background anti-isolation p_{T} ranges variations, fixing the minimum of the range at 2 GeV/c. Bottom panel, ratio to the reference range. (b) Associated relative uncertainty in % taking the average of all the possible variations discussed in the text, the red lines are the result of a fit to constant or linear functions.

5.1.3 Signal-to-background ratio in the simulation

The amount of signal "with respect to the background" in the simulation, labelled as the "MC signal amount", influences the aforementioned leakage effect of signal into the background regions used to estimate the purity. We considered the scale factor, k, as the weight assigned to the signal in the simulation (γ–jet PYTHIA 8 events). When adding it to the background simulation (jet–jet PYTHIA 8 events), so that MC = γ–jet × k + jet–jet. Here, taking k = 1 as a reference and k = 0.5 and 1.5 as variations to estimate the uncertainty.

Figure 5.3(a) shows the purity for the three "k" values considered and the ratio to the reference one, and the relative uncertainty after averaging is shown in Fig. 5.3(b). An exponential function fit from 7 to 20 GeV/c and a constant fit from 40 to 100 GeV/c was applied to avoid the statistical fluctuations, displayed as red lines on Fig. 5.3(b). The resulting uncertainty is 9.1% at 7 GeV/c, decreasing to 2.5% at 20 GeV/c and then increasing until 40 GeV/c, above, it remains constant at 4.2%.

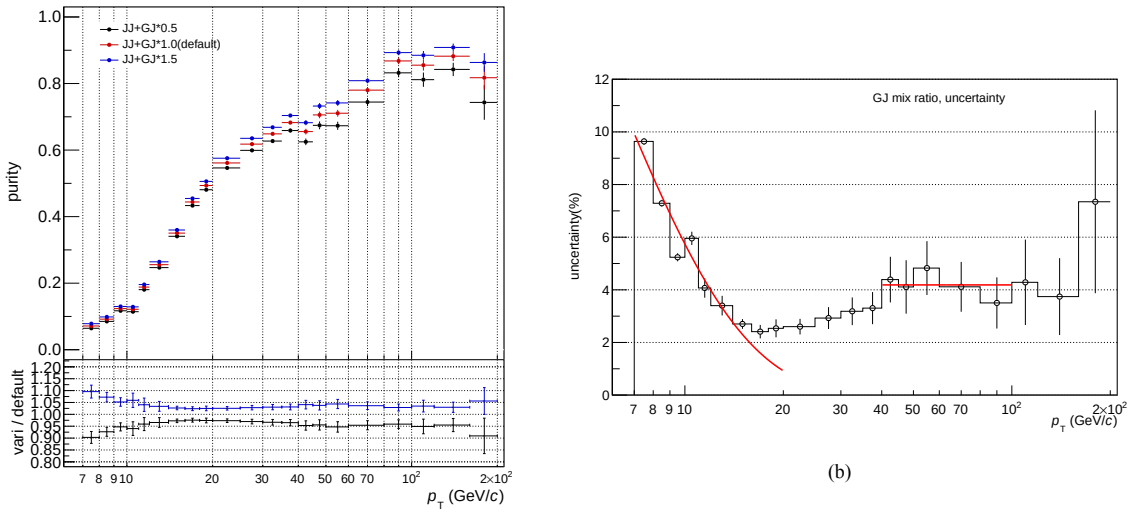

(a) (b)

Figure 5.3: (a) Top panel, purity obtained for different MC scale variations, $k = 0.5, 1.0, 1.5$. Bottom panel, ratio to the reference range, $k = 1.0$. (b) Associated relative uncertainty in % taking the average of the 2 variations, the red line is the constant function fit.

5.1.4 Total purity uncertainty

The contributions from all these uncertainty sources are added in quadrature and are used as the total purity uncertainty (Sec. 5.1.1 to 5.1.3). Figure 5.4 collects all the uncertainty sources for the purity and the total purity systematic uncertainty (red bullet markers).

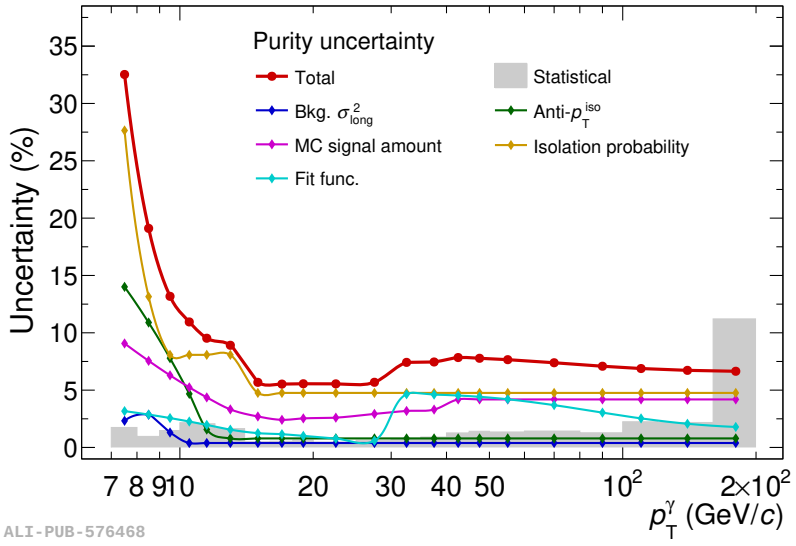

Figure 5.4: Purity uncertainty sources and total uncertainty (red line).

The total purity uncertainty ranges between 6% and 35% being maximal at low p_{T}^{γ} and having a minimum for p_{T}^{γ} between 16 and 30 GeV/c. The main source of systematic uncertainty is the isolation probability. The second most important source of uncertainty is p_{T}^{γ}–dependent: at low p_{T}^{γ} (up to 10 GeV/c) the anti-isolation range, between 30 and 60 GeV/c the uncertainty of the fit to the purity, and for the other p_{T}^{γ}–ranges the MC signal amount.

5.2 Uncertainties associated with the cross section

The considered uncertainty sources for the cross-section yield discussed in this section are:

- The choice of the neutral cluster selection;
- The choice of the signal σ^2_{long} range;
- The description of the shower shape;
- Trigger normalisation;
- The purity, discussed in Sec. 5.1.4;
- The energy scale of the EMCal;
- Material budget;
- Supermodule dependence, discussed in Sec. 3.6.2.

The trigger normalisation has two sources: the use of the trigger efficiency to estimate the trigger rejection factor and correct the yields, and the fit used to calculate the trigger rejection factor. The first source was discussed in Sec. 3.6.3. The uncertainty amounts to 0.25% when L1-γ-low + MB triggers are used and 1 to 3% from 12 to 200 GeV/c when all the triggers are combined. The trigger rejection factor and its uncertainty were presented in Sec. 3.6.4. This uncertainty is considered as a normalisation uncertainty and not added to the yield systematic uncertainty. These uncertainties combined with the σ_{MB} uncertainties give a normalisation and luminosity uncertainty of 1.5% as found in Sec. 4.5.

5.2.1 Neutral cluster selection

The uncertainties due to the neutral cluster selection criteria in this analysis are evaluated via the variations of: the charged particle veto residual distance selection, the number of local maxima, distance to masked channels, and the abnormal energy depositions removal parameter F_{+}.

The uncertainty due to the charged particle veto is estimated by varying the parameters of the track p_{T}-dependent selection of Eq. (3.9) to looser ones $\Delta\eta^{\mathrm{residual}} > 0.025$ and $\Delta\varphi^{\mathrm{residual}} > 0.03$ radians. The uncertainty of the charged particle veto is present in Fig. 5.5. We take a constant fit from 7 to 160 GeV/c as the systematic uncertainty. The fit result, whose value is 0.3%, is shown as a red line in the plot.

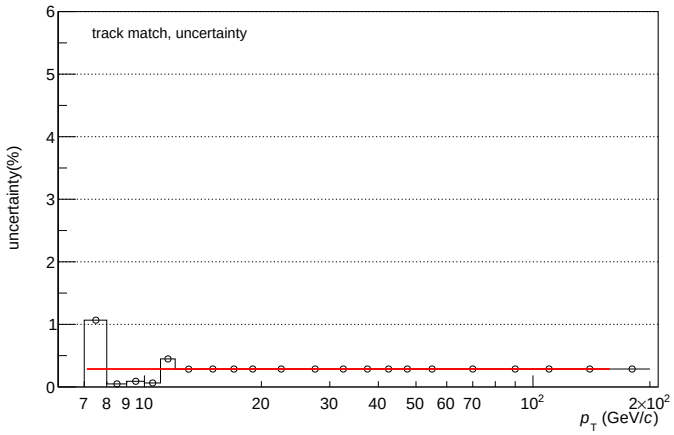

Figure 5.5: Relative uncertainty in % from the charged particle veto selection, the red line is a constant function fit between 7 and 160 GeV/c.

The uncertainty related to the selection on the number of local maxima is obtained by varying the threshold from 2 to 3. Figure 5.6 shows the uncertainty of the number of local maxima selection. Considering that points fluctuate, we take the result of a constant fit from 8 to 50 GeV/c as systematic uncertainty below 50 GeV/c resulting in 1.18%. A linear fit was applied in the range [50, 100] GeV/c, the uncertainty changes from 2% at 50 GeV/c to about 8% at 200 GeV/c. The fit result is shown as red lines in the plot.

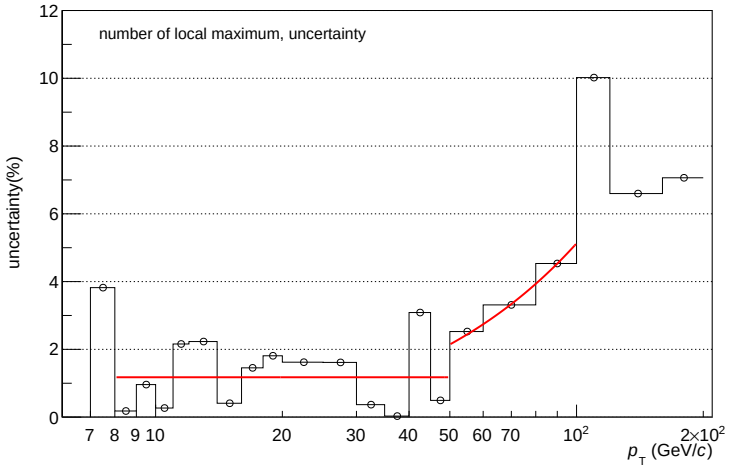

Figure 5.6: Relative uncertainty in % from the number of local maximum, the red line is a constant function fit between 7 and 50 GeV/c and a linear function fit between 50 and 100 GeV/c.

The requirement on the distance to masked channels is decreased from $d_{\text{mask}} > 2$ to 0 cells, 0 cells meaning that the misbehaving or dead channels are effectively removed from the cluster but the presence of these cells in the proximity of the cluster has no further effect. Figure 5.7 shows the associated relative

uncertainty to this variation. We consider a constant uncertainty resulting from a constant fit from 7 to 80 GeV/c obtaining 2.5%, shown as a red line in the plot.

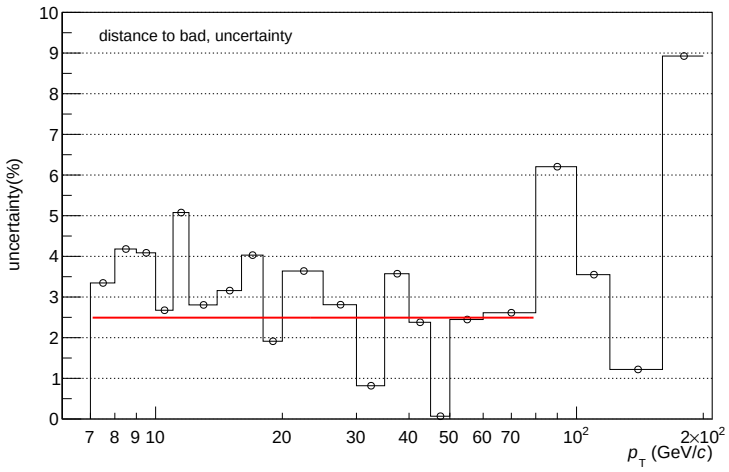

Figure 5.7: Relative uncertainty in % from the distance to masked channels, the red line is given by a constant function fit.

The F_+ is varied from 97% to 95%. The obtained uncertainty from this variation is shown in Fig. 5.8. The red line in the figure is the result of a constant function fit from 7 to 50 GeV/c. The constant value of the fit is 1.6%, value used as F_+ uncertainty.

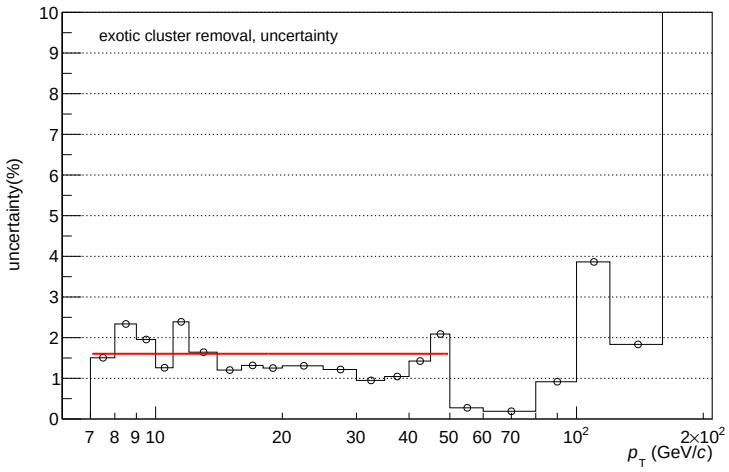

Figure 5.8: Relative uncertainty in % from F_+, the red line is a constant function fit between 7 and 50 GeV/c.

As seen in Fig. 4.12, the $|t| < 20$ ns window captures most of the expected real signal with no significant out-of-bunch pileup, but the tails in the distribution might indicate a contribution from exotic clusters under the signal distribution. The analysis was repeated using $|t| < 10$ ns and $|t| < 40$ ns

windows to study how much the cluster distribution changes. Figure 5.9 presents the ratio of each ABCD cluster spectra within the time windows of $|t| < 10$ and 40 ns over $|t| < 20$ ns. One can see that the cluster p_{T} distribution changes when the numerator is $|t| < 10$ ns at most by 3% above 20–30 GeV/c, in all cases except for isolated wide clusters, that are more suppressed. When compared to $|t| < 40$ ns the variation has the same p_{T} dependence but a smaller magnitude, 1% at maximum except for isolated wide that reaches 2–3%. In any of the cases, no or negligible effect is observed below 16 GeV/c. Since the time cut only affects data, the data-driven purity from Eq. (4.12) is recalculated and shown in Fig. 5.10, when the time cut is $|t| < 10$ ns this uncorrected purity increases 1–3% at high p_{T}, mostly due to the larger deviation observed for the isolated wide clusters. Multiplying the isolated narrow spectrum and the purity, without other corrections, one gets the relative difference of the two variations and their average in Fig. 5.11. Taking the average and fitting it above 20 GeV/c we get a relative uncertainty of 1.4%.

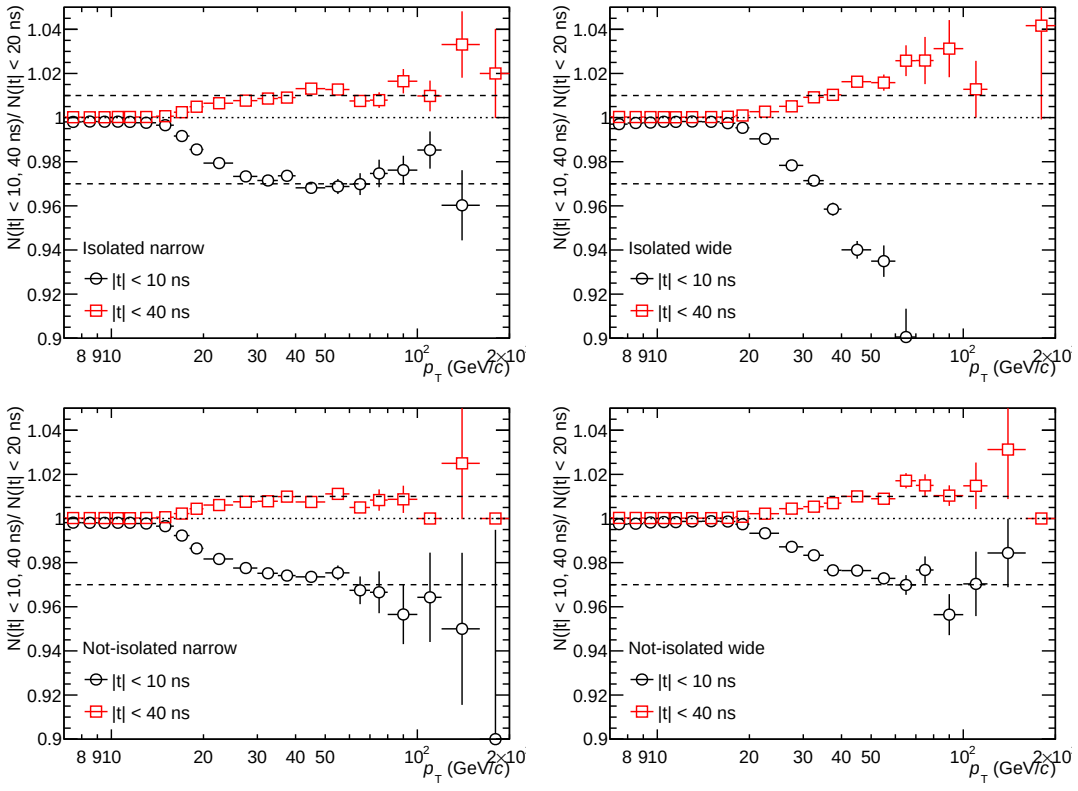

Figure 5.9: Fraction of isolated or not isolated narrow or wide cluster spectrum selected within a time window of 10 or 40 ns divided by the default 20 ns window.

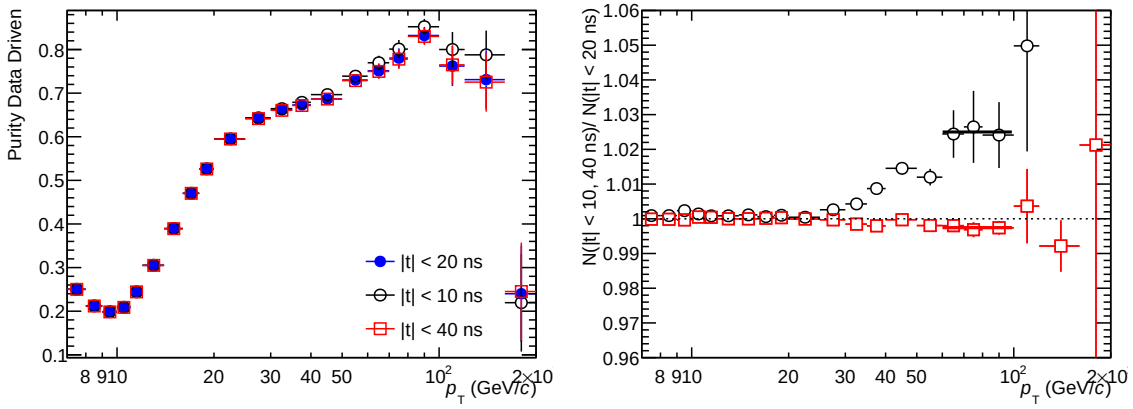

Figure 5.10: Left: Data driven purity from Eq. (4.12) for different time windows $|t| < 10$, 20 or 40 ns. Right: ratio to $|t| < 20$ ns.

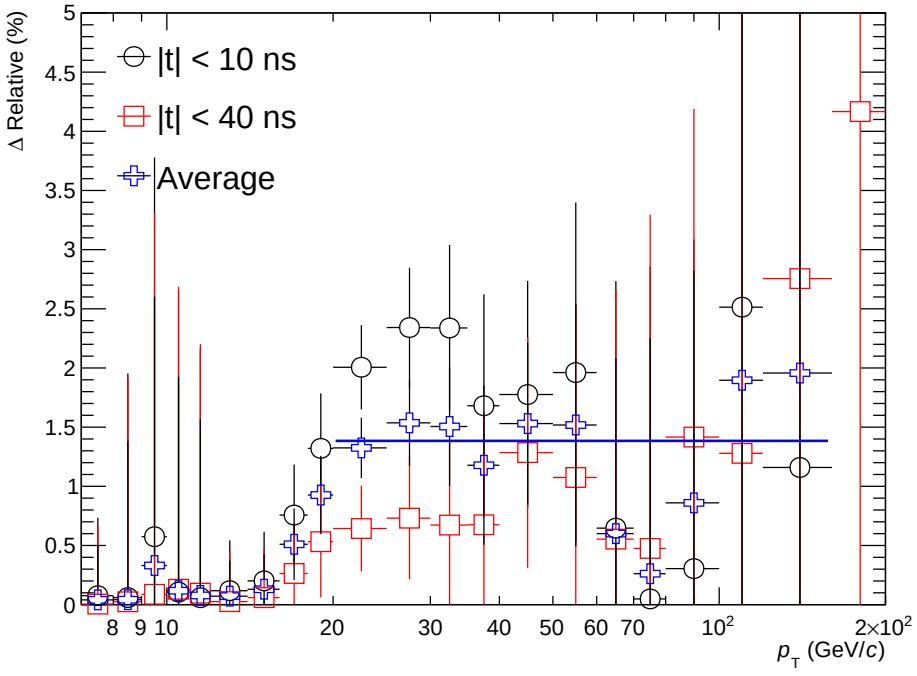

Figure 5.11: Relative uncertainty in % when comparing the time cut $|t| < 20$ ns to $|t| < 10$, 40 ns and their average. The average is fitted above 20 GeV/c by a constant resulting in 1.4%.

5.2.2 The shower shape description and its selection in signal region

The description of the shower shape in simulations can also affect the efficiency measurement, while the effect on the purity is negligible. It is estimated from the difference between standard simulations and those including the modelling of the cross talk observed in the EMCal readout cards, and it is labelled as "no MC tuning".

As a variation here, we turn off the cross-talk emulation in the simulation when calculating the isolated photon efficiency. Half of the deviation from unity of the ratio of the efficiency calculated without cross-talk emulation to the one with emulation is taken as uncertainty, same as what we did at the $\sqrt{s}$ = 7 TeV paper [44]. Figure 5.12 presents the relative uncertainty of the description of shower shape. Above 10 GeV/c, the uncertainty considered is the result of using a constant function fit above 20 GeV/c shown as a red line in the figure. The associated uncertainty decreases with p_{T}^{γ} from 12% at 7 GeV/c to 3.4% at 10 GeV/c and above.

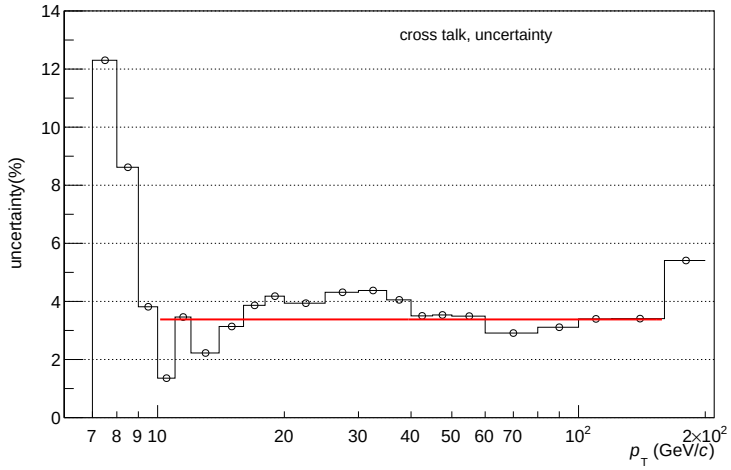

Figure 5.12: Uncertainty from the cross-talk emulation in %, the red line is a constant function fit used as uncertainty above 10 GeV/c.

The choice of the signal range of the σ^2_{long} of narrow photon-like showers is important for the efficiency calculation but also influences the background estimate via a "leakage" of photon showers to the control regions. The uncertainty due to the choice of the signal range is estimated by varying the upper limit of the range to σ^2_{long} = 0.27 and 0.37. Figure 5.13(a) shows the comparison between the variations and the reference yield distribution and ratio to the reference. The associated relative uncertainty is presented in Fig. 5.13(b). A constant function is used to fit 7 to 20 GeV/c and 20 to 70 GeV/c, results can be seen as the red lines in Fig. 5.13(b), and is found to lie at 3.3% below p_{T}^{γ} = 20 GeV/c and 4% above.

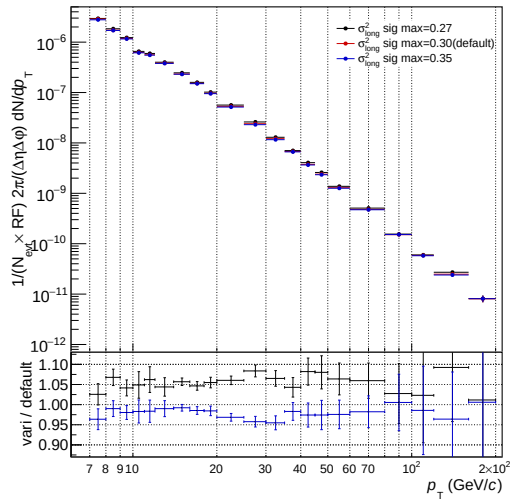

(a)

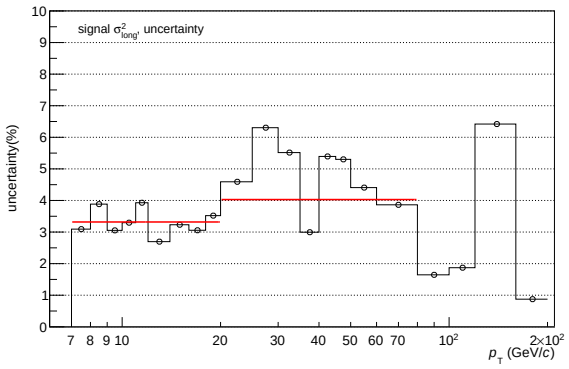

(b)

Figure 5.13: (a) Top panel, cross-section p_T distribution obtained for different signal σ^2_{long} ranges variations. Bottom panel, ratio to the reference range. (b) Associated relative uncertainty in % taking the average of the 2 variations, the red lines are the constant function fit.

5.2.3 Energy scale and material budget

The uncertainty on the energy scale of the EMCal was estimated to be ±1% in pp collisions, determined from the analysis of test beam data and a comparison of the π^0 mass-peak position and the energy-to-momentum ratio of electron tracks in data and Monte Carlo [74]. The x-axis of the spectra is moved up and down by 0.5% and fitted to a power law function: $a \cdot p_T^b$, the average of the relative difference between the fits gave the uncertainty. Figure 5.14 top panel presents the corrected isolated photon spectra scaled x-axis by ±0.5% and fitted to power law function. The uncertainty from each variation is at the bottom panel. The effect of this uncertainty on the measured cross section amounts to 2%.

A material budget uncertainty accounting for an imperfect description in the simulation of the material of the different detectors traversed by photons before they reach the EMCal has been previously determined in Ref. [101] and amounts to 2.1%.

5.2.4 Total uncertainty

Adding all the different sources plus the purity relative uncertainty quadratically, we obtain the total systematic uncertainty on the cross section as the black line in Fig. 5.15. The coloured lines in the figure indicate the uncertainty from different sources, and the gray shading represents the statistical error of the samples. The resulting uncertainty decreases from close to 35% at p_T^γ = 7 GeV/c to close to 10% at p_T^γ = 25 GeV/c and it increases slowly at higher p_T^γ reaching close to 13% at p_T^γ = 200 GeV/c.

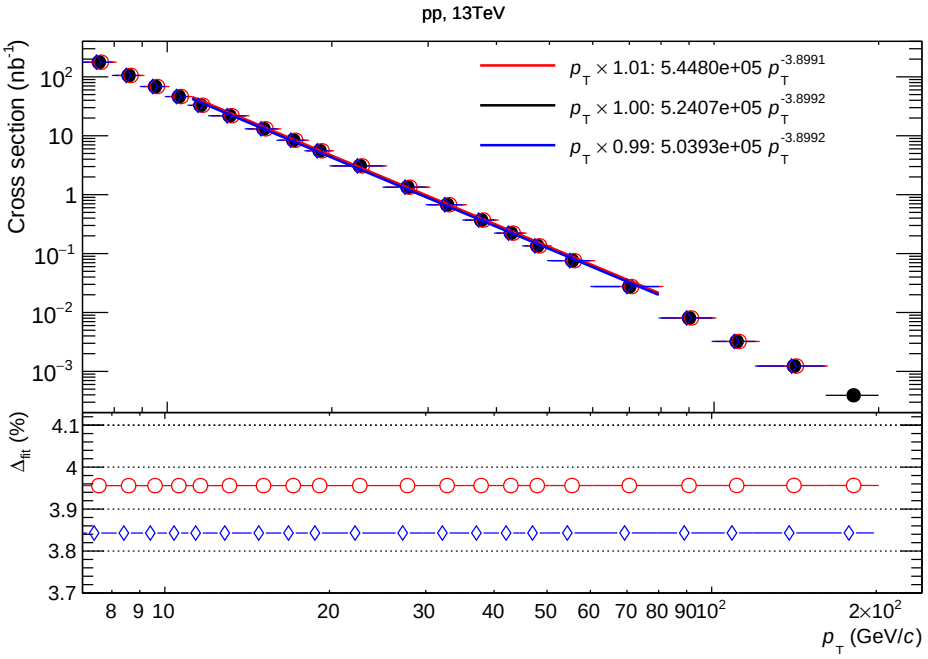

Figure 5.14: Top, corrected isolated photon spectra scaled x axis by ±0.5% and fitted to power law function. Bottom, relative uncertainty from the energy scale for each variation.

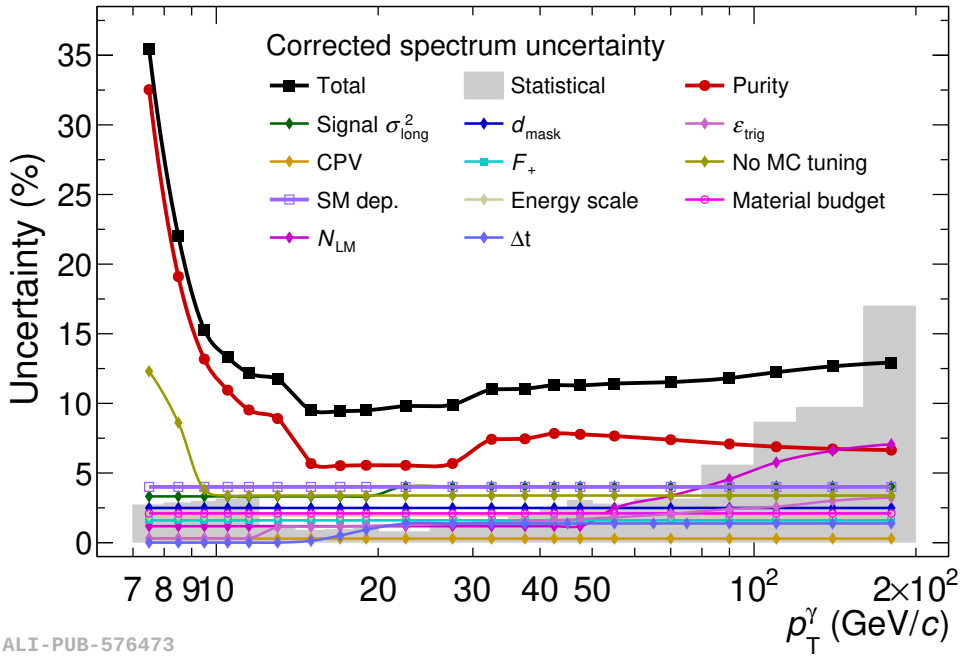

Figure 5.15: Cross section uncertainties, the black line is the total relative uncertainty and the coloured lines are the different uncertainty sources.

The dominant source of the systematic relative uncertainty is the total purity relative uncertainty up to $p_{\mathrm{T}}^{\gamma} = 100$ GeV/c, while for larger p_{T}^{γ} the effect of varying the selection on the number of local maxima becomes dominant. Nonetheless, for $p_{\mathrm{T}}^{\gamma} = 100$ GeV/c, the measurement is dominated by statistical uncertainties.

The values of the systematic uncertainties for the different sources and total are reported in Tab. 5.1 for the lowest and highest p_{T} bins and two intermediate but significant ones (above trigger threshold and intermediate p_{T}).

Table 5.1: Summary of uncorrelated relative systematic uncertainties in per cent for selected p_{T} bins of the isolated photon measurement. The luminosity normalization uncertainty of 1.9% is not included in this table.

p_{T} (GeV/c)	7 – 8	10 – 11	40 – 45	160 – 200
σ^2_{long} background range	2.3%	0.4%	0.4%	0.4%
$p_{\mathrm{T}}^{\mathrm{iso,\ ch,\ UE}}$ background range	14.0%	4.7%	0.8%	0.8%
MC scale	9.1%	5.2%	4.2%	4.2%
Isolation probability	27.6%	8.1%	4.8%	4.8%
Fitting	3.2%	2.3%	4.5%	1.8%
Purity total unc.	32.5%	10.9%	7.8%	6.6%
σ^2_{long} signal range	3.3%	3.3%	4.0%	4.0%
No MC tuning ($\varepsilon_{\gamma}^{\mathrm{iso}}$ unc.)	12.3%	3.4%	3.4%	3.4%
Energy scale	2.0%	2.0%	2.0%	2.0%
Trigger effic. $\varepsilon_{\mathrm{trig}}$	0.3%	0.3%	1.6%	3.2%
Material budget	2.1%	2.1%	2.1%	2.1%
SM dependence	4.0%	4.0%	4.0%	4.0%
Charged particle veto	0.3%	0.3%	0.3%	0.3%
N_{LM}	1.2%	1.2%	1.2%	7.1%
F_{+}	1.6%	1.6%	1.6%	1.6%
$d_{\mathrm{bad\ channel}}$	2.5%	2.5%	2.5%	2.5%
Δt	0%	0%	1.4%	1.4%
Yield total unc.	35.4%	13.3%	11.3%	12.9%
Statistical unc.	2.7%	3.1%	2.4%	17.0%

6 Isolated photon measurement results and discussion

This chapter presents the final results of this thesis on the measurement of the isolated-photon production cross section at mid-rapidity in pp collisions at $\sqrt{s}$ = 13 TeV, including the systematic uncertainties discussed in the previous section, and the corresponding discussion and comparison with theoretical models. First, a comparison of isolated-photon purity at different collision energies is presented, revealing minimal variation. Next, the final cross-section distribution for isolated photons within the p_{T}^{γ} range of 7 to 200 GeV/c is examined. The measurement is found to agree with theoretical predictions within the uncertainty. Meanwhile, this work extends significantly those measured by the ATLAS and CMS experiments towards lower p_{T}^{γ} at the same collision energy with a small overlap between the measurements. Finally, this chapter presents a compilation of the x_{T}^{γ} distribution for all available isolated-photon cross section measurements. This work provides the lowest x_{T}^{γ} of any isolated-photon measurements at mid-rapidity to date and is consistent with all existing pp and $\mathrm{p\overline{p}}$ collisions measurements at different energies when the distribution is scaled by $(\sqrt{s})^{4.5}$.

6.1 Isolated photon purity

As discussed in Sec. 4.4, the purity is one of the key correction factors to obtain the isolated prompt photon cross section. It estimates the background from mainly neutral mesons that pass the isolation selection criteria. A priory, this purity will change when changing the collision energy since the photon over π^0 ratio changes as seen in Fig. 1.6. The isolated-photon purity as a function of p_{T}^{γ} for pp collisions at $\sqrt{s}$ = 13 TeV is presented in Fig. 4.21. A comparison of isolated-photon purity for pp collisions at different $\sqrt{s}$ and peripheral Pb–Pb collisions at $\sqrt{s_{\mathrm{NN}}}$, as measured by ALICE is presented in Fig. 6.1 left side. The isolation cone size, with a radius R = 0.4, is the same across all collision systems and energies. For pp collisions at $\sqrt{s}$ = 7 TeV, shown as the black circle, the isolation energy criterion requires that the sum of the p_{T} of charged and neutral particles within the isolation cone to be less than 2 GeV/c, without subtracting the UE contribution [44]. The blue open squares show the purity for pp collision at $\sqrt{s}$ = 5.02 TeV [51] and orange bullets at $\sqrt{s}$ = 8 TeV [52], and the red squares for peripheral Pb–Pb collisions at $\sqrt{s_{\mathrm{NN}}}$ = 5.02 TeV [51]. As for the measurement reported in this thesis in pp collisions at $\sqrt{s}$ = 13 TeV (pink crosses), the isolation energy threshold is set to 1.5 GeV/c but in contrast, the UE contribution to the isolation cone is subtracted event by event [51]. Figure 6.1-right shows the purity calculated from PYTHIA simulations for the same collision systems and energies. Note that the MC and data purity are not expected to be exactly in agreement but the trends and magnitude should be close.

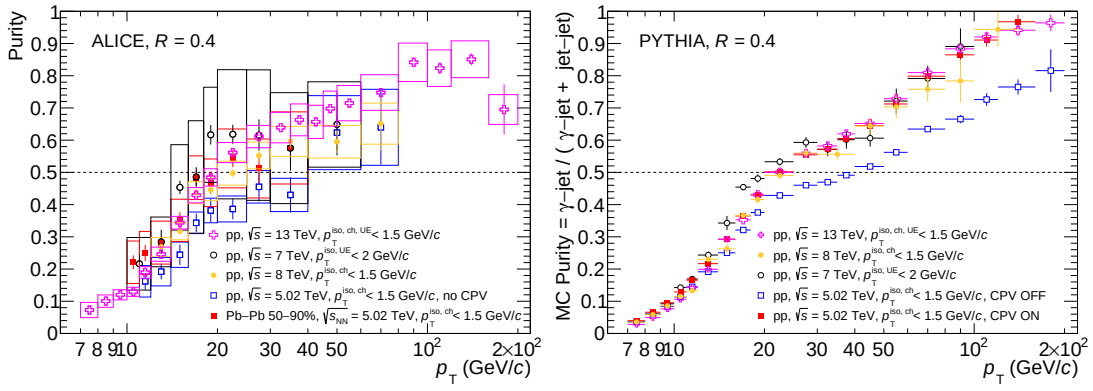

Figure 6.1: Isolated-photon purity in pp collisions at $\sqrt{s}$ = 5.02, 7, 8, 13 TeV and 50–90% Pb–Pb collisions (peripheral collisions similar to pp collisions) at $\sqrt{s_{\rm NN}}$ = 5.02 TeV. All purities are shown for ALICE measurement (left) and PYTHIA MC (right) calculated as the ratio of prompt photons from γ–jet processes over prompt photons plus clusters from jet–jet processes all passing the isolation and shower shape selection criteria. Isolation energy ($p_{\rm T}^{\rm iso}$) changes from isolation using only charged particles (pp $\sqrt{s}$ = 13 TeV, 8 TeV and 5.02 TeV, and Pb–Pb $\sqrt{s_{\rm NN}}$ = 5.02 TeV) and using neutral (calorimeter) and charged particle information (pp $\sqrt{s}$ = 7 TeV), and subtracting the underlying event from the isolation energy (pp $\sqrt{s}$ = 5.02 TeV and 8 TeV, and Pb–Pb $\sqrt{s_{\rm NN}}$ = 5.02 TeV) and not subtracting it (pp $\sqrt{s}$ = 7 and 13 TeV). The cone size is R = 0.4 common to all systems. The charged particle veto selection (CPV) discussed in Sec. 3.5.2 is used in all the measurements except pp collisions at $\sqrt{s}$ = 5.02 TeV. The measured purity at $\sqrt{s}$ = 7 TeV in pp collision is from Ref. [44], at $\sqrt{s_{\rm NN}}$ = 5.02 TeV in pp and Pb–Pb collisions are from Ref. [51] and $\sqrt{s}$ = 8 TeV in pp collision is from Ref. [52].

The purity distribution at different energies in pp collisions shows minimal variation both in experimental measurements and MC simulations (Fig. 6.1–right). Only the purity for pp collisions at $\sqrt{s}$ = 5.02 TeV seems to be slightly lower in all the $p_{\rm T}$ ranges compared to the other pp collision energies. The MC results, shown on the right, confirm this observation with reduced statistical uncertainty. In contrast, the peripheral Pb–Pb collisions at $\sqrt{s_{\rm NN}}$ = 5.02 TeV, which should have similar behavior as pp collisions at the same collision energy, exhibit purity similar to those observed at different energies in pp collisions. The main difference between the pp and Pb–Pb analyses at $\sqrt{s_{\rm NN}}$ = 5.02 TeV is the use of the cluster-track matching selection veto (see Sec. 3.5.2) that was not applied in the pp analysis due to the not inclusion of the TPC in the data taking for this sample (note that ITS tracks were used to calculate $p_{\rm T}^{\rm iso,\ ch}$). This explains the lower purity. In pp collisions at $\sqrt{s}$ = 7 TeV one can observe slightly higher purity around 15–20 GeV/c both in data and simulation. The origin is not clear but it could be due to a reduced acceptance of the calorimeter ($\eta < 0.27$ compared to $\eta < 0.67$ in the other measurements) that is used in this sample and the inclusion of DCal in the $\sqrt{s}$ = 13 TeV sample. Also, the cross-talk in the central η region (missing in DCal) compared to the external region considered (used in the $\sqrt{s}$ = 13 TeV analysis) is larger which could impact the separation of single and merged photons. It may be possible a better rejection is obtained including the neutral component in the isolation that is not reproduced reducing the isolation momentum selection from 2 GeV/c to 1.5 GeV/c for only

charged particles. I find that the purity depends more on the selection criteria than the collision energy, and that the use or not of the UE subtraction in the isolation momentum is not affecting significantly this correction, at least within the available uncertainties in data. Additionally, one can observe that the large statistics of the $\sqrt{s} = 13$ TeV samples contribute significantly to the reduction of systematic uncertainties, and therefore, the extension of the measurement to the lowest p_{T} so far.

6.2 Differential p_{T} cross section

The isolated-photon cross section as a function of p_{T}^{γ} is presented in Fig. 6.2, covering the range from 7 to 200 GeV/c. Error bars indicate the statistical uncertainties and boxes represent the systematic

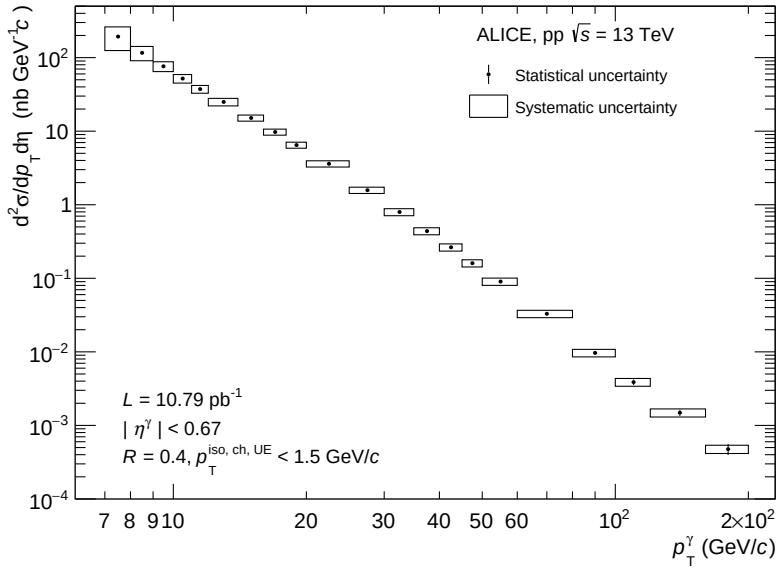

Figure 6.2: Differential cross section of isolated-photons measured in pp collisions at $\sqrt{s} = 13$ TeV. Vertical black lines and open boxes represent data statistical and systematic uncertainties, respectively.

uncertainties, respectively. The result is again shown on the top panel of Fig. 6.3 together with a theoretical calculation using NLO pQCD, performed with JETPHOX 1.3.1 [102, 103]. The parton distribution function used in the calculations is NNPDF4.0 [104], and the fragmentation function is BFG II [105]. The center values of the predictions were obtained by choosing factorization, normalization, and fragmentation scales equal to the photon transverse momentum ($\mu_f = \mu_R = \mu_F = p_{\mathrm{T}}^{\gamma}$). Scale uncertainties were determined varying all scales simultaneously to 0.5 and 2 times their nominal values. The uncertainties related to the PDF are obtained by performing calculations for each of the 101 members of NNPDF4.0. The resulting uncertainties are reported at 90% CL. The isolation criterion in pQCD calculations corresponds to a restriction of the available phase space to final-state radiation in a cone of $R < 0.4$ [102]. The threshold of $p_{\mathrm{T}}^{\mathrm{iso}} < 2$ GeV/c, which includes both charged and neutral particle

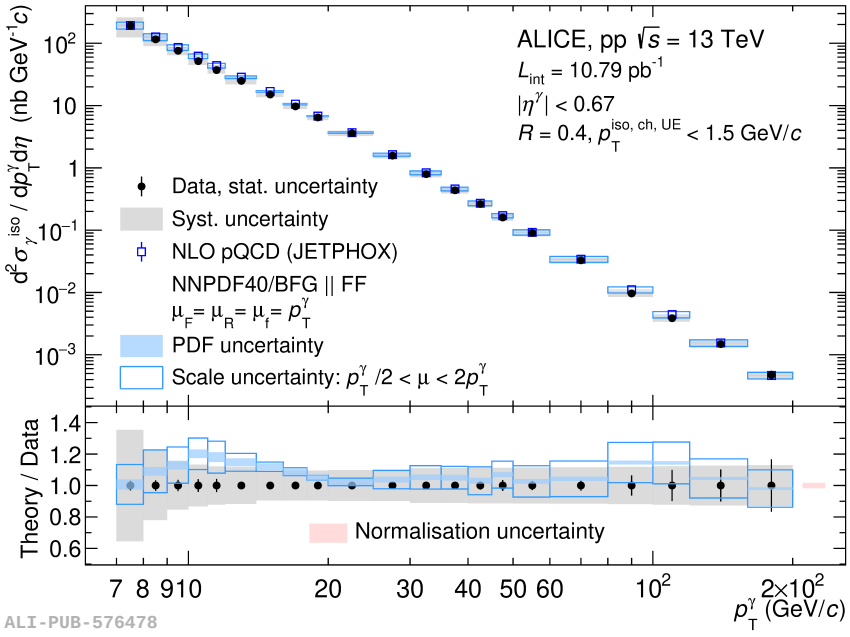

Figure 6.3: Top panel: Differential cross section of isolated-photons measured in pp collisions at $\sqrt{s}$ = 13 TeV. Vertical black lines and grey-filled boxes represent data statistical and systematic uncertainties, respectively. The blue boxes correspond to pQCD calculations with JETPHOX, open boxes for scale uncertainty and filled boxes for PDF uncertainty, respectively. Bottom panel: Ratio between the JETPHOX calculation results and data displayed in the blue boxes, vertical boxes size shows the theory scale and PDF uncertainties. Experimental uncertainties are shown here on the black points centered at unity. The normalization uncertainty of 1.5%, described in Sec. 4.5, is included only in the bottom panel and shown as a red box at 200 GeV/c.

transverse momenta, is used since it is equivalent to the one in data of $p_{\mathrm{T}}^{\mathrm{iso,\ ch,\ UE}} < 1.5$ GeV/c that only uses transverse momenta of charged particles. This was checked by studying the isolation fraction of prompt photons from γ–jet PYTHIA processes. The theoretical predictions describe the measured isolated-photon cross section within uncertainties in the full transverse momentum range of the measurement as demonstrated by the theory-to-data ratio shown in Fig. 6.3 (bottom). In particular, above 20 GeV/c the ratio deviations from unity are small, a constant fit to the points gives 3.6%. An additional normalization uncertainty of 1.5% coming from both measured minimum bias cross section and the rejection factors from the EMCal triggering from Eq. (4.22) is not included in the systematic uncertainties on the data points, but shown as a separate box in the bottom panel with the theory-to-data ratio.

To further check the impact of PDF choices on the theoretical predictions, two additional PDF sets – CT18 [106] and MSHT20 [107] – were used, with no scale or PDF uncertainties estimated, just statistical uncertainty. It is expected that the additional PDFs have similar precision to NNPDF4.0. Figure 6.4 shows the ratios of theoretical predictions to data for all three PDFs. The ratios are found to be similar within the uncertainty across the measured p_{T} range, indicating that the differences among these PDF

parametrizations are not significant at the current level of experimental precision. Our measurement confirms the expectations with the different PDFs, but given that the measured uncertainties are larger than the PDF uncertainties, our result will constrain only partially the PDFs.

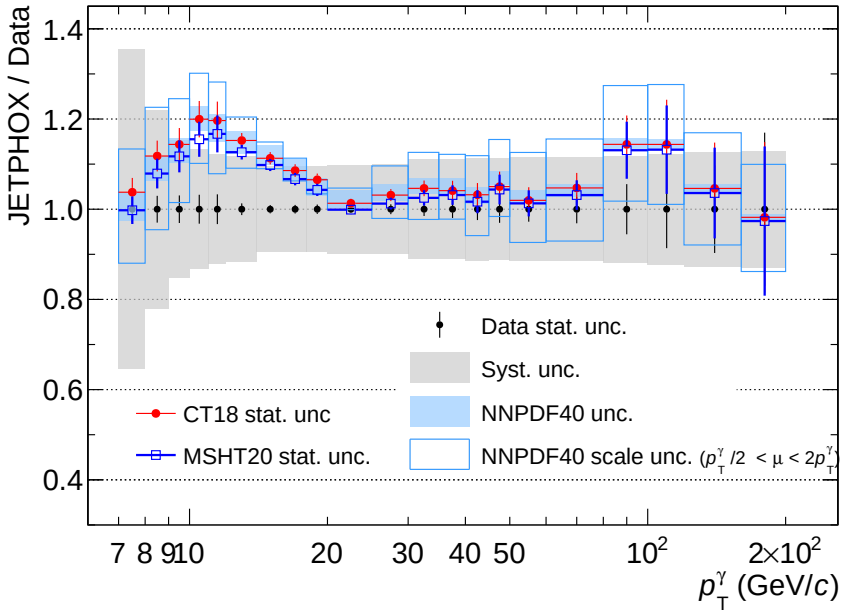

Figure 6.4: Ratios of theory to data using three PDF sets —NNPDF40 (cyan) [104], CT18 (red) [106], and MSHT20 (blue) [107] —as a function of p_T^γ. Experimental uncertainties are shown here on the black points centered at unity, and the experimental systematic uncertainties are represented as gray bands. The ratio between the JETPHOX NNPDF40 calculation results and data displayed in the blue boxes, vertical boxes size shows the theory scale and PDF uncertainties. The ratio between CT18 or MSHT20 and the data is only presented with statistical uncertainty.

The measurement is done for the first time in the p_T^γ range of 7–10 GeV/c in any collision system at the LHC, showing agreement with the theory calculation. The ratio at $10 < p_T^\gamma < 20$ GeV/c tends to deviate from unity, but it is still consistent within uncertainties. The small deviation between data and theory predictions in this p_T^γ region might, in part, be due to a small potential under-correction of the purity, which has a steep rise in the 10–20 GeV/c interval. It is also noteworthy that the systematic uncertainty on the measured cross section in this p_T^γ range is significantly dominated by the uncertainty on the purity determination.

Figure 6.5 presents the differential cross section as a function of p_T^γ for isolated-photons measured with the photon in the EMCal for pp collisions at $\sqrt{s}$ = 5.02, 7, 8, and 13 TeV. The isolation criteria for $\sqrt{s}$ = 5.02, 7, and 13 TeV are given when discussing the purity in Sec. 6.1 and shown in the figure legend. The measurement in pp collisions at $\sqrt{s}$ = 8 TeV, using only charged particle and subtracting the UE from the isolation energy, with an isolation energy threshold of 1.5 GeV/c. All the cross sections

are shown for ALICE measurements and NLO JETPHOX calculation with NNPDF40 and BFG II for the fragmentation function. The NLO pQCD calculations are scaled down by the partonic to hadronic isolation efficiency κ^{iso} (sew Sec. 4.3).

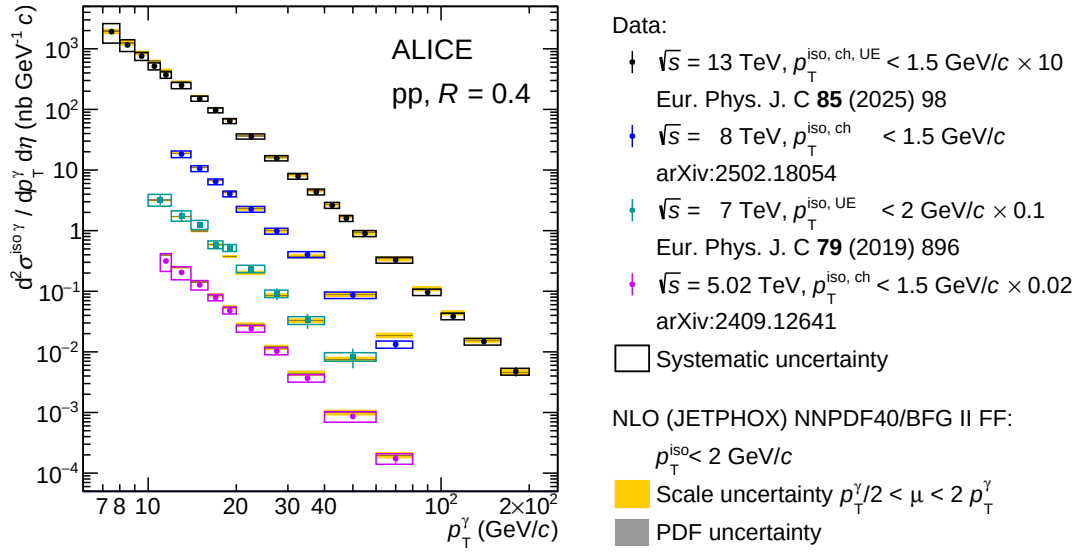

Figure 6.5: Isolated-photon cross section measured with the photon EMCal in pp collision at $\sqrt{s} = 5.02$ [51], 7 [44], 8 [52], and 13 [108] (this work) TeV. All cross sections p_{T} spectra are shown for ALICE measurement and NLO JETPHOX calculation with NNPDF40 and BFG II for the fragmentation function. The NLO calculations are scaled down by the partonic to hadronic isolation efficiency κ^{iso}. The isolation momentum threshold for each collision system is reported in the legend. The cone size is $R = 0.4$ common to all systems.

All measurements at different collision energies exhibit results that are compatible with NLO pQCD calculations. This consistency demonstrates the capability of NLO pQCD to accurately describe direct photon production in pp collisions. Given that these calculations rely on PDFs, NNPDF40 in those calculations, the agreement between theory and experiment underscores the validity of NNPDF40 for modeling direct photon generation in pp collisions. Consequently, this PDF set can be confidently applied to other analyses involving direct photons, thereby providing a robust foundation for further research in this domain.

The comparison of the ratios between theoretical prediction and measurements for p_{T}-differential isolated-photon cross sections in pp collisions at $\sqrt{s}$ = 13 TeV from ALICE [108] (NLO), ATLAS [36] (NNLO), and CMS [45] (NLO) is presented in Fig. 6.6. The comparison is made on ratios of data to prediction using equivalent isolation criteria since those criteria differ among these experiments such that a direct comparison of the isolated-photon cross sections is not fully adequate. There is a small overlap region between ALICE and the other experiments in the p_{T}^{γ} interval between 125 (ATLAS) and

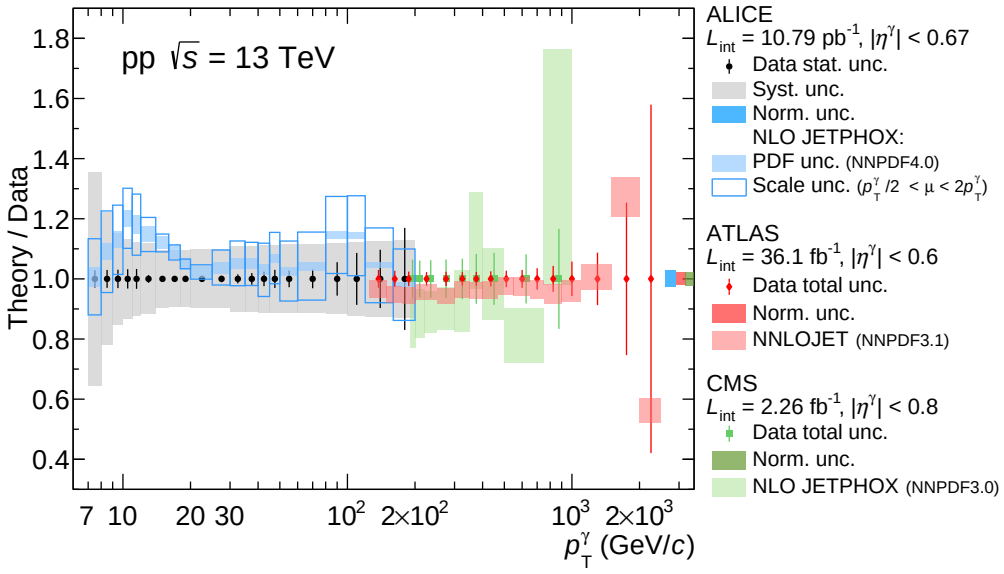

Figure 6.6: Ratio between theory predictions for the isolated-photon differential cross section and measurements for ATLAS [36], CMS [45], and ALICE [108]. The isolation required transverse energy for ATLAS is $E_{\mathrm{T}}^{\mathrm{iso}} < 4.2 \times 10^{-3} \times E_{\mathrm{T}}^{\gamma} + 4.8$ GeV, for CMS is $p_{\mathrm{T}}^{\mathrm{iso,UE}} < 5$ GeV, and for ALICE, this work, is $p_{\mathrm{T}}^{\mathrm{iso,\,ch,\,UE}} < 1.5$ GeV. The isolation radii are $R = 0.4$ for the three. Theory predictions are obtained for ATLAS with NNLOJET [109] NNLO NNPDF3.1 PDFs [110], for CMS with JETPHOX NLO and NNPDF3.0 PDFs [111], and for ALICE with JETPHOX NLO and NNPDF4.0 PDFs [104]. Experimental uncertainties are shown here on the points centered at unity, for CMS and ATLAS statistical and systematic uncertainties are added in quadrature and shown as a vertical error bar. ALICE error bars are statistical uncertainties and boxes are systematic uncertainties. The colored boxes centered at the ratio indicate the theoretical uncertainty on the PDF and scales. The luminosity normalization uncertainty of each experiment is presented as an overall box around unity at the right of the figure centered at unity.

190 (CMS) to 200 GeV/c, where the ratios are in agreement with each other within the uncertainties. It is worth noticing the contribution of ALICE to the isolated-photon measurements in pp collisions at $\sqrt{s} = 13$ TeV since the p_{T}^{γ} range is decreased by an order of magnitude compared to ATLAS and CMS. The ATLAS and CMS results use larger values and different definitions for the isolation momentum selection criterion, about 5 GeV/c for CMS and approximately 4 GeV/c at $p_{\mathrm{T}}^{\gamma} = 200$ GeV/c and increasing with p_{T}^{γ} for ATLAS, both with the same cone radius $R = 0.4$ but including contributions from neutral and charged particles. In JETPHOX predictions, increasing the isolation threshold should reflect a larger fragmentation contribution in the total cross section without necessarily increasing the total isolated-photon cross section compared to smaller isolation momentum selection criteria. However, the theory-to-data ratios should be consistent between the experiments as is observed in the figure. The ALICE NLO-to-data ratio for $p_{\mathrm{T}}^{\gamma} > 20$ GeV/c is almost on top of unity, while CMS (NLO) and ATLAS (NNLO) ratios are consistently below but in agreement with unity within the uncertainties. For ATLAS, the NLO-to-data ratio was also shown in Refs. [36, 112] lying below the NNLO-to-data ratio which might indicate the need for higher pQCD orders when the isolation momentum criterion is not tight enough to

reproduce the contribution from fragmentation photons better.

Figure 6.7-left presents the ratio of the isolated-photon cross section for pp collisions at $\sqrt{s}$ = 13 TeV relative to those at $\sqrt{s}$ = 7 TeV, alongside a comparison with the corresponding ratios calculated at NLO. The ALICE measurement at $\sqrt{s}$ = 7 TeV, obtained from Ref. [44], is divided by the corresponding κ^{iso} since it was not done in the publication (the NLO calculation was multiplied instead by this factor). On the right is the cross section ratio for $\sqrt{s}$ = 13 TeV over $\sqrt{s}$ = 5.02 TeV, taken from Ref. [51].

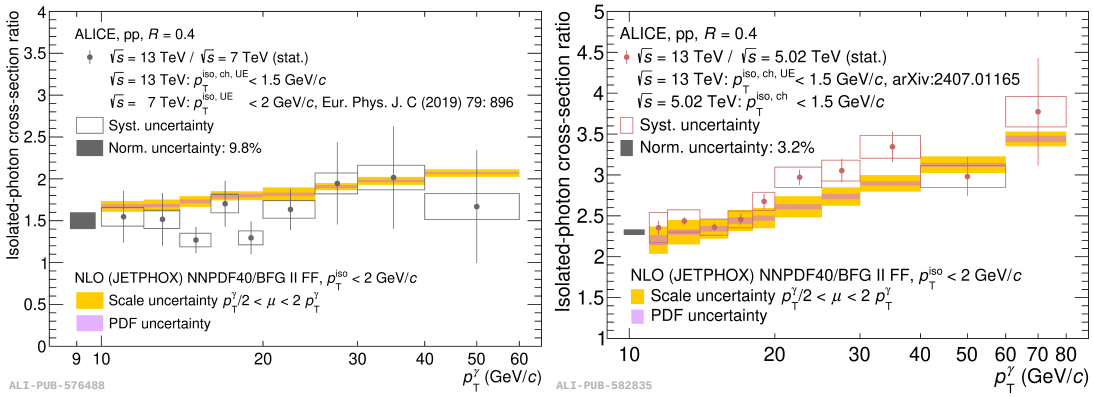

Figure 6.7: Isolated-photon cross-section ratio of pp collisions at $\sqrt{s}$ = 13 TeV (this work, as Ref. [108]) over $\sqrt{s}$ = 7 TeV from Ref. [44] (left) and $\sqrt{s}$ = 5.02 TeV from Ref. [51] in data and NLO calculation from JETPHOX for R = 0.4. Error bars and empty boxes are the data statistical and systematic uncertainties, respectively. Filled boxes represent the theory scale (orange) and PDF (pink) uncertainties.

Almost all systematic uncertainties can be cancelled out in those ratios either completely or partially. Further uncertainty details for the $\sqrt{s}$ = 13 TeV / $\sqrt{s}$ = 7 TeV ratio can be found in ref. [108] and for the $\sqrt{s}$ = 13 TeV / $\sqrt{s}$ = 5.02 TeV ratio in ref. [95]. The uncertainties in these two cross-section ratios are the same for most sources and in some cases the same value, as they are based entirely on 13 TeV measurement. The large normalization uncertainty in $\sqrt{s}$ = 13 TeV / $\sqrt{s}$ = 7 TeV compared to $\sqrt{s}$ = 13 TeV / $\sqrt{s}$ = 5.02 TeV is due to the trigger uncertainty of the 7 TeV sample.

For both ratios, the data agree with NLO pQCD calculations within the uncertainties. For more detail, we can find that in the left plot, the ratio of $\sqrt{s}$ = 13 TeV over $\sqrt{s}$ = 7 TeV, the data ratio seems rather constant as a function of p_{T}^{γ}, showing a value of about 1.5, but is also compatible within the uncertainties to the NLO slow rise from close to 1.6 at 10–12 GeV/c to close to 2.1 at 40–60 GeV/c. The $\sqrt{s}$ = 13 TeV over $\sqrt{s}$ = 5.02 TeV ratio follows a clear rise with increasing p_{T}^{γ} from about 2.2 at 11 GeV/c to close to 3.5 at 80 GeV/c, p_{T} dependence better seen than in the $\sqrt{s}$ = 13 TeV / $\sqrt{s}$ = 7 TeV ratio due to the measurement at $\sqrt{s}$ = 5.02 TeV has more statistics but also lower $\sqrt{s}$. For completeness, Fig. 6.8 shows the cross section ratio for $\sqrt{s}$ = 7 TeV to the one at $\sqrt{s}$ = 5.02 TeV. The data show a

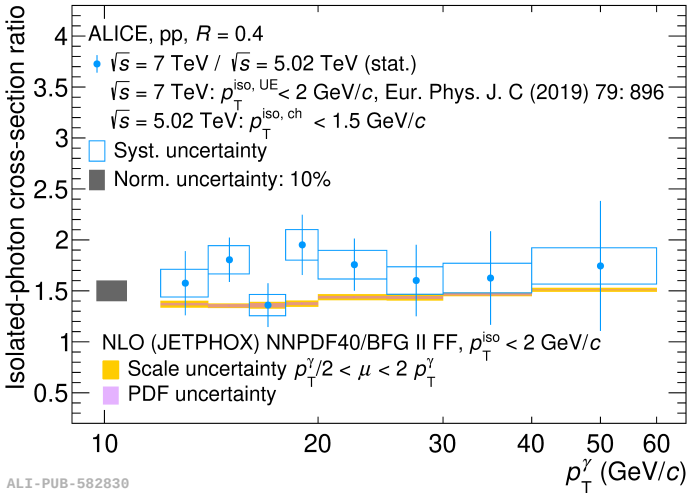

Figure 6.8: Ratio of isolated-photon cross sections measured in pp collisions at $\sqrt{s}$ = 7 TeV (taken from Ref. [44]) over the one at $\sqrt{s}$ = 5.02 TeV from Ref. [51] compared to NLO calculations from JETPHOX shown as colored boxes.

value at the level of 1.5 with a possible slight rise with p_{T}^{γ}. The magnitude of the ratio is in agreement with the NLO pQCD predictions. Unfortunately, the small $\sqrt{s}$ difference and the large experimental uncertainties do not allow us to draw a firm conclusion on the small rise with p_{T}^{γ} predicted by the NLO pQCD calculations: from 1.35 at 11–12 GeV/c, up to about 1.5 at 40–60 GeV/c.

The agreement of the isolated-photon cross section ratio in data and NLO pQCD calculations shown in Fig. 6.7 and Fig. 6.8 from Ref. [51] for the ratio $\sqrt{s}$ = 13 TeV over $\sqrt{s}$ = 5.02 TeV indicates that the underlying mechanisms in the theoretical approach are valid.

6.3 x_{T}^{γ} distribution

For a comparison of cross sections measured at different $\sqrt{s}$, it is more appropriate to use the variable x_{T}^{γ}, as defined in Eq. (1.4) , which is also closely related to the Bjorken x [113] at mid-rapidity. A compilation of all available data on isolated-photon cross section measurements in collider experimentshas been performed in [44, 114] and all x_{T}^{γ} spectra are compatible with a single curve when scaled by the factor $(\sqrt{s})^{n}$ with $n = 4.5$.

The measurement of this work and the latest LHC measurements are presented in Fig. 6.9 together with older measurements at different collision energies. A common trend was observed in all the measurements. The measurement reported here, allows us to extend the x_{T}^{γ} reach to the lowest values measured at mid-rapidity, which is reaching $1.1 - 3 \times 10^{-3}$ for the first time.

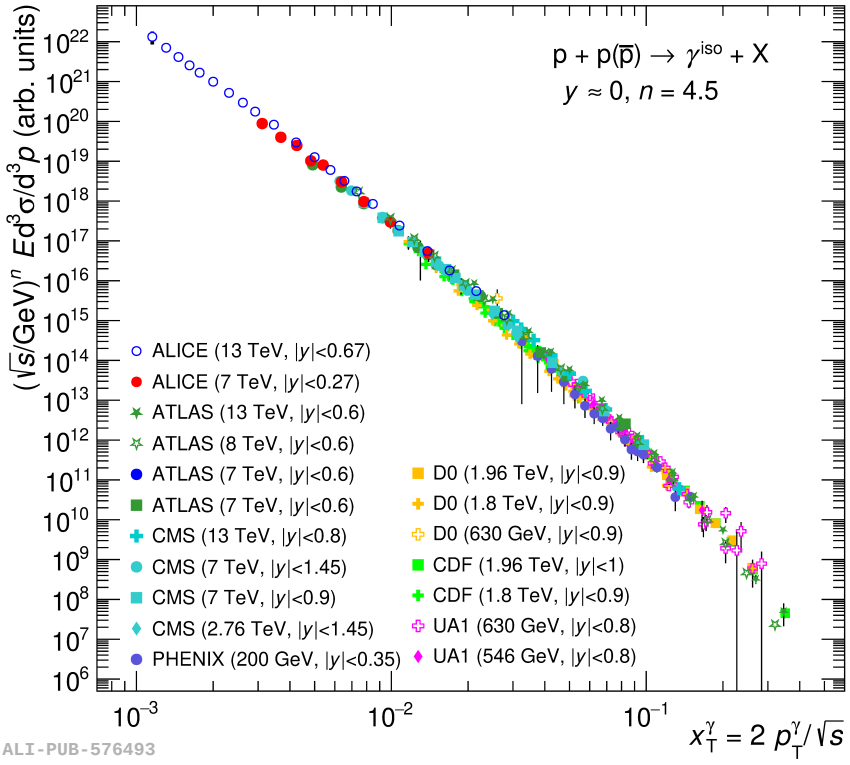

Figure 6.9: ALICE data compared to previous measurements of isolated-photon spectra in pp and p$\bar{\text{p}}$ collisions as a function of x_{T} where the invariant cross sections have been scaled by $(\sqrt{s})^n$ with $n = 4.5$ (taken from Ref. [114]). For this comparison, only the results covering mid-rapidity are shown.

The agreement between the invariant cross sections at different $\sqrt{s}$ at mid-rapidity, suggests that all data are sensitive to the same production mechanisms. This measurement will help to constrain further the gluon PDF at mid-rapidity in the region $x \approx 1 - 3 \times 10^{-3}$ and reduce its uncertainty values. However, the value $n = 4.5$ deviates from the $1/(p_{\text{T}}^{\gamma})^{n=4}$ dependence expected for the leading-twist partonic production mechanisms. This is due to effects like the running coupling and the evolution of PDFs, and indicates significant contributions from fragmentation photons and higher-twist diagrams [115].

7 Conclusion and outlook

We have reported the isolated-photon cross section ($p_{\mathrm{T}}^{\mathrm{iso,\ ch}} < 1.5$ GeV/c and $R = 0.4$) in pp collisions at $\sqrt{s} = 13$ TeV at mid-rapidity ($|\eta| < 0.67$) using a data sample collected with ALICE in years 2016, 2017, and 2018, with integrated luminosity $\mathcal{L}_{\mathrm{int}} = 10.79\ \mathrm{pb}^{-1}$. The measurement is performed in the photon transverse momentum range $7 < p_{\mathrm{T}}^{\gamma} < 200$ GeV/c and correspondingly $1.1 \times 10^{-3} < x_{\mathrm{T}}^{\gamma} < 30.8 \times 10^{-3}$.

In high-energy pp collisions like the ones provided by the LHC, measurements of the particle productions and cross-sections serve as critical tools to test perturbative QCD theory predictions and constrain the FF and the proton PDF. Direct prompt photons produced via $2 \rightarrow 2$ hard scattering processes offer valuable insights into the gluon PDF in the proton, which is not well known, owing to their clean experimental signatures and direct connection to the initial–state partons.

In the ALICE experiment, the photon measurement at high energy relies on the high-precision detection and triggering of the EMCal. The photon triggering capability combined with the particle cluster cell energy and spread information (shower shape) from the EMCal are used for the full exploitation of the LHC luminosity and photon candidate selection, respectively. The shower shape is used to distinguish between single photon showers, $0.1 < \sigma^2_{\mathrm{long}} < 0.3$, and showers from overlapping pairs of photons from neutral meson decays at high transverse momentum (mainly π^0 but also η above 6 and 40 GeV/c, respectively) $\sigma^2_{\mathrm{long}} > 0.4$. This discrimination is further improved towards direct prompt photon selection accounting the charged hadronic background in a cone around the candidate: the isolation analysis. The isolation condition is set as the sum of the charged particles p_{T} is less than 1.5 GeV/c in an isolation cone of $R = 0.4$ with the candidate photon as the trigger.

The measurement presented here was confronted with two main problems that needed careful checks and developments during my thesis work. On one hand, when analyzing the signals of very high p_{T} photon candidates ($E > 100$ GeV), a significant contribution from anomalous pseudo-signals created by neutrons hitting directly the APD of the EMCal towers was found. Such fake signals induce significant electronics cross-talk signals in nearby cells to the main one in the calorimeter, creating clusters with an energy spread that could be misidentified as photons. Since this cross-talk only affects cells sitting in the same readout card, and since at such high energies real photon clusters deposit their energy in several readout cards, an additional novel selection of clusters was implemented for this work, that the cluster must have an energy spread in at least two of the readout cards for high energy clusters

($E > 80$ GeV/c). On the other hand, the EMCal trigger performance and stability are key elements of this measurement since it relies heavily on the Run 2 EMCal-triggered sample. While checking the candidate photon rates it was found that different regions of the calorimeter had different responses which depended also on the period. This triggered a careful study on the trigger activity to identify and mask dead or too active areas (electronic noise, imperfect calibration) in the calorimeter. With those masks, needed for all EMCal-related analyses, the agreement on the performance between regions was significantly improved.

In this work, the measurement covers a larger photon p_{T} range than the previous measurement of ALICE at $\sqrt{s} = 7$ TeV in pp collisions which is $10 < p_{\mathrm{T}}^{\gamma} < 60$ GeV/c and $2.9\times10^{-3} < x_{\mathrm{T}}^{\gamma} < 17.1\times10^{-3}$, due to the 20 times larger luminosity but also to the larger photon acceptance considered. The final results are compared to pQCD calculations and ATLAS and CMS measurements. The mutual agreement of the data sets with the theory supports the theoretical calculations and demonstrates the consistency of the different measurements.

The measurement is done for the first time in the range of 7–10 GeV/c in any collision systems at the LHC. It extends down by an order of magnitude compared to ATLAS ($p_{\mathrm{T}}^{\gamma} > 125$ GeV/c) and CMS ($p_{\mathrm{T}}^{\gamma} > 190$ GeV/c) at the same collision energy. The lower p_{T}^{γ} reach of ALICE compared to the other LHC experiments at mid-rapidity will be useful for future studies of isolated-photon cross sections and correlations of isolated photons to jets or hadrons used to constrain pQCD calculations, PDFs, and FFs, in particular. Moreover, this work lays a foundation for studying medium-induced modifications of hard probes in nucleus–nucleus collisions and the QGP-like modification factor in small colliding systems.

The measurement also provides the lowest Bjorken-x probed with isolated photons at mid-rapidity to date, showing an agreement between all the measurements with a common scale of $(\sqrt{s})^{n=4.5}$ over several orders of $x_{\mathrm{T}}^{\gamma} \approx$ Bjorken-x. The low-x measured will provide constraints on the gluon PDF.

With a significant increase of the luminosity at the LHC Run 3 and Run 4, the isolated photon measurements can be done with reduced systematic uncertainties as we have seen when comparing the purity of Run 2 statistically rich $\sqrt{s} = 13$ TeV measurements to other samples, adding stronger constraints to the theoretical predictions. With the increase of the sample size, another interesting measurement could be the isolated-photon cross section as a function of the particle multiplicity in pp collisions. Since photons are not modified in the hypothetical presence of a QCD medium, such measurement can be used to estimate the biases that the particle-multiplicity selection induces (presence of jets in the event, collision geometrical considerations) in all other particle or jet cross-section particle-multiplicity-based measure-

ments. In particular, the role of the particle-multiplicity selection in small systems like pp collisions should be considered, as it may influence observed phenomena and shed light on the potential existence of QGP in these systems. Although QGP is traditionally associated with heavy-ion collisions, recent studies suggest that under certain conditions, small systems might also exhibit QGP-like behavior [116]. Furthermore, by comparing the results from pp collisions with those from heavy-ion collisions, one can disentangle cold nuclear matter effects from hot QCD medium effects. This comparative approach will enhance our ability to isolate the specific contributions of the QGP to parton energy loss and fragmentation, providing clearer evidence for the existence and properties of the QGP. The comparison becomes especially significant when examining small systems, as it may reveal new mechanisms or conditions for QGP formation, thereby expanding our knowledge of this extreme state of matter.

The studies of the angular distributions and kinematic properties of isolated photon–jet pairs will be instrumental in refining our understanding of parton fragmentation processes since photon remaining unchanged while traversing the medium, sets the reference of the initial hard scattering kinematics, whereas the associated hadrons convey the information on the modifications experienced by the parton inside the medium, therefore, one can tag the jets with isolated-photons and study the medium induced jet modifications and induced wake effects using the future data available at LHC and ALICE.

References

[1] E. Rutherford. LXXIX. The scattering of α and β particles by matter and the structure of the atom. *The London, Edinburgh, and Dublin Philosophical Magazine and Journal of Science*, 21(125):669–688, 2009.

[2] E. Marsden. On a diffuse reflection of the α-particles, 2000.

[3] CERN. Cosmic Rays Home page. Website. Last accessed on 10/12/2024.

[4] D. Dominguez. Standard Model. Le modèle standard. General Photo, 2015.

[5] M. D. Schwartz. *Quantum Field Theory and the Standard Model*. Cambridge University Press, 2013.

[6] T. Lancaster and S. J. Blundell. *Quantum Field Theory for the Gifted Amateur*. Oxford University Press, 2014.

[7] R. P. Feynman. Space-Time Approach to Quantum Electrodynamics. *Phys. Rev.*, 76:769–789, 1949.

[8] G. Dissertori, I. G. Knowles, and M. Schmelling. *Quantum Chromodynamics: High Energy Experiments and Theory*. Oxford University Press, 2009.

[9] F. Wilczek. QCD Made Simple. *Physics Today*, 53(8):22–28, 2000.

[10] Particle Data Group. Review of Particle Physics. *PTEP*, 2020(8):083C01, 2020.

[11] J. C. Collins, D. E. Soper, and G. F. Sterman. Factorization of Hard Processes in QCD. *Adv. Ser. Direct. High Energy Phys.*, 5:1–91, 1989.

[12] P. Skands. Introduction to QCD. In *Searching for New Physics at Small and Large Scales*, pages 341–420. WORLD SCIENTIFIC, 2013.

[13] V.N. Gribov and L.N. Lipatov. Deep inelastic electron scattering in perturbation theory. *Phys. Lett. B*, 37(1):78–80, 1971.

[14] G. P. Salam. An Introduction to leading and next-to-leading BFKL. *Acta Phys. Polon. B*, 30:3679–3705, 1999.

[15] E. Perez and E. Rizvi. The Quark and Gluon Structure of the Proton. *Rept. Prog. Phys.*, 76(4):046201, 2013.

[16] H1 and ZEUS Collaboration. Combination of measurements of inclusive deep inelastic $e^{\pm}p$ scattering cross sections and QCD analysis of HERA data. *Eur. Phys. J. C*, 75(12):580, 2015.

[17] ALICE Collaboration. Letter of Intent: A Forward Calorimeter (FoCal) in the ALICE experiment. Technical report, CERN, 2020.

[18] A. H. Mueller. A Simple derivation of the JIMWLK equation. *Phys. Lett. B*, 523:243–248, 2001.

[19] T. Lappi and H. Mäntysaari. Next-to-leading order Balitsky-Kovchegov equation with resummation. *Phys. Rev. D*, 93(9):094004, 2016.

[20] J. Rojo, A. Accardi, R. D Ball, and et al. The PDF4LHC report on PDFs and LHC data: results from Run I and preparation for Run II. *J. Phys. G*, 42(10):103103, 2015.

[21] H1 Collaboration. Measurement of the proton structure function F2 (x, Q2) in the low-x region at HERA. *Nucl. Phys. B*, 407(3):515–535, 1993.

[22] ATLAS Collaboration. Determination of the strong coupling constant α_s from transverse energy–energy correlations in multijet events at $\sqrt{s} = 8$ TeV using the ATLAS detector. *Eur. Phys. J. C*, 77(12), 2017.

[23] J. J. Ethier and E. R. Nocera. Parton Distributions in Nucleons and Nuclei. *Annual Review of Nuclear and Particle Science*, 70:43–76, 2020.

[24] J. Paquet, C. Shen, G. S. Denicol, and et al. Production of photons in relativistic heavy-ion collisions. *Phys. Rev. C*, 93(4):044906, 2016.

[25] P. Aurenche, P. Chiappetta, M. Fontannaz, and et al. Next to leading order bremsstrahlung contribution to prompt-photon production. *Nucl. Phys. B*, 399(1):34–62, 1993.

[26] C. Gale. Photon Production in Hot and Dense Strongly Interacting Matter. *Landolt-Bornstein*, 23:445, 2010.

[27] J. Pumplin, D. R. Stump, J. Huston, and et al. New generation of parton distributions with uncertainties from global QCD analysis. *JHEP*, 07:012, 2002.

[28] L. Bourhis, M. Fontannaz, and J. P. Guillet. Quark and gluon fragmentation functions into photons. *Eur. Phys. J.*, 2(3):529–537, 1998.

[29] B. A. Kniehl, G. Kramer, and B. Potter. Fragmentation functions for pions, kaons, and protons at next-to-leading order. *Nucl. Phys. B*, 582:514–536, 2000.

[30] Photons Working Group. Hard probes in heavy-ion collisions at the LHC: Photon physics in heavy ion collisions at the LHC. *arXiv*, 2004.

[31] F. Jonas. *Probing the initial state of heavy-ion collisions with isolated prompt photons*. PhD thesis, University of Münster, 2023.

[32] J. M. Campbell, R. K. Ellis, and C. Williams. Direct Photon Production at Next-to–Next-to-Leading Order. *Phys. Rev. Lett.*, 118(22):222001, 2017.

[33] R. Ichou and D. d'Enterria. Sensitivity of isolated photon production at TeV hadron colliders to the gluon distribution in the proton. *Phys. Rev. D*, 82:014015, 2010.

[34] M. McLaughlin, J. Biel, C. Bromberg, and et al. Inclusive Production of Direct Photons in 200-GeV/c Collisions. *Phys. Rev. Lett.*, 51:971–974, 1983.

[35] ATLAS Collaboration. Measurement of the cross section for inclusive isolated-photon production in pp collisions at $\sqrt{s}$ = 13 TeV using the ATLAS detector. *Phys. Lett. B*, 770:473–493, 2017.

[36] ATLAS Collaboration. Measurement of the inclusive isolated-photon cross section in pp collisions at $\sqrt{s}$ = 13 TeV using 36 fb^{-1} of ATLAS data. *JHEP*, 2019(10):203, 2019.

[37] W. Vogelsang and M. R. Whalley. A compilation of data on single and double prompt photon production in hadron - hadron interactions. *J. Phys. G*, 23(7A):A1, 1997.

[38] S. Holmes, R. S. Moore, and V. Shiltsev. Overview of the Tevatron Collider Complex: Goals, Operations and Performance. *JINST*, 6(08):T08001, 2011.

[39] ATLAS Collaboration. Measurement of the inclusive isolated prompt photon cross section in pp collisions at $\sqrt{s}$ = 7 TeV with the ATLAS detector. *Phys. Rev. D*, 83:052005, 2011.

[40] ATLAS Collaboration. Measurement of the inclusive isolated prompt photon cross-section in pp collisions at $\sqrt{s}$ = 7 TeV using 35 pb^{-1} of ATLAS data. *Phys. Lett. B*, 706:150–167, 2011.

[41] CMS Collaboration. Measurement of the Differential Cross Section for Isolated Prompt Photon Production in pp Collisions at 7 TeV. *Phys. Rev. D*, 84:052011, 2011.

[42] CMS Collaboration. Measurement of the Isolated Prompt Photon Production Cross Section in pp Collisions at $\sqrt{s}$ = 7 TeV. *Phys. Rev. Lett.*, 106:082001, 2011.

[43] CMS Collaboration. Measurement of isolated photon production in pp and Pb–Pb collisions at $\sqrt{s_{NN}}$ = 2.76 TeV. *Phys. Lett. B*, 710:256–277, 2012.

[44] ALICE Collaboration. Measurement of the inclusive isolated photon production cross section in pp collisions at $\sqrt{s}$ = 7 TeV. *Eur. Phys. J. C*, 79(11):896, 2019.

[45] CMS Collaboration. Measurement of differential cross sections for inclusive isolated-photon and photon+jets production in proton-proton collisions at $\sqrt{s}$ = 13 TeV. *Eur. Phys. J. C*, 79(1):20, 2019.

[46] ALICE Collaboration. Multiplicity and event-scale dependent flow and jet fragmentation in pp collisions at $\sqrt{s}$ = 13 TeV and in p–Pb collisions at $\sqrt{s_{\mathrm{NN}}}$ = 5.02 TeV. *JHEP*, 03:092, 2024.

[47] ALICE Collaboration. Transverse momentum spectra and nuclear modification factors of charged particles in pp, p–Pb and Pb–Pb collisions at the LHC. *JHEP*, 11:013, 2018.

[48] ALICE Collaboration. Production of charged pions, kaons, and (anti-)protons in Pb–Pb and inelastic pp collisions at $\sqrt{s_{NN}}$ = 5.02 TeV. *Phys. Rev. C*, 101(4):044907, 2020.

[49] CMS Collaboration. Constraints on the Initial State of Pb–Pb Collisions via Measurements of Z-Boson Yields and Azimuthal Anisotropy at $\sqrt{s_{\mathrm{NN}}}$ = 5.02 TeV. *Phys. Rev. Lett.*, 127:102002, 2021.

[50] ALICE Collaboration. Centrality determination of Pb–Pb collisions at $\sqrt{s_{NN}}$ = 2.76 TeV with ALICE. *Phys. Rev. C*, 88:044909, 2013.

[51] ALICE Collaboration. Measurement of the inclusive isolated-photon production cross section in pp and Pb–Pb collisions at $\sqrt{s_{\mathrm{NN}}}$ = 5.02 TeV. *Eur. Phys. J. C*, 85(5):553, 2025.

[52] ALICE Collaboration. Measurement of isolated prompt photon production in pp and p-Pb collisions at the LHC. *arXiv*, Feb. 2025.

[53] ALICE Collaboration. Measurement of isolated photon-hadron correlations in $\sqrt{s_{\mathrm{NN}}}$ = 5.02 TeV pp and p–Pb collisions. *Phys. Rev. C*, 102(4):044908, 2020.

[54] C. Arata. *Isolated photon-hadron correlations in Pb–Pb collisions at $\sqrt{s_{\mathrm{NN}}}$ = 5.02 TeV*. PhD thesis, Université Grenoble Alpes, 2024.

[55] L. Evans and P. Bryant. LHC Machine. *JINST*, 3(08):S08001, 2008.

[56] E. Lopienska. The CERN accelerator complex, layout in 2022. Complexe des accélérateurs du CERN en janvier 2022. General Photo, 2022.

[57] J. Wenninger. LHC status and performance. *PoS*, CHARGED2018:001, 2019.

[58] ATLAS Collaboration. The ATLAS Experiment at the CERN Large Hadron Collider. *JINST*, 3(08):S08003, 2008.

[59] CMS Collaboration. The CMS experiment at the CERN LHC. *JINST*, 3(08):S08004, 2008.

[60] ATLAS Collaboration. Observation of a new particle in the search for the Standard Model Higgs boson with the ATLAS detector at the LHC. *Phys. Lett. B*, 716(1):1–29, 2012.

[61] CMS Collaboration. Observation of a new boson at a mass of 125 GeV with the CMS experiment at the LHC. *Phys. Lett. B*, 716(1):30–61, 2012.

[62] LHCb Collaboration. The LHCb Detector at the LHC. *JINST*, 3(08):S08005, 2008.

[63] ALICE Collaboration. The ALICE experiment at the CERN LHC. *JINST*, 3(08):S08002, 2008.

[64] ALICE Collaboration. *ALICE forward detectors: FMD, TO and VO: Technical Design Report*. Technical design report. ALICE. CERN, Geneva, 2004. Submitted on 10 Sep. 2004.

[65] A. Tauro. ALICE Schematics. General Photo, 2017.

[66] ALICE collaboration. Performance of the ALICE VZERO system. *JINST*, 8(10):P10016, 2013.

[67] ALICE Collaboration. Alignment of the ALICE Inner Tracking System with cosmic-ray tracks. *JINST*, 5(03):P03003, 2010.

[68] ALICE Collaboration. Technical Design Report for the Upgrade of the ALICE Inner Tracking System. *J. Phys. G*, 41(8):087002, 2014.

[69] ALICE collaboration. Upgrade of the ALICE ITS detector. *Nucl. Instrum. Meth. A*, 1032:166632, 2022.

[70] ALICE Collaboration. The ALICE TPC, a large 3-dimensional tracking device with fast readout for ultra-high multiplicity events. *Nucl. Instrum. Meth. A*, 622:316–367, 2010.

[71] ALICE Collaboration. Study of the dE/dx resolution of a GEM Readout Chamber prototype for the upgrade of the ALICE TPC. *EPJ Web Conf.*, 174:01002, 2018.

[72] ALICE Collaboration. Performance of the ALICE Experiment at the CERN LHC. *Int. J. Mod. Phys. A*, 29:1430044, 2014.

[73] ALICE Collaboration. Upgrade of the ALICE Experiment: Letter Of Intent. *J. Phys. G*, 41(8):087001, 2014.

[74] ALICE Collaboration. Performance of the ALICE Electromagnetic Calorimeter. *JINST*, 18(08):P08007, 2023.

[75] ALICE Collaboration. Calibration of the photon spectrometer PHOS of the ALICE experiment. *JINST*, 14(05):P05025, 2019.

[76] ALICE-EMCal collaboration. The ALICE EMCal L1 trigger first year of operation experience. *JINST*, 8(01):C01013–C01013, 2013.

[77] H. Muller, T. C. Awes, N. Novitzky, and et al. Hierarchical trigger of the ALICE calorimeters. *Nucl. Instrum. Meth. A*, 617(1-3):344–347, 2010.

[78] ALICE Collaboration. ALICE Electromagnetic Calorimeter Technical Design Report. Technical report, CERN, 2008.

[79] T. Sjöstrand, S. Ask, J. R. Christiansen, and et al. An Introduction to PYTHIA 8.2. *Comput. Phys. Commun.*, 191:159–177, 2015.

[80] P. Skands, S. Carrazza, and J. Rojo. Tuning PYTHIA 8.1: the Monash 2013 Tune. *Eur. Phys. J. C*, 74(8):3024, 2014.

[81] R. Brun, F. Bruyant, F. Carminati, and et al. GEANT Detector Description and Simulation Tool. Technical report, CERN, 1994.

[82] ALICE Collaboration. EMCal MC Production Cross section. ALICE Internal Twiki Website. Last accessed on 29/08/2024.

[83] T. C. Awes, F. E. Obenshain, F. Plasil, and et al. A Simple method of shower localization and identification in laterally segmented calorimeters. *Nucl. Instrum. Meth. A*, 311:130–138, 1992.

[84] ALICE EMCal Collaboration. ALICE EMCal Physics Performance Report. *arXiv*, 2010.

[85] G. Conesa. Study and emulation of cell energy cross-talk in EMCal. *ALICE Analysis Note (Internal)*, 2018.

[86] G. Conesa. Study of the strong interaction with high-energy photons at LHC: Experience with the ALICE-EMCal detector operation and measurements. *HDR*, 2019.

[87] G. Conesa. Measurement of the inclusive isolated photon production cross section yield in pp and Pb–Pb collisions at $\sqrt{s_{\mathrm{NN}}}$ = 5.02 TeV. *ALICE Analysis Note (Internal)*, 2024.

[88] W. Bialas and D. A. Petyt. Mitigation of anomalous APD signals in the CMS ECAL. *JINST*, 8:C03020, 2013.

[89] G. Conesa. High energy exotic clusters. ALICE Internal Website, 2020.

[90] G. Conesa, M. Cosentino, A. Morreale. Rejection of exotic clusters in EMCal. *ALICE Analysis Note (Internal)*, 2014.

[91] G. Conesa, R. Xu. Presentation on the dicrepancy between EMCal and DCal in EMCal meeting. ALICE Internal Website, 21/01/22.

[92] G. Conesa. Presentation on the dicrepancy between EMCal and DCal in EMCal meeting. ALICE Internal Website, 04/02/22.

[93] ALICE Collaboration. Production of π^0 and η mesons up to high transverse momentum in pp collisions at 2.76 TeV. *Eur. Phys. J. C*, 77(5), 2017.

[94] CDF Collaboration. Study of jet shapes in inclusive jet production in $p\bar{p}$ collisions at $\sqrt{s}$ = 1.96 TeV. *Phys. Rev. D*, 71:112002, 2005.

[95] ALICE Collaboration. Supplemental figures: Measurement of the inclusive isolated-photon production cross section in pp and Pb–Pb collisions at $\sqrt{s_{\rm NN}}$ = 5.02 TeV, 2024.

[96] Christian Bierlich, Smita Chakraborty, Nishita Desai, and et al. A comprehensive guide to the physics and usage of PYTHIA 8.3. *SciPost Phys. Codebases*, page 8, 2022.

[97] F. Jonas. Measurement of isolated photon production in pp and p–Pb collisions at $\sqrt{s}$ = 8 TeV and $\sqrt{s_{\rm NN}}$ = 8.16 TeV. *ALICE Analysis Note (Internal)*, 2024.

[98] S. Chandra, S. Chattopadhyay, and G. Conesa. Isolated photons measurement in pp collisions at $\sqrt{s}$ = 8 TeV with the ALICE detector at LHC. *ALICE Analysis Note (Internal)*, 2024.

[99] ALICE Collaboration. ALICE luminosity determination for pp collisions at $\sqrt{s}$ = 13 TeV. *ALICE-PUBLIC-2016-002*, 2016.

[100] ALICE Collaboration. ALICE 2016-2017-2018 luminosity determination for pp collisions at $\sqrt{s}$ = 13 TeV. *ALICE-PUBLIC-2021-005*, 2021.

[101] ALICE Collaboration. Direct photon production at low transverse momentum in proton-proton collisions at $\sqrt{s}$ = 2.76 and 8 TeV. *Phys. Rev. C*, 99(2):024912, 2019.

[102] S. Catani, M. Fontannaz, J. P. Guillet, and et al. Cross section of isolated prompt photons in hadron-hadron collisions. *JHEP*, 05:028, 2002.

[103] P. Aurenche, J. Ph. Guillet, E. Pilon, and et al. Recent critical study of photon production in hadronic collisions. *Phys. Rev. D*, 73:094007, 2006.

[104] NNPDF Collaboration. The path to proton structure at 1% accuracy. *Eur. Phys. J. C*, 82(5):428, 2022.

[105] L. Bourhis, M. Fontannaz, and J.P. Guillet. Quark and gluon fragmentation functions into photons. *Eur. Phys. J. C*, 2:529–537, 1998.

[106] M. Yan, T. Hou, P. Nadolsky, and et al. CT18 global PDF fit at leading order in QCD. *Phys. Rev. D*, 107(11):116001, 2023.

[107] S. Bailey, T. Cridge, L. A. Harland-Lang, and et al. Parton distributions from LHC, HERA, Tevatron and fixed target data: MSHT20 PDFs. *Eur. Phys. J. C*, 81(4):341, 2021.

[108] ALICE Collaboration. Measurement of the inclusive isolated-photon production cross section in pp collisions at $\sqrt{s}$ = **13** TeV. *Eur. Phys. J. C*, 85(1):98, 2025.

[109] X. Chen, T. Gehrmann, N. Glover, and et al. Isolated photon and photon+jet production at NNLO QCD accuracy. *JHEP*, 04:166, 2020.

[110] NNPDF Collaboration. Parton distributions from high-precision collider data. *Eur. Phys. J. C*, 77:663, 2017.

[111] NNPDF Collaboration. Parton distributions for the LHC Run II. *JHEP*, 04:040, 2015.

[112] ATLAS Collaboration. Inclusive-photon production and its dependence on photon isolation in pp collisions at $\sqrt{s}$ = 13 TeV using 139 fb^{-1} of ATLAS data. *JHEP*, 07:86, 2023.

[113] J. D. Bjorken and E. A. Paschos. Inelastic Electron-Proton and γ-Proton Scattering and the Structure of the Nucleon. *Phys. Rev.*, 185:1975–1982, 1969.

[114] D. d'Enterria and J. Rojo. Quantitative constraints on the gluon distribution function in the proton from collider isolated-photon data. *Nucl. Phys. B*, 860(3):311 – 338, 2012.

[115] F. Arleo, S. J. Brodsky, D. S. Hwang, and et al. Higher-Twist Dynamics in Large Transverse Momentum Hadron Production. *Phys. Rev. Lett.*, 105:062002, 2010.

[116] ALICE Collaboration. Enhanced production of multi-strange hadrons in high-multiplicity proton–proton collisions. *Nature Physics*, 13:535–539, 2017.

Appendix A Isolation probability

A.1 The ratio of isolation fraction in data to simulation

A.1.1 The double ratio distribution and background fit range variation for $k = 1.0$

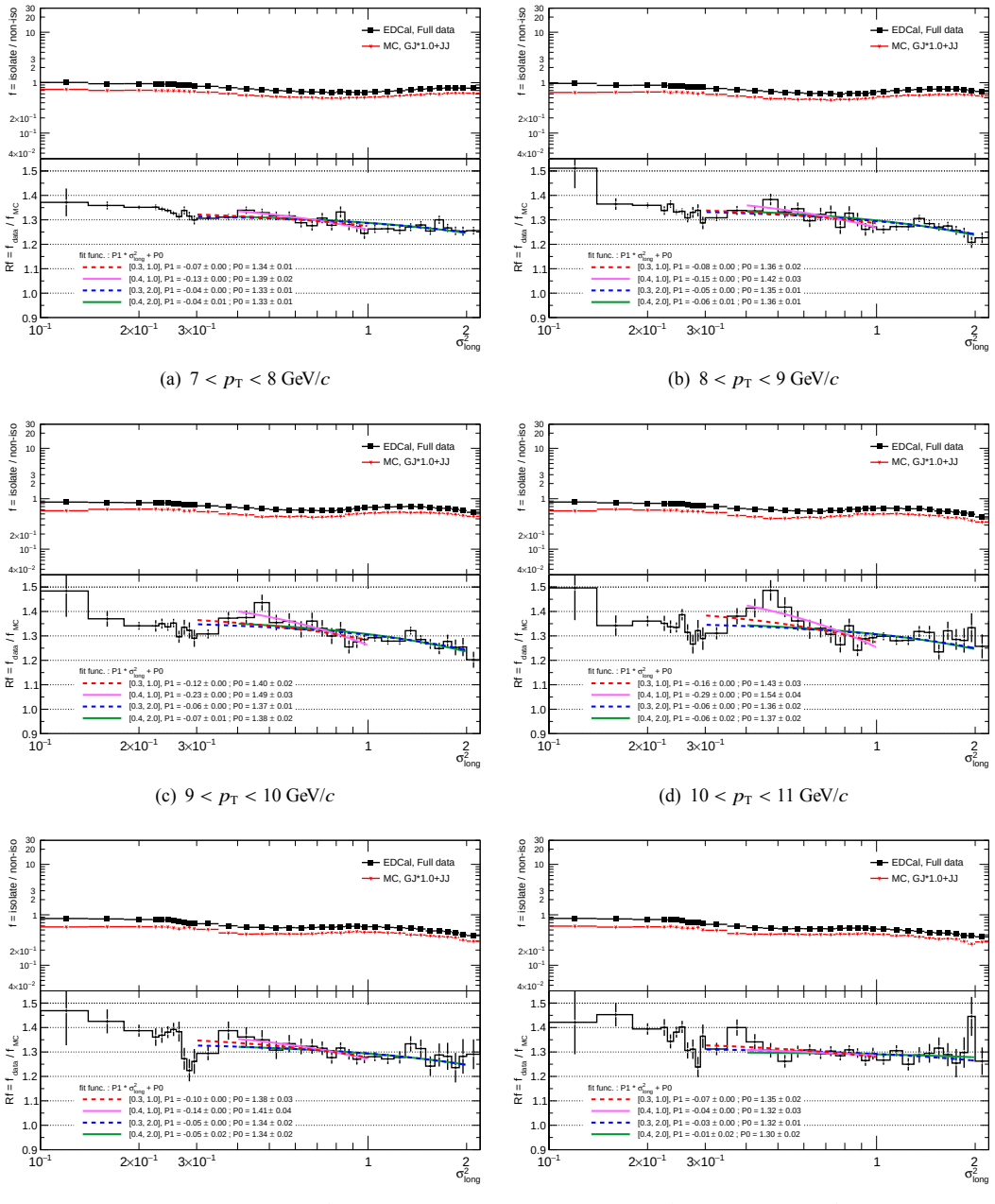

(a) $7 < p_{\mathrm{T}} < 8$ GeV/c (b) $8 < p_{\mathrm{T}} < 9$ GeV/c

(c) $9 < p_{\mathrm{T}} < 10$ GeV/c (d) $10 < p_{\mathrm{T}} < 11$ GeV/c

(e) $11 < p_{\mathrm{T}} < 12$ GeV/c (f) $12 < p_{\mathrm{T}} < 14$ GeV/c

Figure A.1: Isolation fraction double ratio (data to MC) R_f (Eq. 4.16) in different cluster p_{T} interval from 7 to 14 GeV/c, fit by a first order polynomial function in different background σ^2_{long} range.

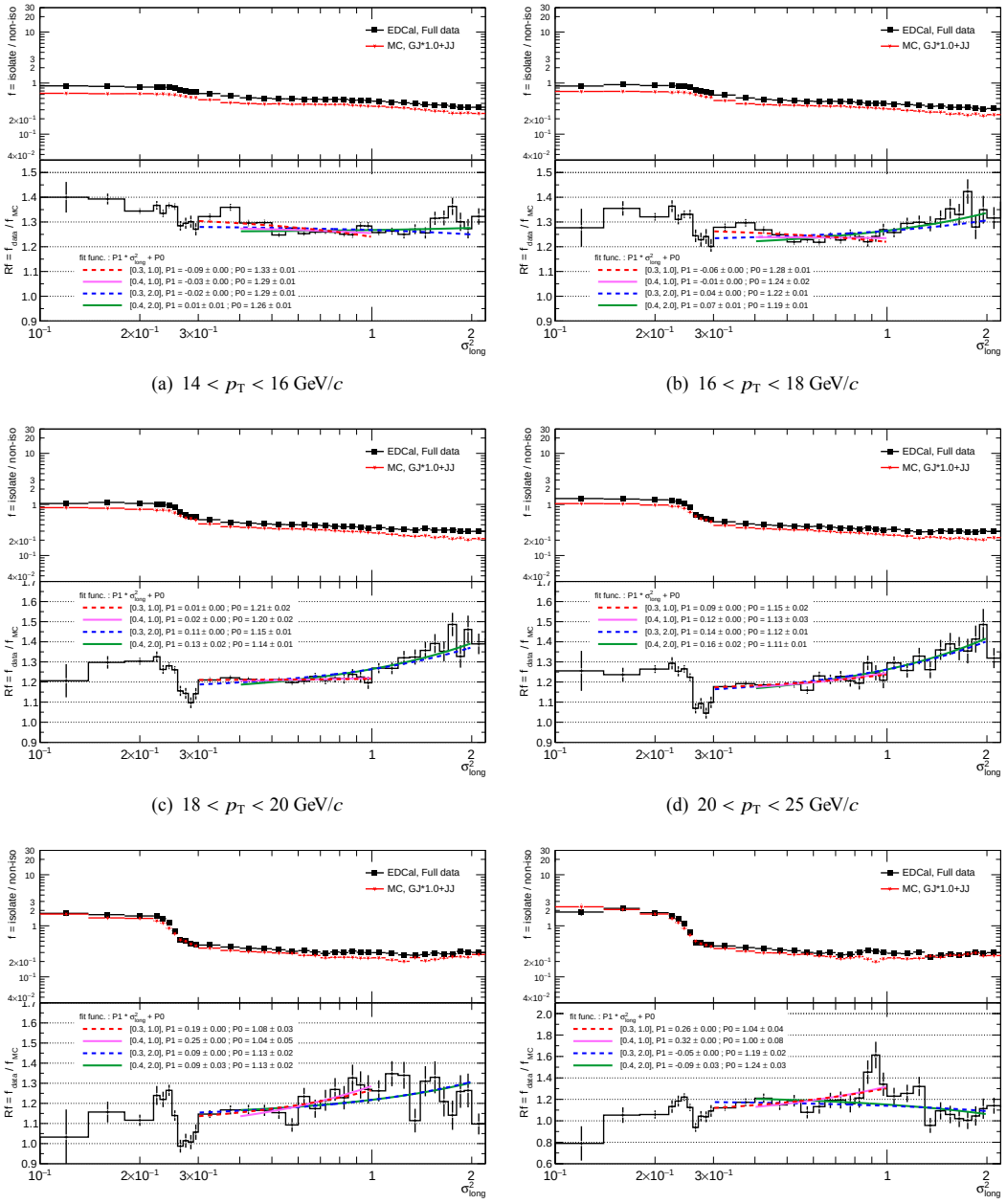

(a) $14 < p_{\mathrm{T}} < 16$ GeV/c

(b) $16 < p_{\mathrm{T}} < 18$ GeV/c

(c) $18 < p_{\mathrm{T}} < 20$ GeV/c

(d) $20 < p_{\mathrm{T}} < 25$ GeV/c

(e) $25 < p_{\mathrm{T}} < 30$ GeV/c

(f) $30 < p_{\mathrm{T}} < 35$ GeV/c

Figure A.2: Isolation fraction double ratio (data to MC) R_f (Eq. 4.16) indifferent cluster p_{T} interval from 14 to 35 GeV/c, fit by a first order polynomial function in different background σ^2_{long} range.

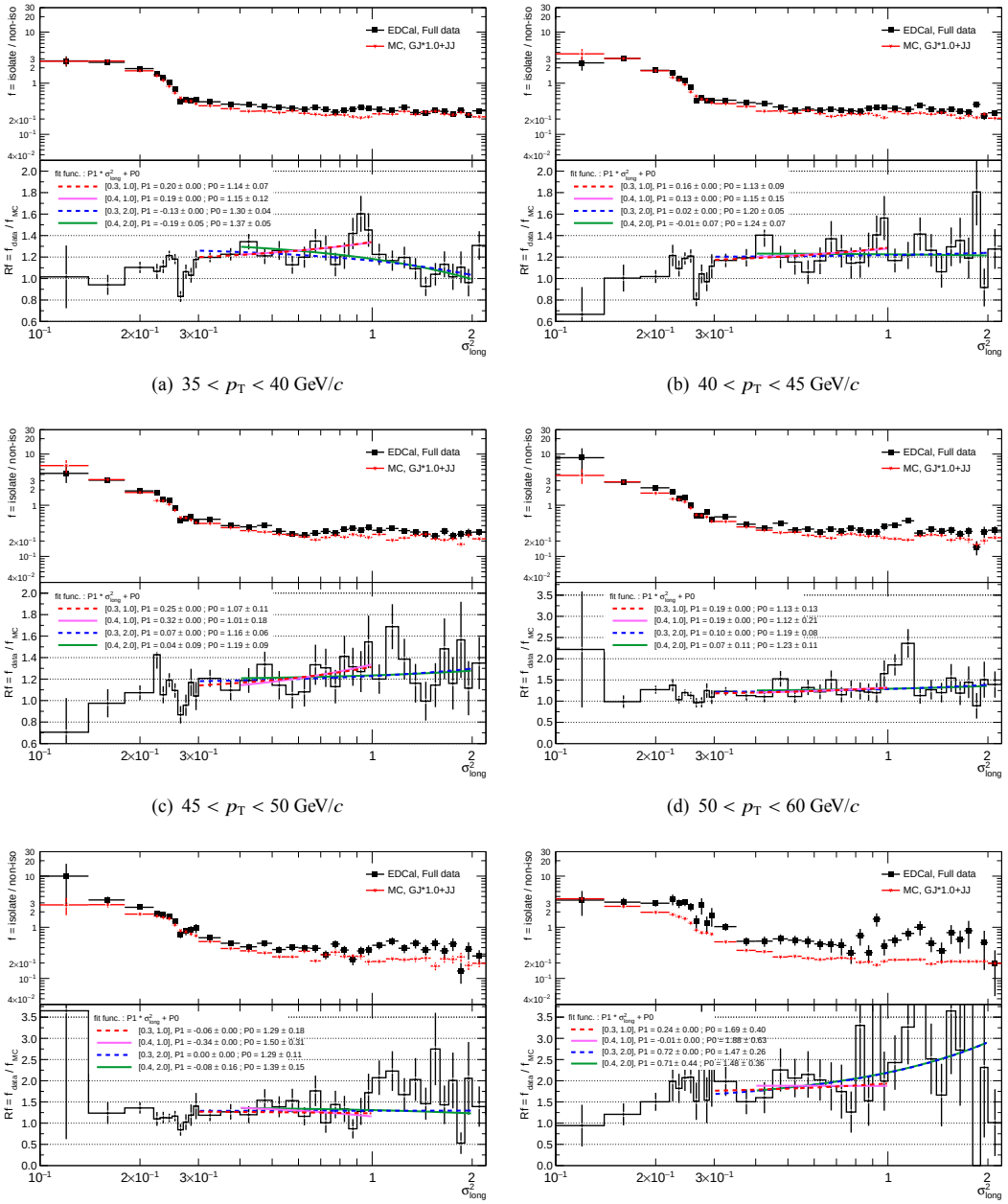

(a) $35 < p_{\mathrm{T}} < 40$ GeV/c (b) $40 < p_{\mathrm{T}} < 45$ GeV/c

(c) $45 < p_{\mathrm{T}} < 50$ GeV/c (d) $50 < p_{\mathrm{T}} < 60$ GeV/c

(e) $60 < p_{\mathrm{T}} < 80$ GeV/c (f) $80 < p_{\mathrm{T}} < 200$ GeV/c

Figure A.3: Isolation fraction double ratio (data to MC) R_f (Eq. 4.16) indifferent cluster p_{T} interval from 35 to 200 GeV/c, fit by a first order polynomial function in different background σ^2_{long} range.

A.1.2 The double ratio distribution and background fit range variation for $k = 0.0$

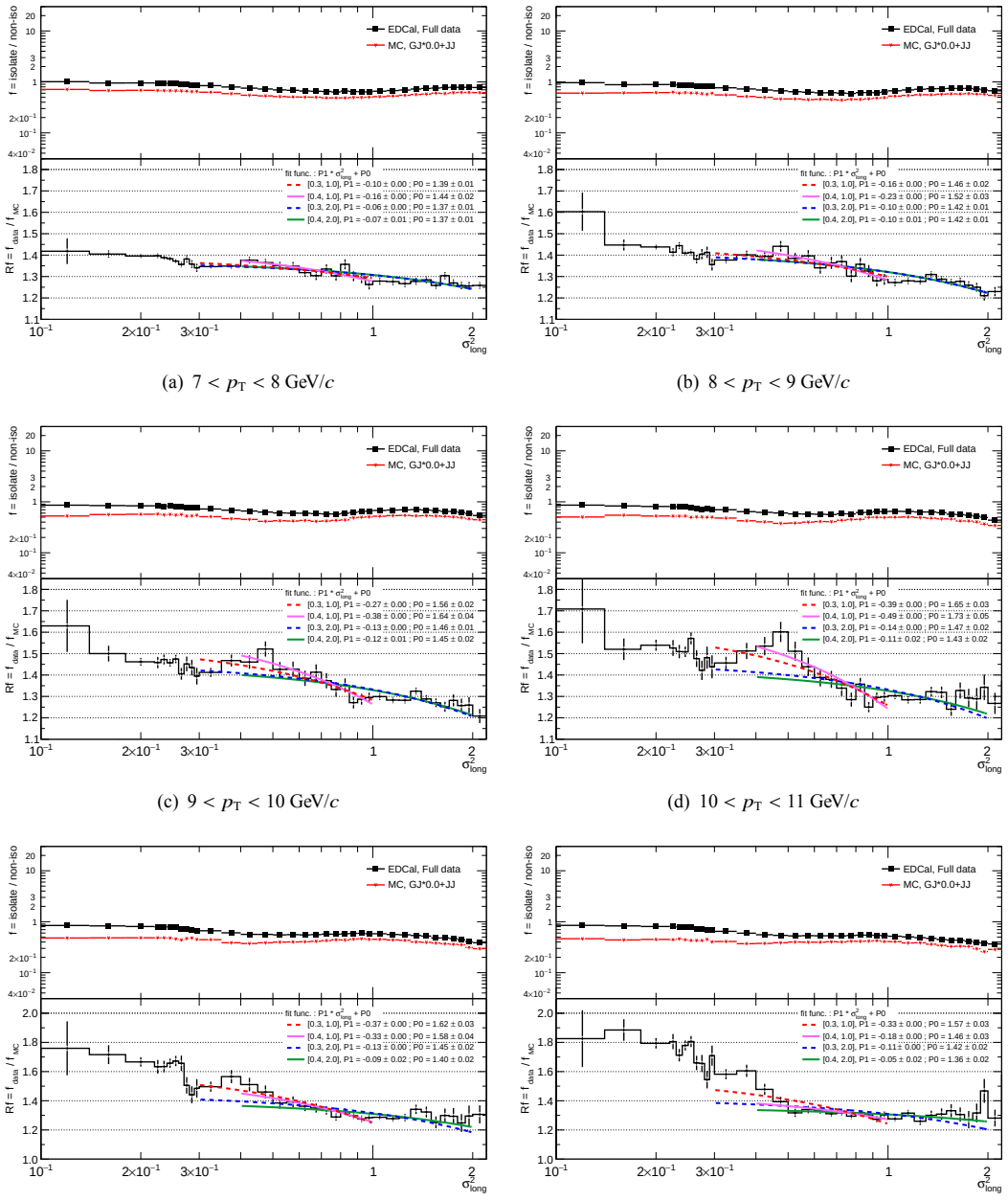

(a) $7 < p_{\mathrm{T}} < 8$ GeV/c (b) $8 < p_{\mathrm{T}} < 9$ GeV/c

(c) $9 < p_{\mathrm{T}} < 10$ GeV/c (d) $10 < p_{\mathrm{T}} < 11$ GeV/c

(e) $11 < p_{\mathrm{T}} < 12$ GeV/c (f) $12 < p_{\mathrm{T}} < 14$ GeV/c

Figure A.4: Isolation fraction double ratio (data to MC) R_f (Eq. 4.16) indifferent cluster p_{T} interval from 7 to 14 GeV/c, fit by a first order polynomial function in different background σ^2_{long} range.

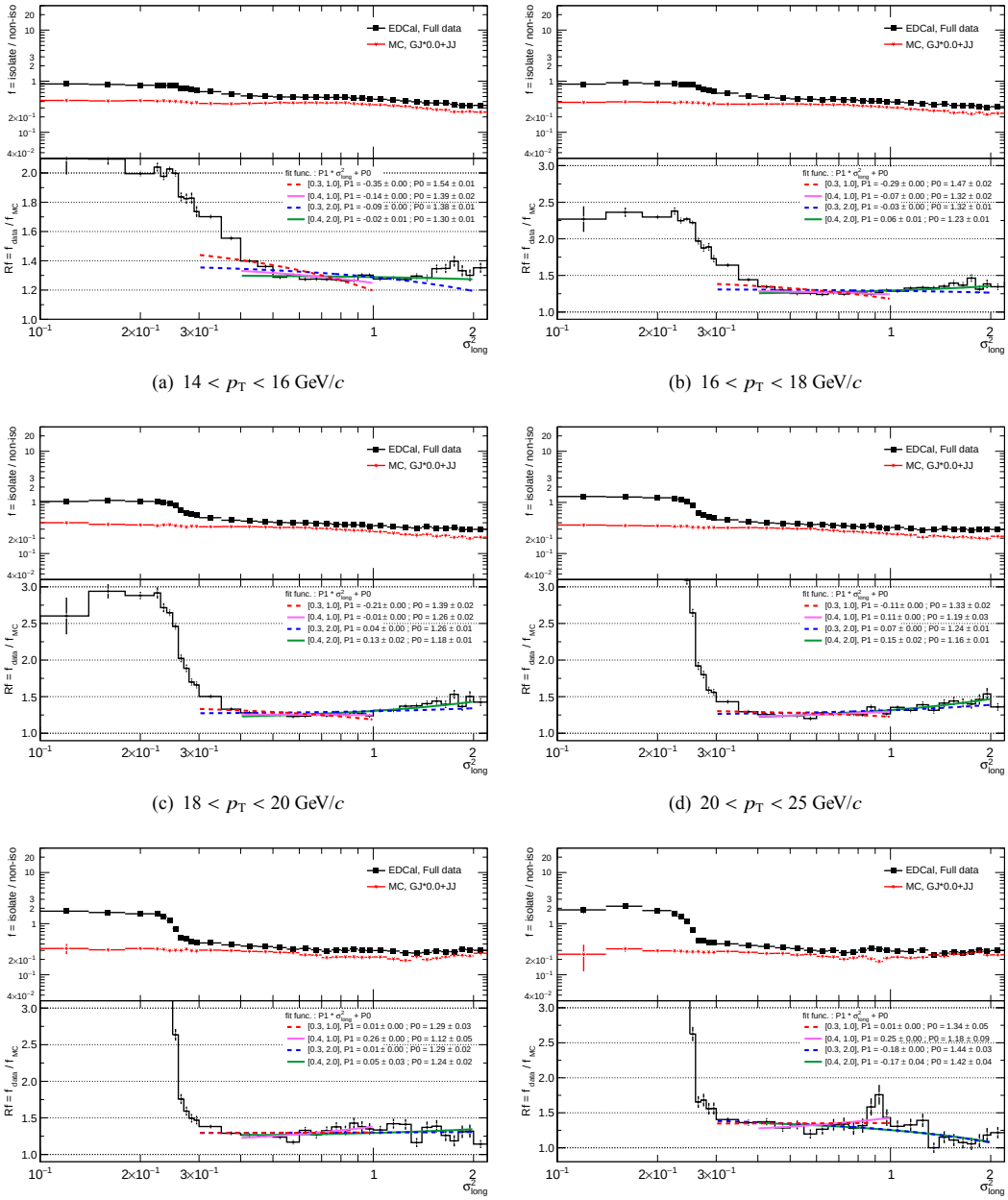

(a) $14 < p_{\mathrm{T}} < 16$ GeV/c (b) $16 < p_{\mathrm{T}} < 18$ GeV/c

(c) $18 < p_{\mathrm{T}} < 20$ GeV/c (d) $20 < p_{\mathrm{T}} < 25$ GeV/c

(e) $25 < p_{\mathrm{T}} < 30$ GeV/c (f) $30 < p_{\mathrm{T}} < 35$ GeV/c

Figure A.5: Isolation fraction double ratio (data to MC) R_f (Eq. 4.16) indifferent cluster p_{T} interval from 14 to 35 GeV/c, fit by a first order polynomial function in different background σ^2_{long} range.

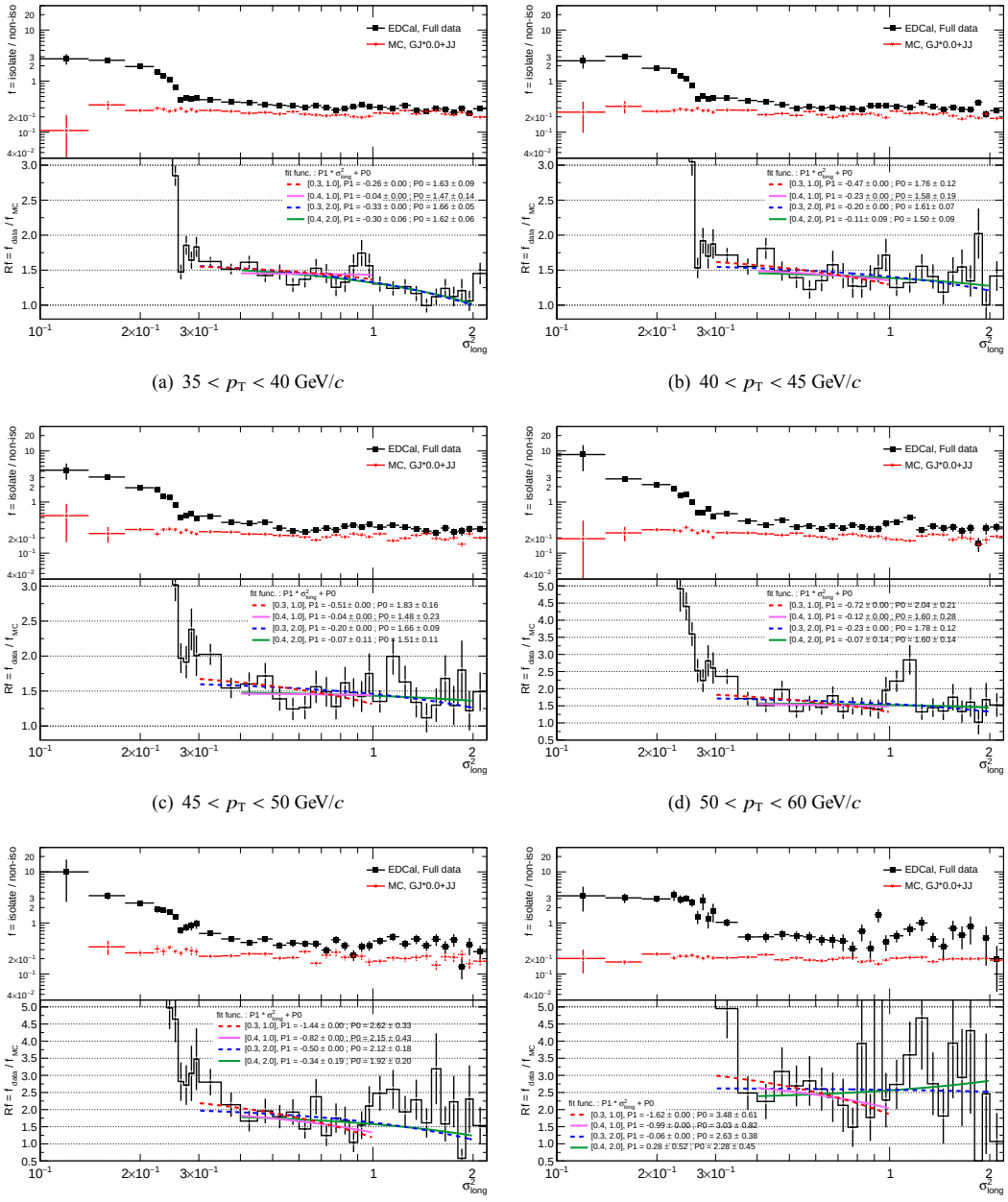

(a) $35 < p_{\mathrm{T}} < 40$ GeV/c

(b) $40 < p_{\mathrm{T}} < 45$ GeV/c

(c) $45 < p_{\mathrm{T}} < 50$ GeV/c

(d) $50 < p_{\mathrm{T}} < 60$ GeV/c

(e) $60 < p_{\mathrm{T}} < 80$ GeV/c

(f) $80 < p_{\mathrm{T}} < 200$ GeV/c

Figure A.6: Isolation fraction double ratio (data to MC) R_f (Eq. 4.16) indifferent cluster p_{T} interval from 35 to 200 GeV/c, fit by a first order polynomial function in different background σ^2_{long} range.

A.1.3 The double ratio distribution and background fit range variation for $k = 0.5$

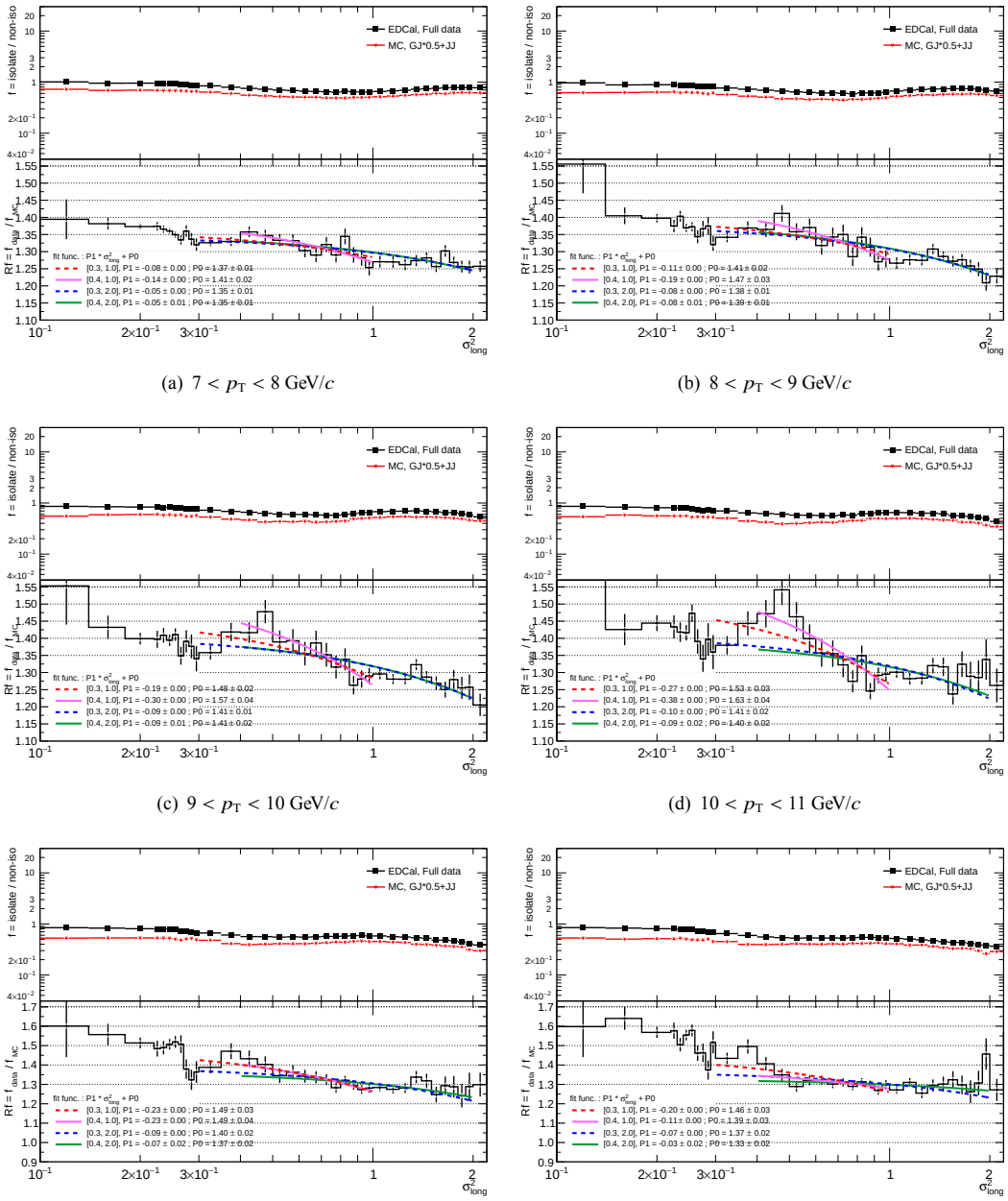

(a) $7 < p_{\mathrm{T}} < 8$ GeV/c (b) $8 < p_{\mathrm{T}} < 9$ GeV/c

(c) $9 < p_{\mathrm{T}} < 10$ GeV/c (d) $10 < p_{\mathrm{T}} < 11$ GeV/c

(e) $11 < p_{\mathrm{T}} < 12$ GeV/c (f) $12 < p_{\mathrm{T}} < 14$ GeV/c

Figure A.7: Isolation fraction double ratio (data to MC) R_f (Eq. 4.16) indifferent cluster p_{T} interval from 7 to 14 GeV/c, fit by a first order polynomial function in different background σ^2_{long} range.

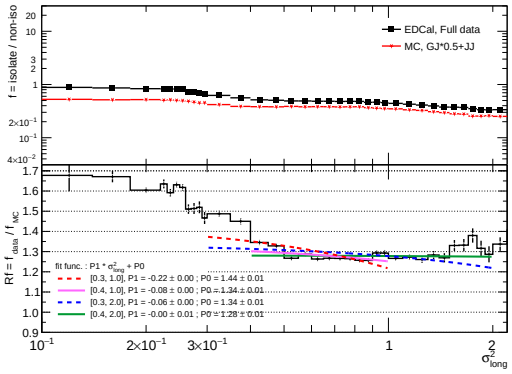

(a) $14 < p_{\mathrm{T}} < 16$ GeV/c

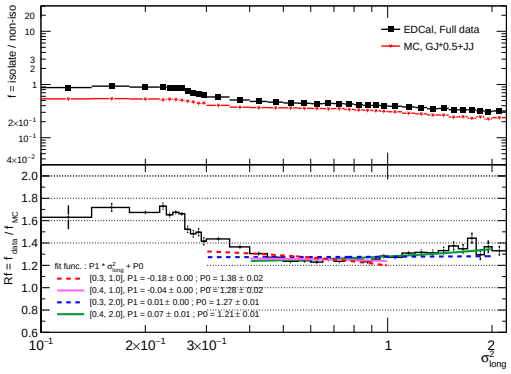

(b) $16 < p_{\mathrm{T}} < 18$ GeV/c

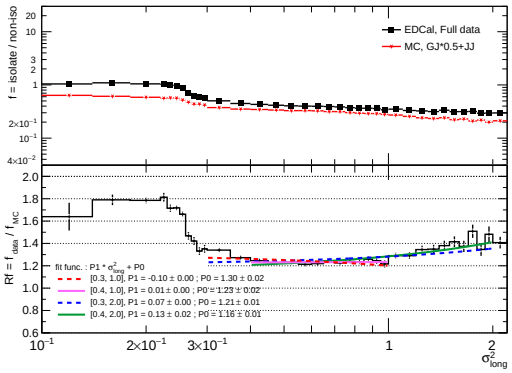

(c) $18 < p_{\mathrm{T}} < 20$ GeV/c

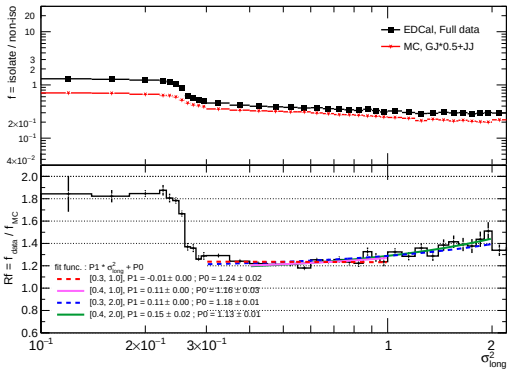

(d) $20 < p_{\mathrm{T}} < 25$ GeV/c

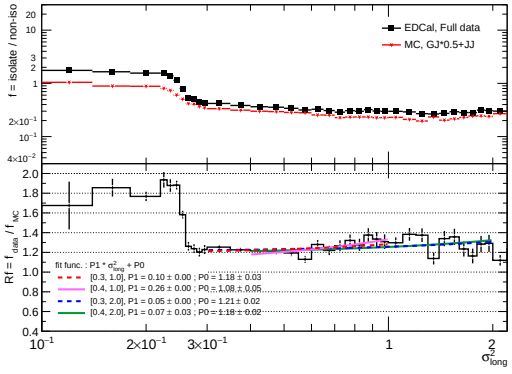

(e) $25 < p_{\mathrm{T}} < 30$ GeV/c

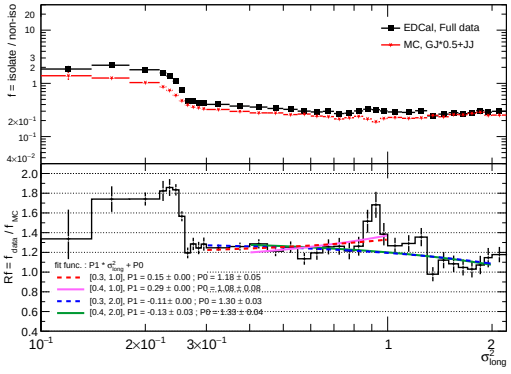

(f) $30 < p_{\mathrm{T}} < 35$ GeV/c

Figure A.8: Isolation fraction double ratio (data to MC) R_f (Eq. 4.16) indifferent cluster p_{T} interval from 14 to 35 GeV/c, fit by a first order polynomial function in different background σ^2_{long} range.

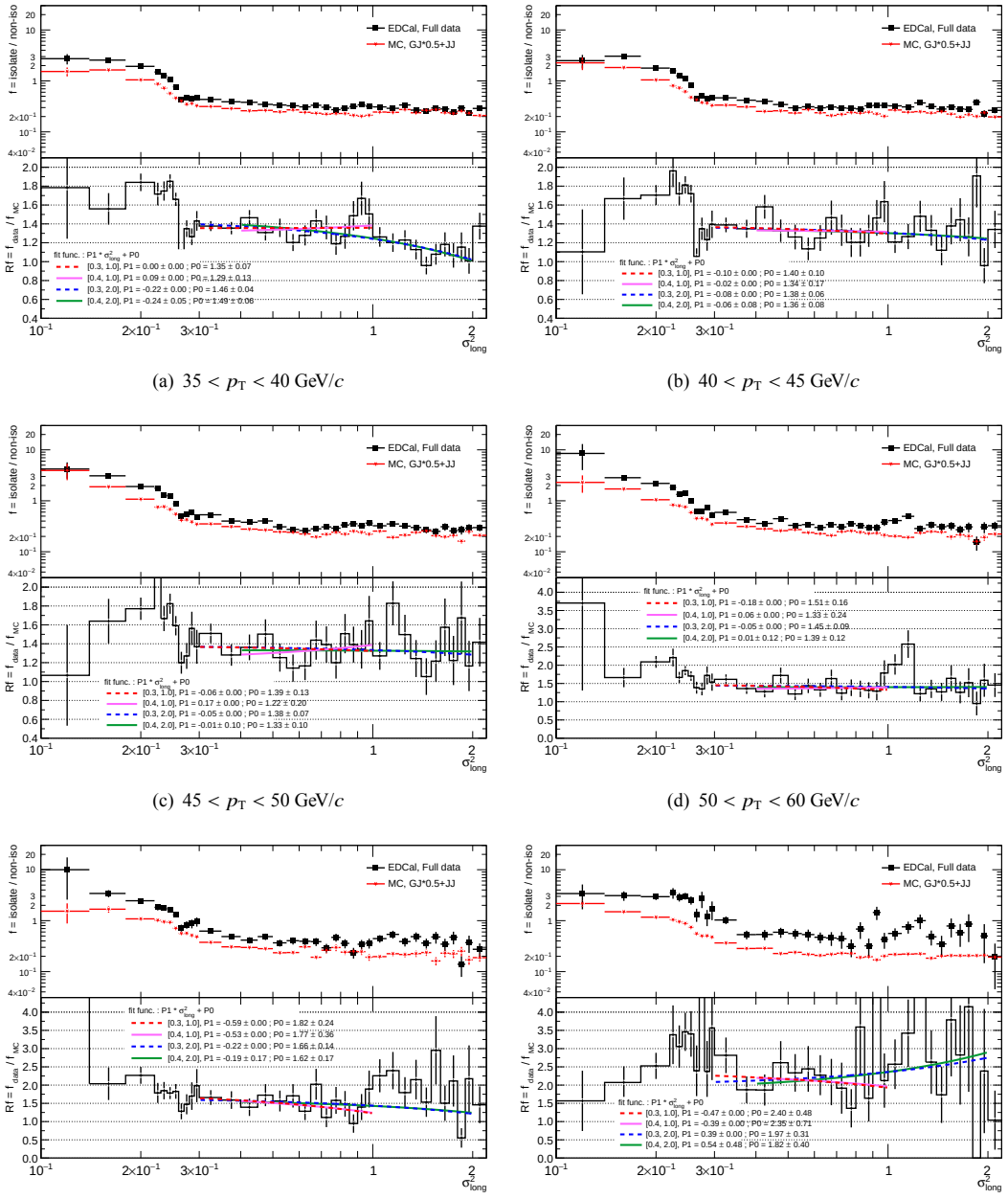

(a) $35 < p_{\mathrm{T}} < 40$ GeV/c

(b) $40 < p_{\mathrm{T}} < 45$ GeV/c

(c) $45 < p_{\mathrm{T}} < 50$ GeV/c

(d) $50 < p_{\mathrm{T}} < 60$ GeV/c

(e) $60 < p_{\mathrm{T}} < 80$ GeV/c

(f) $80 < p_{\mathrm{T}} < 200$ GeV/c

Figure A.9: Isolation fraction double ratio (data to MC) R_f (Eq. 4.16) indifferent cluster p_{T} interval from 35 to 200 GeV/c, fit by a first order polynomial function in different background σ^2_{long} range.

A.1.4 The double ratio distribution and background fit range variation for $k = 1.5$

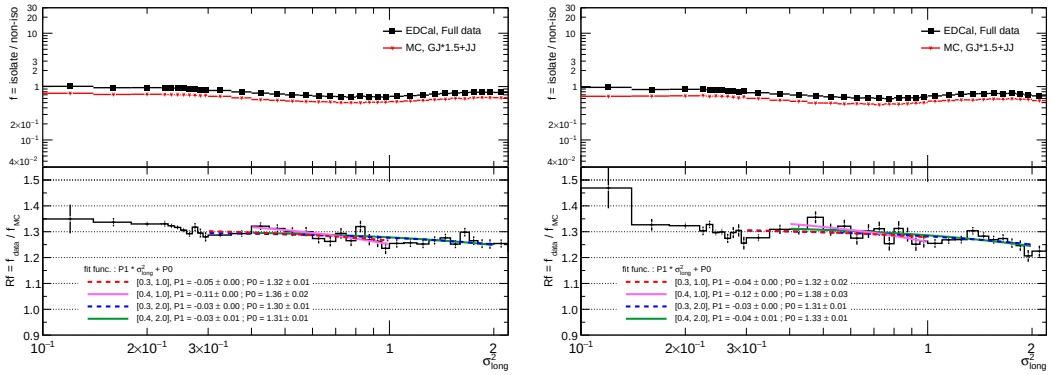

(a) $7 < p_{\mathrm{T}} < 8$ GeV/c

(b) $8 < p_{\mathrm{T}} < 9$ GeV/c

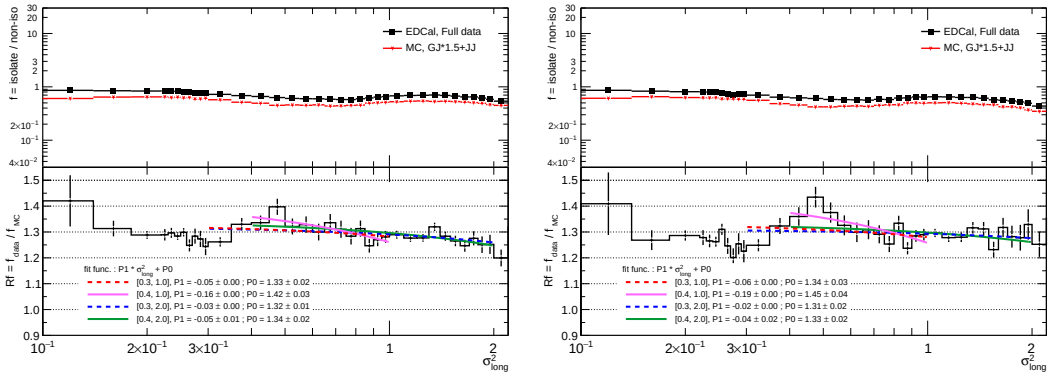

(c) $9 < p_{\mathrm{T}} < 10$ GeV/c

(d) $10 < p_{\mathrm{T}} < 11$ GeV/c

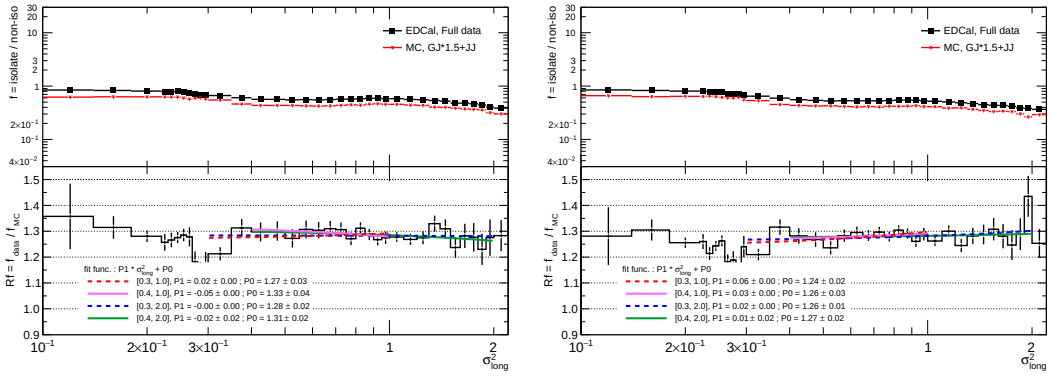

(e) $11 < p_{\mathrm{T}} < 12$ GeV/c

(f) $12 < p_{\mathrm{T}} < 14$ GeV/c

Figure A.10: Isolation fraction double ratio (data to MC) R_f (Eq. 4.16) in different cluster p_{T} interval from 7 to 14 GeV/c, fit by a first order polynomial function in different background σ^2_{long} range.

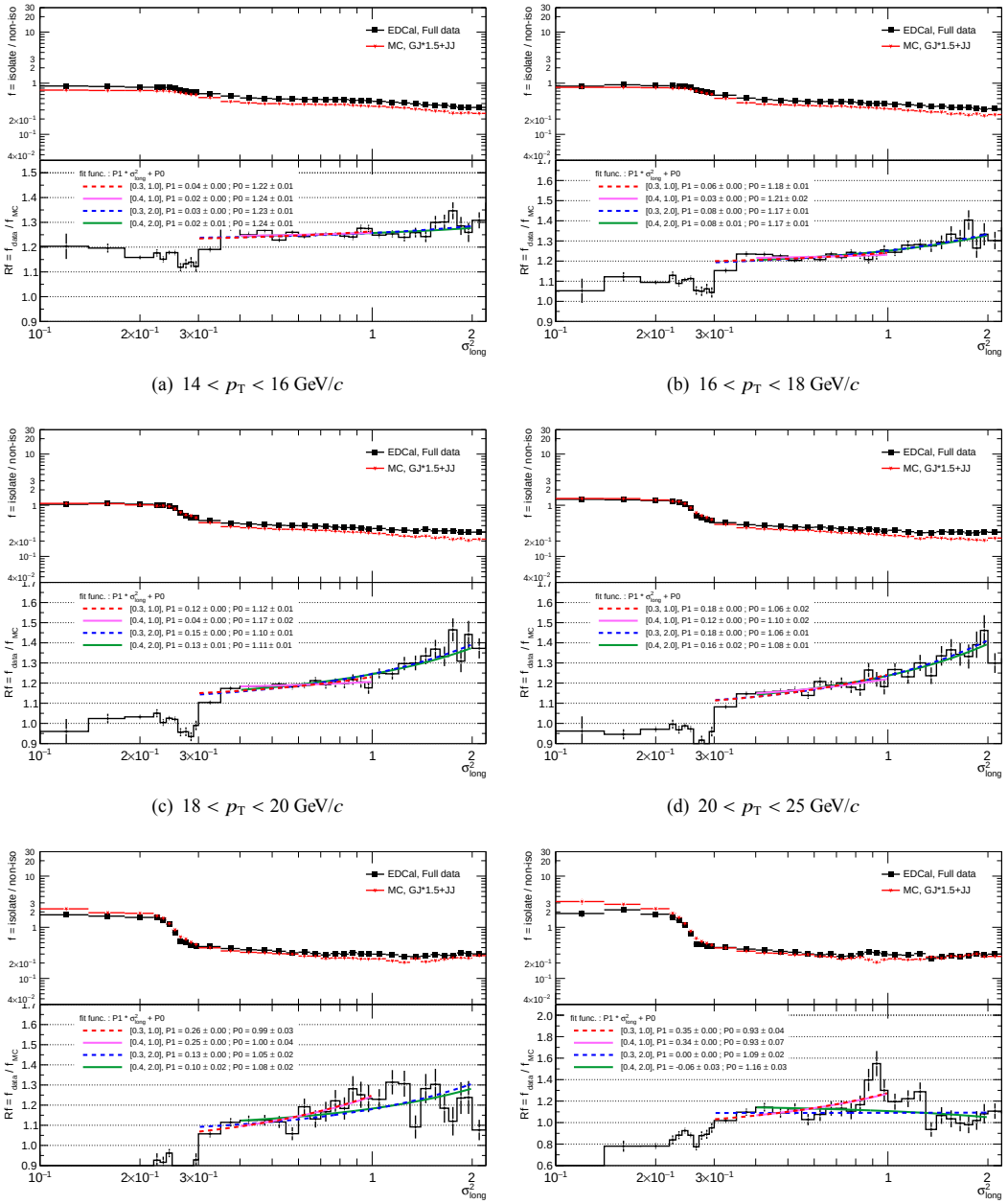

(a) $14 < p_{\mathrm{T}} < 16$ GeV/c (b) $16 < p_{\mathrm{T}} < 18$ GeV/c

(c) $18 < p_{\mathrm{T}} < 20$ GeV/c (d) $20 < p_{\mathrm{T}} < 25$ GeV/c

(e) $25 < p_{\mathrm{T}} < 30$ GeV/c (f) $30 < p_{\mathrm{T}} < 35$ GeV/c

Figure A.11: Isolation fraction double ratio (data to MC) R_f (Eq. 4.16) in different cluster p_{T} interval from 14 to 35 GeV/c, fit by a first order polynomial function in different background σ^2_{long} range.

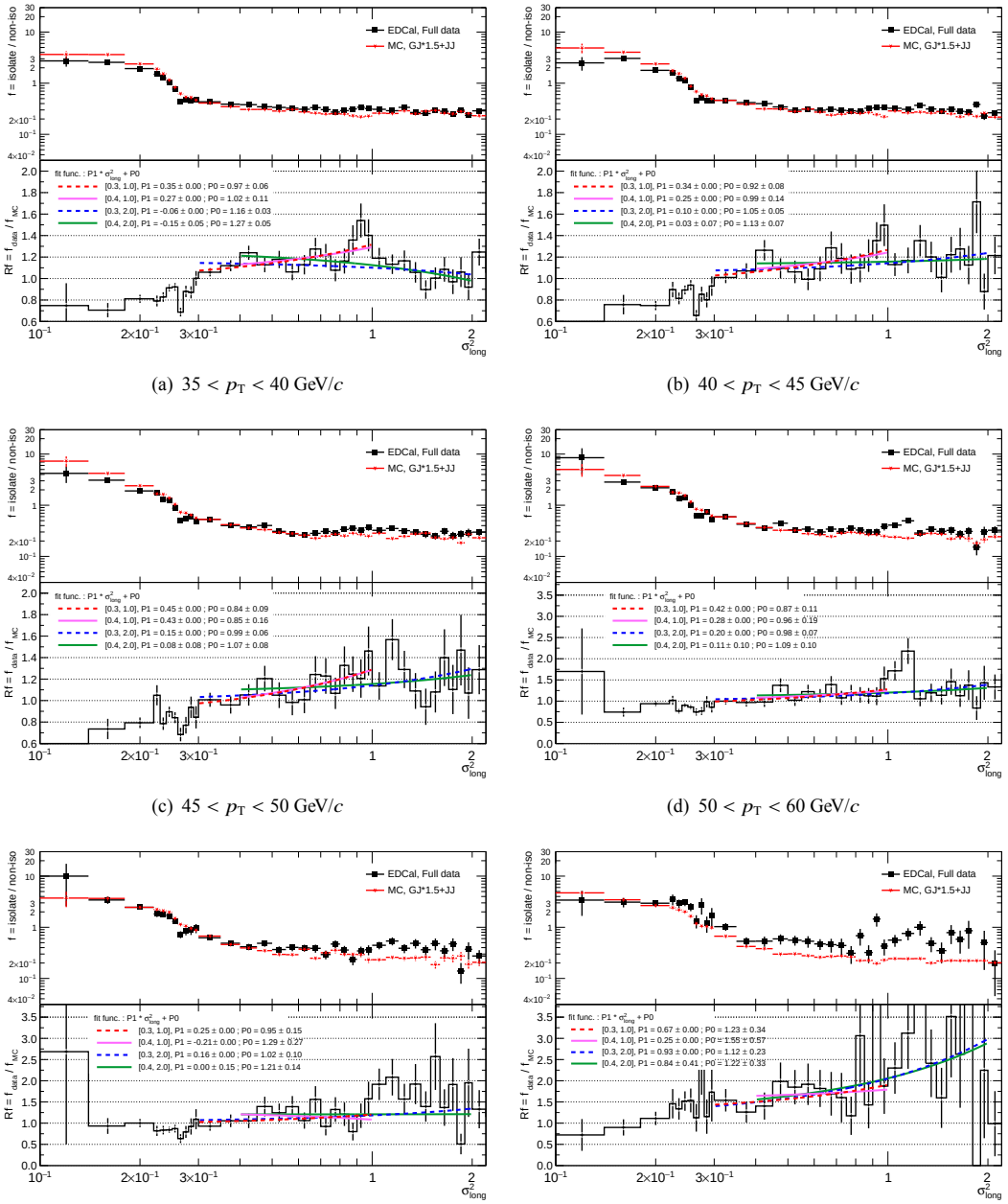

(a) $35 < p_{\mathrm{T}} < 40$ GeV/c

(b) $40 < p_{\mathrm{T}} < 45$ GeV/c

(c) $45 < p_{\mathrm{T}} < 50$ GeV/c

(d) $50 < p_{\mathrm{T}} < 60$ GeV/c

(e) $60 < p_{\mathrm{T}} < 80$ GeV/c

(f) $80 < p_{\mathrm{T}} < 200$ GeV/c

Figure A.12: Isolation fraction double ratio (data to MC) R_f (Eq. 4.16) in different cluster p_{T} interval from 35 to 200 GeV/c, fit by a first order polynomial function in different background σ^2_{long} range.

A.1.5 The double ratio distribution and background fit range variation for $k = 2.0$

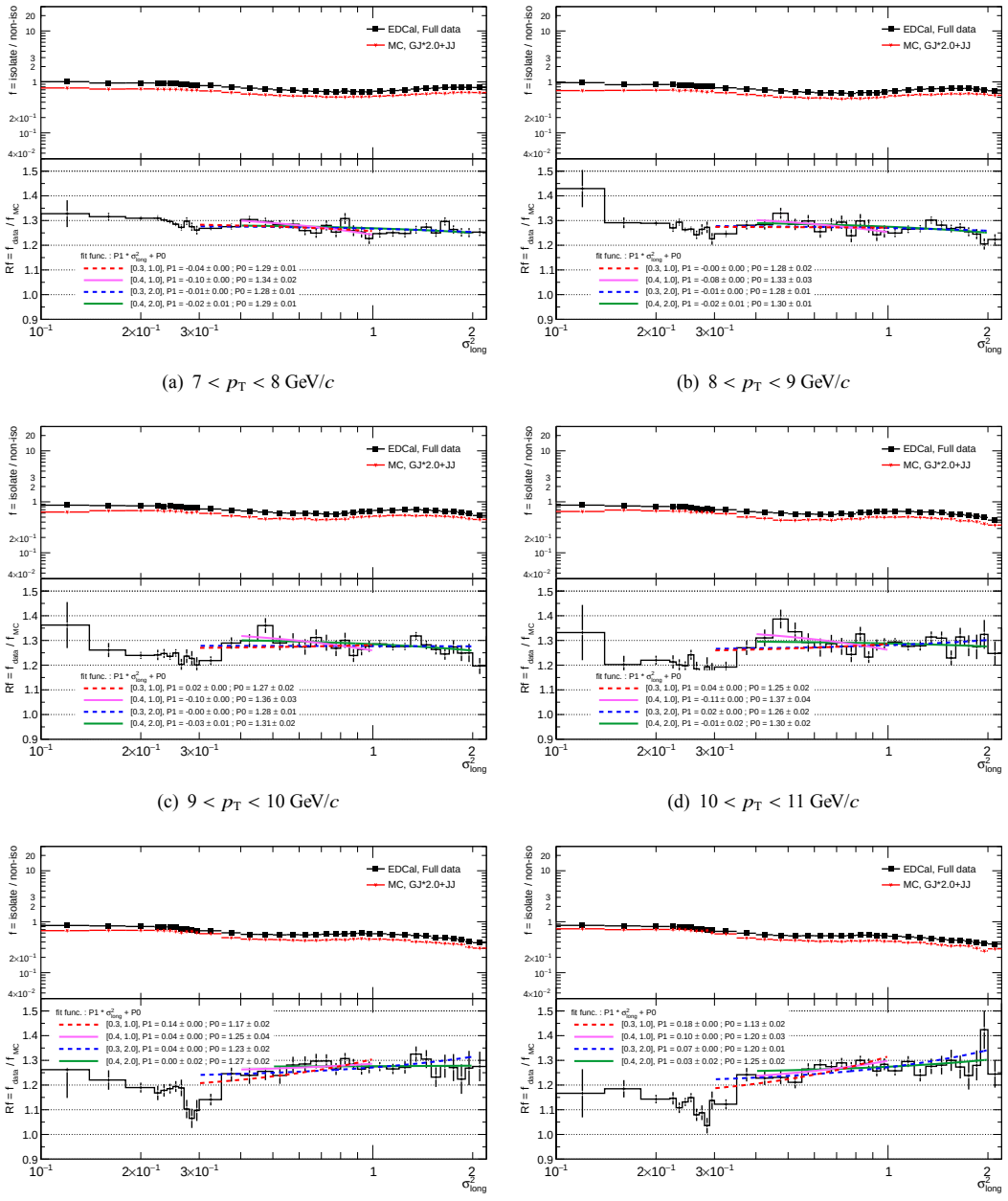

(a) $7 < p_{\mathrm{T}} < 8$ GeV/c

(b) $8 < p_{\mathrm{T}} < 9$ GeV/c

(c) $9 < p_{\mathrm{T}} < 10$ GeV/c

(d) $10 < p_{\mathrm{T}} < 11$ GeV/c

(e) $11 < p_{\mathrm{T}} < 12$ GeV/c

(f) $12 < p_{\mathrm{T}} < 14$ GeV/c

Figure A.13: Isolation fraction double ratio (data to MC) R_f (Eq. 4.16) in different cluster p_{T} interval from 7 to 14 GeV/c, fit by a first order polynomial function in different background σ^2_{long} range.

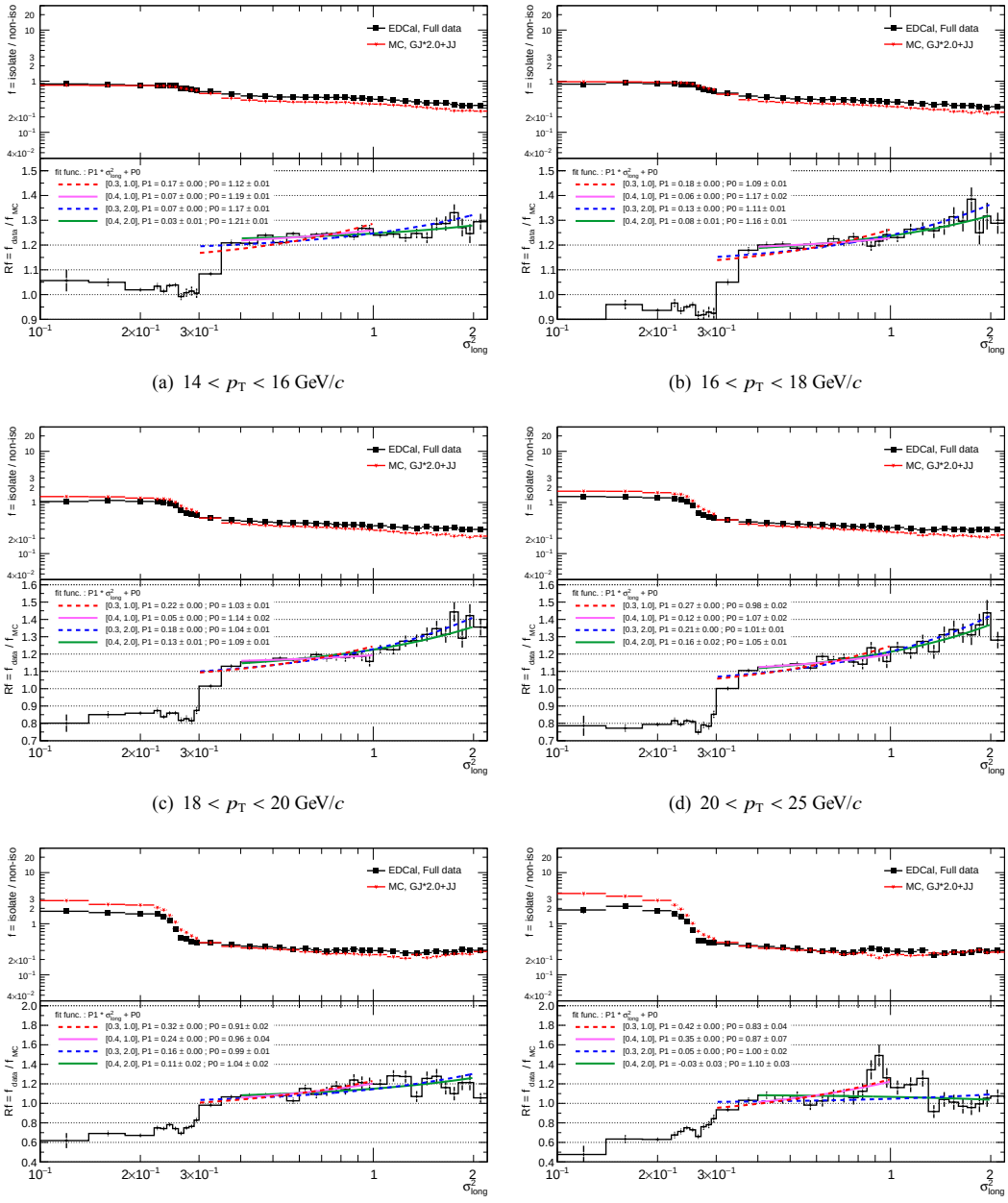

(a) $14 < p_{\mathrm{T}} < 16$ GeV/c

(b) $16 < p_{\mathrm{T}} < 18$ GeV/c

(c) $18 < p_{\mathrm{T}} < 20$ GeV/c

(d) $20 < p_{\mathrm{T}} < 25$ GeV/c

(e) $25 < p_{\mathrm{T}} < 30$ GeV/c

(f) $30 < p_{\mathrm{T}} < 35$ GeV/c

Figure A.14: Isolation fraction double ratio (data to MC) R_f (Eq. 4.16) in different cluster p_{T} interval from 14 to 35 GeV/c, fit by a first order polynomial function in different background σ^2_{long} range.

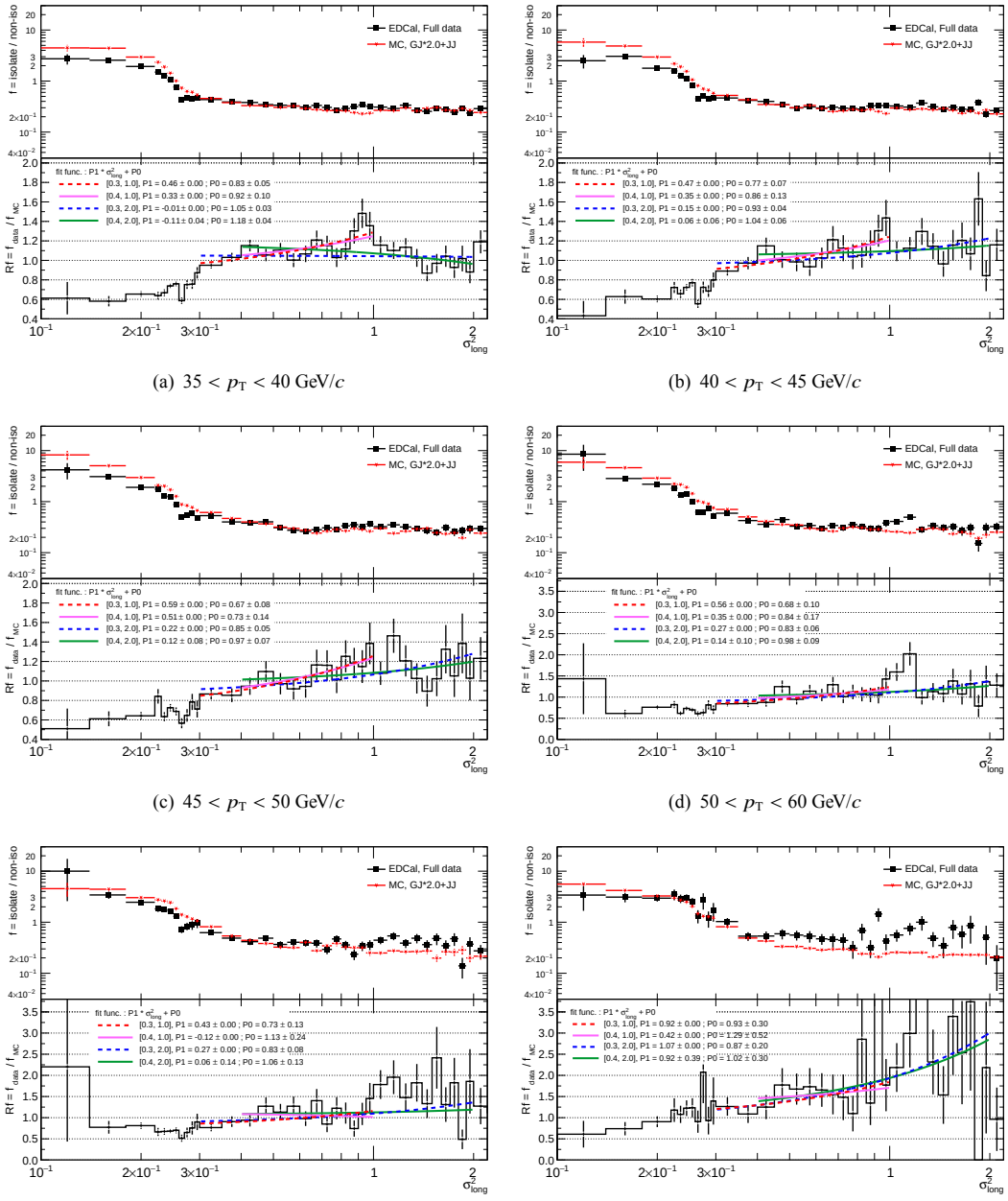

(a) $35 < p_{\mathrm{T}} < 40$ GeV/c

(b) $40 < p_{\mathrm{T}} < 45$ GeV/c

(c) $45 < p_{\mathrm{T}} < 50$ GeV/c

(d) $50 < p_{\mathrm{T}} < 60$ GeV/c

(e) $60 < p_{\mathrm{T}} < 80$ GeV/c

(f) $80 < p_{\mathrm{T}} < 200$ GeV/c

Figure A.15: Isolation fraction double ratio (data to MC) R_f (Eq. 4.16) in different cluster p_{T} interval from 35 to 200 GeV/c, fit by a first order polynomial function in different background σ^2_{long} range.

A.2 Parameters obtained by fitting with a first order polynomial function to different R_f background ranges

A.2.1 Fit results of the background fit range variation

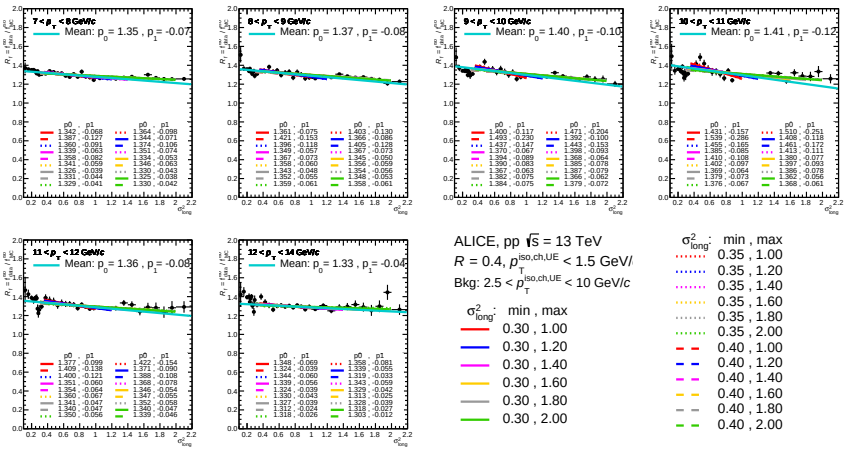

(a) $7 < p_{\mathrm{T}} < 14$ GeV/c

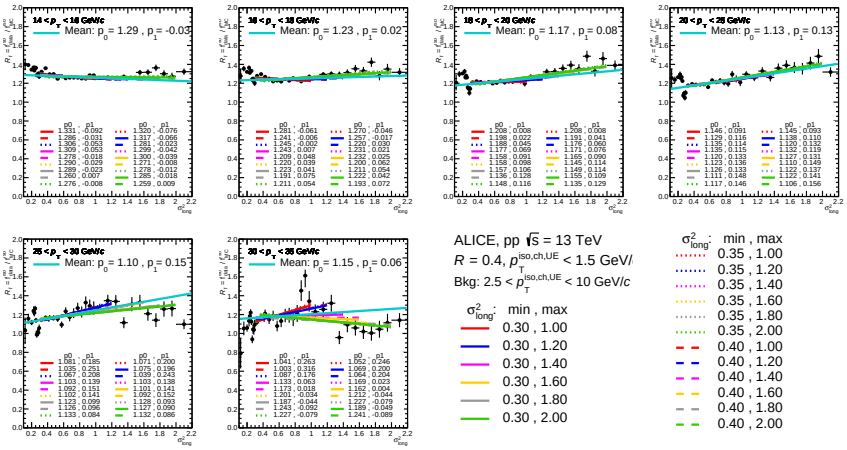

(b) $14 < p_{\mathrm{T}} < 35$ GeV/c

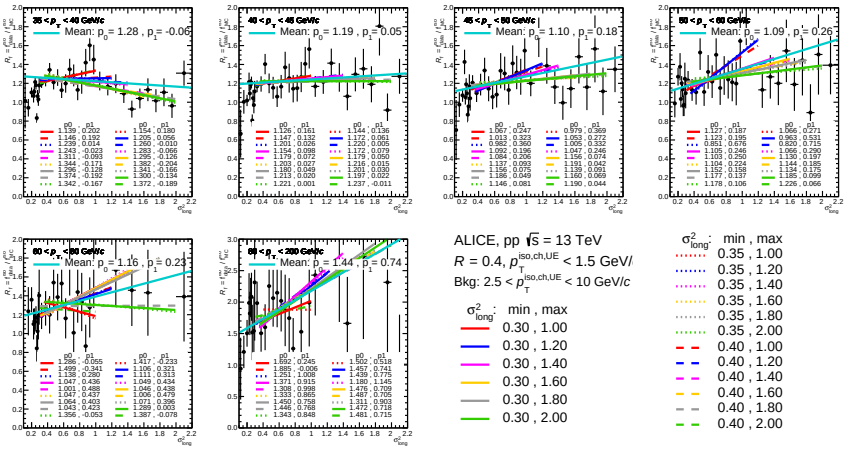

(c) $35 < p_{\mathrm{T}} < 200$ GeV/c

Figure A.16: R_f (Eq. 4.16) fitted by a first order polynomial function to different background intervals. The constant and slope parameters obtained by the fitted function and the corresponding mean values are in different colours and styles. Cluster p_{T} interval from 7 to 200 GeV/c, scale factor $k = 1$.

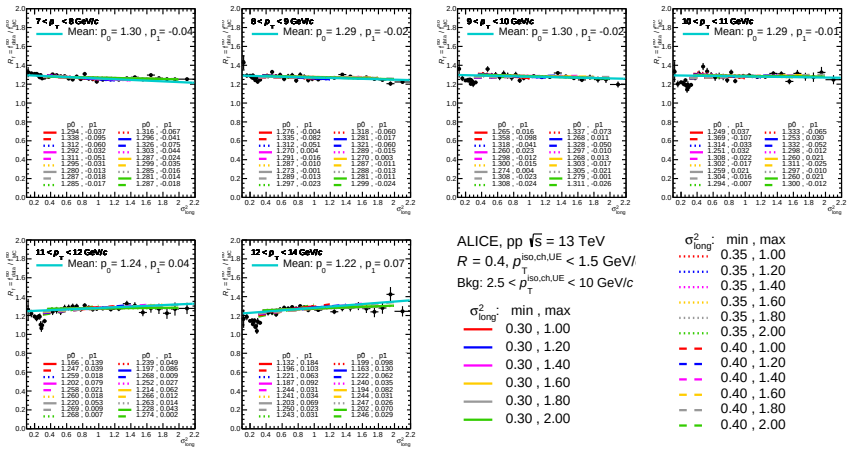

(a) $7 < p_T < 14$ GeV/c

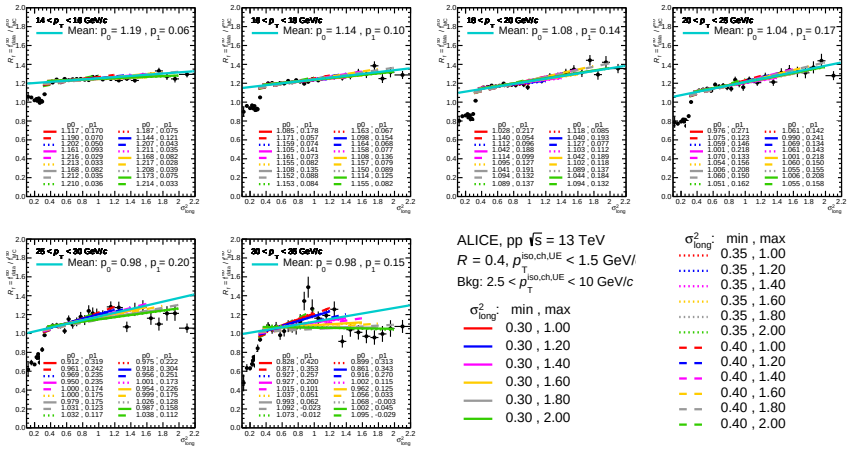

(b) $14 < p_T < 35$ GeV/c

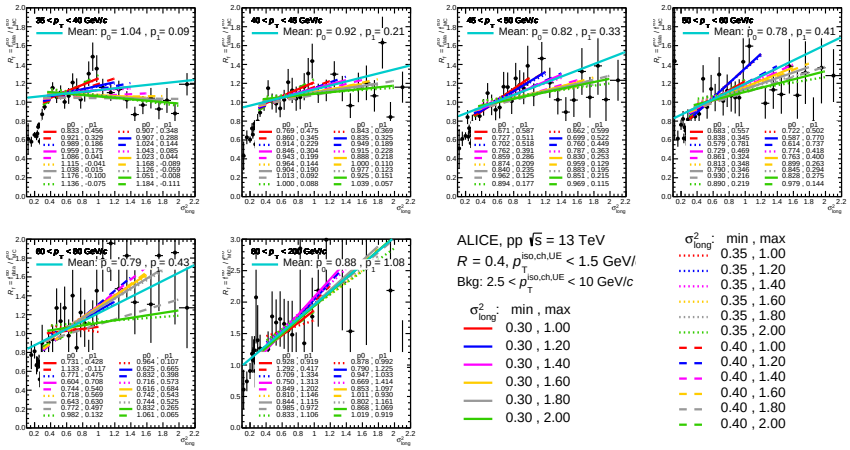

(c) $35 < p_T < 200$ GeV/c

Figure A.17: R_f (Eq. 4.16) fitted by a first order polynomial function to different background intervals. The constant and slope parameters obtained by the fitted function and the corresponding mean values are in different colours and styles. Cluster p_T interval from 7 to 200 GeV/c, scale factor $k = 2$.

A.2.2 Constant parameter obtained by the multi-background range fitted function

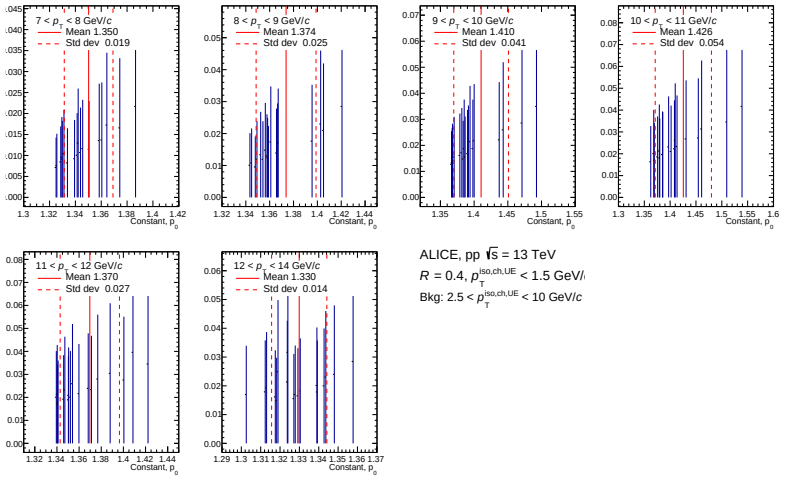

(a) $7 < p_{\mathrm{T}} < 14$ GeV/c

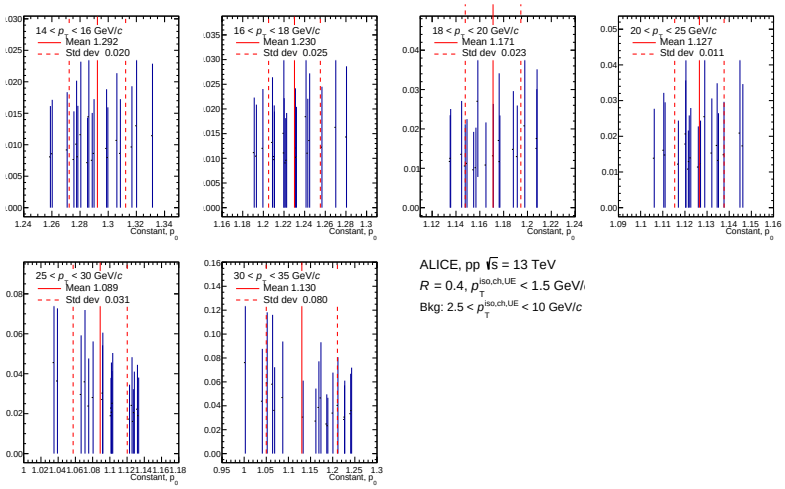

(b) $14 < p_{\mathrm{T}} < 35$ GeV/c

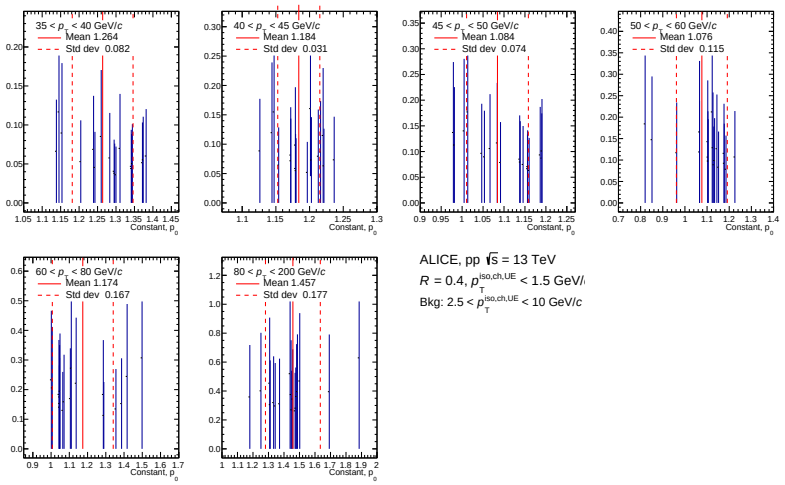

(c) $35 < p_{\mathrm{T}} < 200$ GeV/c

Figure A.18: The constant parameters obtained by fitting a first order polynomial function to different background ranges of the R_f (Eq. 4.16) and the corresponding mean values, cluster p_{T} interval from 7 to 200 GeV/c, scale factor $k = 1$.

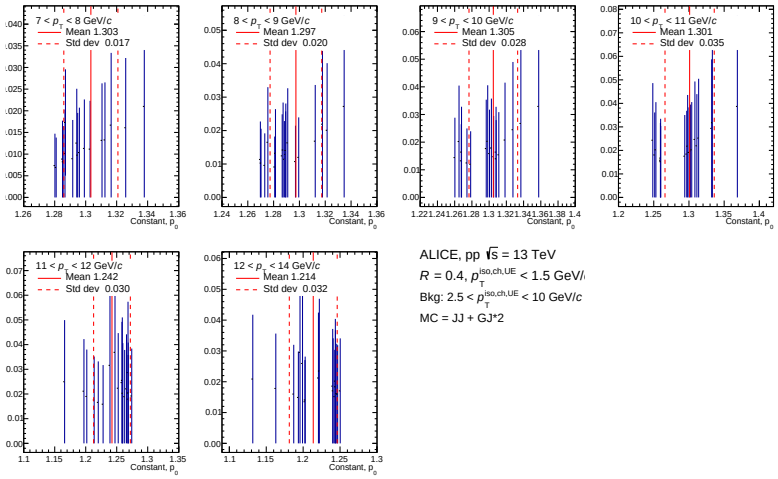

(a) $7 < p_{\mathrm{T}} < 14$ GeV/c

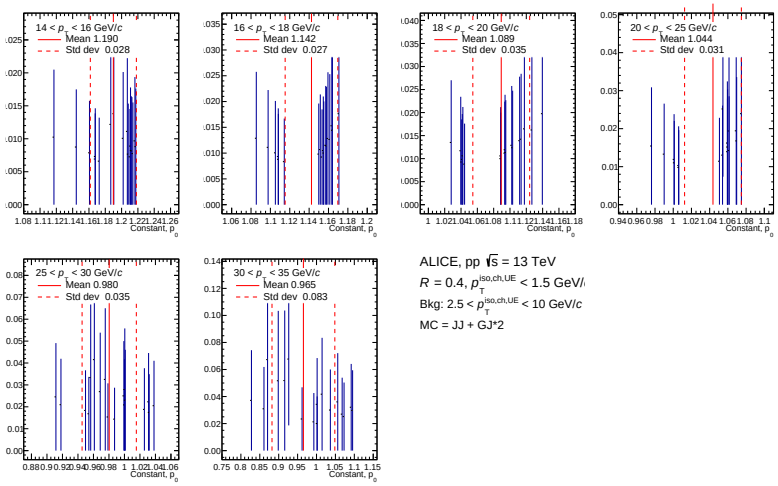

(b) $14 < p_{\mathrm{T}} < 35$ GeV/c

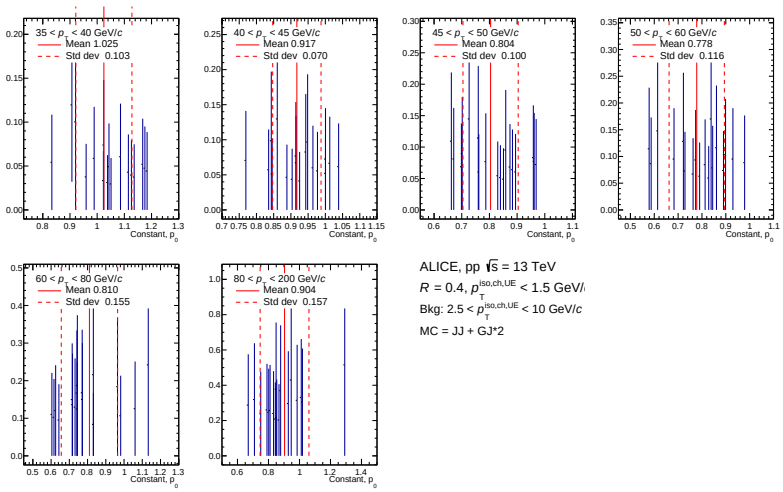

(c) $35 < p_{\mathrm{T}} < 200$ GeV/c

Figure A.19: The constant parameters obtained by fitting a first order polynomial function to different background ranges of the R_f (Eq. 4.16) and the corresponding mean values, cluster p_{T} interval from 7 to 200 GeV/c, scale factor $k = 2$.

A.2.3 Slope parameter obtained by the multi-background range fitted function

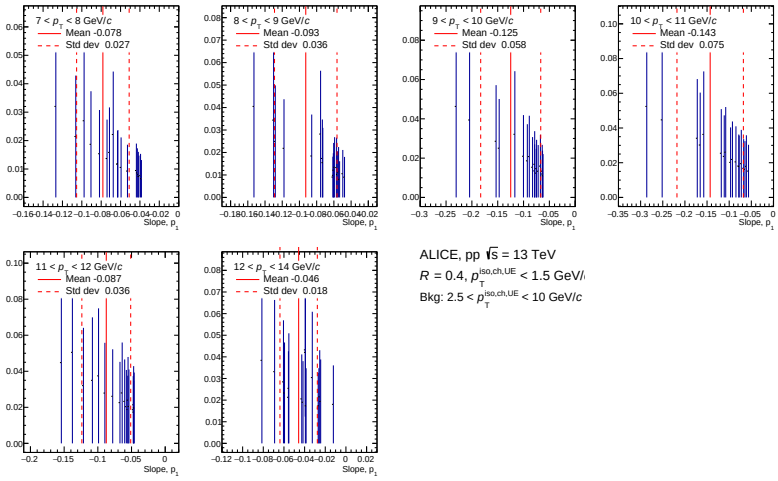

(a) $7 < p_{\mathrm{T}} < 14$ GeV/c

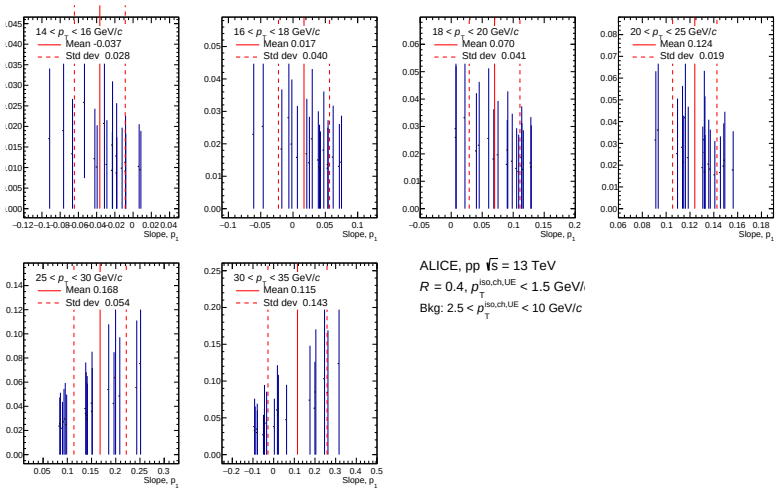

(b) $14 < p_{\mathrm{T}} < 35$ GeV/c

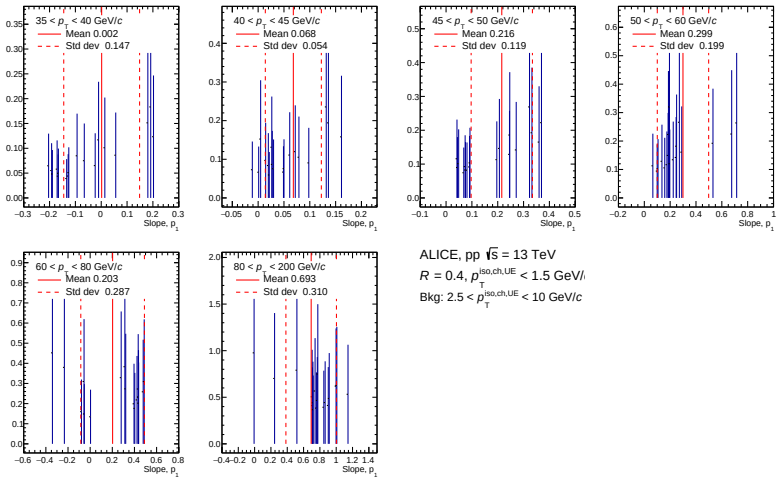

(c) $35 < p_{\mathrm{T}} < 200$ GeV/c

Figure A.20: The slope parameters obtained by fitting a first order polynomial function to different background ranges of the R_f (Eq. 4.16) and the corresponding mean values, cluster p_{T} interval from 7 to 200 GeV/c, scale factor $k = 1$.

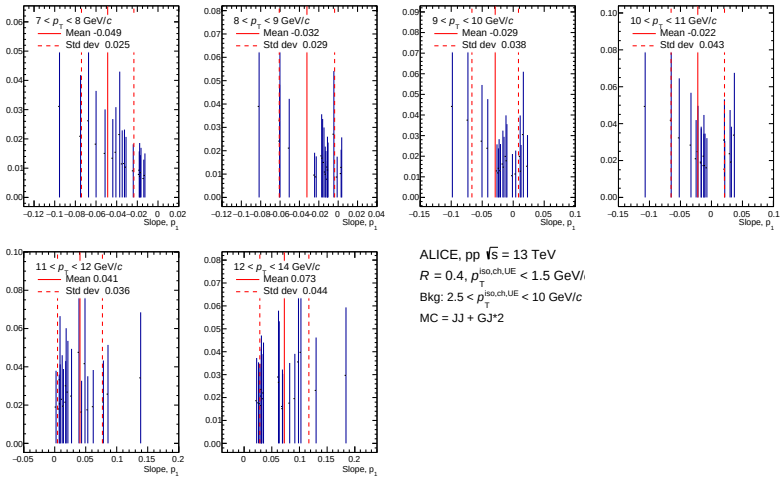

(a) $7 < p_{\mathrm{T}} < 14$ GeV/c

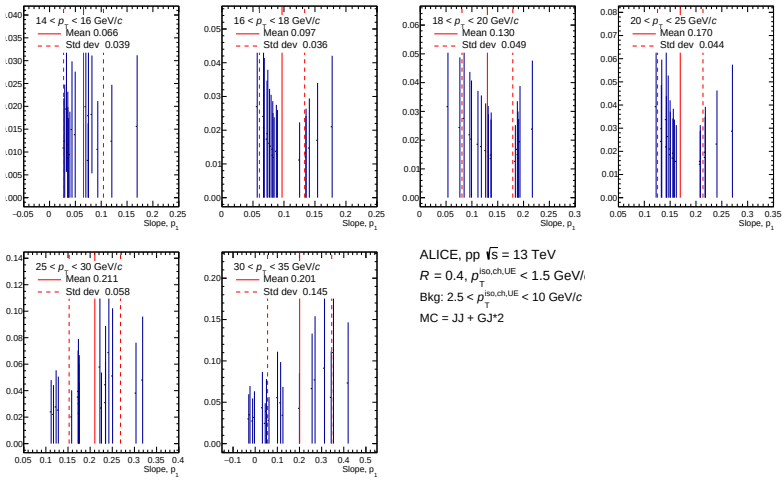

(b) $14 < p_{\mathrm{T}} < 35$ GeV/c

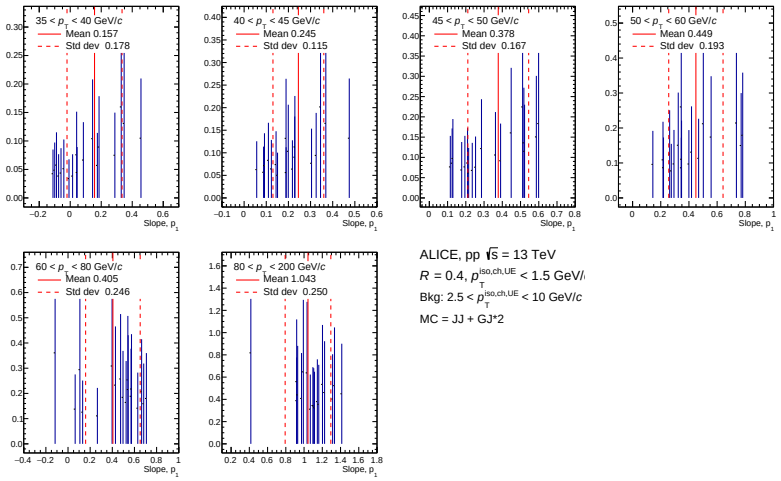

(c) $35 < p_{\mathrm{T}} < 200$ GeV/c

Figure A.21: The slope parameters obtained by fitting a first order polynomial function to different background ranges of the R_f (Eq. 4.16) and the corresponding mean values, cluster p_{T} interval from 7 to 200 GeV/c, scale factor $k = 2$.

Appendix B Purity function fit range variable

Here presents the isolated photon purity sigmoid function fitted result ratio to the purity histogram, with different function fit range.

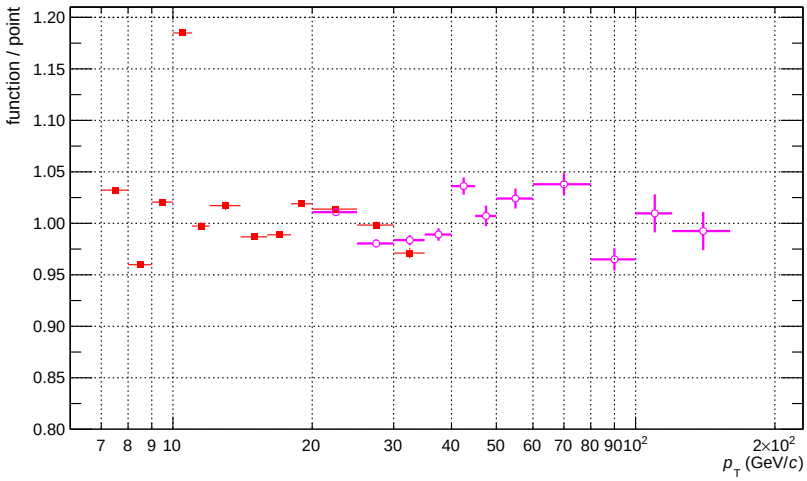

(a) fit ranges $7 < p_T < 35$ and $20 < p_T < 160$ GeV/c

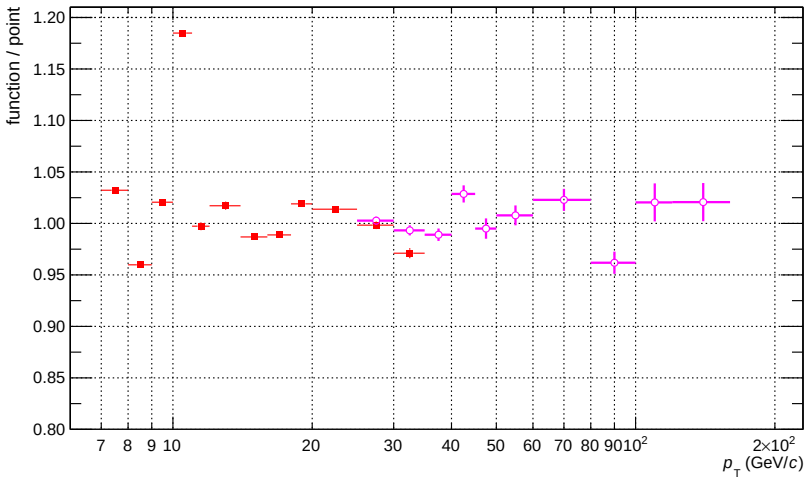

(b) fit ranges $7 < p_T < 35$ and $25 < p_T < 160$ GeV/c

Figure B.1: Ratio, purity Sigmoid fit divided by points, fit range varied in each panel.

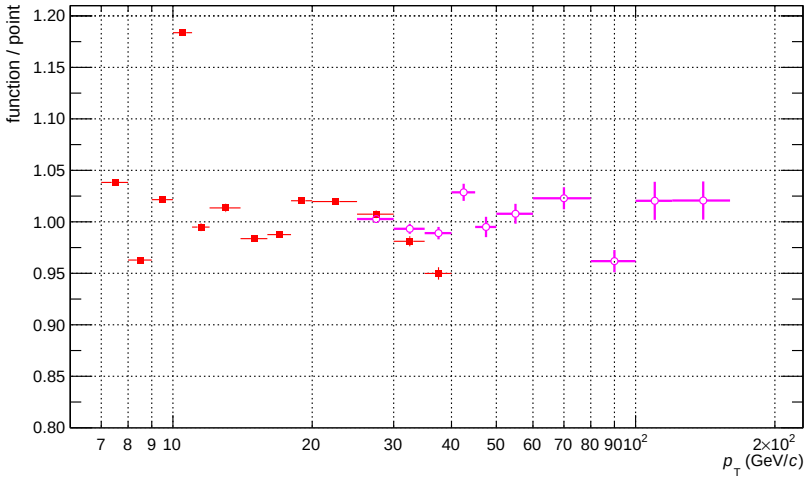

(a) fit ranges $7 < p_{\mathrm{T}} < 40$ and $25 < p_{\mathrm{T}} < 160$ GeV/c

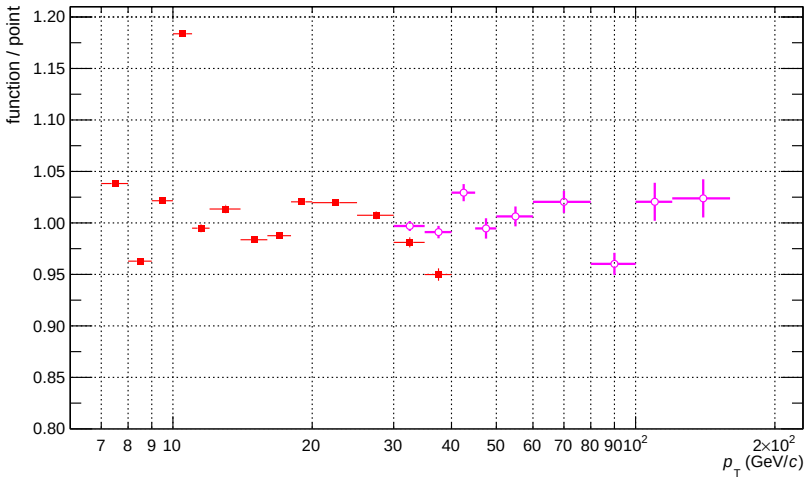

(b) fit ranges $7 < p_{\mathrm{T}} < 40$ and $30 < p_{\mathrm{T}} < 160$ GeV/c

Figure B.2: Ratio, purity Sigmoid fit divided by points, fit range varied in each panel.

Appendix C 博士论文中文简介

C.1 背景简介

20 世纪中期建立的粒子物理学标准模型（Standard Model, SM）是用于描述自然界四种基本力中的三种力（强力、电磁力和弱力）及其基本粒子的理论框架，包括夸克和轻子，以及三种基本力的媒介物 — 胶子、光子、W、Z 及希格斯玻色子。其中，夸克和胶子之间的强相互作用由量子色动力学（QCD）描述，其核心特性表现为色禁闭和渐近自由两大属性。色禁闭意味着夸克和胶子不能单独存在，只能约束在介子、重子等呈色中性的粒子内部。这也解释了为什么我们无法“看到”单个的胶子或夸克。渐近自由则表明，在非常高能量或很短距离下，强作用力减弱，粒子可以更自由地相互作用。由于强耦合，夸克和胶子之间的相互作用是复杂的，QCD 所描述的强相互作用高度非线性化，因此直接求解 QCD 方程几乎不可能。在高能区，即 Q^2（能量尺度）较大时，QCD 表现出渐近自由特性，这意味着耦合常数 α_s（描述强相互作用强度随 Q^2 变化的 QCD 耦合常数）变得足够小，从而允许使用微扰论方法展开。微扰量子色动力学（pQCD）就是基于此构建的系统化计算框架，使得在高能量条件下研究强相互作用成为可能，为理论计算提供了有力工具。部分子分布函数（PDFs）是预测高能碰撞中强子行为的重要理论工具。它通过量化强子内部夸克、反夸克及胶子（统称为部分子）携带不同动量分数（x，通常称为 Bjorken-x）的概率分布，桥接了非微扰过程的 QCD 理论和微扰过程主导的实验测量。研究质子–质子（pp）碰撞中的硬散射过程可以更直观探究质子内部结构。值得注意的是，某些硬散射过程（例如通过 $q+g \to q+\gamma$ 产生瞬时光子的过程）能够有效探测质子中胶子的 PDF。这一特性在低 x 区域尤为重要，因为该区域其他测量往往难以提供足够的信息量。

此外，在部分子强子化过程中也会产生光子，这类通过碎裂机制产生的光子称为碎裂光子（fragmentation photon）。与瞬时光子不同的是，碎裂光子和衰变光子通常伴随着其他粒子的产生，其周围具有较强的强子活动。因此，利用孤立判据（isolation criterion）可以有效区分瞬时光子与其他类型的光子，从而提高信号纯度。光子不参与强相互作用，它们能够携带着其产生时刻的相关信息直到被实验仪器探测到。在强子对撞过程中，末态强子衰变产生的光子称为衰变光子（decay photon），所有非强子衰变产生的光子统称为直接光子（direct photon），其中由碰撞初期硬散射过程直接产生的光子称为瞬时光子（direct prompt photon）。瞬时光子携带着初态部分子的信息，能够对描述强相互作用的 pQCD 理论预测进行更直接的检测，并对强子的部分子分布函数（PDF）提供严格的约束。在 pQCD 的领头阶（leading order，LO）近似下，瞬时光子主要来自康普顿散射（$q+g \to q+\gamma$，主要过程）、正反夸克湮灭（$q+\overline{q} \to g+\gamma$）以及双光子产生过程（$q+\overline{q} \to \gamma+\gamma$，相当稀少）。此外，硬散射过程的出射部分子在强子化过程中也会产生光子，这种碎裂过程产生的光子称为碎裂光子（fragmentation photon）。与瞬时光子不同的是，碎裂光

子和衰变光子在产生时周围存在其他伴随粒子。相比之下，瞬时光子周围强子活动较低，一般没有同一硬过程产生的其他伴随粒子。基于此，瞬时光子能够通过孤立方法（isolation method）被有效甄别出来。如图1.7 所示的 JETPHOX 模拟结果表明孤立判据（isolation criteria）的施加可以有效去除来自碎裂光子的贡献，同时还发现这些经过“孤立”的光子主要来自康普顿散射过程 [33]。基于此，测量孤立光子的散射截面可以检验 pQCD 预言以及约束胶子 PDF，而胶子 PDF 是受约束最少的 PDF 之一且无法通过深度非弹性散射（deep inelastic scatttering，DIS）测量直接得到。

C.2 探测器简介

欧洲核子研究中心（CERN）的大型强子对撞机（LHC）是目前世界最大、最先进的粒子加速器，为强子–强子和核–核对撞（pp、Pb–Pb、p–Pb 和 Xe–Xe）提供了目前可用的最高质心系能量（$\sqrt{s}$）。对于 pp 对撞，LHC 的目标是加速和对撞能量为 7 TeV 的质子束，使质心系的总能量达到 14 TeV；对于核核碰撞，加速和对撞能量为 2.75 TeV/核子的铅束，使其质心系的总能量达到 5.5 TeV。迄今为止，LHC 采集的数据相关对撞系统及对应质心系能量见表2.1。碰撞点的亮度（$\mathscr{L}$）是表征粒子加速器性能的指标之一，可以理解为在给定时间内测量到散射截面为 σ_{event} 的特定物理过程的碰撞事件数，表达式如公式2.1所示。亮度主要取决于每个碰撞粒子束流的束流强度、碰撞粒子束流的交叉角度以及在相互作用点处粒子束的聚焦程度。近几十年，LHC 上已经进行了一系列与瞬时光子产额相关的测量，广泛测量了 pp 对撞中各种粒子产生过程的横动量（p_{T}）微分截面。例如，对孤立瞬时光子散射截面的精确测量改进了对胶子 PDF 的测定。此外，这些测量还促进了对部分子簇射（parton shower）演化以及微扰和非微扰 QCD 效应之间相互作用的研究。目前，ALICE（A Large Ion Collider Experiment）、ATLAS（A Toroidal LHC Apparatus）以及 CMS（Compact Muon Solenoid）实验组对 LHC 上 pp 碰撞中孤立光子散射截面的测量结果与理论计算给出的结果在误差允许范围内相吻合，如图1.8, 1.9 以及1.10 所示。同时也可以发现仅考虑 NLO 的理论计算结果略微低于实验测量结果，通过加入 NLO 以外的修正可以加以改善。ATLAS 和 CMS 对孤立光子散射截面的测量优势在高横动量区间（高于 20 GeV/c），而中低横动量区间的测量受背景复杂性、探测器设计优先级和理论模型的限制，测量未能实现全面覆盖。而 ALICE 合作组，其电磁量能器（EMCal）[74] 可以提供高分辨率的能量测量，这对于在复杂的碰撞环境中准确重建和识别光子、中性介子和电子至关重要。同时，时间投影室（TPC）[70] 和内部径迹系统（ITS）[67] 能够精确实现对带电粒子径迹重建和背景剔除，以确保探测到的信号尽可能不受污染。此外，低动量跟踪能力允许在更宽能量范围产生的粒子进行更全面的分析，从而提高散射截面测量的总体精度。这些特点使得 ALICE 探测器特别适合分离和分析像孤立光子产生这类稀有过程。

C.3 孤立直接光子鉴别

EMCal 的校准是确保精确测量粒子沉积能量的关键步骤，校准技术介绍及相关筛选条件设置见论文3.4章。本研究首次利用 ALICE 实验二期（Run 2）在 pp 碰撞中收集的数据，通过 EMCal 对光子进行测量，并将测量的能量范围从之前的最高 60 GeV/c [44] 扩展至超过 100 GeV 。鉴于此能量范围的扩展，原有的伪信号处理方法需进行相应的调整和优化，以确保高能区间的测量精度和可靠性。EMCal 采用铅-闪烁体夹层结构，整个探测器由 17664 个探测单元（cell）构成[74]，如图2.6所示。粒子在穿过 EMCal 时，大部分能量沉积在一个探测单元中，其余部分则分布在多个相邻的单元中。这些沉积能量的探测单元组合在一起，称为一个“团簇”（cluster）。在分析 100–200 GeV 的光子候选团簇时，发现其数量显著超出理论预期。进一步分析表明，这些异常信号大多数是源于中子直接撞击雪崩光电二极管（APD）产生的伪信号（fake signal）。这类伪信号的能量分布高度集中单个或少数探测单元，且主导探测单元的能量超过整个团簇能量的 97%。低能量伪信号通过拓扑程序可以有效消除，例如选择 $F_+ < 0.97$ 的团簇，其中 F_+ 定义见公式3.10。但是在高能量（> 100 GeV ）下，拓扑程序的局限性凸显。这些伪信号会在 EMCal 主探测单元附近诱导出显著的电子学串扰信号（cross-talk signal），形成容易被误判成光子的能量分布。由于此类串扰信号只会影响位于同一读出模块（2×8 探测单元矩阵）内的探测单元，而真实光子信号在此种情况下通常会形成跨越多个读出模块的团簇。基于此，本研究针对团簇引入一个新的筛选条件：超过 80 GeV 的高能团簇的能量分布必须在至少两个读出模块中有响应。结果表明，在添加这一筛选条件后，高能区伪信号可有效消除。相关介绍见论文3.5.3章以及参考文献 [74] 第 3.4.3 章。

另一方面，EMCal 作为触发（trigger）探测器能够筛选出包括高能信号的事件，在 Run 2 期间该触发系统全程启用。EMCal 触发响应在选定的 EMCal 区域以及触发数据采集期间应保持均匀性，同时屏蔽触发器性能较差的区域。系统研究 EMCal 触发器性能，在数据质量检验时发现量能器不同区域响应特性存在显著差异且具有时间依赖性，通过系统研究触发器性能，定位并屏蔽量能器中的死区或异常活跃区（电子噪声，校准缺陷等），建立基于数据采集周期的动态触发映射关系。这些屏蔽规则适用于所有基于 EMCal Run 2 数据的光子，电子，中性介子以及喷注测量等分析。通过应用这些屏蔽规则，各区域的触发性能一致性得到了显著改善但仍存在一定差异。通过测量各区间未识别团簇（unidentified cluster）的离散性来量化这一差异，观测到离散度（dispersion）为 4%。该离散度将被归类为光子分析（本测量）及其他 EMCal 相关分析的系统误差。更多详细讨论见论文3.6.2章。

pp 碰撞中产生的光子大多数来自强子的衰变。其中，中性 π 介子（π^0）衰变产生的光子是测量直接光子的主要背景，其产额比直接光子高出一个数量级以上。π^0 和 η 介子衰变成双光子的过程（$\pi^0 \to \gamma\gamma$，$\eta \to \gamma\gamma$）中，两个衰变光子之间的夹角（opening angle）随着 π^0（η）能

量的升高而减小，如图4.1所示。当 π^0 能量超过 5 GeV 时，两个衰变光子所形成的团簇开始逐渐重叠；对于 η 介子，这一阈值为 22 GeV 。随着 π^0（η）能量进一步升高至 $\pi^0 > 16$ GeV 或 $\eta > 60$ GeV 时，衰变双光子的夹角接近或小于探测单元的物理尺寸 [74]，此时团簇构建算法无法将两个衰变光子分离为独立团簇，二者合并为一个团簇。EMCal 上团簇的构建算法见文献 [74]，本次测量采用的是 “V1” 算法。一旦团簇形成，其能量 E 可以通过将属于该团簇的所有探测单元的能量相加来确定，计算过程见论文3.3章。通常情况下，这些团簇可能会具有较大的尺寸，因此可以重建由两个粒子重叠形成的团簇。团簇在 EMCal 上的能量分布可以通过参数化其在 EMCal 表面的簇射形状（shower shape）的椭圆轴参数来表征。更多细节可参考文献 [84] 以及示意图3.2。表征参数长轴（σ^2_{long}）和短轴（σ^2_{short}）的相关描述在论文3.3.1章。鉴于 σ^2_{long} 在中性粒子鉴别方面显著的区分能力 [74]，研究使用 σ^2_{long} 为表征参数。本研究中，团簇 σ^2_{long} 随 p_{T} 的分布如4.2(a)所示，大多数单光子团簇（不与其他粒子团簇重叠）的重建结果在 $\sigma^2_{\text{long}} \approx 0.25$ 处呈现显著分布峰值，此区间包含有单光子团簇以及高 p_{T} 下由中性介子衰变双光子合并形成的团簇，其余情形则对应更高 σ^2_{long} 值。在 σ^2_{long} 分布的主峰上方，存在一条具有明显 p_{T} 依赖的带状结构（图3.3和4.2(a)所示），该结构对应于由 π^0 衰变产生的双光子相互重合构成一个团簇的情形。本分析选择 $0.1 < \sigma^2_{\text{long}} < 0.3$ 的团簇作为光子候选团簇（photon candidates），这种团簇也称 “窄形团簇”（narrow cluster）。同样，$\sigma^2_{\text{long}} > 0.4$ 的团簇称为 “宽形团簇”（wide cluster）。结合团簇 σ^2_{long} 和能量沉积量信息，可以有效去除中性介子衰变产生的光子。然而，如前文所说，在高 p_{T} 时 σ^2_{long} 并不能有效区分衰变光子和直接光子。为有效抑制碎裂光子及中性介子衰变光子的背景干扰，研究引入孤立判据：以光子候选粒子为中心轴构建半径 $R = 0.4$ 的锥形区域，要求该区域内带电粒子横向动量总和（$p_{\text{T}}^{\text{iso, ch, UE}}$）小于 1.5 GeV/$c$。该复合孤立判据可以优化直接瞬时光子的选择效率，实现对直接瞬时光子的可靠鉴别与精确测量。关于 σ^2_{long} 的详细介绍见论文4.1章，孤立判据介绍见论文4.2章。

C.4 孤立直接光子散射截面测量

在应用团簇筛选条件及孤立判据之后，依据公式4.3可计算出各触发样本的原始孤立光子谱，结果见图4.13。结合 EMCal L1 trigger 能量阈值（$G2 = 4$ GeV ； $G1 = 9$ GeV），本分析在 $7 < p_{\text{T}} < 12$ GeV/c 区间采用 MB 和 EMCal G2 trigger 的合并样本，高于 12 GeV/c 采用 MB，EMCal L1 trigger（G2+G1）合并样本。由于探测器性能的限制（如 EMCal 屏蔽区域、死区或能量分辨率不足），并非所有产生的光子均可被有效探测。此外，分析过程中采用的多重筛选标准（如 σ^2_{long} 选择、孤立判选等）进一步降低了有效信号的捕获效率。因此，研究用 “效率”（efficiency）这一修正因子，来量化粒子在探测、重建及鉴别过程中的有效保留程度，并修正因探测器限制和分析筛选导致的信号损失。本分析通过 PYTHIA8 [79, 80, 96] 生成的 γ–jet 模拟事件来评估本分析的 “效率”，为实验测量的孤立光子谱与模拟中产生且满足孤立条件的光子谱的比值（如公

式4.5所示），效率曲线如图4.15所示。此外，关于孤立判据中能量阈值（$p_{\mathrm{T}}^{\mathrm{iso,\ ch}}$）计算是否需扣除底层事件（underlying event, UE）的贡献，通过分析验证发现：pp 碰撞中的底层事件密度较低，对产生层次（generator level）效率的影响可忽略，因此无需额外扣除。这一结论进一步简化了 pp 碰撞中孤立光子分析的效率评估流程。关于效率的更多讨论以及 UE 对效率影响的验证见论文4.3章。

重建的孤立光子中仍存在来自 π^0，η 衰变光子的贡献，因此需要计算孤立光子的“纯度”（purity，论文4.4章）。孤立光子纯度 P 定义为满足所有筛选条件的孤立光子中真实直接光子的占比，本分析采用的是 ABCD 方法计算。该方法已被多个实验组在相关研究中采用，例如 ATLAS[39, 40]、CMS[42] 和 ALICE[44] 在 7 TeV pp 碰撞中对直接光子快速生产的测量，以及 ALICE 在 5.02 TeV pp 和铅核–铅核（pb–pb）碰撞中的相关分析 [51, 95]。该方法基于 $p_{\mathrm{T}}^{\mathrm{iso,\ ch,\ UE}}$ 和 σ^2_{long} 构建相空间，根据信号筛选标准（$p_{\mathrm{T}}^{\mathrm{iso,\ ch,\ UE}} < 1.5$ GeV/c 及 $0.1 < \sigma^2_{\mathrm{long}} < 0.3$），相空间被划分为四个区域——信号区域（$\mathbb{A}$）和三个背景区域（$\mathbb{B}$，$\mathbb{C}$，$\mathbb{D}$），如图4.18所示。各区域之间通过 $p_{\mathrm{T}}^{\mathrm{iso,\ ch,\ UE}}$ 和 σ^2_{long} 参数设立间隔带，以规避边缘效应并抑制信号泄漏至背景区域，同时这些间隔也为系统误差分析提供了参数调节空间。ABCD 方法的核心目标是基于数据样本直接评估信号区域 $\mathbb{A}$ 中背景 $B_{\mathrm{n}}^{\mathrm{iso}}$ 的贡献，其假设如下：

1. 直接光子在背景区间的贡献可忽略不计，表达式见公式4.9。
2. 背景粒子形成的团簇通过孤立阈值 $p_{\mathrm{T}}^{\mathrm{iso,\ ch}}$ 的概率与其 σ^2_{long} 大小无关，表达式见公式4.10。

对这些假设的验证和理解在论文4.4.2章阐述，验证得出这些假设并非完全成立。修正项 α_{MC}（公式4.13）可以通过蒙特卡洛（MC）模拟获得，修正后的纯度表达式如式4.15 所示。
α_{MC} 修正后的纯度分布见图4.21，其随光子横动量（p_{T}^{γ}）的变化源于物理机制与探测器效应的共同作用：一方面，直接光子的 p_{T} 谱比中性介子（如 π^0）的更硬，这主要归因于中性介子在产生过程中经历了碎裂（fragmentation），在 pQCD 计算中亦被证实（如文献 [30, 84] 所述）。因此，直接光子与（π^0）衰变光子的散射截面比 $N_{\gamma_{2\to2}}/N_{\gamma(\pi^0)}$ 随 p_{T}^{γ} 的增加而上升，从而孤立光子纯度同步提高。同时，随着 p_{T}^{γ} 升高，直接光子通过孤立判选的概率逐渐上升而衰变光子通过固定孤立锥的概率逐渐降低，纯度也会升高。另一方面，π^0 和 η 的衰变双光子夹角随 p_{T}^{γ} 升高而减小使得在高 p_{T} 时对 π^0 和 η 的去除效率会下降，纯度因而下降。结合图4.2(a)可以看到，在本分析中，$p_{\mathrm{T}}^{\gamma} < 18$ GeV/c 时，衰变光子作为主要背景，表现为衰变光子对重叠（非融合）在一个团簇（σ^2_{long} 较大）中。高于 18 GeV/c 时，很大一部分衰变光子对会高度重合，所形成的团簇与单光子团簇相似从而满足团簇的判选条件。在 PYTHIA8 jet–jet 事件模拟结果中，p_{T} 在 14–16 GeV/c 时，约 6% 满足团簇筛选条件的窄形团簇来源于 π^0 衰变光子。当 p_{T} 升高到 20–25 GeV/c 时，大于 30% 的窄形团簇来自 π^0 衰变光子；而 $p_{\mathrm{T}} > 60$ GeV/c，这一占比约为 80%。同时，$p_{\mathrm{T}} > 60$ GeV/c

时，η 衰变光子对重叠形成的团簇也有概率被判定为窄形团簇，但是仍然是 π^0 衰变光子占主要贡献。相反，当 $40 < p_{\mathrm{T}} < 60$ GeV/c 时，大部分 η 衰变光子对的团簇会被判定为宽形团簇，从而被 σ^2_{long} 筛选条件去除。使得来自衰变光子的团簇对窄形团簇的贡献减少了，这是该区间纯度升高的部分原因。这些机制共同作用使得纯度在低 p_{T}^{γ} 时逐渐上升，$18 < p_{\mathrm{T}}^{\gamma} < 40$ GeV/c 达到饱和，至 40 GeV/c 再次开始升高，最后在 80 GeV/c 达到饱和。为避免将纯度用于计算散射截面时，纯度中数据涨落引起误差，用 Sigmoid 函数（公式4.19）对纯度进行分段拟合。第一段拟合范围为 7–30 GeV/c，得到参数结果为 $a_1 = 0.617 \pm 0.003$，$b_1 = 0.292 \pm 0.002$，$c_1 = 14.28 \pm 0.05$；第二段拟合范围是 20–160 GeV/c，对应参数结果为 $a_2 = 0.852 \pm 0.014$，$b_2 = 0.034 \pm 0.003$，$c_2 = 2.4 \pm 1.0$。通过拟合，可以得到各个参数及对应的误差，表格4.1给出的变量便是基于此得到的，这些变量将用于估算拟合引起的系统误差。

本研究旨在利用 ALICE 探测器于 2016 年至 2018 年采集的质心系能量 $\sqrt{s} = 13$ TeV pp 碰撞数据样本，测量孤立光子微分散射截面。对高能量光子的测量则依赖于 EMCal 的高精度探测和触发系统。EMCal 由上下两部分组成，各部分在相空间范围如图2.8所示，其中 EMCal 下半部分也称为双喷注量能器（DCal）。EMCal 上下两部分均提供输入信号用于 ALICE 中的触发决策过程，触发逻辑在文献 [76] 中有详细讨论。通过使用这些触发条件，可以针对性储存事件，从而提高样本的有效统计率。关于触发实现的更多细节可以在文献 [78] 中找到。需要说明的是，本研究选取的 EMCal L1 光子（L1-γ）触发 [76] 信号包含两个用于事件选择的阈值，低阈值（L1-γ-low，G2）为 $E_{\mathrm{trig}} > 4$ GeV，高阈值（L1-γ-high，G1）是 $E_{\mathrm{trig}} > 9$ GeV。表3.1给出 ALICE 在 2016 年至 2018 年 pp 碰撞中 $\sqrt{s} = 13$ TeV 的最小偏差（MB）事件和基于 EMCal L1 光子触发的事件数。触发机制对样本的增益能力通过参数“触发移除因子”（Trigger Rejection Factor，RF^{trig}）来量化，该参数描述为了获得一个有效的触发事件所需的 MB 事件的数量，定义式见公式3.13。针对触发效率的研究表明，在高横动量区间 EMCal L1-γ 触发机制并不完全有效。这种在特定区域内的不完全有效性引起的偏移可能会导致原本预期的平台区出现斜率变化，如图3.14所示。为量化这些畸变和效率损失，在模拟中对触发效率进行了估算。基于此估算，RF^{trig} 通过公式3.14计算可得，结果如图3.16所示。本研究使用了大约 1.59×10^9 个 MB 事件，1.36×10^8 个 EMCal G2 触发事件（$RF^{\mathrm{trig,G2/MB}} = 471 \pm 3$），以及 9.35×10^7 个 EMCal G1 触发事件（$RF^{\mathrm{trig,G1/MB}} = 5960 \pm 40$），详细信息见表3.6。相互作用截面按年度事件数加权计算得出，其中事件数为各触发器对应事件数的总和，并通过 RF^{trig} 进行修正。三年数据采集的平均截面为 $\sigma_{\mathrm{MB}}^{\mathrm{average}} = 58.05 \pm 0.90$ mb，所用数据样本的积分亮度为 $\mathcal{L}_{\mathrm{int}} = 10.79\ \mathrm{pb}^{-1}$。EMCal trigger 相关介绍见论文3.6章，相互作用截面平均值及积分亮度计算见论文4.5章。

所测量的孤立光子的微分散射截面依据公式4.23计算得出，并在图4.42中以纯统计误差形式呈现。本测量考虑的系统误差分为两大类：与纯度相关的误差以及与散射截面相关的误差。纯

度总误差同样作为散射截面误差的来源之一。这些误差通过调整分析中参数的数值获得，具体讨论在论文第5章。其中论文5.1章讨论了与纯度相关的误差，与散射截面相关的误差讨论则在论文5.2章。纯度总误差范围为 6% 至 35%，其最大值出现在低 p_{T}^{γ} 区间，在 16–30 GeV/c 达到最小值。纯度总误差及其误差来源贡献见图5.4。纯度系统误差的主要来源是与 α_{MC} 相关的孤立概率（isolation probability）。第二大误差来源随 p_{T} 不同而不同：对于低 p_{T}^{γ}（≤ 10 GeV/c），第二大误差是反孤立阈值（anti–$p_{\mathrm{T}}^{\mathrm{iso,\ ch,\ UE}}$）范围选择的不确定性；在 $30 < p_{\mathrm{T}}^{\gamma} < 60$ GeV/c，为 Sigmoid 函数拟合纯度时的误差；对于其余 p_{T}^{γ} 区间，第二大误差则源于 MC 模拟中信号样本占比。对于微分散射截面而言，$p_{\mathrm{T}}^{\gamma} \leq 100$ GeV/c 时系统误差主要源于纯度总误差，在更高 p_{T}^{γ} 区间，团簇的局部极大值引起的不确定性为系统误差的主要来源。微分散射截面的系统误差及其各来源贡献见图5.15。需要说明的是，当 p_{T}^{γ} 超过 100 GeV/c，测量结果的误差受统计误差主导。表5.1中分别列出了最低和最高 p_{T}^{γ} 区间，以及两个具有物理意义的中间区间（高于触发阈值和中间 p_{T}^{γ} 区间）不同误差来源及总误差的具体数值。

C.5 结果讨论与展望

本论文论述了 ALICE 实验中，质心能量 $\sqrt{s} = 13$ TeV pp 碰撞在中等快度区（$|\eta^{\gamma}| < 0.67$）孤立光子散射截面的测量。测量采用的孤立半径 $R = 0.4$，孤立阈值为 $p_{\mathrm{T}}^{\mathrm{iso,\ ch,\ UE}} < 1.5$ GeV/c。测量的孤立光子横动量区间为 $7 < p_{\mathrm{T}}^{\gamma} < 200$ GeV/c，孤立光子微分散射截面如图6.2所示。

测量的纯度与其他 ALICE 孤立直接光子测量的纯度在图6.1中进行了比较，结果表明在使用相似选择标准情况下，pp 碰撞中孤立直接光子的纯度具有良好的稳定性。此外，ALICE 在 $\sqrt{s} = 13$ TeV pp 碰撞中数据样本的大统计量显著降低了纯度的不确定性，特别是散射截面测量中的主导不确定性，在大部分 p_{T}^{γ} 范围内均得到了明显改善。

相较于 ALICE 在 $\sqrt{s} = 7$ TeV pp 碰撞中对孤立直接光子的测量（$10 < p_{\mathrm{T}}^{\gamma} < 60$ GeV/c，以及 $2.9 \times 10^{-3} < x_{\mathrm{T}}^{\gamma} = 2p_{\mathrm{T}}^{\gamma}/\sqrt{s} < 17.1 \times 10^{-3}$），本研究将孤立直接光子测量范围扩展至更宽区间。这得益于积分亮度提高了 20 倍，同时也考虑了更大的光子接收度。图6.3展示了测量结果与 NLO pQCD 计算（使用 JETPHOX 工具）的对比，两者 p_{T}^{γ} 分布的一致性验证了 pQCD 计算的可靠性。与 ATLAS 和 CMS 在同能标下的测量结果在误差范围内的相吻合（图6.6），体现了不同实验测量间的一致性。此外，如图6.7、6.8所示，不同质心能量下的散射截面比值与理论计算相吻合，进一步验证了 pQCD 计算的可靠性。

本研究首次在 LHC 碰撞系统中测量了 7–10 GeV/c 孤立光子散射截面。相较于 ATLAS（$p_{\mathrm{T}}^{\gamma} > 125$ GeV/c）和 CMS（$p_{\mathrm{T}}^{\gamma} > 190$ GeV/c）在同能标下的测量范围，本研究向更低动量区间扩展了一个数量级。相较于 LHC 其他实验组，ALICE 在中等快度区间较低 p_{T}^{γ} 区间的测量，有助于未来孤立直接光子散射截面的研究，以及孤立直接光子与喷注或强子之间的关联研究，这些研究

可用于约束 pQCD 计算、部分子分布函数（PDF）和碎裂函数（FF）。此外，本研究为探索核-核碰撞中硬探针的介质修饰效应以及小系统碰撞中的类 QGP 修正因子奠定了基础。

本研究还提供了迄今为止通过孤立直接光子在中等快度区间探测到的最低 Bjorken-x 值，范围为 $1.1\times10^{-3} < x \approx x_{\mathrm{T}}^{\gamma} = 2p_{\mathrm{T}}^{\gamma}/\sqrt{s} < 30.8\times10^{-3}$，如图6.9所示。该图展示了在不同 $\sqrt{s}$ 下，pp 和 $\mathrm{p\bar{p}}$ 碰撞中所有可用的孤立光子测量结果在统一标度 $(\sqrt{s})^{n=4.5}$ 下的良好一致性，跨越多个 Bjorken-x（即 $x_{\mathrm{T}}^{\gamma} \approx x$）数量级。所测得的低 x 值将为胶子部分子分布函数（PDF）提供重要约束。

得益于 LHC 第三和第四运行阶段亮度的显著提升，孤立直接光子的测量可以在更低的系统误差下进行。正如通过比较 Run 2 中大统计量的 $\sqrt{s} = 13$ TeV pp 碰撞测量的纯度与其他样本的纯度所看到的，系统误差得到了进一步降低，这为理论预测提供了更严格的约束。随着样本量的增加，另一项值得关注的测量可能是 pp 碰撞中孤立直接光子的散射截面随粒子多重数的分布情况。由于光子在“假设存在的 QCD 介质”中不会发生改变，这一测量可用于估算由多重性选择（例如事件中喷注的存在、碰撞的几何学因素等）引起的偏差，并为所有基于粒子多重性的其他粒子或喷注散射截面测量提供参考。此外，小系统中粒子多重数的选择标准可能会影响到观测到现象，而这些现象可以揭示系统中可能存在的 QGP。尽管 QGP 通常与重离子碰撞相关联，但最近的研究表明，在某些条件下，小系统也可能表现出类似于 QGP 的行为。

此外，通过将 pp 碰撞的结果与重离子碰撞的结果进行比较，可以区分冷核物质效应与高温 QCD 介质效应。这种对比方法将进一步提高我们分离 QGP 对部分子能量损失和碎裂过程贡献的能力，从而为 QGP 的存在及其性质提供更明确的证据。小系统中，这种对比的方法也同样适用，通过对比不同条件下的结果，可能能够揭示 QGP 形成的新机制或条件，从而拓宽我们对这种极端物质状态的了解。对孤立直接光子–喷注关联的方位角分布及运动学性质的研究有助于深化我们对部分子碎裂过程的理解。光子不参与强相互作用，在穿越核介质时基本保持不变，因此它保留了初始硬散射过程的信息，可作为研究硬散射的重要参照；而与之关联的喷注则源于在散射过程中与光子成对产生的部分子，其在穿越介质过程中会与介质发生相互作用，携带有介质内部的热力学和流体动力学演化的信息。因此，可以通过孤立直接光子标记喷注，并利用未来 LHC–ALICE 实验的数据，研究介质诱导的喷注修正以及尾流效应。

Appendix D Synthèse par chapitre en Français

D.1 Introduction à la physique des particules de haute énergie

Le modèle standard de la physique des particules, élaboré au début des années 1970, a permis d'expliquer la quasi-totalité des résultats expérimentaux et de prédire avec précision une grande variété de phénomènes. Il intègre avec succès les forces électromagnétiques, faibles et fortes dans un cadre théorique unifié. Parmi ces forces, l'interaction forte est décrite par la chromodynamique quantique (QCD, acronyme en anglais). La QCD possède deux propriétés essentielles : le confinement des couleurs et la liberté asymptotique. Le confinement des couleurs signifie que les quarks et les gluons ne peuvent pas exister de manière isolée, mais doivent exister dans des états liés neutres du point de vue de la couleur. C'est pourquoi nous ne pouvons pas « voir » des gluons ou quarks seuls. La liberté asymptotique indique qu'à des énergies très élevées ou sur de courtes distances, la force forte s'affaiblit et les particules peuvent interagir plus librement. L'interaction entre les quarks et les gluons est complexe en raison des couplages forts, et les interactions fortes décrites par la QCD sont fortement non linéaires. Il est donc presque impossible de résoudre directement l'équation de la QCD. Parallèlement, dans la région des hautes énergies, où Q^2 (l'échelle d'énergie) est grande, la QCD présente une liberté asymptotique, ce qui signifie que α_s (constante de couplage de la QCD qui décrit l'intensité de l'interaction forte en fonction de Q^2) devient suffisamment petite, permettant ainsi l'application de la théorie des perturbations. En d'autres termes, la chromodynamique quantique perturbative (pQCD, acronyme en anglais) peut être utilisée pour les calculs. La pQCD permet de traiter les interactions fortes à des énergies élevées en approximant progressivement les phénomènes physiques réels par une expansion d'ordre.

Les fonctions de distribution des partons (PDF, acronyme en anglais) sont des outils essentiels pour prédire le comportement des hadrons dans les collisions à haute énergie. Elles quantifient les probabilités de trouver des quarks, des antiquarks et des gluons - collectivement appelés « partons » - dans les hadrons à différentes fractions d'impulsion, généralement appelé x de Bjorken. Ces distributions comblent le fossé entre le régime nonperturbatif de la QCD, où la constante de couplage fort est grande, et le domaine perturbatif accessible par les expériences des collisionneurs. Les processus de diffusion dure dans les collisions proton–proton (pp) jouent un rôle essentiel dans l'étude de la structure interne du proton. En effet, la probabilité d'un événement de diffusion dure augmente considérablement lorsqu'un ou plusieurs partons portent une petite fraction de la quantité de mouvement du proton, ce qui correspond au régime de faible x. En outre, certains processus de diffusion dure, tels que ceux produisant des photons prompts via le processus de diffusion Compton $qg \rightarrow q\gamma$, permettent d'obtenir la PDF du gluon dans le proton,

en particulier à des valeurs x faibles où d'autres mesures peuvent être moins informatives.

Les photons n'interagissent pas avec l'interactions forte, ce qui leur permet de transporter l'information sur leur temps de production sans être altérés par des effets de l'état final jusqu'à leur détection dans l'appareil expérimental. La majorité des photons produits dans les collisions pp proviennent de désintégrations hadroniques, principalement $\pi^0 \rightarrow \gamma\gamma$. Les photons qui ne proviennent pas de désintégrations hadroniques sont appelés photons directs. Les photons prompt (instantanés, de production rapide) sont produits dans la phase initiale d'un processus de diffusion dure. Au premier ordre (LO, acronyme en anglais) de la pQCD, les photons prompts sont produits par difussion Compton ($qg \rightarrow q\gamma$, processus dominant), par annihilation ($q\overline{q} \rightarrow \gamma g$) et par production de photons doubles (section efficace très faible). A l'ordre suivant (NLO, acronyme en anglais) de la pQCD, des photons prompts sont également produits lors de la fragmentation d'un des partons sortants dans son processus d'hadronisation. Les photons prompts produits dans le processus Compton sont sensibles à la PDF du gluon qui est l'une des PDF les moins contraintes et qui ne peut être directement accessible par des mesures de diffusion inélastique profonde (DIS en anglais). Comme les photons prompts sont produits avec une faible activité hadronique autour d'eux alors et que le photon de désintégration et le photon de fragmentation ne le sont pas, la méthode d'isolation est un moyen efficace de sélectionner les photons prompts parmi les photons inclusifs. Les résultats de la simulation JETPHOX montrent que les photons de fragmentation sont fortement rejetés et que la majorité des photons prompts proviennent du processus Compton après application des critères d'isolation, voir Fig. 1.7 et Ref. [33]. Ainsi, la mesure de la section efficace des photons isolés peut tester les prédictions de la pQCD et contraindre la PDF du gluon qui n'est pas bien connue à l'heure actuelle.

Au cours des dernières décennies, des mesures liées à la production de photons prompts ont été effectuées. Les mesures de la section efficace des photons isolés dans les collisions pp au LHC (Grand collisionneur de hadrons acronyme en anglais) par les expériences ALICE (A Large Ion Collider Experiment), ATLAS (A Toroidal LHC Apparatus) et CMS (Compact Muon Solenoid) montrent que les calculs théoriques donnent une description cohérente avec les données relatives aux photons isolés, qui sont en accord avec les mesures effectuées à des énergies de collision plus faibles, voir le rapport entre diverses mesures et les predictions théoriques en Figs. 1.8, 1.9 et 1.10. Les calculs effectués à NLO sont légèrement sous-estimés et peuvent être améliorés en incluant des corrections au-delà de NLO. La mesure précise de la section efficace de production de photons prompts isolés a permis d'améliorer la détermination du PDF du gluon. En outre, ces mesures ont facilité l'étude de l'évolution de la fragmentation hadronique du parton emis à l'opposé du photon et de l'interaction entre les effets perturbatifs

et nonperturbatifs de la QCD. Tandis qu'ATLAS et CMS continuent à faire progresser les études sur les photons prompt à haute p_{T} (au-dessus de 20 GeV/c), les mesures de p_{T} faible à moyenne, accessibles par ALICE, restent limitées par la complexité du bruit de fond, les priorités de conception des détecteurs et les ambiguïtés théoriques, ce qui nécessitera de futures mises à niveau ou des expériences complémentaires pour obtenir une couverture complète.

D.2 Configuration expérimentale

Le LHC au CERN (Organisation européenne pour la recherche nucléaire) offre un environnement sans pareil pour les expériences de physique à haute énergie, en proposant les plus hautes énergies de centre de masse ($\sqrt{s}$) pour les collisions hadroniques actuellement disponibles (pp, Pb–Pb, p–Pb, et Xe–Xe), qui sont essentielles pour sonder les interactions fondamentales et les propriétés des particules élémentaires. Il y a quatre points d'interaction principaux où les particules accélérées entrent en collision. Chaque point d'interaction correspond aux positions d'un détecteur de particules, chaqu'un dédié aux études expérimentales en mettant l'accent sur différents sujets de physique. Les quatre collaborations expérimentales sont ATLAS [58], CMS [59], ALICE [63] et LHCb (Large Hadron Collider beauty) [62]. Pour les collisions pp, le LHC vise à accélérer et à faire entrer en collision des faisceaux de protons à une énergie de 7 TeV, ce qui donne une énergie totale au centre de la masse de 14 TeV, et des faisceaux de Pb de 2,75 TeV/nucléon, conduisant à une énergie au centre de la masse de 5,5 TeV. La liste des collisions et énergies attaintes est presenté dans la Table 2.1.

La luminosité ($\mathscr{L}$) aux points d'interaction est une mesure cruciale pour un accélérateur. La luminosité est le nombre d'événements de collision par seconde $\mathrm{d}N_{\mathrm{event}}/\mathrm{d}t$ pour un événement donné avec une section transversale σ_{event} est donnée par l'Eq. (2.1). La luminosité dépend principalement du nombre de particules présentes dans chaque faisceau en collision, de leur fréquence de rotation et du degré de focalisation du faisceau au point d'interaction. En outre, les deux faisceaux doivent entrer en collision à un angle de croisement au point d'interaction, ce qui réduit la luminosité mais permet d'orienter individuellement l'apport de luminosité à chacun des quatre points d'interaction et de supprimer les collisions non souhaitées à l'extérieur du point de collision.

Cette thèse presente des mesures faites avec les détecteurs de l'expérience ALICE. Le système central d'ALICE comporte plusieurs systèmes de détection pour mesurer les particules chargées et neutres. Le système de trajectographie central couvrant une pseudorapidité de $|\eta| < 0.9$ se compose du système de trajectographie interne (ITS), de la chambre de projection temporelle (TPC), du détecteur de rayonnement de transition (TRD) et du détecteur de temps de vol (TOF). Dans la région centrale,

ALICE comprend deux systèmes de calorimètre électromagnétique : le spectromètre PHOton (PHOS) et le calorimètre électromagnétique (EMCal).

Le ITS [67] et la TPC [70] sont utilisés pour mesurer et identifier les particules chargées, qui laissent des signaux lorsqu'elles traversent les six couches de silicium du ITS et puis la TPC. La TPC est un détecteur cylindrique rempli d'un mélange gazeux. Les particules chargées traversent le volume de gaz de la TPC laissant une trace d'électrons d'ionisation le long de leur chemin. Les électrons libérés sont accélérés vers les chambres de lecture via un champ électrique uniforme, appliqué entre les embouts et les électrodes situées au centre du détecteur. Après le temps de dérive les électrons libérés atteignent la chambre de lecture, composée de chambres proportionnelles multifils (MWPC, acronyme en anglais) avec lecture par tampon, permettant la détermination d'une projection bidimensionnelle de la trajectoire de la particule chargée dans le détecteur. En mesurant le temps de dérive des électrons libérés, on peut calculer la troisième coordonnée spatiale, obtenant ainsi la mesure tridimensionnelle de la trajectoire de la particule chargée. Ces signaux de l'ITS et la TPC sont combinés pour reconstruire la trajectoire d'une particule donnée, ce que l'on appelle le « track » (en anglais). La proximité de l'ITS avec le point d'interaction permet de reconstruire la position à laquelle une collision s'est produite (le point d'interaction). En outre, les points d'espace supplémentaires fournis par l'ITS à proximité du point d'interaction primaire permettent de suivre et d'identifier les particules à faible p_{T}. Le suivi des particules à fort p_{T} bénéficie également de l'ITS lorsqu'il est utilisé avec l'TPC, où les points d'espace supplémentaires améliorent la résolution globale de la mesure de l'impulsion des particules.

Le EMCal [74] est un calorimètre d'échantillonnage à couches de plomb–scintillateur utilisé pour mesurer les photons, les électrons et la partie neutre des jets par le biais des gerbes électromagnétiques que les différentes particules produisent dans les cellules du calorimètre. Le calorimètre est composé de tours de base 6×6 cm qu'on appel cellules, il y a 17644 cellules en total. Il couvre deux plages azimutales distinctes, comme le montre la Fig. 2.6. La partie supérieure couvre $|\eta| < 0.7$ en pseudorapidité et $80° < \varphi < 187°$ en angle azimutal et la partie inférieure, appelée calorimètre Di-Jet (DCal), contient deux parties : $260° < \varphi < 320°$ avec $0.22 < |\eta| < 0,7$ et $320° < \varphi < 327°$ avec $|\eta| < 0.7$. EMCal et DCal fournissent tous deux des entrées aux décisions de déclenchement de niveau 0 (L0) et de niveau 1 (L1) dans ALICE, la logique de déclenchement est discutée dans Ref. [76]. Le sous-système de déclenchement réside dans des cartes matérielles spécifiques qui fournissent des signaux FastOR correspondant à des sommes numériques de 2×2 cellules. L'unité de région de déclenchement (TRU, acronyme en anglais) [77] est utilisée pour numériserles signaux FastOR fournis par les cartes electroniques de lecture des signaux (FEE, acronyme en anglais) et pour calculer et générer les déclenchements

locaux L0 [76], le déclenchement de premier niveau. Dès réception d'un déclencheur L0 accepté par le processeur central de déclenchement (CTP, acronyme en anglais), les sommes de cellules numérisées de 2×2 provenant de chaque TRU sont transmises à l'unité de déclenchement de synthèse (STU, acronyme en anglais). Dans la STU, les sommes cellulaires superposées de 4×4 sont à nouveau formées, mais à travers les limites de l'TRU sur l'acceptance complète pour fournir un déclencheur de la gerbe à haute énergie L1 amélioré, appelé déclencheur de photons L1-γ [76]. Les déclencheurs L1 permettent de définir deux seuils pour la sélection de l'événement, appelés seuils haut et bas. On trouvera plus de détails techniques sur la mise en œuvre des déclencheurs dans [78].

Dans cette analyse, la reconstruction des photons est effectuée à l'aide du EMCal, tandis que les particules chargées utilisées dans les critères de sélection de l'isolement des photons sont reconstruites avec la combinaison de l'ITS et de la TPC.

D.3 Sélection, reconstruction et calibration des données EMCal

L'analyse utilise les données de collisions pp à $\sqrt{s} = 13$ TeV collectées avec ALICE en 2016, 2017 et 2018. Les données ont été prises avec un déclencheur d'interaction à biais minimal (MB) et des déclencheurs dédiés aux photons EMCal L1 (L1-γ). Le déclencheur MB était basé sur la réponse du détecteur V0, deux déclencheurs EMCal L1-γ ont été utilisés, consistant en des dépôts d'énergie supérieurs à 4 GeV (L1-γ-low, étiqueté comme G2) ou 9 GeV (L1-γ-high, étiqueté comme G1) dans 4×4 cellules adjacentes, voir la description détaillée des déclencheurs EMCal dans Refs. [74, 76].

L'amélioration de l'échantillon déclenché par rapport à l'échantillon MB est quantifiée par le « facteur de rejet du déclenchement » (marqué comme RF^{trigger}), qui est également utilisé pour calculer correctement la luminosité. Il reflète la capacité d'amélioration du déclenchement, c'est-à-dire qu'il tient compte du nombre d'événements MB nécessaires pour obtenir un de ces événements déclenchés. Cependant, les études sur l'efficacité des déclenchements montrent que les déclenchements EMCal L1-γ ne deviennent pas pleinement efficaces à p_{T} élevé et que les biais cinématiques peuvent conduire à des pentes résiduelles dans la région du plateau, comme le montre la Fig. 3.14. Pour ces distorsions et inefficacités, une efficacité de déclenchement est estimée dans la simulation. En tenant compte de cet effet, le RF^{trig} est calculé par l'Eq. (3.14) et représenté sur la Fig. 3.16. Dans cette analyse, on utilise environ 1.59×10^{9} d'événements MB, 1.36×10^{8} G2 (correspondant $RF^{\text{trig,G2/MB}} = 471 \pm 3$) d'événements déclenchés et 9.35×10^{7} G1 (correspondant $RF^{\text{trig,G1/MB}} = 5960 \pm 40$) d'événements déclenchés. Les informations détaillées sont présentées dans le Tab. 3.6.

La réponse du détecteur est modélisée par des simulations de Monte Carlo (MC) reproduisant les conditions du détecteur pendant la période de prise de données. Les événements MC sont obtenus en utilisant PYTHIA 8 (version 8.210 [79] utilisant l'accord Monash 2013 [80]) comme générateur de particules. Deux types de processus PYTHIA 8 sont générés dans les intervalles de l'impusion transversale de la diffusion dure pour cette analyse : d'une part, les processus durs de Compton et d'annihilation 2→2 émettant un photon et un parton, conduisant à des événements dits γ–jet (GJ) : ceux-ci sont utilisés ici pour reproduire un signal de photon prompt. Les photons ont été sélectionnés au niveau du générateur pour tomber dans l'acceptance de EMCal et DCal afin de réduire la taille de la sortie ; d'autre part, les processus durs résultant de l'émission de deux partons opposés, conduisant à des événements jet–jet (JJ), l'événement est accepté lorsqu'au moins un jet produit un photon de haute p_{T} provenant d'une désintégration hadronique dans l'acceptance de EMCal. Cela permet d'augmenter le nombre des photons de decroissance des mesons π^0 et η, qui constituent le principal élément de polution de l'analyse presenté dans cette thèse. Trois seuils de déclenchement ont été considérés : 3,5 GeV/c (JJ bas), 7 GeV/c (JJ haut) et 28 GeV/c (JJ supplémentaire). Chacun des échantillons déclenchés par les simulations JJ est utilisé pour des corrections dans différentes rangées en p_{T} du spectre, de sorte que les limitations statistiques de chaque échantillon à des sont réduites. La plage d'utilisation dépend de la limite inférieure d'applicabilité de l'échantillon JJ, généralement proche de 2 fois le seuil de déclenchement du p_{T}, ce qui correspond approximativement au p_{T} inférieur du méson neutre qui a été déclenché.

Les particules déposent la majeure partie de leur énergie dans une seule cellule de l'EMCal, et le reste dans plusieurs cellules voisines. On veut former un « groupe » de cellules qu'on appel cluster, où une particule donnée dépose de l'énergie, bien que, selon l'énergie, la granularité, l'algorithme de clusterisation ou le type d'événement, ces groupes puissent avoir des contributions de différentes particules [74]. Les clusters représentent idéalement l'énergie qu'une particule a déposée dans le calorimètre, en particulier pour les photons et les électrons. La méthode de clusterisation définit les cellules qui appartiennent à un cluster. Des détails sur le fonctionnement des clusteriseurs dans EMCal peuvent être trouvés dans Ref. [74]. Pour l'analyse, nous utilisons le clusteriseur dit "V1". Il démarre les clusters en sélectionnant une cellule de départ dont l'énergie est supérieure à un seuil donné $E_{\mathrm{seed}} = 500$ MeV. Ensuite, il regroupe dans le cluster toutes les cellules ayant un côté commun avec la cellule de départ si leur énergie est supérieure à $E_{\mathrm{agg}} = 100$ MeV. Une cellule ne peut appartenir à plus d'un cluster [85]. En règle générale, ces clusters peuvent être de grande taille. Il est donc possible de reconstruire des clusters formés par le chevauchement de deux particules. Une fois le cluster formé, son énergie E peut être calculée comme la somme des énergies des cellules qui appartiennent au cluster. La distribution de l'énergie au sein d'un cluster, appelée « forme de la gerbe » electromagnétique, est décrite à l'aide

d'une paramétrisation des axes de l'ellipse de la surface de la gerbe. Pour plus de détails, voir Ref. [84] et la description schematique de la Fig. 3.2. La distribution de l'énergie le long des directions η (pseudorapidité) et φ (azimut) est représentée par une matrice de covariance avec des termes $\sigma^2_{\varphi\varphi}$, $\sigma^2_{\eta\eta}$ et $\sigma^4_{\eta\varphi}$, qui sont présents dans l'Eq. (3.5). Les paramètres de forme de la gerbe σ^2_{long} (axe long) et σ^2_{short} (axe court) sont définis comme les valeurs propres de la matrice de covariance, et sont représentés sur la Fig. 3.2 et calculés comme Eq. (3.6). Pour les particules neutres, le σ^2_{long} a un pouvoir de discrimination évident pour identifier les particules, tandis que le σ^2_{short} n'est pas aussi efficace [74]. C'est pourquoi nous utilisons le paramètre σ^2_{long} dans cette analyse pour identifier les particules neutres auxquelles le groupe appartient. Les unités du paramètre sont des tailles de cellules, mais pour des raisons de simplicité, ce paramètre est présenté sans unités. La Fig. 3.3 montre la distribution de σ^2_{long} en fonction de du p_{T} mesuré en collisions pp à $\sqrt{s} = 13$ TeV dans les données mesurés et la simulation.

L'étalonnage de l'EMCal est une étape essentielle pour garantir une mesure précise de l'énergie déposée par ces particules. Différents types d'étalonnages sont effectués sur l'EMCal afin d'obtenir des mesures précises: en énergie à l'aide de la mesure de la masse invariante des mésons π^0; en temps d'arrivé des particules au detecteur; temperature qui affecte l'énergie; et l'etude de la stabilité des cellules qui peuvent étre électroniquemen bruyantes ou inactives et doivent être masqués. Des détails techniques ou de performance concernant l'EMCal d'ALICE peuvent être trouvés dans le document sur les performances de l'EMCal [74]. Enfin, la reponse de l'EMCal n'est pas lineaire, à cause de pertes d'energie entre cellules et effets de saturation electronique. Une correction de non-linéarité énergétique dérivée des données du faisceau de test d'électrons [74] est appliquée à l'énergie de l'amas reconstruit. Elle s'élève à environ 6% à $E = 1$ GeV diminuant à environ 2% entre 20 et 100 GeV et augmentant à environ 3% à 200 GeV en raison de la saturation du signal. Étant donné que la simulation ne reproduit pas exactement la linéarité de l'énergie, un facteur de correction supplémentaire est appliqué pour faire correspondre la masse π^0 obtenue dans les simulations aux mesures correspondantes dans les données. La valeur de cette correction est de 1,025 à $E = 1$ GeV, diminuant à 0,975 au-dessus de 7 GeV.

Deux défis inattendus ont été rencontrés lors de cette mesure et nécessitent des travaux techniques supplémentaires au sein de la communauté ALICE-EMCal. Pour la première fois, des énergies de photons supérieures à 100 GeV ont été atteintes et le traitement des faux signaux déjà connus doit être ajusté et amélioré. C'est une partie de mon travail pendant le doctorat, en plus de l'analyse physique. En analysant les signaux des clusters de photons candidats à très haute énergie ($p_{\text{T}} > 100$ GeV/c), une contribution significative de pseudo-signaux anormaux créés par des neutrons frappant directement les APDs des tours EMCal a été trouvée. Ces signaux à basse énergie peuvent être rejetés selectionnant des

clusters avec plus de 97% de l'energies dans une seul cellule avec le paramètre $F_+ < 0.97$ definit en Eq. 3.10. Mais, ces faux signaux induisent des signaux de diaphonie électronique significatifs dans les cellules voisines de la cellule principale du calorimètre, créant des clusters avec un étalement d'énergie qui pourrait être confondu avec des photons. À des énergies aussi élevées, les vrais signaux de photons créent des clusters couvrant plus d'une carte de lecture (2×8 cellules). Une nouvelle sélection de clusters a été mise en œuvre pour ce travail afin d'éliminer les faux signaux : les clusters de haute énergie supérieurs à 80 GeV doivent avoir un étalement d'énergie dans au moins deux des cartes de lecture. D'autre part, les performances de l'EMCal ont été vérifiées afin que la réponse au déclenchement soit uniforme sur la région sélectionnée de l'EMCal et sur les périodes de prise de données déclenchées, masquant ainsi les régions moins performantes. Les performances et la stabilité du déclenchement de l'EMCal sont des éléments clés de cette mesure puisqu'elle repose en grande partie sur l'échantillon déclenché par l'EMCal lors du Run 2. Au cours de l'étude de la qualité des données obtenues avec le déclencheur, la vérification des taux de photons candidats a révélé que différentes régions du calorimètre présentaient des réponses différentes, qui dépendaient également de la période. Cela a déclenché une étude minutieuse de l'activité du déclencheur afin d'identifier et de masquer les zones mortes ou trop actives (bruit électronique, étalonnage imparfait) dans le calorimètre.

Afin d'avoir un qualité suffissant des clusters pour identifier et mesurer les photons proprement, les clusters doivent contenir au moins deux cellules afin de garantir une taille minimale et d'éliminer les fluctuations du bruit électronique des cellules individuelles. De plus, la cellule la plus énergétique du cluster doit être à une distance d'au moins deux cellules d'une cellule masqué connue pour son mauvais comportement afin d'éviter une éventuelle influence électronique entre les canaux, ou d'une cellule morte afin d'éviter des trous dans la répartition énergétique des clusters. Pour limiter les fuites d'énergie aux frontières du calorimètre, une distance d'au moins une cellule dés la cellule la plus énergétique du cluster à la frontière du calorimetre est requise. Considerant ces sélections, l'acceptance d'EMCal et de DCal utilisée est de $81.2° < \varphi < 185.8°$ donc $\Delta\varphi = 104.6°$ et $|\eta| < 0.67$ donc $\Delta\eta = 1.34$ et la partie inférieure (appelée DCal) de $261.2° < \varphi < 318.8°$ donc $\Delta\varphi = 57.6°$ et $0.25 < \eta| < 0.67$ donc $\Delta\eta = 0.42$ et $321.2° < \varphi < 325.8°$ donc $\Delta\varphi = 4.6°$ et $|\eta| < 0.67$.

Autres critères de sélection : Pour garantir la sélection des clusters appartenant à la collision principale (plusieurs collisions secondaires, pile-up, peuvent passer dans la fenêtre de temps ou la collision es mesuré), le temps mesuré de la cellule la plus énergétique des clusters par rapport autemps de la collision principale doit satisfaire à $\Delta t < 20$ ns; Les clusters ne peuvent contenir plus de deux cellules locales maximales (des cellule autour desquelles il y a des cellules avec moins d'énergie); aucune division de

cluster n'est effectuée. Enfin, pour selectionner des photons on s'assure que ces photons ne sont pas associés à une trace provenant de la TPC pour exclure electrons ou hadrons. Si la trajectoire d'une trace prolongé à la surface de l'EMCal est proche de 1-2 cellules, ce cluster est exclu. La selection est dependent du p_{T} de la trace et des angle azimuthal et la pseudorapidité et est definit dans l'Eq. (3.9). Ces clusters "neutres" sont le point de depart pour l'identification final des photons.

D.4 L'identification et mesure de la section efficace des photons prompt

La majorité des photons produits dans les collisions pp proviennent de la désintégration des hadrons. Les photons de désintégration des mésons π^0 est connu comme la contamination principale pour la mesure des photons prompt. L'angle d'ouverture lors de la decroissance en deux photons des mésons π^0 et η est tel que les cellules externes des clusters des photons peuvent se chevaucher à des énergies supérieures à 5 GeV pour les mésons π^0 et 22 GeV pour les mésons η. Au-dessus de 16 GeV pour les mésons π^0 et 60 GeV pour les mésons η, l'angle d'ouverture minimum est proche ou inférieur à la taille de la cellule [74], les deux photons de décroissance sont trop proches pour être separés par l'algorithme de clusterisation. La plupart des clusters de photons simples purs (qui ne se chevauchent à d'autres clusters de particules) sont reconstitués sous forme de la gerbe des clusters avec un pic prononcé à $\sigma^2_{\mathrm{long}} \approx 0.25$, d'autres cas contribuent à des valeurs plus élevées. Au-dessus du pic principale dans la distribution de σ^2_{long}, une bande clairement dépendante de p_{T} est observée dans les Figs 3.3 et 4.2(a). Cette bande est peuplée de deux photons de désintégration π^0 contribuant à un seul cluster. Les principales contributions à la région de forme de pluie étroite sont des photons simples (à faible p_{T}) ou des photons fusionnés provenant de désintégrations de mésons neutres (à haut p_{T}). Une limite inférieure à $\sigma^2_{\mathrm{long}} = 0.1$ est définie pour nettoyer l'échantillon du cluster de quelques dépositions anormales à haute énergie qui passent toujours la sélection F_+. Le σ^2_{long} en fonction de l'énergie du cluster est également observé quand la sélection $F_+ < 0.97$ n'est pas appliquée, montrant une population de cluster exotique claire pour $\sigma^2_{\mathrm{long}} < 0.1$ à haut p_{T}, voir Fig. 4.3, qui peut être nettoyé en appliquant la condition d'avoir des clusters ayant des cellules dans plus d'une carte de lecture. Dans cette analyse, les "candidats photon" se réfèrent à des clusters avec une forme "étroite" définie par $0.1 < \sigma^2_{\mathrm{long}} < 0.3$.

Un critère d'isolement est appliqué au candidat photon pour supprimer la contribution par fragmentation et désintégration de la production de photons. Un critère d'isolement équivalent est généralement inclus dans les calculs théoriques pour tenir compte de la suppression de la contribution de la fragmentation à la section transversale rapide totale du photon. Le critère d'isolement est basé sur l'«impulsion d'isolement» $p_{\mathrm{T}}^{\mathrm{iso}}$, c'est-à-dire la somme de p_{T} de toutes les particules mesurées à l'intérieur d'un cône

dans l'espace angulaire η (pseudorapidité) et φ (angle azimutale) de rayon R autour du photon candidat, situé à η^{γ} et φ^{γ}, defini par Eq. (4.1). Le rayon du cône $R = 0,4$ est choisi car il contient la fraction dominante de l'énergie du jet [94]. Selon le type de particule associé au candidat dans le cône d'isolement, il y a trois possibilités : ne considérer que les particules chargées (tracks combinés de l'ITS et TPC), que les particules neutres (clusters de calorimètres) et la somme des deux. En outre, on peut envisager d'estimer et de retirer la contribution de la densité d'énergie de l'événement sous-jacent, nécessaire dans les collisions Pb–Pb et p–Pb, pas tant dans les collisions pp comme discuté ci-dessous. Dans cette analyse, l'impulsion d'isolement définie comme $p_{\mathrm{T}}^{\mathrm{iso,\ ch,\ UE}} = \sum p_{\mathrm{T}}^{\mathrm{track}}$, devrait être inférieur à 1.5 GeV/c pour selectionner les photons.

Avec les critères de sélection d'isolement et de la forme de gerbe du cluster appliqués, le spectre de photons isolés brut, calculé comme Eq. (4.3), peut être obtenu pour chaque échantillon déclenché. Le photon isolé reconstitué a encore une contribution non négligeable des photons de désintégration des mésons neutres, donc une bonne estimation de la "pureté" de l'échantillon de cluster sélectionné est cruciale. En plus, en raison des performances des détecteurs, tous les photons ne peuvent pas être mesurés, et certains sont perdus dans les différentes étapes de sélection pendant les critères de reconstruction, d'identification et d'isolement. Il faut évaluer ce que l'on appelle l' «efficacité» pour reconstruire et identifier de telles particules. L'efficacité peut être obtenue par l'utilisation de simulations PYTHIA8 [79, 80, 96] γ-jet, qui sont utilisées pour reproduire le signal d'intérêt. Le nombre de photons isolés mesurés est ensuite comparé au nombre de photons qui ont été générés à l'origine dans la region angulaire couverte par l'analyse. Ceci explique les pertes potentielles d'acceptance dues à des régions masquées ou mortes dans EMCal où des photons isolés peuvent être reconstitués et des effets de résolution des détecteurs. Les différents critères de sélection de l'analyse déterminent l'efficacité globale de l'analyse. Ici, il est calculé comme le rapport des spectres definit en Eq. (4.5). Le dénominateur est le nombre de photons générés et isolés, et les facteurs dans le numérateur sont les spectres reconstitués après différents critères de sélection. L'eficacité totale est calculé et montré à la Fig. 4.15. Un étude sur la necessité de soustraire l'evenement sousjacent du calcule de l'impulsion d'isolement est fait montrant son effet sur l'efficacité au niveau generateur et concluant que ce n'est pas necessaire en collisions pp.

La pureté du photon isolé, P, est définie comme le rapport des photons isolés mesurés qui étaient en fait des photons de la signal qu'on cherche sur tous les photons candidats après l'application des différents critères de sélection. La méthode de calcul de la pureté ABCD, que j'ai utilisée dans cette analyse, a été utilisée dans plusieurs publications, telles que la mesure de la production rapide isolée dans les collisions pp à $\sqrt{s} = 7$ TeV par ATLAS [39, 40], CMS [42] et ALICE [44], la mesure dans les

collisions pp et Pb–Pb à $\sqrt{s_{\rm NN}}$ = 5.02 TeV par ALICE [51, 95]. Cette methode considère un espace de phase basé sur l'impulsion d'isolation mesurée à l'intérieur du cône d'isolement, $p_{\rm T}^{\rm iso,\ ch,\ UE}$, et sur la forme de la gerbe de cluster, $\sigma^2_{\rm long}$. En fonction des coupes d'analyse de sélection de signal ($p_{\rm T}^{\rm iso,\ ch,\ UE}$ <1.5 GeV/c et 0.1 <$\sigma^2_{\rm long}$ < 0.3), l'espace de phase peut être divisé en 4 régions – une région de signal ($\mathbb{A}$) et trois régions de de contrôle de la contamination ($\mathbb{B}$, $\mathbb{C}$, et $\mathbb{D}$), presenté schématiquement dans la Fig. 4.18. Les régions de contrôle de la contamination ($\mathbb{B}$, $\mathbb{C}$ et $\mathbb{D}$) sont séparées de la région du signal ($\mathbb{A}$) par un espace en termes de $p_{\rm T}^{\rm iso,\ ch,\ UE}$ et $\sigma^2_{\rm long}$. Ceci vise à éviter les effets de bord dans la mesure de chaque population, et toute fuite de signal dans les régions de contrôle de la contamination. En outre, le fait d'avoir un écart entre les différentes régions nous a permis de faire varier les valeurs correspondantes pour déterminer les incertitudes systématiques associées aux mesures de pureté. L'intérêt principal de la méthode ABCD est d'évaluer la contamination $B_{\rm n}^{\rm iso}$ dans la region signal $\mathbb{A}$ d'une manière basé le plus possible que sur les données. La détermination de la contribution $B_{\rm n}^{\rm iso}$ est basée sur deux hypothèses fortes sur les propriétés des clusters dans les régions de contrôle $\mathbb{B}$, $\mathbb{C}$, et $\mathbb{D}$:

1. Les photons prompts contribuent de manière négligeable aux régions de contrôle.
2. Les clusters créés par des photons de decroissance ont la même probabilité de passer le seuil d'isolement $p_{\rm T,\ max}^{\rm iso,\ ch,\ UE}$ qu'ils aient une forme étroite (bas $\sigma^2_{\rm long}$, régions $\mathbb{A}$ et $\mathbb{C}$) ou large (haut $\sigma^2_{\rm long}$, régions $\mathbb{B}$ et $\mathbb{D}$);

Cependant, ces hypothèses n'étaient pas exactement vraies. La méthode d'estimation de la pureté doit être corrigée par un terme, $\alpha_{\rm MC}$ (Eq. (4.13)) obtenu a partir de simulations MC, et donc l'expression de la pureté corrigée du photon isolé P devient comme indiqué dans Eq. (4.15). La distribution calculé de la pureté est presenté à la Fig. 4.21. La dépendance en $p_{\rm T}^{\gamma}$ de la pureté est causée par une interaction entre la physique et les effets des détecteurs. La majeure partie de la contamination est due aux photons π^0-decay. D'une part, les spectres en fonction du $p_{\rm T}$ des photons prompts sont plus durs que ceux des pions neutres, principalement parce que ces derniers subissent une fragmentation, comme cela a également été constaté dans les calculs pQCD [30, 84]. Pour cette raison, le rapport de section efficicace $N_{\gamma_{2\to2}}/N_{\gamma(\pi^0)}$ augmente avec $p_{\rm T}^{\gamma}$, et la pureté des photons augmente également. De plus, la probabilité de marquer un photon comme isolé varie en fonction de $p_{\rm T}^{\gamma}$. À un $p_{\rm T}^{\gamma}$ plus élevé pour des photons de désintégration, l'isolement est moins probable pour une impulsion d'isolement fixe. D'un autre côté, le rejet des clusters des mésons π^0 et η à un $p_{\rm T}$ élevé devient moins efficace en raison de la diminution de l'angle d'ouverture du photon de désintégration lors de l'augmentation du $p_{\rm T}$ du méson. En dessous de 18 GeV/c, la contamination est dominée par des photons de désintégration simples (c'est-à-dire non fusionnés) provenant des mésons π^0, les contributeurs restants étant principalement des photons issus des

désintégrations des mésons η. Au-dessus de 18 GeV/c, une grande fraction des désintégrations $\pi^0 \to \gamma\gamma$ produit deux photons avec un angle d'ouverture étroit et donne naissance à des clusters fusionnés dans l'EMCal avec une forme de douche étroite qui satisfait à la condition du signal à photon unique, comme on peut l'apprécier sur la Fig. 4.2(a). Dans les simulations PYTHIA 8 jet–jet, à $p_{\mathrm{T}} = 14$–16 GeV/c environ 6% des clusters reconstruits dans la région de forme de douche étroite proviennent de clusters π^0, puis à $p_{\mathrm{T}} = 20$–25 GeV/c, ils sont supérieurs à 30% et au-dessus de 60 GeV/c cette contribution s'élève à environ 80%. Les clusters produits par les photons fusionnés à partir des désintégrations de mésons η contribuent à la région étroite de forme de gerbe pour $p_{\mathrm{T}} > 60$ GeV/c mais ceux-ci restent sous-dominants par rapport aux amas de désintégrations π^0 fusionnés. Au lieu de cela, dans la plage $40 < p_{\mathrm{T}} < 60$GeV/c, la plupart des clusters de désintégration η fusionnés ont de larges formes de gerbes, ce qui est en partie la raison de l'augmentation de la pureté dans cette région p_{T}^{γ} puisque la contribution des clusters de photons simples des désintégrations η aux clusters étroits diminue. L'effet combiné de ces mécanismes conduit à une augmentation de la pureté à faible p_{T}, une saturation pour $18 < p_{\mathrm{T}}^{\gamma} < 40$ GeV/c, puis une augmentation au-dessus de 40 GeV/c, et enfin une saturation au-dessus de 80 GeV/c.

Pour réduire les fluctuations statistiques point à point de la pureté utilisée pour corriger la sections efficiance de production brute de photons isolés, la distribution est ajustée par deux fonctions sigmoïdes (Eq. (4.19)) pour reproduire la tendance de la distribution avec p_{T}^{γ}. Dans cette analyse, le premier ajustement est fait de $p_{\mathrm{T}}^{\gamma} = 7$ à 30 GeV/c avec les paramètres d'ajustement obtenus étant $a_1 = 0.617 \pm 0.003$, $b_1 = 0.292 \pm 0.002$, et $c_1 = 14.28 \pm 0.05$. Le deuxième ajustement est fait de $p_{\mathrm{T}}^{\gamma} = 20$ à 160 GeV/c avec les paramètres $a_2 = 0.852 \pm 0.014$, $b_2 = 0.034 \pm 0.003$, et $c_2 = 2.4 \pm 1.0$. Pour chaque paramètre, la valeur ajustée et son erreur associée du processus d'ajustement peuvent être obtenues. Pour attribuer une incertitude systématique à l'ajustement, les paramètres de la fonction ont été modifiés de la manière prévue dans Tab. 4.1.

La section efficace d'interaction est calculée en pondérant le nombre d'événements par année, où le nombre d'événements est la somme des événements pour chaque déclencheur, ajustée par le facteur de rejet. Le tableau 4.2 montre la section efficace d'interaction et son incertitude associée pour chaque année, ainsi que la section efficace moyenne d'interaction et son incertitude correspondante. La section d'interaction résultante moyenne sur les trois années de prise de données est $\sigma_{\mathrm{MB}}^{\mathrm{average}} = 58.05 \pm 0.90$ mb. La luminosité intégrée recueillie avec chacun des déclencheurs utilisés ($\mathscr{L}_{\mathrm{int}}^{\mathrm{trigger}}$) a été déterminée à l'aide de l'expression Eq. (4.20). La section finale de production est mesurée en fonction de p_{T}, ainsi, les différents déclencheurs sont combinés en fonction du seuil de déclenchement. Le seuil de déclenchement

L1-γ-high est à $E = 9$ GeV mais il n'est pleinement efficace que peu de GeV après, il a donc été décidé de combiner les trois déclencheurs au-dessus de $p_{\mathrm{T}} = 12$ GeV/c. Par conséquent, la distribution au-dessous de $p_{\mathrm{T}} = 12$ GeV/c est une combinaison de MB et L1-γ-low déclencheurs et au-dessus est la combinaison des trois déclencheurs. La luminosité échantillonnée résultante de la mesure actuelle est calculée comme Eq. (4.21) et résultant en Eq. (4.22).

La section efficace différentielle du photon isolé en fonction de p_{T}^{γ} entre 7 et 200 GeV/c est calculée suivant l'équation (4.23) et montré à la Fig. 4.42 seulement avec incertitudes statistiques.

D.5 Incertitudes systématiques

Les incertitudes systématiques sont divisées en deux catégories, celles liées à la pureté et celles liées à la section efficace. L'incertitude de la pureté totale est également une source d'incertitude dans la section efficace. Elles sont obtenues par la variation des diverses paramètres de l'analyse.

L'incertitude de la pureté totale se situe entre 6% et 35% étant maximale à faible p_{T}^{γ} et ayant un minimum pour p_{T}^{γ} entre 16 et 30 GeV/c. La principale source d'incertitude systématique est la probabilité d'isolement relié a α_{MC} et comment la forme de la gerbe et l'isolation sont reproduites au MC. La deuxième source d'incertitude la plus importante est p_{T}^{γ}-dépendant: à faible p_{T}^{γ} (jusqu'à 10 GeV/c) la variation de la plage d'anti-isolement utilisé pour definir les regions ABCD, entre 30 et 60 GeV/c l'incertitude de l'ajustement à la pureté avec la fonction sigmoïde, et pour l'autre p_{T}^{γ}–s'étend la quantité de signal consideré dans la simulation MC.

La source dominante de l'incertitude systématique pour la section efficace est l'incertitude relative de pureté totale jusqu'à $p_{\mathrm{T}}^{\gamma} = 100$ GeV/c, tandis que pour les plus grands p_{T}^{γ}, l'effet de la variation de la sélection sur le nombre de maxima locaux du cluster devient dominant. Néanmoins, pour $p_{\mathrm{T}}^{\gamma} = 100$ GeV/c, la mesure est dominée par des incertitudes statistiques. Les valeurs des incertitudes systématiques pour les différentes sources et le total sont rapportées dans l'onglet. 5.1 pour les plages les plus bas et les plus élevés en p_{T} et deux plages intermédiaires mais significatifs (au-dessus du seuil de déclenchement et intermédiaire en p_{T}).

D.6 Résultats de mesures de photons isolés, conclusions et perspectives

Cette these présente la section efficace de production des photons isolés en collision pp à $\sqrt{s} = 13$ TeV avec rayon de du cône d'isolation $R = 0.4$ et une coupure d'isolation $p_{\mathrm{T}}^{\mathrm{iso,\ ch,\ UE}} < 1.5$ GeV/c à rapidité centrale $|\eta^{\gamma}| < 0.67$ dans et $7 < p_{\mathrm{T}}^{\gamma} < 200$ GeV/c dans la Fig. 6.2.

La pureté de la mesure est comparé a la pureté d'autres mesures de photons isolés à ALICE en Fig. 6.1, montrant la stabilité du résultat en collisions pp en utilisant des critères de sélection similaires et que la grand nombre d'evenements fournis par le LHC en collisions pp à $\sqrt{s} = 13$ TeV aide a diminuer significativement les uncertitudes de la pureté et en particulier de la mesure de la section efficace qui est dominé par cette uncertitude la plus part du range en p_{T}^{γ} couvert.

Dans ce travail, la mesure couvre une plage de photons en p_{T} plus large que la mesure précédente d'ALICE en collisions pp à $\sqrt{s} = 7$ TeV, soit $10 < p_{\mathrm{T}}^{\gamma} < 60$ GeV/c et $2,9 \times 10^{-3} < x_{\mathrm{T}}^{\gamma} = 2p_{\mathrm{T}}^{\gamma}/\sqrt{s} < 17,1 \times 10^{-3}$, en raison de la luminosité 20 fois supérieure, mais aussi de la plus grande acceptance de photons considérée. Les résultats finaux sont comparés aux calculs NLO pQCD avec JETPHOX en Fig. 6.3 et aux mesures ATLAS et CMS en Fig. 6.6. La concordance des données avec la théorie confirme les calculs théoriques et démontre la cohérence des différentes mesures. L'accord entre les rapports des sections efficaces à diverses energies mesurés et calculés, montrés dans les Figs. 6.7 et 6.8 renforcent cette conclusion.

Cette mesure est réalisée pour la première fois dans la gamme de 7–10 GeV/c dans un système de collision au LHC. Elle s'étend d'un ordre de grandeur inférieur à celui d'ATLAS ($p_{\mathrm{T}}^{\gamma} > 125$ GeV/c) et de CMS ($p_{\mathrm{T}}^{\gamma} > 190$ GeV/c) à la même énergie de collision. La portée en GeV/c plus faible d'ALICE, comparée aux autres expériences du LHC à rapidité centrale, sera utile pour les études futures des sections efficaces de photons isolés et des corrélations entre photons isolés et jets ou hadrons, utilisées pour contraindre les calculs pQCD, les PDF et les FF, en particulier. De plus, ces travaux jettent les bases de l'étude des modifications induites par le milieu des sondes dures lors des collisions noyau–noyau et du facteur de modification de type QGP dans les petits systèmes en collision.

La mesure fournit également le x de Bjorken le plus faible sondé à ce jour avec des photons isolés à rapidité centrale, $1,1 \times 10^{-3} < x \approx x_{\mathrm{T}}^{\gamma} = 2p_{\mathrm{T}}^{\gamma}/\sqrt{s} < 30,8 \times 10^{-3}$, montrant dans la Fig 6.9 une concordance entre toutes les mesures de photons isolés disponibles a diverses $\sqrt{s}$ en collisions pp at p$\bar{\mathrm{p}}$ à rapidité centrale avec une échelle commune de $(\sqrt{s})^{n=4,5}$ sur plusieurs ordres de $x_{\mathrm{T}}^{\gamma} \approx x$ de Bjorken. Le faible x mesuré fournira des contraintes sur la PDF du gluon.

Grâce à une augmentation significative de la luminosité lors des Runs 3 et 4 du LHC, les mesures de photons isolés peuvent être réalisées avec des incertitudes systématiques réduites, comme nous l'avons constaté en comparant la pureté des mesures à $\sqrt{s} = 13$ TeV, statistiquement riches, du Run 2 à celles d'autres échantillons, ce qui renforce les contraintes des prédictions théoriques. Avec l'augmentation de la taille de l'échantillon, une autre mesure intéressante pourrait être la section efficace de photons

isolés en fonction de la multiplicité des particules dans les collisions pp. Les photons n'étant pas modifiés en présence hypothétique d'un milieu QCD, cette mesure peut être utilisée pour estimer les biais induits par la sélection de la multiplicité des particules (présence de jets dans l'événement, considérations géométriques de la collision) dans toutes les autres mesures de sections efficaces de particules ou de jets basées sur la multiplicité des particules. En particulier, le rôle de la sélection de la multiplicité des particules dans les petits systèmes comme les collisions pp doit être pris en compte, car il peut influencer les phénomènes observés et éclairer l'existence potentielle de QGP dans ces systèmes. Bien que le QGP soit traditionnellement associé aux collisions d'ions lourds, des études récentes suggèrent que, sous certaines conditions, de petits systèmes pourraient également présenter un comportement similaire au QGP.

De plus, en comparant les résultats des collisions pp à ceux des collisions d'ions lourds, il est possible de distinguer les effets de la matière nucléaire froide des effets du milieu QCD chaud. Cette approche comparative améliorera notre capacité à isoler les contributions spécifiques du QGP à la perte d'énergie et à la fragmentation des partons, fournissant ainsi des preuves plus claires de son existence et de ses propriétés.

Cette comparaison est particulièrement importante lors de l'examen de petits systèmes, car elle pourrait révéler de nouveaux mécanismes ou conditions de formation du QGP, élargissant ainsi notre connaissance de cet état extrême de la matière.

Les études des distributions angulaires et des propriétés cinématiques des paires photon isolé–jet contribueront à affiner notre compréhension des processus de fragmentation des partons, car le photon restant inchangé lors de sa traversée du milieu définit la référence de la cinématique initiale de diffusion dure, tandis que les hadrons associés transmettent les informations sur les modifications subies par le parton à l'intérieur du milieu. Par conséquent, on peut étiqueter les jets avec des photons isolés et étudier les modifications des jets induites par le milieu et les effets de sillage induits en utilisant les futures données disponibles au LHC et à ALICE.

Contributions on behalf of ALICE Collaboration

Paper:

- **Performance of the ALICE Electromagnetic Calorimeter**

Contribution to the exotic cluster removal section

JINST 18 (2023) P08007

- **Measurement of the inclusive isolated-photon production cross section in pp collisions at $\sqrt{s}$ = 13 TeV**

ALICE Collaboration, PC members: G. Conesa Balbastre, R. Xu, Y. Mao, D. Zhou

Eur. Phys. J. C 85, 98 (2025)

As highlight of the January/February 2025 issue of CERN Courier

Major conference talks:

- **CLHCP2023, 16–20 November 2023, Shanghai, China**

"Study of isolated photon production with ALICE"

- **CLHCP2022, 2–6 November 2022, online**

"Measurement of isolated photon production cross section in pp collisions at 13 TeV with ALICE"

- **ICHEP2022, 6–13 July 2022, Bologna, Italy**

"Probing the initial state with isolated photon production in small collision systems with ALICE"

- **FCPPL2021, 13–16 December 2021, online**

"Isolated Photon measurement in pp and p–Pb collisions with ALICE at the LHC"

Service work:

- 03/2018 –03/2020: **PWGGA train operator**

Acknowledgements

Time flies—my doctoral research is now coming to a close. Looking back on this challenging yet rewarding journey, I am filled with gratitude. Throughout these years of study, I have not only gained knowledge and skills, but also experienced unwavering support and encouragement from my supervisors, colleagues, family, and collaborators.

First and foremost, I would like to express my deepest gratitude to my supervisors, Prof. Daicui Zhou, Prof. Yaxian Mao, and Dr. Gustavo Conesa Balbastre. Their expert guidance, unwavering support, and deep commitment to scientific inquiry have been instrumental in shaping this research on the measurement of isolated photon cross sections in proton–proton collisions at a center-of-mass energy of 13 TeV. Their insightful comments, patience, and encouragement throughout the years have not only helped me overcome various challenges in the field of high-energy physics but also inspired me to keep growing and making progress on the path of scientific research. Beyond academic instruction, their commitment to scientific truth and open-minded, inclusive spirits has had a profound impact on me. It is from their example that I have learned how to pursue excellence in detail, as well as the importance of embracing diverse perspectives—qualities that will remain among the most treasured assets in both my professional and personal life.

I am deeply thankful to my thesis committee members —Prof. Guoliang Ma, Dr. François Arleo, Prof. Shuang Li, Dr. Cvetan Valeriev Cheshkov, Dr. Marie Germain, Prof. Xiaomei Li, Prof. Johann Collot, and Prof. Yaping Wang —for their valuable feedback, constructive suggestions, and the time they invested in reviewing my work.

I would like to acknowledge the professors and teachers in the Institute of Particle Physics (IOPP) and Laboratoire de Physique Subatomique et de Cosmologie (LPSC). The stimulating discussions and shared insights at both institutions have significantly enriched my understanding and approach to measuring isolated photon cross sections at $\sqrt{s} = 13$ TeV using the ALICE experiment. My sincere gratitude also goes to the technical and administrative staff at IOPP and LPSC, whose dedicated efforts in maintaining the necessary infrastructure and resources.

This work is based on the ALICE international collaboration. I sincerely thank all scientists and engineers in the ALICE collaboration for their tireless efforts, which have provided such a vibrant, collaborative, and multicultural environment for frontier high-energy physics research. In particular, I wish to thank Dr. Florien Jonas for providing the theoretical data used in this analysis, as well as for

his patient discussions and expert guidance on various fundamental physics issues related to this work. And also deeply grateful to Dr. Marie Germain for her meticulous guidance and patient explanations during my data analysis, which greatly helped me better understand the core of the research and smoothly advance my work.

In addition, I would also like to express my sincere thanks to the China Scholarship Council (CSC) for making this joint PhD training program possible. The opportunity provided by CSC has been invaluable for both my academic development and personal growth during my studies abroad. I am also truly thankful to my labmates and friends – whether it was late-night discussions over research or mutual care and companionship in daily life – that brought warmth and strength to my journey abroad. Your support and encouragement during difficult times gave me the motivation and confidence to keep going.

Last but not least, I owe my deepest gratitude to my parents and family for your constant understanding, encouragement, and companionship, which have given me enduring strength even when far away from home. No matter what challenges I face, your support remains the greatest driving force behind my perseverance.

With this acknowledgment, I express my sincere appreciation to everyone who has supported, cared for, and accompanied me throughout this chapter of my academic journey.

Ran XU

09/06/2025